VSEBINA – CONTENTS

IZVIRNI ZNANSTVENI ČLANKI – ORIGINAL SCIENTIFIC ARTICLES

STROKOVNI ČLANKI – PROFESSIONAL ARTICLES

DOGODKI – EVENTS

ELECTRIC-ARC-FURNACE PRODUCTIVITY OPTIMIZATION

OPTIMIZACIJA PRODUKTIVNOSTI ELEKTROOBLOČNE PEČI

Klemen Stopar[1], Miha Kovačič[1,2], Peter Kitak[3], Jože Pihler[3]

[1]Štore Steel d.o.o., Železarska cesta 3, 3220 Štore, Slovenia
[2]Laboratory for Multiphase Processes, University of Nova Gorica, Vipavska 13, 5000 Nova Gorica, Slovenia
[3]Faculty of Electrical Engineering and Computer Science, Smetanova ulica 17, 2000 Maribor, Slovenia
klemen.stopar@store-steel.si

Štore Steel Ltd. is one of the largest producers of spring steel, forging steel and extra-machinability steel in Europe. Its electric-arc furnace (EAF) is one of the most important pieces of equipment in the steel plant. An EAF enables a plant to melt scrap as fast as possible with the maximum energy input. An electrical energy input depends on the secondary current and secondary voltage of the furnace transformer tap, influencing the electric-arc burning stability. The most influential EAF-transformer parameters (secondary current, secondary voltage, inductive resistance) have been optimized with the differential-evolution-algorithm method. The optimization results allowed a higher productivity (5 %), lower energy consumption (3.5 %) and lower productivity costs (8.7 %) achieved over a one-year period.

Keywords: electric-arc furnace, transformer, productivity, optimization, differential evolution

Štore Steel, d. o. o., je med največjimi proizvajalci vzmetnih jekel, jekel za kovanje in jekel z izboljšano obdelovalnostjo v Evropi. Elektroobločna (EOP) peč je najpomembnejši agregat v jeklarni. V EOP želimo pretaljevati jekleni odpadek čim hitreje, z največjim vnosom energije. Vnos električne energije je odvisen od sekundarnih napetosti in tokov v izbrani stopnji transformatorja peči, kar vpliva tudi na stabilnost gorenja električnega obloka. Najvplivnejši parametri napajalnega sistema (sekundarna napetost in tok, induktivna upornost) so bili predmet optimizacije z metodo diferenčne evolucije. Z uporabo rezultatov optimizacije smo dosegli višjo produktivnost (5 %), manjšo porabo energije (3,5 %) in manjše stroške proizvodnje (8,7 %) v opazovanem obdobju enega leta.

Ključne besede: elektroobločna peč, transformator, produktivnost, optimizacija, diferenčna evolucija

1 INTRODUCTION

Since its introduction, the EAF has been widely used in the metallurgy and smelting industries. An EAF working-point adjustment is the key factor in the efficiency of the EAF steelmaking. An AC EAF operation has a non-linear, time-varying behaviour. Because of this behaviour, the arc furnace creates harmonic pollution, voltage-flickering changes, frequency shifts and an unbalance of the three-phase system. These problems would severely affect the EAF productivity, the electrical-energy quality, the transmission efficiency and the equipment in a safe operation. An EAF process operation begins with charging the scrap steel into the furnace. Initially, the transformer voltage tap is kept at a low setting due to an instable arc burning when arcing to solid scrap. As the pool of liquid steel forming at the bottom of the arc furnace grows, the voltage setting and, hence, the power level can be increased due to a more stable arc behaviour. To reduce the problems caused by an instable arc burning, the following solutions are available:[1–3]

- decreasing the arc voltage,
- increasing the secondary (arc) current at the same secondary voltage,
- increasing the overall supply-system reactance.

Therefore, to deal with the problems of a reduced productivity, harmonic appearance and reduced flicker in an EAF supply system, this paper puts forward an approach for an optimally selected secondary (arc) current at each furnace-transformer voltage tap, with regard to the given ratio of the arc resistance to the overall supply-system reactance. For the new furnace-transformer secondary voltages, for each tap and stray, the reactance (its voltage drop) could be determined. The stray-reactance voltage drop could be in the range of 6–12 % of the nominal voltage depending on the design of the primary and secondary transformer windings.

The following steps were used:
- determination of the supply-network impedances, without the EAF transformer,
- determination of the arc impedances with regard to the arc-burning stability,
- determination of the EAF model,
- optimization of the EAF operation with regard to the supply-network impedances, the EAF arc impedance and the selected EAF model.

To determine the optimum secondary (arc) current and the furnace stray reactance at a given furnace-transformer secondary voltage, a simplified model of EAF was developed. The arc resistance was calculated according to the Cassie[4] equation and the arc reactance accord-

ing to the Köhle[5] equation. The parameters from the simplified EAF model were used with a differential evolution algorithm in order to determine the optimum arc current and furnace-transformer stray reactance for each tap of the furnace transformer (the secondary voltage). For each transformer tap the maximum electrical power for the conversion is used for a particular length of the electric arc[3] and any deviation from this optimum length impairs the power-utilization efficiency.

In this paper the optimization results for each transformer tap are presented. Because of the optimization results, a higher productivity, lower operational costs and a lower energy consumption were achieved.

2 EXPERIMENTAL BACKGROUND

In general, there are several ways of operating an EAF and different ways of supplying the power. Basically, a more effective way of supplying the power depends on a number of restrictive facts, like the power-supply limitations, the EAF shell dimensions, the electrode configuration and the pitch-circle diameter. The electric-arc radiation on the refractory and water-cooled wall panels depends on the EAF shell diameter and the length of the arc (the arc voltage). In general, there are recommendations about the furnace-transformer apparent power per ton of liquid steel. A typical furnace-transformer power is up to 1.5 MV A/t of liquid steel. Another important parameter is the ratio between the arc resistance and the reactance of the supply network. In a modern design of an EAF supply network, the ratio should be near or below 1.5 in order to assure an acceptable impact of the EAF back on the electric-power-supply system. On the other hand, this ratio assures a stable arc burning in every state of the EAF. Regarding all the restrictions and recommendations, the arc-furnace-transformer secondary voltages have to be defined. Together with the secondary voltages, the arc resistance, the arc reactance and, consequently, the electric-arc burning stability are also defined. In addition, the transformer stray reactance and its voltage drop can be chosen when considering the furnace-transformer winding construction.

2.1 Determination of the supply-network impedances

The supply network (a connection from the point of common connection to the furnace transformer) uses an isolated neutral point. On the supply-network side there are the following limitations:
- the apparent power of the step-down transformer limited to 60 MV A,
- connection lines (4 × 3 × 1 × 300 mm², aluminum) and
- distribution center near the furnace transformer.

The supply-network impedances at the 110 kV and 35 kV voltage levels are converted, over the transforma-tion ratio, to the secondary voltage level of the furnace transformer separately for each tap. The transformation ratio is defined for each tap of the furnace-transformer secondary voltage to its primary voltage. All the impedances are converted as follows:

$$Z' = Z \cdot \frac{1}{t_R^2},\tag{1}$$

Z is the impedance of the device at its rated voltage,
Z' is the impedance of the device producing the furnace-transformer secondary voltage for each tap,
t_R is the transformation ratio.

The impedance at the point of common connection is defined as:

$$Z_{TM} = \frac{(c \cdot U_N^2)}{S_k^"}\tag{2}$$

c is the voltage correction factor at the point of short circuit, $c = 1.1$
$S_k^"$ is the symmetrical short-circuit apparent power.

The impedance of the 35 kV connection lines is based on the data from[6] and defined as $R_{35\,kV} = 0.1\ \Omega/km$ and $X_{35\,kV} = 0.18\ \Omega/km$ for one line. Actually, there are four parallel lines installed with a common length of 440 m:

$$Z_{35kV} = R_{35kV} + jX_{35kV}\tag{3}$$

The impedance of the step-down transformer is defined as:

$$Z_{SDT} = \frac{u_K \cdot U_N^2}{100 \cdot S_N}\tag{4}$$

According to[6] for a high-voltage apparatus, the resistance value being 10 % of the impedance can be defined as:

$$R_{SDT} = 0.1 \cdot Z_{SDT}\tag{5}$$

The reactance for the step-down transformer is defined as:

$$X_{SDT} = \sqrt{Z_{SDT}^2 - R_{SDT}^2}\tag{6}$$

According to equations (4), (5) and (6), the impedance, resistance and reactance for a furnace transformer can be defined in the same way. For the new furnace transformer the stray reactance and its voltage drop are not yet known. Therefore, just a range of the voltage drop (in fractions from 6 % to 12 %) caused by the stray reactance is given.

By now the impedances of the high-voltage supply network have been defined and converted into the secondary-voltage level for each tap of the furnace transformer. The impedances on the secondary side of the furnace transformer could not be measured. On the secondary side, there are the impedance from the high-current lines (short-circuit impedance) and the arc impedance. The measurements of the short-circuit impedances are made by diving two electrodes at the same time into the melt

for a short period of time. Three measurements should be done each time with two different electrodes. At the time of the measurements, the furnace transformer should be set to the lowest voltage tap to prevent the secondary current of the furnace transformer from rising over the rated value. These measurement results are as follows:

$$Z_{SC} = R_{SC} + jX_{SC} \qquad (7)$$

2.2 Determination of the arc impedance

The arc impedance is explained with the arc resistance (the Cassie-Mayr arc model) and the arc reactance (the Köhle model). The Cassie-Mayr arc model successfully describes the key arc features as circuit elements.[7] The Cassie-Mayr arc model treats the arc resistance, R_{ARC}, as a dynamic variable, which is described as:

$$\frac{dR_{ARC}}{dt} = \frac{R_{ARC}}{\tau} \cdot \left(1 - \frac{U_{ARC} \cdot I_{ARC}}{P}\right) \qquad (8)$$

Here, I_{ARC} is the current applied to the arc, U_{ARC} is the arc voltage, P is the typical power loss of the arc and τ is the time scale. As Cassie took the higher current in the arc column for his model, the Cassie equation can be used to determine the arc resistance. The electrical arc model can be described as a non-linear time-varying model. It can be described with the impedance that varies according to the scrap melting time in an EAF. The arc resistance can be represented with the Cassie equation without taking into account the complex physical processes of burning arcs. Assuming a constant temperature in the arc column, constant cooling by the entire volume and heat dissipation, the sinusoidal current and large time constants,[4] the following relation can be written:

$$R_{ARC} = \frac{\sqrt{2} \cdot U_{ARC}}{I_{ARC} \sqrt{1 - \frac{\sin(2\omega t + \rho)}{1 + (\omega \vartheta c)^2}}} \qquad (9)$$

where:

$$\vartheta c = \frac{Q}{P_H} = 1, \text{ because of assumption } P_H = Q \qquad (10)$$

Q is the accumulated heat in the arc column,
P_H is the dissipated heat from the arc column,
U_{ARC} is the arc voltage between the cathode and anode,

$$U_{ARC} = \frac{U_{12}}{\sqrt{3}} - \left(U_{kat} + I_{ARC} \cdot \sqrt{R_{SC}^2 + X_{SC}^2}\right) \qquad (11)$$

I_{ARC} is the arc current in the arc column.

It is well known that an EAF has a lower active energy consumption than might be expected according to the calculated arc resistance. An additional reduction in the active power is caused by the arc reactance.[5] Arc reactance is caused by an electromagnetic induction (because of the non-linear and time-varying characte-
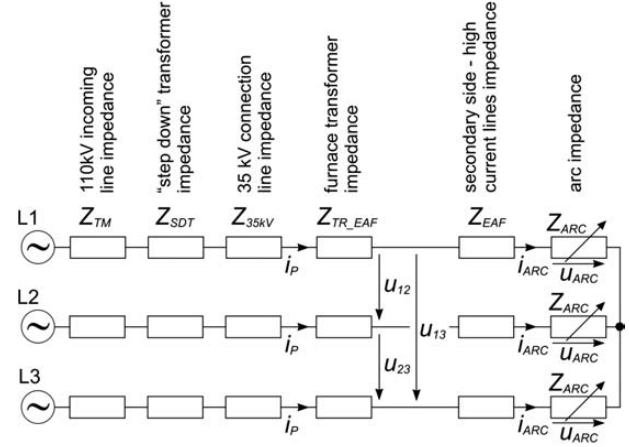
Figure 1: Equivalent-circuit diagram for an EAF
Slika 1: Nadomestno vezje elektroobločne peči

ristic of the burning arc). The arc reactance defined by the Köhle model[5] is expressed as:

$$\frac{X_{ARC}}{X_{SC}} = K_1 \cdot \frac{R_{ARC}}{X_{SC}} + K_E \cdot \left(K_2 \cdot \frac{R_{ARC}}{X_{SC}} + K_3 \cdot \left(\frac{R_{ARC}}{X_{SC}}\right)^2\right) \qquad (12)$$

where constants $K_1 = 0.08$, $K_2 = 0.13$, $K_3 = 0.04$ and time $T_X = 18$ min are defined experimentally:

$$K_E = e^{-\frac{t}{T_X}} \qquad (13)$$

For the EAF in Store Steel Ltd. the equivalent-circuit diagram is shown in **Figure 1**.

2.3 Determination of an EAF model

For an EAF model all the supply-network impedances, the arc impedance and secondary voltages for each tap of the furnace transformer are needed as the input data. From this data it is possible to determine all the necessary parameters of the EAF model. For a selected secondary-voltage tap and a given secondary current the furnace operating point can be calculated as follows:

$$U_{1S}' = t_r \cdot (U_1 - I_p \cdot Z_p) \qquad (14)$$

$$t_r = \frac{U_{1zS}}{U_{1zp}} \qquad (15)$$

$$I_p = I_S \cdot t_r) \qquad (16)$$

$$S_S = \sqrt{3} \cdot U_1' \cdot I_S \qquad (17)$$

$$P_S = \sqrt{S_S^2 - Q_S^2} = \sqrt{S_S^2 - (3 \cdot I_S^2 \cdot X_{SC})^2} \qquad (18)$$

$$P_{ARC} = P_S - P_{SIZG} = P_S - 3 \cdot I_S^2 \cdot R_{SC} \qquad (19)$$

$$R_{ARC} = \frac{P_{ARC}}{3 \cdot I_S^2} \text{ or } R_{ARC} = \frac{\sqrt{2} \cdot U_{ARC}}{I_{ARC} \sqrt{1 - \frac{\sin(2\omega t + \rho)}{1 + (\omega \vartheta c)^2}}} \qquad (20)$$

$$X_{ARC} = R_{ARC} \cdot K_1 + K_E \cdot K_2 \cdot R_{ARC} + K_E \cdot K_3 \cdot \frac{R_{ARC}^2}{X_{SC}} \quad (21)$$

$$X'_{1SUM} = t_r^2 \cdot (X_{TM} + X_{SDT} + X_{35kV} + X_{TR_{EAF}}) \quad (22)$$

$$K_S = \frac{X_{SC} + X'_{1SUM}}{R_{ARC}} \quad (23)$$

In addition to the secondary voltage, the EAF working point is also determined by the secondary current. The result of the criteria function is used to determine, at which EAF-transformer secondary voltage and current the arc burning is stable.

3 EAF OPERATION OPTIMIZATION

The differential-evolution method is a relatively new optimization algorithm that was presented by Price and Storn.[8] It is based on the origins of new populations in the evolution of mankind.

DE is the so called steady-state algorithm where new candidates do not compose an entirely new population but are simply added to the existing one. This method accelerates the convergence of the algorithm because the currently calculated quality individuals are immediately
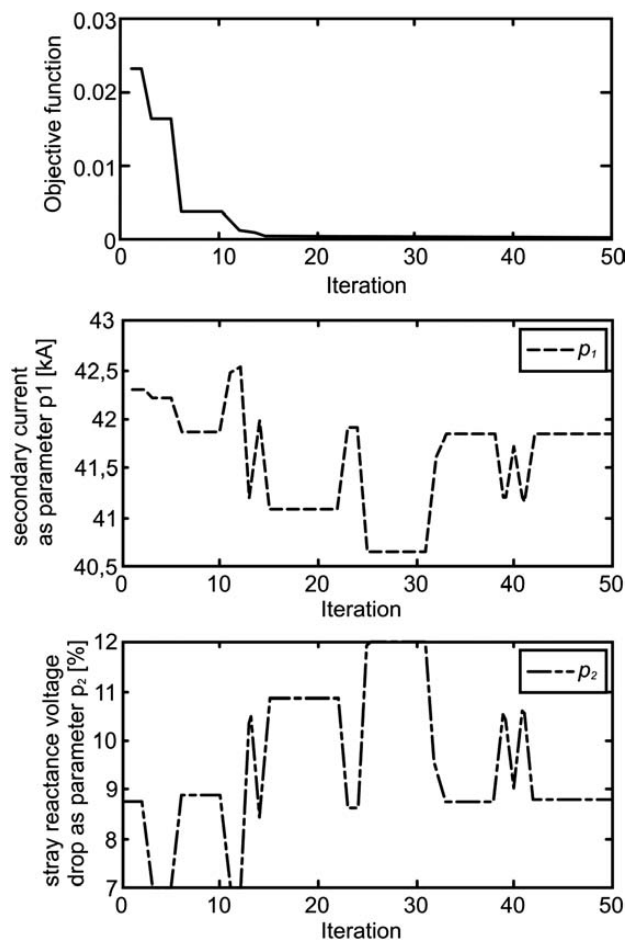
Figure 2: Differential-evolution iteration results
Slika 2: Rezultat iteracij algoritma diferenčne evolucije

used for the new-candidate generation. In addition to the good convergence properties of DE, its algorithm is simple to understand and to implement. DE is also particularly easy to work with as it has only a few control variables that remain fixed throughout the entire optimization procedure.[8]

The following evolutionary parameters were selected for the process of simulated evolutions: 20 for the size of the population of organisms (*NP*), 50 for the maximum number of iterations, 0.8 for the crossover probability (*CR*) and 0.6 for the mutation factor (*F*). The crossover strategy of RAND/1/bin was selected.

A differential-evolution algorithm was run for each furnace-transformer voltage tap. The EAF-transformer secondary voltage and current should be chosen opti-
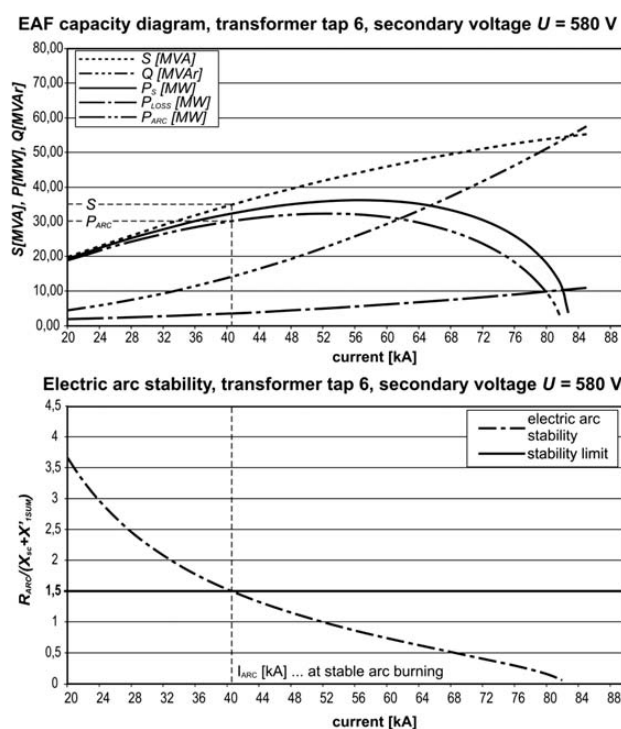
Figure 3: Capacity diagram for transformer voltage tap 6
Slika 3: Diagram moči za 6-napetostno stopnjo transformatorja

Table 1: Differential-evolution-method calculation results
Tabela 1: Rezultati izračuna z metodo diferenčne evolucije

Transformer voltage tap	Secondary voltage (V)	p_1/kA	p_2/%	Reactance (mΩ)
1	430	36.32	10.18	0.294
2	460	37.84	9.3	0.307
3	490	38.92	9.63	0.361
4	520	40.14	8.95	0.378
5	550	40.64	10.07	0.476
6	580	41.06	10.86	0.571
7	610	41.60	10.92	0.634
8	640	42.58	9.64	0.617
9	670	42.12	11.48	0.804
10	700	42.42	11.29	0.865
11	730	42.86	10.66	0.889

mally at a given ratio K_S (criteria function, equation 23). The secondary voltage and current at a given ratio K_S are optimal when the arc is burning stably, causing as little disturbance, voltage dips and asymmetry to the supply network as possible, whereby the EAF is at its most efficient operation and the melting of scrap is fast. As an example of a differential-evolution-algorithm result calculation, the results for furnace-transformer voltage tap 6 are shown (**Figure 2**).

For each transformer-voltage tap, optimization results using differential-evolution algorithm are shown in **Table 1**.

The differential-evolution optimization results for transformer voltage tap 6 can be presented as an EAF capacity diagram (**Figure 3**).

4 CONCLUSION

The overall energy intake to the EAF can be increased in two ways: by increasing the input of electrical power or/and increasing the intake of chemical energy. The EAF system has a very sensitive balance of its optimum operation. The furnace transformer should achieve these optimum values of the secondary voltage and current in order to have the highest possible electrical-energy input to the EAF, with minimum losses and consumption of all the other materials.

At the beginning, a determination of the supply-network impedances was performed. Afterwards the EAF arc impedance was determined with regard to the arc-burning stability. After the EAF-model selection, a differential-evolution algorithm was used for the optimization. An algorithm was run for each EAF-transformer voltage tap, and the calculation results of the stray reactance (or its voltage drop) and secondary current were determined for each transformer voltage tap. Also, a capacity diagram was plotted for each voltage tap. By installing a new furnace transformer, in comparison to the old furnace transformer, the following results were achieved:

- The tap-to-tap time was reduced from 90 min to 85 min (a 5.88 % shorter tap-to-tap time).
- The average daily production of the EAF has risen by 50 t of liquid steel (approximately 5 %).
- The consumption of electrical energy has been reduced by 3.5 %, from 450 kW h/t to 440 kW h/t.
- The consumption of the refractory material per year has been reduced, due to a higher productivity, from 4.25 EUR/t of liquid steel to 4.1 EUR/t of liquid steel (a reduction of 3.7 %).
- The consumption of other energy sources has also been reduced by 1.5 % per ton of liquid steel.

The outcomes of this paper relating to the EAF-transformer properties and a determination of the furnace working point at stable arc burning can be effectively utilized to enhance the productivity and reduce all the expenses during an EAF production.

5 REFERENCES

[1] J. Bratina, Elektroobločna peč za proizvodnjo jekla, Slovenske železarne, Ravne na Koroškem 1994

[2] K. Stopar, Izbira lastnosti novega transformatorja EOP in obratovanje elektroobločne peči, Štore 2007

[3] S. Köhle, Model based of AC electric arc furnaces, consultation: Electrical Engineering of Arc Furnaces, Veranstaltung 51/03, Hamburg, 2003, 1–23

[4] J. Pihler, Stikalne naprave elektroenergetskega sistema, Druga dopolnjena izdaja, FERI, Maribor 2005

[5] S. Köhle, M. Knoop, R. Lichterbeck, Lichtbogenreaktanzen von Drehstrom – Lichtbogenöfen, IEW Elektrowärme international B, 51 (**1993**) 4, 175–185

[6] V. Jurjević, KONČAR Tehnički priručnik, 5th edition, Končar elektroindustrija, d. d., Zagreb 1991

[7] Y. Lee, H. Nordborg, Y. Suh, P. Steimer, Arc stability criteria in AC arc furnace and optimal converter topologies, 1-4244-0714-1/07, IEEE, (**2007**), 1280–1286

[8] K. Price, R. M. Storn, J. A. Lampinen, Differential Evolution: A Practical Approach to Global Optimization (Natural Computing Series), Springer, 2005

MULTIPLE REGRESSION MODELING AND PREDICTION OF THE SURFACE ROUGHNESS IN THE WEDM PROCESS

VEČKRATNO REGRESIJSKO MODELIRANJE IN NAPOVE-DOVANJE HRAPAVOSTI POVRŠINE PRI POSTOPKU WEDM

Mustafa Kemal Kulekci[1], Adnan Akkurt[2], Ugur Esme[1], Iskender Ozkul[3]

[1]Mersin University, Tarsus Technical Education Faculty, 33140 Tarsus-Mersin, Turkey
[2]Gazi University, Technical Education Faculty, Department of Industrial Arts, 06500 Teknikokullar-Ankara, Turkey
[3]Aksaray University, Faculty of Engineering, 68100 Aksaray, Turkey
uguresme@gmail.com

Wire electrical discharge machining (WEDM) process is a specialized thermal machining process capable of accurately cutting and machining mechanical parts with various hardnesses and intricate shapes. WEDM is also a modification of electrical discharge machining (EDM) and it has been widely used for a long time for cutting punches and dies, shaped pockets and other machine parts on conductive work materials. The surface roughness of a machined surface mainly depends on the feed rate, the current and pulse duration in the WEDM machining process. It also depends on the optimum selection of WEDM parameters. The present study focused on the multiple regression modeling and predicting the surface roughness of the Dievar hot-work tool steel during the WEDM process. Mathematical relationships between the surface roughness and WEDM cutting parameters (feed rate, current and pulse on time) have been investigated. The results show that the multiple regression analysis is a successful method for developing a mathematical model to predict the surface roughness.

Keywords: multiple regression model, WEDM, surface roughness

Obdelovanje z žično erozijo (WEDM) je poseben toplotni postopek, ki zagotavlja natančno rezanje in obdelovanje mehanskih delov z različno trdoto in zapleteno obliko. WEDM je modificirana elektroerozija (EDM) in se že dolgo uporablja za rezanje prebijal in orodij, oblikovanih žepov in drugih strojnih delov na prevodnem obdelovancu. Hrapavost površine je predvsem odvisna od hitrosti odvzema, toka in trajanja pulza pri WEDM-procesu obdelave. Odvisna je tudi od optimalne izbire parametrov pri WEDM. Ta študija je osredinjena na večkratno regresijsko modeliranje in napovedovanje hrapavosti površine orodnega jekla za delo v vročem Dievar pri obdelavi z WEDM. Preiskovana je bila matematična odvisnost med hrapavostjo površine in parametri rezanja WEDM (hitrost podajanja, tok in časovni impulzi). Rezultati kažejo, da je večkratna regresijska analiza uspešna metoda za razvoj matematičnega modela za napovedovanje hrapavosti površine.

Ključne besede: model večkratne regresije, WEDM, hrapavost površine

1 INTRODUCTION

Wire electrical discharge machining (WEDM) is a widely accepted, non-traditional material-removal process used to manufacture two- or three-dimensional components with complex shapes and profiles.[1] It is considered as a unique adaptation of the conventional electrical discharge machining (EDM) process, using an electrode to initialize the sparking process. However, WEDM utilizes a continuously travelling wire electrode, made of thin copper, brass or tungsten with a diameter of 0.05–0.3 mm, capable of achieving very small corner radii[1]. The movement of this wire is numerically controlled to achieve a desired three-dimensional shape and accuracy of a workpiece. The wire is kept in tension using a mechanical device reducing the tendency of producing inaccurate shapes. The mechanism of the material removal in the WEDM process involves a complex erosion effect by rapid, repetitive and discrete spark discharges between a wire tool and a workpiece immersed in a liquid dielectric (kerosene/deionized water) medium.[2] These electrical discharges melt and vaporize minute amounts of the work material, which are ejected and flushed away by the dielectric, leaving small craters on the workpiece.[2] **Figure 1** shows a schematic representation of the WEDM process.
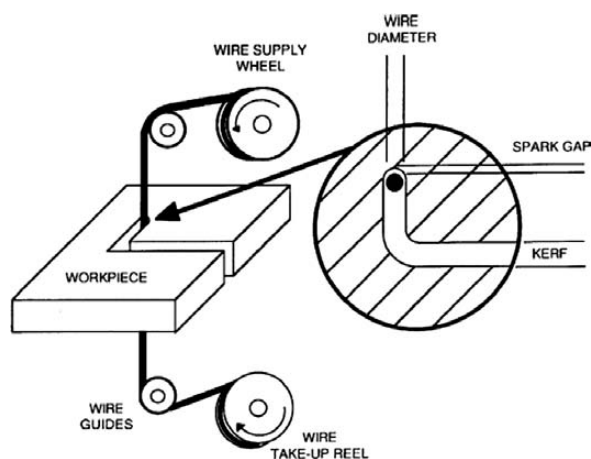
Figure 1: Schematic representation of the WEDM process[3]
Slika 1: Shematski prikaz WEDM-postopka[3]

In this process, as the material is eroded ahead of the wire and there is no relative contact between the tool and the workpiece, the work-material hardness is not a limiting factor for machining the material and there is no residual-stress generation.[2,3]

The selection of optimum machining parameters plays an important role in obtaining a higher cutting speed, a lower dimensional deviation, a better material-removal rate and a higher surface finish. Improperly selected parameters may result in serious consequences like short-circuiting of the wire and wire breakage.[2]

The degree of accuracy of workpiece dimensions obtainable and the fine surface finishes make WEDM particularly valuable for the applications involving a manufacture of stamping dies, extrusion dies and proto-type parts. Without WEDM the fabrication of precision workpieces requires many hours of manual grinding and polishing.[4–6] **Figure 2** shows some parts that were manufactured using the WEDM process.

Tosun et al.[6] determined the effect of machining parameters on the cutting width and material-removal rate on the basis of the Taguchi method. Tosun and Cogun[7] experimentally investigated the effect of cutting parameters on the wire-electrode wear. Tosun et al.[8] investigated, experimentally and theoretically, the effect of cutting parameters on the size of erosion craters (the diameter and the depth) on a wire electrode. Cogun and Savsar[9] investigated the random behavior of the time-lag durations of discharge pulses using a statistical model for different pulse durations, pulse-pause durations and discharge currents in EDM.

Scott et al.[10] developed the formulas for a solution of a multi-objective optimization problem to select the best parameter settings on a WEDM machine. They used a factorial design model to predict the measures of the performances as a function of the variety of machining parameters. Wang and Rajurkar[11] developed a WEDM frequency-monitoring system to detect on-line the thermal load on a wire to prevent the wire from rupture.

Figure 2: Some parts manufactured with the WEDM process[7]
Slika 2: Nekaj delov, izdelanih po WEDM-postopku[7]

Spur and Shoenbeck[12] investigated a finite-element model and explained the impact of a discharge on the anode as a heat source on a semi-infinite solid whose size and intensity are time-dependent in WEDM. Tarng et al.[13] developed a neural-network system to determine the settings of pulse duration, pulse interval, peak current, open-circuit voltage, servo-reference voltage, electric capacitance and wire speed for an estimation of the cutting speed and the surface finish. Spedding and Wang[14] presented a parametric combination using artificial neural networks and they also characterized the roughness and waviness of the workpiece surface and the cutting speed. Liao et al.[15] performed an experimental study to determine the effect of machining parameters on the material-removal rate (MRR), gap width and surface roughness. They determined the level of importance of machining parameters on the MRR. Lok and Lee[16] compared machining performances in terms of the MRR and surface finish by processing two advanced ceramics under different cutting conditions using WEDM. Ramakrishnan and Karunamoorthy[17] developed an artificial neural network with the Taguchi parameter design. Tsai et al.[18] studied the relationships between the heterogeneous second phase and the machinability evaluation of the ferritic SG cast irons in the WEDM process. Sarkar et al.[19] studied the features of a trim-cutting operation of the wire electrical discharge machining of -titanium aluminide. Caydas et al.[20] developed an adaptive neuro-fuzzy inference system (ANFIS) for modeling the surface roughness in the WEDM process. Hewidy et al.[21] developed mathematical models for correlating the inter-relationships of various WEDM process parameters such as peak current, duty factor, wire tension and water pressure on MRR, wear ratio and surface roughness. Puri and Bhattacharyya[22] considered the pulse-on time, wire tool offset and constant cutting speed to model the white-layer depth with the response surface methodology (RSM) technique in the WEDM process. Kuriakose and Shunmugam[23] used a multiple regression model to present the relationship between the input and output variables of the WEDM process, and then employed a non-dominated sorting genetic algorithm to optimize the process. Chiang and Chang[24] applied a gray relational analysis for optimizing the WEDM process while considering the cutting radius of a workpiece, on-time of discharge, off-time of discharge, arc on-time of discharge, arc off-time of discharge, servo voltage, wire feed and water flow as the process parameters, and surface-removal rate and surface roughness as the process responses. Ramakrishnan and Karunamoorthy[25] developed artificial neural network (ANN) based models and a multi-response optimization technique to predict and select the best cutting parameters of the WEDM process.

The previous works show that the research has focused on the effects of machining parameters, discharge energy, theory and experimental verification of

the crater formation on the wire electrode. The present study focuses on the modeling and prediction techniques to determine direct effects of WEDM parameters (pulse duration, current and table feed rate) on the surface roughness which is important for cutting dies and complex shapes.

2 EXPERIMENTAL SET UP AND PROCEDURE

The experimental studies were performed on a *Makino U32* WEDM machine tool. Different settings of pulse duration t (µs), current I (A) and table feed rate f (mm/min) were used in the experiments. During the experiments the voltage (40 V), the dielectric flushing pressure (5 kg/cm^2), the wire speed (12 m/min) and the wire tension (9 kg) were kept constant.

A Dievar hot-work tool-steel plate was used as the workpiece material with the dimensions of 60 mm × 240 mm × 24 mm. The percent chemical composition and mechanical properties of the workpiece material is given in **Table 1**.

Table 1: Chemical composition and mechanical properties of the AA7075 aluminum alloy[26]
Tabela 1: Kemijska sestava in mehanske lastnosti aluminijeve zlitine AA7075[26]

Chemical composition (w/%)	C	Mn	Mo	Cr	V
	0.32	0.5	2.3	5.0	0.5
Mechanical properties	Tensile strength (MPa)	Yield strength (MPa)	Reduction of area (%)	Elongation (%)	Hardness (HRC)
	1640	1380	55	13	48

As shown in **Figure 3**, the workpiece was drilled to insert the cutting wire inside the holes. A total of 24 holes were opened on each sample. After the WEDM machining of the holes, the average of three measurements on three holes was established to determine the surface roughness of the machined parts.

A CuZn37 Suncut brass wire with a 0.30 mm diameter and 1000 N/mm^2 tensile strength was used in the
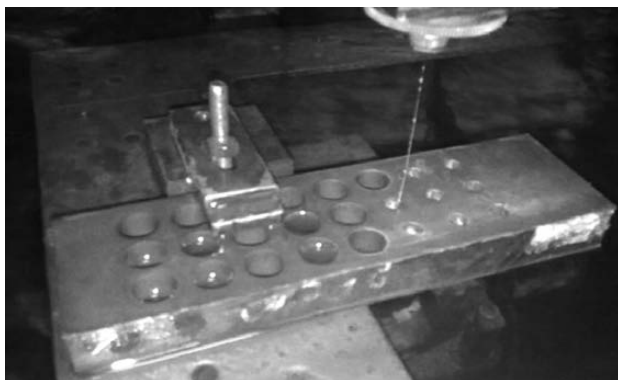
Figure 3: Experiment on the WEDM machine and the workpiece geometry
Slika 3: Preizkus na WEDM-napravi in geometrija obdelovanca

experiments. After the machining process, the measurements of the surface roughness were established using a *Mahr Perthometer M1* surface-roughness measurement device.

In the present study, the pulse duration, current and table feed rate were selected as the input parameters and the surface roughness was selected as the output parameter. A two-level factorial design method was carried out to mathematically model the output parameters. The levels of the factorial design used in the present study are shown in **Table 2**. The two levels of the factors are referred to as the low (–1) and the high (+1) levels.

Table 2: Factors and levels for factorial design
Tabela 2: Dejavniki in stopnje faktorske zasnove

WEDM parameters	Low level (–1)	Base level (0)	High level (+1)
Feed rate, f/(mm/min)	13.77	14.53	15.30
Current, I/A	35.10	37.05	39.00
Pulse duration, t/µs	4.95	5.22	5.50

3 DESIGN OF EXPERIMENTS (DOE)

A scientific approach to planning the experiments must be incorporated in order to perform an experiment most effectively. Statistical design of experiments (DOE) is a process of planning the experiments so that appropriate data can be collected and analyzed with statistical methods resulting in valid and objective conclusions.[4,26,27]

Factorial design is widely used in the experiments involving several factors where it is necessary to investigate the joint effects of the factors on a response variable. A very important special case of a factorial design is the one, where each of the k factors of interest has only two levels. A full factorial design is often used to fit a first-order response-surface model and to generate factor-effect estimates[4,27]. In the present study a full factorial design was employed to determine the minimum number of experiments for obtaining an adequate model of responses. Thus, in the present study, using three parameters, 8 (2^k) number of experiments was carried out to construct a regression model.

If the surface roughness is represented by R_a, the linear regression equation for these experiments can be written as:

$$R_a = \beta_0 + \beta_1 x_1 + \beta_2 x_2 + \beta_3 x_3 + \beta_4 x_4 + \beta_5 x_5 + \beta_6 x_6 \quad (1)$$

where β_0 is the response variable of the surface roughness at the base level; β_1, β_2, β_3 are the coefficients associated with each variable, β_4, β_5, β_6 are the interaction coefficients in the coded forms, x_1 is the feed rate, x_2 is the current and x_3 is the pulse duration at two levels used to arrive at a full two-level factorial experiment.

4 RESULTS AND DISCUSSIONS

The experiments were carried out under different process conditions. **Table 3** shows the full factorial-design matrix used in this study.

Table 3: Full factorial-design matrix
Tabela 3: Zasnova polne faktorske matrike

	Process parameters			Response
Run	f/(mm/min)	I/A	t/μs	R_a/μm
1	4.95	39.0	15.30	2.94
2	4.95	39.0	13.77	2.78
3	5.50	35.1	13.77	2.98
4	4.95	35.1	15.30	2.84
5	5.50	35.1	15.30	3.01
6	4.95	35.1	13.77	2.62
7	5.50	39.0	15.30	3.01
8	5.50	39.0	13.77	2.58

The regression equation obtained from the regression analysis based on the experiment set is expressed as equation (2). After calculating each of the coefficients of equation (1) and substituting the coded values of the variables for any experimental condition, the linear regression equation for the surface roughness can be obtained in actual factor forms as given in equation (2):

$$R_a = -10.9281 + 5.2722f + 0.3914I - 1.1785t - 0.1564fI + 0.04812ft + 0.0287It \qquad (2)$$

These equations indicate that the feed rate that has the biggest coefficient has the most significant effect on the surface roughness. The coefficients of the current and the pulse duration are smaller[4]. Therefore, the contribution order of the parameters obtained is as follows: the feed rate, the current and the pulse duration.

It is evident from **Table 4** that our set of data, predicted with a full factorial design, is close to experimental values. In the prediction of the surface-roughness values the average error is found to be 1.17 %.

According to the analysis of variances (ANOVA), given in **Table 5**, the contribution order of the WEDM parameters for the surface roughness is as follows – the feed rate: 48.98 %, the current: 10.46 % and the pulse duration: 1.05 %.

Table 5: ANOVA results for the circularity-surface-roughness measurements
Tabela 5: ANOVA-rezultati meritev površinske hrapavosti krožnih površin

Parameter	Degree of freedom	Sum of square	Mean square	F	Contribution (%)
f	1	0.0890	0.0890	3.34	48.98
I	1	0.0190	0.0190	0.71	10.46
t	1	0.0019	0.0019	0.07	1.05
fxI	1	0.0560	0.0560	2.12	30.82
fxt	1	0.0008	0.0008	0.03	0.44
Ixt	1	0.0150	0.0150	0.55	8.26
Total	6	0.1817			100

It is clear from the response surface plots shown in **Figures 4** to **6** that the increasing feed rate, current and pulse duration increased the surface roughness. As shown in the related graphs, the feed rate has the biggest effect on these responses. A small increase in the feed rate caused a big increment in the surface-roughness value. The current also has an effect on the responses but not more than the feed rate. It is clear that the pulse duration has a small effect on the responses. The maximum surface roughness of 3.01 μm was obtained
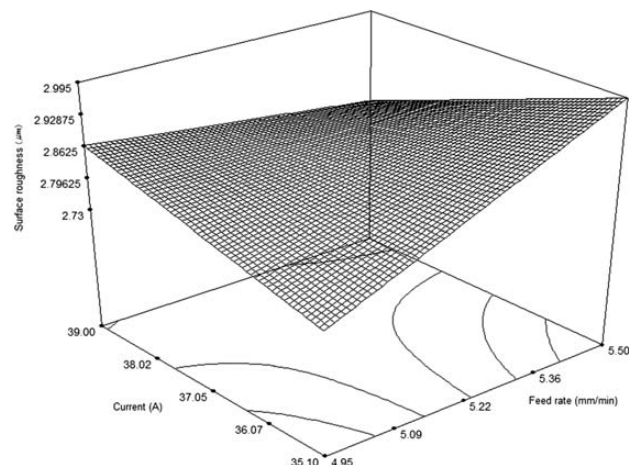
Figure 4: Response surface graph of the effects of the current and feed rate on the surface roughness
Slika 4: Ploskovni diagram vpliva toka in hitrosti podajanja na hrapavost površine

Table 4: Test and comparison sets used for the regression analysis
Tabela 4: Preizkusni in primerjalni podatki, uporabljeni pri regresijski analizi

Exp. no	f/(mm/min)	I/A	t/μs	*Experimental* R_a/μm	*Regression* R_a/μm	*Error* %
1	4.95	36.1	13.77	2.78	2.67	3.97
2	5.50	35.1	15.00	2.99	3.02	−0.91
3	4.95	39.0	14.77	2.86	2.88	−0.86
4	5.50	39.0	14.77	2.83	2.82	0.34
5	4.95	35.1	14.77	2.71	2.72	−0.53
6	5.50	39.0	15.00	2.88	2.87	0.43
			$\%\text{Error} = \dfrac{(R_{a\,\text{experimental}} - R_{a\,\text{predicted}})}{R_{a\,\text{experimental}}} \cdot 100$			*Average error:* 1.17 %

Figure 5: Response surface graph of the effects of the pulse on time and feed rate on the surface roughness
Slika 5: Ploskovni diagram vpliva trajanja pulza in hitrosti podajanja na hrapavost površine
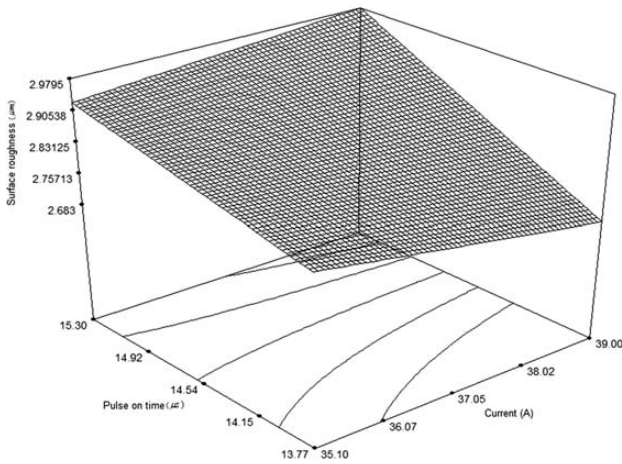
Figure 6: Response surface graph of the effects of the pulse on time and current on the surface roughness
Slika 6: Ploskovni diagram vpliva trajanja pulza in toka na hrapavost površine

with experiments #5 and #7, whereas the minimum surface roughness of 2.58 μm was obtained with experiment #8.

The analysis results for the responses have shown that the value of multiple correlation coefficient R^2 is 0.87 (which means that the explanatory variables explain 87 % of the variability in the response variable) for the surface roughness response. With the adjusted R-square (Adj R^2), the value closer to 1 indicates a better fit. It is generally the best indicator of the fit quality and it was found to be 0.90. The statistical analysis also proved that a full factorial regression analysis fits well with the experimental observations. **Figure 7** presents a comparison of the predicted and actual results for the surface roughness.
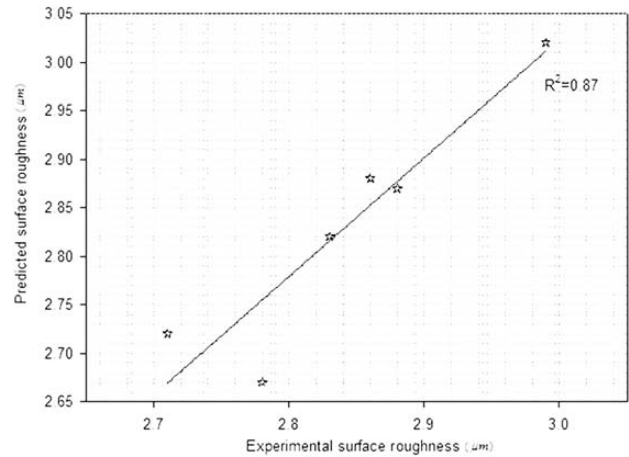
Figure 7: Comparison of experimental and predicted surface-roughness values
Slika 7: Primerjava eksperimentalnih in napovedanih vrednosti za hrapavost površine

5 CONCLUSIONS

The prediction of WEDM parameters for a quality product and dimensional accuracy plays a very important role in the planning of the WEDM process. The following conclusions can be drawn from this study:

- A full factorial regression analysis is a powerful tool for mathematical modeling and predicting the responses using a small number of experiments;
- Mathematical modeling of the response variables (surface roughness) was made using a full factorial design and the experimental results were compared with the predicted values of the response variables to decide about the closeness of the predictions to the experimental values;
- The priority order of WEDM parameters for the surface roughness was found to be as follows: the feed rate, the current and the pulse duration;
- The increasing feed rate caused a big increment in the surface-roughness value;
- Within the range of the input variables for the present case, the results showed that the predicted values calculated with a regression analysis are very close to the experimental values, with $R^2 = 0.87$.

6 REFERENCES

[1] K. H. Ho, S. T. Newman, S. Rahimifard, R. D. Allen, International Journal of Machine Tools & Manufacture, 44 (**2004**), 1247–1259
[2] R. Mukherjee, S. Chakraborty, S. Samanta, Applied Soft Computing, 12 (**2012**), 2506–2516
[3] D. Scott, S. Boyina, K. P. Rajurkar, International Journal of Production Research, 29 (**1991**) 11, 2189–2207
[4] U. Esme, A. Sagbas, F. Kahraman, Iranian Journal of Science & Technology, Transaction B, Engineering, 33 (**2009**), 231–240
[5] N. Tosun, C. Cogun, A. Inan, Machining Science and Technology, 7 (**2003**), 209–219
[6] N. Tosun, C. Cogun, G. Tosun, Journal of Materials Processing Technology, 152 (**2004**), 316–322

[7] N. Tosun, C. Cogun, Journal of Materials Processing Technology, 134 (**2003**) 3, 273–278

[8] N. Tosun, C. Cogun, H. Pihtili, International Journal of Advanced Manufacturing Technology, (**2003**) 21, 857–865

[9] C. Cogun, M. Savsar, International Journal of Machine Tools and Manufacture, 3 (**1990**), 467–474

[10] D. Scott, S. Boyina, K. P. Rajurkar, International Journal of Production Research, 11 (**1991**), 2189–2207

[11] W. M. Wang, K. P. Rajurkar, American Society of Mechanical Engineers, Production Engineering Division (PED), 55 (**1992**), 49–64

[12] G. Spur, J. Shoenbeck, CIRP Ann., 1 (**1993**), 253–256

[13] Y. S. Tarng, S. C. Ma, L. K. Chung, International Journal of Machine Tools Manufacture, 35 (**1995**), 1693–1701

[14] T. A. Spedding, Z. Q. Wang, Precision Engineering, 20 (**1997**), 5–15

[15] Y. S. Liao, J. T. Huang, H. C. Su, Journal of Materials Processing Technology, 71 (**1997**), 487–493

[16] Y. K. Lok, T. C. Lee, Journal of Materials Processing Technology, 63 (**1997**), 839–843

[17] R. Ramakrishnan, L. Karunamoorthy, Journal of Materials Processing Technology, 207 (**2008**), 343–349

[18] T. C. Tsai, J. T. Horng, N. M. Liu, C. C. Chou, K. T. Chiang, Materials and Design, 29 (**2008**), 1762–1767

[19] S. Sarkar, S. Mitra, B. Bhattacharyya, Journal of Materials Processing Technology, 205 (**2008**), 376–387

[20] U. Caydas, A. Hascalik, S. Ekici, 36 (**2009**), 6135–6139

[21] M. S. Hewidy, T. A. El-Taweel, M. F. El-Safty, Journal of Materials Processing Technology, 169 (**2005**), 328–336

[22] A. B. Puri, B. Bhattacharyya, International Journal of Advanced Manufacturing Technology, 25 (**2005**), 301–307

[23] S. Kuriakose, M. S. Shunmugam, Journal of Materials Processing Technology, 170 (**2005**), 133–141

[24] K. T. Chiang, F. P. Chang, Journal of Materials Processing Technology, 180 (**2006**), 96–101

[25] R. Ramakrishnan, L. Karunamoorthy, International Journal of Advanced Manufacturing Technology, 29 (**2006**), 105–112

[26] I. Ozkul, Gazi University Institute of Natural and Applied Sciences, MSc Thesis, 2012

[27] V. Gunaraj, N. Murugan, Welding Research Development Supplement, 9 (**2000**), 286–294

RELATIONSHIP BETWEEN A BAINITIC STRUCTURE AND THE HARDNESS IN THE WELD ZONE OF THE FRICTION-STIR WELDED X80 API-GRADE PIPE-LINE STEEL

ODVISNOST MED BAINITNO MIKROSTRUKTURO IN TRDOTO V PODROČJU ZVARA PRI TORNO VRTILNEM VARJENJU JEKLA X80 API ZA CEVOVODE

Hakan Aydin

Uludag University, Faculty of Engineering and Architecture, Department of Mechanical Engineering, 16059 Gorukle-Bursa, Turkey
hakanay@uludag.edu.tr

The present study focuses on the morphology of the weld zone, especially on the quantitative microstructural characterization of bainitic structures, and the relationship between post-weld bainitic structures and the hardness at the weld zone of the friction-stir welded X80 API-grade pipe-line steel. The employed rotating and traverse speeds of the polycrystalline cubic boron nitride tool during the friction-stir welding process were 350 r/min and 12.7 cm/min (5 inch per minute), respectively. A microstructural analysis of the weld was carried out using optical microscopy, orientation imaging microscopy and transmission electron microscopy, and the hardness variation was also mapped across the weld-plate cross section. The frictional heat and plastic flow during friction-stir welding create a granular bainitic structure (the stir zone), a lath-like upper bainitic structure (the hard zone) and a recrystallized equiaxed polygonal ferritic structure (the heat-affected zone) in the weld zone. The maximum hardness was observed in the classical upper bainitic microstructure in the hard zone. The minimum hardness was found in the heat-affected zone. A good correlation between the post-weld bainitic structures and the hardness in the weld zone was obtained; the hardness increases almost linearly with the decreasing bainite-lath and packet sizes.

Keywords: friction-stir welding, X80 steel, bainite, microhardness

Študija obravnava morfologijo področja zvara, posebno kvantitativno karakterizacijo bainitne mikrostrukture in odvisnost med bainitno strukturo po varjenju in trdoto zvara pri torno vrtilnem varjenju X80 API jekla za cevovode. Uporabljene hitrosti rotacije in prečne hitrosti orodja iz kubičnega bor nitrida med torno vrtilnim varjenjem so bile 350 r/min in 12,7 cm/min (5 inčev na minuto). Mikrostruktura zvara je bila pregledana s svetlobnim mikroskopom, z mikroskopijo usmerjenosti slik in s presevno elektronsko mikroskopijo. Prikazano je spreminjanje trdote po prečnem prerezu zvara. Toplota zaradi trenja in plastični tok materiala med torno vrtilnim varjenjem povzročita nastanek zrnate bainitne strukture (cona mešanja), latasti zgornji bainit (trda cona) in rekristalizirano poligonalno feritno strukturo (toplotno vplivana cona) v zvaru. Najvišja trdota je bila opažena v navadni mikrostrukturi gornjega bainita v trdi coni. Najnižja trdota je bila v toplotno vplivani coni. Ugotovljena je bila dobra korelacija med bainitno strukturo zvara in trdoto v coni zvara: trdota narašča skoraj linearno z manjšanjem bainitnih lat in velikostjo bainitnega sestava.

Ključne besede: torno vrtilno varjenje, jeklo X80, bainit, mikrotrdota

1 INTRODUCTION

The commercial high-strength low-alloy (HSLA) type X80 API-grade (American Petroleum Institute) steels produced with thermo-mechanically controlled processing (TMCP), which produces uniformly refined microstructures consisting of ferrite and bainite, are typically used in several oil and gas operations. The high strength, good toughness and excellent corrosion resistance of the X80 steel are obtained with chemical composition design, controlled rolling and controlled cooling. Welding is the essential process for large-scale pipelines for a long-distance transportation of crude oil or natural gas under a high pressure. A large heat input in the conventional fusion-welding processes such as the arc and laser-beam welding alters the microstructure, deteriorates the mechanical properties, promotes solidification cracking and expedites hydrogen embrittlement in the weld zone. For the pipeline industry in particular, friction-stir welding (FSW) is a promising technique that has several advantages over the conventional fusion-welding processes, due to its low heat input and absence of the melting and solidification process.[1,2] Compared to the conventional fusion-welding methods, the advantages of the FSW process include better mechanical properties, a low residual stress and distortion, and a reduced occurrence of defects.[3,4] FSW is also a "green technology" as it produces no arc radiation, no fumes and no hazardous waste. In addition, in the case of steels, it is expected that hydrogen-induced cracking is severely reduced.

FSW is a solid-state materials-joining process invented by TWI in 1991, which is presently attracting a considerable interest and has been extensively developed for aluminum alloys, as well as for magnesium, copper, titanium and steel.[1–5] The FSW process utilizes a non-consumable tool that is inserted into the abutting edges of the base metal. In this process, a cylindrical tool is rotated and traversed along a square-butt weld joint similar to the milling technique.[2] The joined material is

plasticized by the heat generated by the friction between the surface of the plates and the contact surface of a special tool, composed of two main parts: a shoulder and a pin.[6]

FSW has recently become an attractive process for joining HSLA-type steels.[7–11] However, it is very difficult to friction-stir weld on HSLA-type steels due to their high strength and high-heat-input demands for adequate welding. An interest in using this process to join steels has become popular due to the advancements in the friction-stir-welding tool development. Currently, the tool pins used such as polycrystalline boron nitride (PCBN) have been successful in welding HSLA-type steels.[7,10–12]

The microstructure and mechanical properties of friction-stir welds are dependent on the chemical composition and the microstructure of the base metal, the thermo-mechanical conditions during the FSW process and the cooling rate to room temperature. As mentioned above, the FSW process affects the material not only thermally but also mechanically. An understanding of the microstructural evolution during the FSW process and the mechanisms, with which the associated microstructures affect the mechanical and physical properties such as strength, fatigue, creep and corrosion, is critical.[13] So, the morphology of the weld zone for friction-stir welds need to be characterized.

The bainitic structures formed at the weld zone are the primary factor affecting the post-weld properties of FSWed X80 steels. Therefore, it is vital to carry out a characterization of the bainitic structures acquiring quantitative data in the weld zone in order to develop a more fundamental understanding of the FSW process in X80 steels. Although there are several studies on the microstructure and mechanical properties of FSWed HSLA steels, especially of the HSLA 65 steel, in the literature,[10–12,14] only a few limited studies focused on the microstructure and properties of the FSWed X80 steel.[15–18] The present study focuses on the morphology of the weld zone, especially on the quantitative microstructural characterization of bainitic structures and the relationship between the post-weld bainitic structures and the hardness at the weld zone in the FSWed X80 API-grade pipe-line steel.

2 EXPERIMENTAL DETAILS

The material used in this work was a commercial API X80-grade pipe-line steel plate with a thickness of 11 mm, whose chemical composition (mass fractions, w/%) is listed in **Table 1**. The test plate was friction-stir

Figure 1: RM-2 model FSW machine[19]
Slika 1: Model RM-2 stroja za FSW[19]
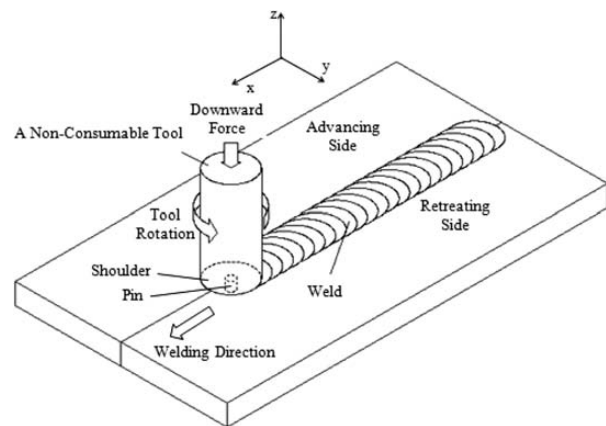
Figure 2: Schematic illustration of the FSW process
Slika 2: Shematski prikaz FSW-procesa

welded longitudinally parallel to the rolling direction in the bead-on-plate configuration using a modified MTI RM-2 FSW machine built with the stiffness and spindle characteristics designed specifically for the FSW of steels, including a full data acquisition and display capability (**Figures 1** and **2**).[19] This equipment uses servo-controlled axes and a variable frequency drive on the spindle, with the speed range of up to 1800 r/min and the motor torque of up to 550 N m. A polycrystalline cubic boron nitride (PCBN) CS4 tool was used for the weld

Table 1: Chemical composition (w/%) of the X80 steel used in this investigation
Tabela 1: Kemijska sestava (w/%) jekla X80, uporabljenega v tej preiskavi

Fe	C	Si	Mn	S	P	Ni	Cr	Cu	Ti	Mo	Nb	N	Al	V
Balance	0.04	0.135	1.7	0.001	0.013	0.147	0.41	0.263	0.014	0.005	0.102	0.006	0.031	0.002
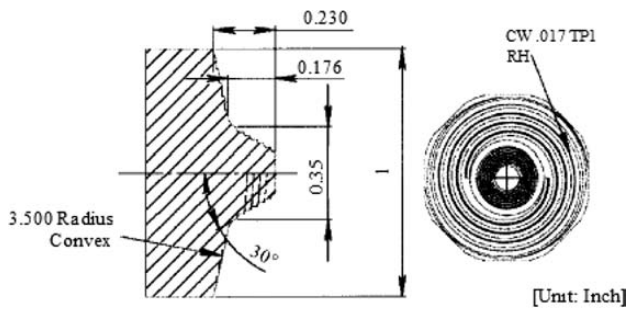
Figure 3: Geometry of the CS4 tool used in the welding[10,11]
Slika 3: Geometrija orodja CS4, uporabljenega pri varjenju[10,11]

(**Figure 3**). The employed rotating and traverse speeds of the tool during the FSW process were 350 r/min and 12.7 cm/min (5 inch per minute), respectively. All the welds were performed in the partial-penetration mode using a depth-controlled process (**Figure 4**). The tilt degree of the stir pin relative to the work-piece was set equal to 0.5° during the plunge and welding process. An argon gas atmosphere, at a flow rate of 1.1 m³/h, was used, as the shielding gas, to prevent a surface oxidation during the weld cycle and to prolong the tool life. The shielding-gas flow is realized by means of the canals in the tool holder (**Figure 5**).[20]

After welding, the FSW sample was cross-sectioned perpendicularly to the welding direction using a water-jet cutter for microstructural examinations and micro-hardness measurements. An Olympus GX51 microscope was used for optical observation. Orientation-imaging-microscopy (OIM) examination was carried out using an FEI XL-30 SFEG. The scan-step size was 0.15 μm. An electron beam of 25 kV and a spot size of 5 were used with a specimen working distance of 14 mm and a specimen tilt angle of 70°. The electron-backscatter-diffraction (EBSD) data was collected and analyzed with TSL OIM Data Collection version 5.2 and OIM Analysis version 5.2, respectively. The crystallographic data was expressed as an inverse pole figure (IPF) with image quality (IQ) maps and grain-boundary (GB) maps. Transverse samples for transmission-electron-microscopy (TEM) studies were prepared by cutting 3-mm-diameter cylinders with an electrical discharge
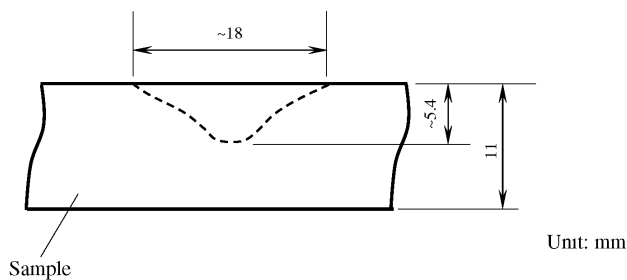
Figure 4: Partial-penetration mode (the FS weld nugget indicated with a dashed line)
Slika 4: Način delne penetracije (jedro FS-zvara je prikazano s črtkano linijo)
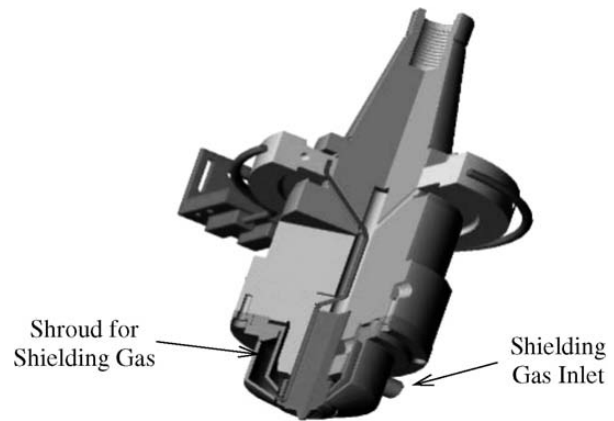
Figure 5: Shielding-gas flow in the tool holder[20]
Slika 5: Pretok varovalnega plina v nosilcu orodja[20]

cutting machine (EDM) from the selected areas of the sample. The electron-transparent thin sections for the TEM analysis were prepared by means of double jet electro-polishing, using a solution of 10 % (volume fraction) perchloric acid and 90 % glacial acetic acid with 25 V below 0 °C in the icy water. These thin foil specimens were examined with a Philips FEG model transmission-electron microscope at 300 kV to observe the microstructural details. In order to identify different zones in the weld region to be scanned in the OIM examinations and establish a correlation between the hardness and the post-weld bainitic structure, the hardness variation was mapped across the weld-plate cross-section using a LECO LM 100AT microhardness tester and the Amh43 version software using a diamond pyramid indenter with a load 500 g, dwell time 15 s and a indent spacing (vertical and horizontal) 400 μm. The microhardness map for the FSW sample was obtained with approximately 1800 and 1200 hardness indents in horizontal and vertical directions, respectively.

3 RESULTS AND DISCUSSION

The hardness map is a direct indicator of a microstructural evaluation during the FSW process. The hardness map of the FSWed X80 steel shows several features in the weld zone (**Figure 6**): the softening on both sides of the weld, the heat-affected zone (HAZ); almost the same hardness of the weld nugget as that of the base metal (BM), the stir zone (SZ); and the hardest region, the hard zone (HZ) within the advancing side (AS) of the weld zone, where the high temperature and strain were applied. The post-weld microstructures in the weld zone are influenced greatly by the peak temperature, the level of deformation and the local cooling rate to room temperature during the FSW process. The non-uniform distribution of hardness correlates to the non-uniform strain and heat gradient generated in the weld zone. The higher stresses on the AS of the weld result in an asymmetric heat generation across the SZ.
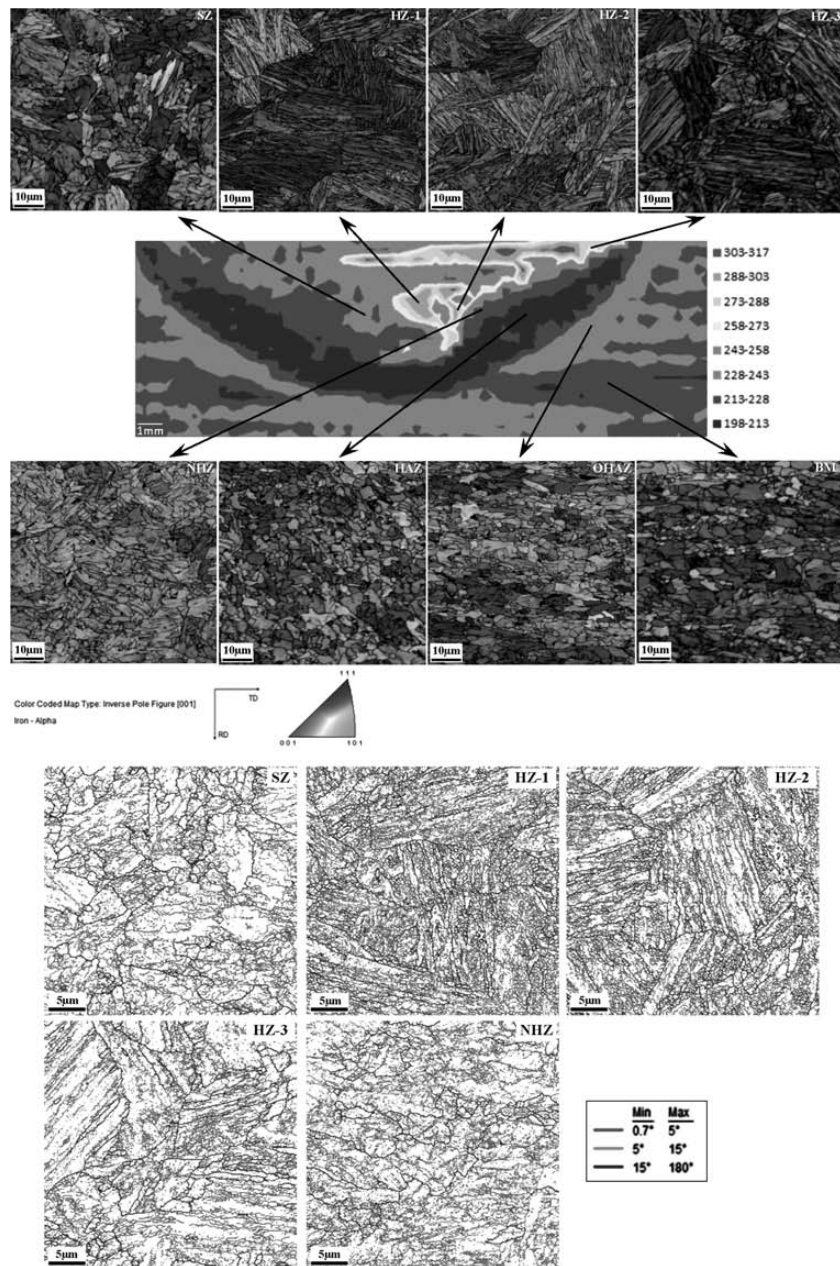
Figure 6: IPF with IQ and GB maps of various FSW zones (SZ: stir zone; HZ: hard zone; NHZ: near-hard zone; OHAZ: outer heat-affected zone)
Slika 6: IPF z IQ- in GB-prikazom različnih področij FSW (SZ: področje mešanja, HZ: trdo področje, NHZ: toplotno vplivano področje, OHAZ: izven toplotno vplivanega področja)

The hardness peaks commonly follow a line on the AS of the weld close to the location of the shoulder and the edge of the weld tool. This is due to a greater amount of the material shearing in this region, leading to a higher strain and greater heating, thereby resulting in a re-austenitization and subsequent transformation to a completely lath-bainitic microstructure during the FSW process.[10] That is, the strain rate and the peak temperature in the weld zone play a key role in the re-austenitization during the FSW process.

The BM microstructure is mainly composed of elongated fine-grained polygonal ferrites, with the average grain size of 6.09 μm, and a small amount of refined upper-bainite islands (**Figures 6** and **7**). There is no evidence of the BM microstructure in the SZ and HZ regions (**Figure 6**). The elongated grains in the BM have completely transformed to a bainitic microstructure with well-defined lath-like upper bainite, consisting of thin, relatively straight and long, parallel ferrite laths in the HZ regions. This microstructure indicates that the BM has reached the peak temperature in excess of A3 and that the cooling rate is fast enough for a formation of the classical upper-bainitic structure in the HZ regions
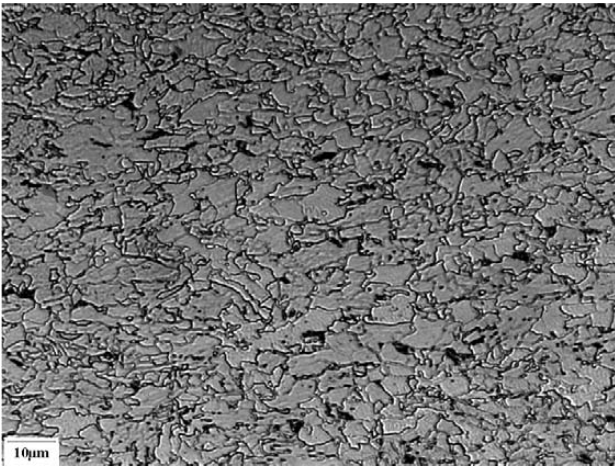
Figure 7: Base-metal microstructure of the X80 API-grade steel
Slika 7: Mikrostruktura osnovnega jekla X80 API

during the FSW process. As mentioned above, the bainitic structures of the HZs in different regions of the weld zone vary depending on the peak temperature and the strain rate on the AS of the weld zone during the FSW process. The SZ and the near-hard-zone (NHZ) microstructures display coarser bainitic structures and the bainite-lath boundaries in these bainitic structures are not as thin, straight and parallel as in the HZ regions (deformed lath bainite). Also, the SZ and NHZ have the polygonal ferrites distributed in a random manner and some martensite/austenite (M/A) islands are scattered throughout the coarse bainitic matrix. This microstruc-

ture is called granular bainite. It is formed at a slower cooling rate than the upper bainite.[21] The HAZ and the outer heat-affected zone (OHAZ) do not have a lath-bainitic microstructure. The elongated ferrite grains in the BM recrystallize and change into equiaxed polygonal ferrites in the HAZ, partially also in the OHAZ, during the FSW process. It is possible to say that the temperature in the HAZ was sufficient to cause a significant coarsening and a spheroidization of the carbides. The effective grain sizes of the HAZ, OHAZ and BM characterized with the EBSD analysis are 4.16 μm, 5.89 μm and 6.09 μm, respectively.
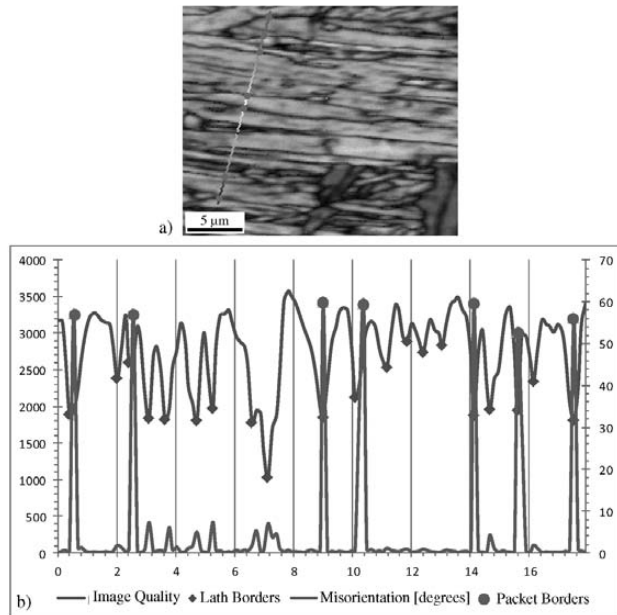
It is well-known that the bainitic microstructures in the weld zone are crucial for the post-weld properties. Therefore, a characterization of the bainitic structures needs to be done acquiring quantitative data in the weld zone for the FSWed X80 steel. It is known that bainite is a microstructure made up of packets of parallel, low-misorientation ferritic laths, which exhibit the same crystallographic orientation in the so-called morphological packets. Bainite packets are separated by high-angle boundaries, defined as the misorientation angles higher than 15°. Bainite-packet and lath size measurements of a bainite microstructure can be made from an IPF with an IQ map and a misorientation profile. An example of these measurements can be seen in **Figure 8**; the misorientation curve exhibits seven peaks, whose misorientation angles are higher than 15°. It shows six packets existing along this trace line. In short, the bainite packet size is the distance between the misorientation angles higher than 15°. Similarly, the bainite-lath size measurement can be made from an IPF with an IQ map and an IQ value curve (**Figure 8**); the lath boundaries

Figure 8: Bainite packet/lath size measurement: a) IPF with an IQ map with a trace line across the bainite microstructure; b) misorientation profile
Slika 8: Merjenje velikosti bainitnega sestava in bainitnih lat: a) IPF z IQ-področjem s sledovi linije preko bainitne mikrostrukture; b) profil razlike v kristalografski orientaciji
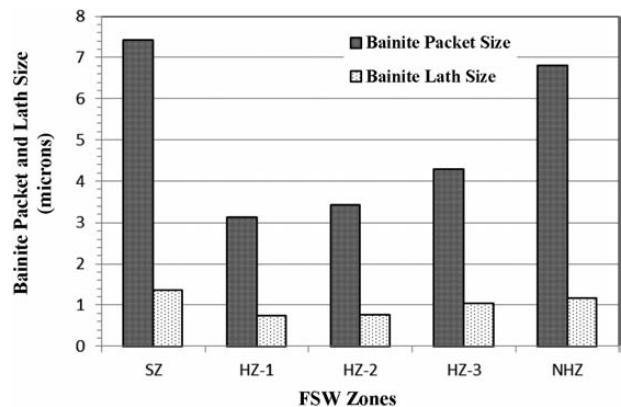
Figure 9: Bainite packet and lath sizes in different FSW zones
Slika 9: Velikost bainitnega sestava in bainitnih lat v različnih področjih FSW

Table 2: Bainite packet and lath sizes in different FSW zones
Tabela 2: Velikost bainitnega sestava in bainitnih lat v različnih področjih FSW

Weld zone	SZ	HZ-1	HZ-2	HZ-3	NHZ
Bainite packet size (μm)	7.42	3.14	3.43	4.29	6.80
Bainite lath size (μm)	1.35	0.73	0.76	1.05	1.16
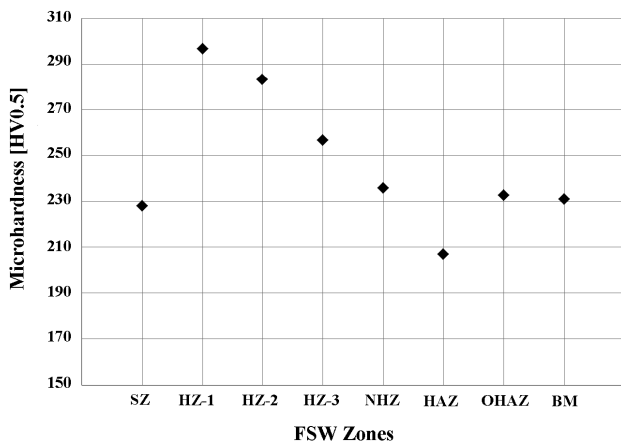
Figure 10: Microhardness profile in the weld zone of the FSW sample (the hardness values were obtained in the zones indicated with the arrows in **Figure 6**)

Slika 10: Profil mikrotrdote v področju zvara v vzorcih FSW (vrednosti trdote so bile izmerjene na področjih, označenih s puščico na **sliki 6**)
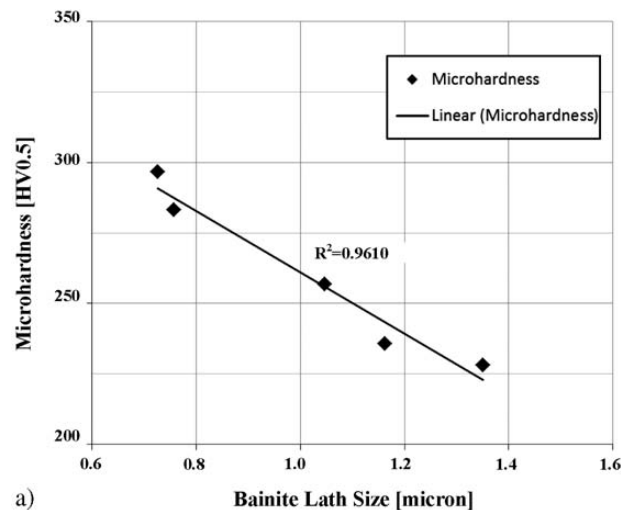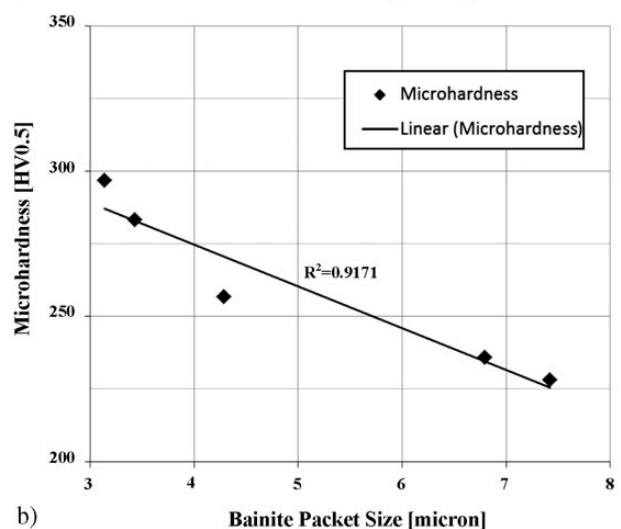
Figure 11: a) Bainite lath and b) bainite packet size versus microhardness in the FSW sample

Slika 11: a) Latasti bainit in b) velikost bainitnega sestava v odvisnosti od mikrotrdote v FSW-vzorcu

have a lower IQ value and so the lath size is the distance between the lower peaks of these quantities. The measurements were made at 15 locations on each zone to acquire statistical data of the bainite-lath and packet sizes in the weld-zone microstructures, using crystallographic data on the IPF with the IQ maps shown in **Figure 6**. The obtained results from the quantitative measurements can be seen in **Table 2** and **Figure 9**. As expected, the HZ regions have finer bainitic microstructures and GBs showing misorientations of 0.7–15° in the HZ regions, particularly in the HZ-1 and HZ-2 regions; their lath-bainitic structures are finer than those in the other zones (**Figure 6**). Bainite-lath and packet sizes of the HZ regions in different regions of the weld zone vary depending on the heat input and strain rate during the FSW process. The SZ and NHZ have coarse bainitic microstructures.

The hardness values in different regions of the weld zone of the FSW sample, depending on their microstructures, can be seen in **Figure 10**. Essentially, the hardness in the weld zone varies depending on the bainitic structures. As can also be seen in **Figure 11**, there is a direct relationship between the post-weld bainitic structures and the hardness values in the weld zone: the hardness increases almost linearly with the decreasing bainite-lath and packet size.

The TEM images of the SZ and HZ microstructures of the FSW sample are shown in **Figure 12**. The microstructure in the SZ is complicated, including differently shaped ferrites, such as non-equiaxial and interwoven, partially parallel lathy ferrites with high-density dislocations and coarse, dark phases distributed intra-lath and along the lath boundaries (**Figures 12a** to **12c**). There are also ultrafine particles inside the laths or among the laths. A fairly high dislocation density in this matrix is an essential characteristic of the intermediate transformation products[22] that form with a transformation mode between ferrite and martensite. The dark phases are M/A constituents or retained austenite.[23] As mentioned above, such a ferrite matrix is typically found in granular bainite. The formation of M/A constituents may be attributed to the partitioning of carbon during the transformation to bainite and the post-transformation of carbon-enriched austenite. An M/A constituent is a kind of a brittle mixture, its size and shape have a great effect on the toughness of steel. An M/A constituent converging to a block is beneficial to the improvement of the toughness compared with an M/A strip.[24] Thin M/A strips are observed in the well-defined lath-boundary locations in the HZ microstructure (**Figures 12d** and **12e**). It may be expected from the HZ region to exhibit a lower toughness than the SZ region since the HZ has more M/A strips.

Also, as can be seen in the TEM images, the widths of the bainite laths in the HZ are less than 1 μm, whereas the widths of the laths in the SZ are more than 1 μm. It is
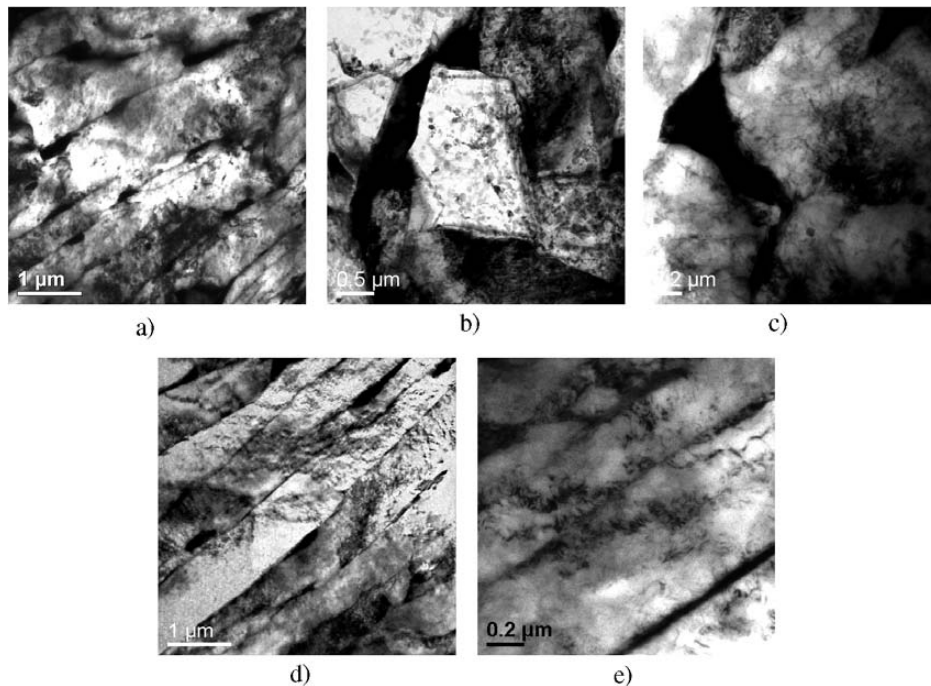
Figure 12: TEM micrographs of: a), b), c) the SZ region and d), e) the HZ-1 region of the FSW sample
Slika 12: TEM-posnetki: a), b), c) področja SZ in d), e) področja HZ-1v FSW-vzorcu

clear that this is the reason for the increased hardness of the HZ region (**Figures 11** and **12**).

4 CONCLUSIONS

The morphology of the weld zone, especially the quantitative microstructural characterization of bainitic structures, and the relationship between post-weld bainitic structures and the hardness at the weld zone of the friction-stir welded X80 API-grade pipe-line steel have been investigated in this study. In the FSWed X80 steel, the frictional heat and plastic flow create a granular bainitic structure in the stir zone, the classical lath-like upper bainitic structure in the hard zone, and a recrystallized equiaxed polygonal ferritic structure in the heat-affected zone. The maximum hardness was observed in the classical upper bainitic microstructure in the hard zone. The lowest hardness was associated with the heat-affected zone. The hardness values in the weld zone vary depending on the bainitic structure. A direct relationship between the post-weld bainitic structures and the hardness values in the weld zone has been determined: the hardness increases almost linearly with the decreasing bainite-lath and packet sizes.

5 REFERENCES

[1] Y. H. Zhao, S. B. Lin, L. Wu, F. X. Qu, Mater Lett., 59 (**2005**), 2948–2952
[2] N. Rajamanickam, V. Balusamy, Indian J Eng Mater Sci., 15 (**2008**), 293–299
[3] W. M. Thomas, E. D. Nicholas, J. C. Needham, M. G. Church, P. Templesmith, C. J. Dawes, GB Patent Application No. 9125978.9, 1991
[4] S. R. Ren, Z. Y. Ma, L. Q. Chen, Scr Mater., 56 (**2007**), 69–72
[5] R. S. Mishra, Z. Y. Ma, I. Charit, Mater Sci Eng., A 341 (**2003**) 1–2, 307–310
[6] H. Aydin, A. Bayram, U. Esme, Y. Kazancoglu, O. Güven, Mater. Tehnol., 44 (**2010**) 4, 205–211
[7] S. J. Barnes, A. R. Bhatti, A. Steuwer, R. Johnson, J. Altenkirch, P. J. Withers, Metall Mater Trans., A 43 (**2012**) 7, 2342–2355
[8] D. Forrest, J. Nguyen, M. Posada, J. DeLoach, D. Boyce, J. Cho, P. Dawson, Simulation of HSLA-65 Friction Stir Welding, 7th International Conference on Trends in Welding Research, Pine Mountain, 2006, 279–286
[9] S. Jindal, R. Chhibber, N. Mehta, Adv Mat Res., 365 (**2011**), 44–49
[10] L. Wei, T. W. Nelson, Characterization of microstructures and transformation behavior in friction stir welded HSLA-65, Trends in Welding Research, Proc. of the 8th Inter Con., Pine Mountain, 2008, 391–397
[11] L. Wei, T. W. Nelson, Weld J., 90 (**2011**), 95–101
[12] P. J. Konkol, M. F. Mruczek, Weld J., 86 (**2007**) 7, 187–195
[13] D. P. Field, T. W. Nelson, Y. Hovanski, K. V. Jata, Metall Mater Trans A, 32 (**2001**), 2869–2877
[14] P. S. Pao, R. W. Fonda, H. N. Jones, C. R. Feng, D. W. Moon, Friction stir welding of HSLA-65 steel, Friction Stir Welding and Processing, IV (**2007**), 243–252

[15] H. Farhat, I. N. A. Oguocha, Effect of welding speed on weld quality and microstructure of tandem submerged arc welded X80 pipeline steel, Materials Science & Technology Conference and Exhibition, Pittsburg, 2009, 2457–2468

[16] A. Ozekcin, H. W. Jin, J. Y. Koo, N. V. Bangaru, R. Ayer, Int J Offshore Polar Eng., 14 (**2004**) 4, 284–288

[17] T. F. A. Santos, T. F. C. Hermenegildo, C. R. M. Afonso, R. R. Marinho, M. T. P. Paes, A. J. Ramirez, Eng Fract Mech., 77 (**2010**), 2937–2945

[18] J. Defalco, R. Steel, Weld J., 88 (**2009**) 5, 44–48

[19] http://www.mtiwelding.com/files/FSW_RM2_vWeb.pdf

[20] http://fsrl.byu.edu/presentations/Dual%20Phase%20Steel.pdf

[21] S. K. Dhua, D. Mukerjee, D. S. Sarma, Metall Mater Trans A, 34 (**2003**), 2493–2504

[22] J. L. Lee, M. H. Hon, G. H. J. Cheng, J Mater Sci., 22 (**1987**), 2767–2777

[23] C. Xu, K. Shi, Y. Zhou, X. Li, Y. Liu, H. Wang, Trans Jpn Weld Res Inst., Special Issue on Welding Science and Engineering, (**2011**), 51–54

[24] J. Niu, L. Qi, Y. Liu, L. Ma, Y. Feng, J. Zhang, Trans Nonferrous Met Soc China, 19 (**2009**), 573–578

LADLE-NOZZLE OPENING AND GENETIC PROGRAMMING

ODPIRANJE IZLIVKA PONVE S PODŽIGANJEM IN GENETSKO PROGRAMIRANJE

Miha Kovačič[1,2], Beno Jurjovec[1], Luka Krajnc[1]

[1]Štore Steel, d. o. o., Železarska cesta 3, 3220 Štore, Slovenia
[2]University of Nova Gorica, Laboratory for Multiphase Processes, Vipavska 13, 5000 Nova Gorica, Slovenia
miha.kovacic@store-steel.si

Štore Steel Ltd. faces a huge problem with the ladle nozzle opening during the production of a wide variety of steel grades. After a ladle treatment the steel melt is poured from the ladle through the sliding gate and the nozzle into the tundish on the continuous casting machine. Due to frequent clogging the ladle nozzle must be opened with oxygen which can cause melt pollution. The purpose of this paper is to present an attempt to reduce ladle-nozzle openings. In this attempt the genetic-programming method was used. The experimental data on 115 consecutively cast heats was used. The steelmaking-technology number, the batch sequence number, the time spend for secondary metallurgy, the sustainability of the upper-nozzle brick, the sustainability of the nozzle seating block, the sustainability of the lower-nozzle brick, the ladle number, the sustainability of the ladle and of the foreman of secondary metallurgy and the melt chemical composition (Al, C, Mn and Si) were taken into account for the prediction of the ladle-nozzle opening. The best genetically developed model for the ladle-nozzle-opening prediction correctly predicts 107 out of 115 situations of opening the ladle. The results of the genetic-programming-based modeling have been used in practice to change several steelmaking technologies.

Keywords: secondary metallurgy, ladle-nozzle opening, modeling, genetic programming

Štore Steel, d. o. o., se spopada s težavo podžiganja izlivka ponve pri izdelavi ogromnega števila različnih kvalitet jekla. Po obdelavi na ponovči peči se taline skozi drsno zapiralo in izlivek prelije v vmesno ponovco na kontinuirni livni napravi. Zaradi pogostega mašenja se izlivki odpirajo s kisikovim kopjem, kar lahko povzroča onesnaženje taline. Namen študije je bil zmanjšati število podžiganj. Uporabljena je bila metoda genetskega programiranja. Pri napovedovanju podžiganja smo upoštevali število tehnološkega postopka izdelave jekla, zaporedno številko šarže pri sekvenci, čas sekundarne metalurgije, vzdržnost zunanjega izlivka ter ponovce, ponovčarja in kemično sestavo taline (Al, C, Mn in Si). Najboljši genetsko dobljeni model je napovedal 107 od 115 dejansko izvršenih podžiganj. Rezultati modeliranja z genetskim programiranjem so privedli do sprememb več tehnologij izdelave jekla.

Ključne besede: sekundarna metalurgija, podžiganje, modeliranje, genetsko programiranje

1 INTRODUCTION

Steelmaking begins with scrap melting in an electric-arc furnace. After scrap and carburizing agents melting the carbon, the carriers, in general, are coke, anthracite, graphite and slag additives, regulating basicity, viscosity, thermal and electric conductivity, desulphurization, dephosphorization, neutrality towards the furnace fireproof linings and the non-metallic inclusion-filtration capability.[1,2]

The melting bath heated up to the tapping temperature according to the further treatment procedures is discharged into the casting ladle after electric-arc furnace melting. After discharging the melting bath is deoxidized and desulphurized, the nonmetallic inclusions are filtered out, the slag metallic oxides are reduced, the hydrogen and nitrogen are partly degassed, the melting bath and the temperature field are homogenized, the formed slag is exchanged and the major alloying is completed.

After melting and alloying in the electric-arc and ladle furnace, billets are continuously cast from the melting bath. The melting bath flows through the sliding-gate system (**Figure 1**) and the ladle shroud towards the tundish. After filling up the tundish, a mould filling system with tundish stoppers and submerged pouring tubes is established. The billets with a square section of 180 mm or 140 mm are cast. After reaching a certain melting-bath level the potentiometer starts the flattening system which drags the billet out of the mould. In this way continuous casting is established. The billet goes through the cooling zone toward the gas cutters, where it is cut and laid off onto a cooling bath.

After a melt has been cast, the ladle has to be emptied of the remains of the slag. These are scraped using a construction machine. Especially the top of the ladle has to be carefully cleaned so as to prevent the slag remains from mixing with the steel melt. The next step of the process is to clean the sliding gate at the bottom of the ladle, which is, at first, done manually and then with an oxygen lance.

When the slide-gate parts, the upper- and lower-nozzle bricks, the nozzle seating block, the inner and collector nozzles and the slide-gate plates, are damaged they are replaced.
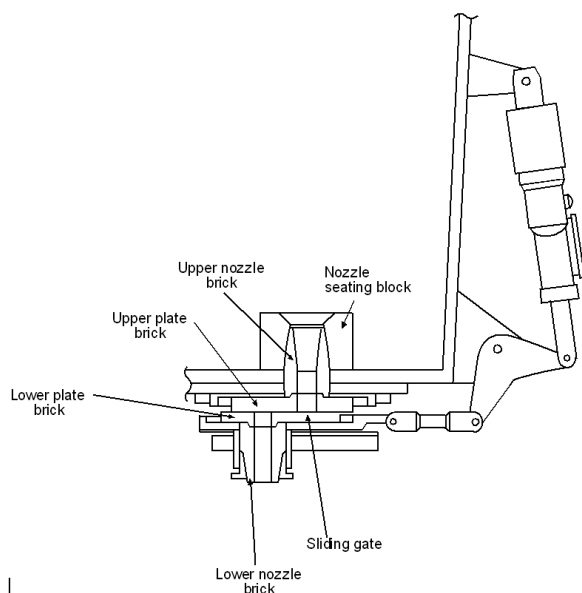
Figure 1: Ladle and opening system in Štore Steel Ltd.
Slika 1: Sistem odpiranja ponovce v podjetju Štore Steel, d. o. o.

The ladle is then positioned vertically; the top part is thoroughly checked and repaired if necessary. After that it goes to the reheating station, where a mixture of natural gas and air heats the ladle to the correct temperature. The slide-gate filling sand is poured through a tube to the slide gate just before the ladle is positioned in the casting pit. There is a standard amount of the filling sand that has to be used.

The ladle then goes to the ladle furnace where chemical and temperature homogeneities are achieved.

In recent years there has been a significant increase in the number of heats, when an oxygen lance has to be used to cut through the ladle slide gate and allow the liquid steel to pour through. In good steelmaking practice, we want to avoid, as much as possible, having these kinds of heats, because the oxygen that is blown in the melt causes a reoxidation of the melt and impurities may be formed.

In the present paper the dependence between the ladle-nozzle opening, the steelmaking parameters, the chemical composition and the fire-proof material is discussed. For the ladle-nozzle-opening modeling the genetic-programming method was used. The experimental data was collected during the standard production.

2 EXPERIMENTAL BACKGROUND

The data for the analysis was collected on the basis of 115 consecutively cast heats in Štore Steel Ltd. (**Table 1**). The data is taken from the technological documentation of the cast heats and from the chemical archive. The goal was to get as wide a range of variables as possible.

There are several different steelmaking technologies used:
- aluminum killed steel (#1),
- silicon killed steel (#2),
- aluminum killed calcium-free steel (#3) and
- extra machinability steel (#4).

It is also important to know how many batches of the same steel grade are cast in a sequence. The conditions for casting a single batch are different from the ones for casting several batches, one after another, with respect to

Table 1: Experimental data
Tabela 1: Eksperimentalni podatki

#	Steelmaking technology number	Batch sequence number	Time spend for secondary metallurgy (min)	Sustainability of the upper nozzle brick (number of batches)	Sustainability of the nozzle seating block (number of batches)	Sustainability of the lower nozzle brick (number of batches)	Ladle number	Sustainability of the ladle (number of batches)	Foreman of secondary metallurgy	w(Al) /%	w(C) /%	w(Mn) /%	w(Si) /%)	Nozzle opening: Yes=1, No=0
1	1	0	60	4	10	4	11	10	1	0.004	0.51	0.79	0.26	1
2	2	1	110	11	11	3	6	53	3	0.023	0.27	0.82	0.28	0
3	2	2	70	3	32	3	8	32	3	0.028	0.28	0.79	0.24	0
4	2	0	70	13	25	3	12	25	2	0.024	0.22	1.31	0.22	0
5	2	0	110	5	11	1	11	11	8	0.021	0.75	0.74	0.34	0
6	2	0	100	12	12	4	6	54	2	0.023	0.45	0.62	0.26	0
7	2	0	140	14	26	4	12	26	2	0.026	0.2	1.16	0.28	1
8	2	0	95	6	12	2	11	12	10	0.017	0.28	1.45	0.59	1
9	2	0	128	1	13	1	6	55	10	0.025	0.49	0.73	0.27	1
10	2	0	110	1	27	1	12	27	6	0.021	0.15	1.03	0.27	1
11	2	0	90	7	13	3	11	13	7	0.026	0.22	1.23	0.22	0
12	3	0	125	2	14	2	6	56	7	0.009	0.99	0.34	0.23	0
13	1	1	90	2	28	2	12	28	1	0.005	0.47	0.74	0.26	1
14	1	2	70	8	14	4	11	14	1	0.005	0.48	0.71	0.25	0
15	4	0	38	3	29	3	12	29	1	0.022	0.18	1.17	0.26	0
115	4	1	38	1	15	1	11	15	2	0.024	0.17	1.1	0.23	0

the casting temperature, the time and fire-resistant material conditions.

According to the ladle and tundish system the data on the sustainability of the inner nozzle, the well block, the collector nozzle and the ladle is needed.

Secondary metallurgy also influences the pouring of the melted steel from the ladle to the tundish. That is why alloying (the melt chemical composition in the ladle) and steelmaking (timing and organization) are also important.

3 NOZZLE-OPENING MODELING WITH GENETIC PROGRAMMING

Genetic programming is probably the most general evolutionary optimization method.[3–6] The organisms that undergo an adaptation are in fact mathematical expressions (models) for a nozzle-opening prediction consisting of the available function genes (i.e., the basic arithmetical functions) and terminal genes (i.e., independent input parameters and random floating-point constants). In our case the models consist of: the function genes of addition (+), subtraction (–), multiplication (*) and division (/), the terminal genes of the steelmaking technology number (*tech*), the batch sequence number (*seq*), the time spend for secondary metallurgy (*t*), the sustainability of the upper-nozzle brick (*s_unb*), the sustainability of the nozzle seating block (*s_nsb*), the sustainability of the lower-nozzle brick (*s_lnb*), the ladle number (*ladle*), the sustainability of the ladle (*s_l*), the foreman of secondary metallurgy (*man*), the weight percentage of Al (*Al*), C (*C*), Mn (*Mn*) and Si (*Si*).

Random computer programs of various forms and lengths are generated by means of selected genes at the beginning of the simulated evolution. Afterwards, the varying of the computer programs during several iterations, known as the generations, by means of genetic operations is performed. For the progress of the population only the reproduction and crossover are sufficient. After the completion of the varying of the computer programs, a new generation is obtained that is evaluated and compared with the experimental data, too.

The process of changing and evaluating the organisms is repeated until the termination criterion of the process is fulfilled. This is the prescribed maximum number of the generations.

For the process of simulated evolutions the following evolutionary parameters were selected: the size of the population of organisms 500, the greatest number of generation 100, the reproduction probability of 0.4, the crossover probability of 0.6, the greatest permissible depth in creating population 6, the greatest permissible depth after the operation of the crossover of two organisms 10 and the smallest permissible depth of organisms in generating new organisms 2. Genetic operations of reproduction and crossover were used. For the selection of organisms the tournament method with a tournament size of 7 was used. For the evaluation of the organisms the number of the correct predictions of ladle-nozzle openings was used.

We have developed 100 independent civilizations of mathematical models for the nozzle-opening prediction. Each civilization has the most successful organism – a mathematical model for the nozzle-opening prediction. The best most successful organism from all of the civilizations is presented here:

$$
\left(\left(2c+mn-seq\right)s\_unb\left(\frac{tech+s\_unb}{s\_lnb}+\left(ladle-man+tech+s\_lnb\right)\left(-si-tech+al\left(c-s\_lnb\right)+s\_unb+\frac{s\_unb\left(-al-tech+s\_lnb+s\_unb\right)}{seq\left(-man+\frac{tech}{seq}\right)\left(-ladle+s\_unb\right)}\right)\right)\right)\Big/
$$

$$
\left(\left(al\,ladle\,man+s\_unb\right)\left(s\_l+\frac{-man+\frac{tech}{seq}}{-si-2tech+al\left(c-s\_lnb\right)+s\_unb+\frac{s\_unb\left(-al+s\_lnb+s\_unb\right)}{seq\left(-man+\frac{tech}{seq}\right)\left(-s\_lnb+s\_unb\right)}}\right)\left(-s\_lnb+\left(ladle+man\right)\left(1+\frac{-man+\frac{tech}{seq}}{-ladle+s\_lnb+s\_unb}\right)\right)\right) \quad (1)
$$

$$
\left(-al+mn+\left(ladle+s\_unb\right)\left(ladle+\frac{s\_unb}{man}\right)+man\left(-si-tech+al\,s\_lnb+s\_unb+\frac{\left(-man+\frac{mn+tech}{seq}\right)\left(-al+c+mn-tech-s\_lnb\right)\left(-seq+s\_unb\right)}{\left(-man+\frac{tech}{seq}\right)\left(-mn+s\_unb\right)\left(-al-tech+s\_lnb+s\_unb\right)}\right)\right)
$$

$$
\left(s\_lnb+\left(tech+s\_unb\right)\Big/\left(al\,ladle\left(c-seq+\frac{s\_unb\left(-al+s\_lnb+s\_unb\right)}{\left(ladle+man\right)mn\,seq\left(-man+\frac{tech}{seq}\right)}\right)\left(s\_lnb+ladle\left(ladle+\frac{s\_unb}{man}\right)\right)\right)\right)
$$

and it correctly predicts 107 out of 115 situations of the ladle-nozzle opening.

The influences of individual parameters are presented in the following figure (**Figure 2**). For example, we can see that the steelmaking-technology number can increase the number of ladle-nozzle openings from 4 to 10 with respect to 115 consecutively cast heats. On the other hand, an Al addition can reduce the number of ladle-nozzle openings up to 11 heats with respect to 115 consecutively cast heats.
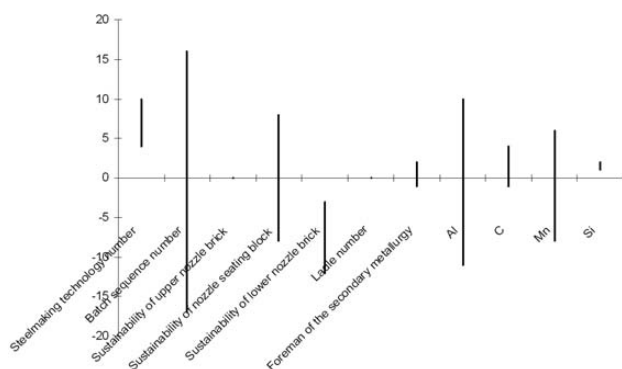
Figure 2: Influences of individual parameters on the ladle-nozzle opening with respect to 115 consecutively cast heats
Slika 2: Vplivi posamičnih parametrov na podžiganje glede na podatke 115 zaporedno odlitih šarž

4 CONCLUSION

The purpose of this paper was to reduce the ladle-nozzle openings where an oxygen lance is used and an unwanted reoxidation of the melt can occur. In this attempt the genetic-programming method was used. The experimental data on 115 consequently cast heats was used. The steelmaking-technology number, the batch-sequence number, the time spend for secondary metal-lurgy, the sustainability of the upper-nozzle brick, the sustainability of the nozzle seating block, the sustain-ability of the lower-nozzle brick, the ladle number, the sustainability of the ladle, the foreman of secondary metallurgy and the melt chemical composition (Al, C, Mn and Si) were taken into account for the prediction of the ladle-nozzle opening. The best genetically developed model for the ladle-nozzle-opening prediction correctly predicts 107 out of 115 situations of opening the ladle. It was also found that the batch-sequence number, the sustainability of the nozzle seating block, the percentage of Al and Mn in the melt are the most influential para-meters.

If a heat is cast later in the sequence, it is less likely that clogging will happen. This is due to the fact that the heats cast later in the sequence have a shorter melting time in the ladle. It is important that heats are cast on time and, for this reason, some heats have to be prepared beforehand. The more the melt is in contact with the nozzle seating block, the more likely it is for clogging to occur. So, replacing the ladle and the opening system is also essential. The Al and Mn additions are connected with different steelmaking technologies and different steel grades. So, a change in the steelmaking techno-logies with respect to the most critical grades (i.e., the spring steel and the steel for the applications in forging) was also required. The results of the research have been used in practice.

Acknowledgements

5 REFERENCES

[1] J. R. Fruehan, The Making, Shaping and Treating of Steel, 11th ed., The AISE Steel Foundation, Pittsburgh 1998
[2] A. Ghosh, Secondary Steelmaking: Principles and Applications, CRC Press, Florida 2001
[3] M. Kovačič, B. Šarler, Application of the genetic programming for increasing the soft annealing productivity in steel industry, Materials and Manufacturing Processes, 24 (**2009**) 3, 369–374
[4] M. Kovačič, S. Senčič, Modeling of PM10 emission with genetic programming, Mater. Tehnol., 46 (**2012**) 5, 453–457
[5] M. Kovačič, P. Uratnik, M. Brezočnik, R. Turk, Prediction of the bending capability of rolled metal sheet by genetic programming, Materials and Manufacturing Processes, 22 (**2007**) 5, 634–640
[6] J. R. Koza, Genetic programming III, Morgan Kaufmann, San Francisco 1999

OPTIMIZATION OF THE DIE-SINKING MICRO-EDM PROCESS FOR MULTIPLE PERFORMANCE CHARACTERISTICS USING THE TAGUCHI-BASED GREY RELATIONAL ANALYSIS

OPTIMIRANJE MIKRO-EDM-POSTOPKA POGREZANJA ORODJA ZA DOLOČANJE VEČ ZNAČILNOSTI Z UPORABO TAGUCHIJEVE SIVE RELACIJSKE ANALIZE

Arumugam Kadirvel[1], Pillai Hariharan[2]

[1]Department of Mechanical Engineering, R. M. K Engineering College, Anna University, Chennai, India
[2]Department of Manufacturing Engineering, College of Engineering, Guindy, Anna University, Chennai, India
kadirvel73@gmail.com

In modern industries, the expectation is to manufacture high-quality products with a low cost within a short duration. In order to produce any product with a desired quality by machining, the influence of various parameters such as the material-removal rate (MRR), the tool-wear ratio (TWR) and the surface roughness (R_a) should be considered. This paper presents the methodology of the Taguchi method and grey relational analysis to find the optimum parameters for obtaining a higher MRR, a lower TWR and the minimum surface roughness in the die-sinking micro-EDM process. The experiments were carried out as per L_{16} orthogonal array with each experiment performed under different conditions of the gap voltage, capacitance, feed rate and threshold. Additionally, an analysis of variance (ANOVA) was also applied to identify the most significant factor. The capacitance and the gap voltage were found to be the most significant controlled factors influencing the performance of the machining process.

Keywords: micro-EDM, optimization, Taguchi method, ANOVA, grey relational analysis

Od moderne proizvodnje se pričakuje hitra izdelava kvalitetnih proizvodov z majhnimi stroški. Da bi s struženjem izdelali izdelek z želeno kvaliteto, je treba upoštevati vplive različnih parametrov, kot so hitrost odrezavanja materiala (MRR), hitrost obrabe orodja (TWR) in hrapavost površine (R_a). V tem članku je predstavljena metodologija Taguchijeve metode in sive relacijske analize za iskanje optimalnih parametrov za povečanje MRR, zmanjšanje TWR in minimalno hrapavost površine pri mikro-EDM-postopku pogrezanja orodja. Eksperimenti so bili izvršeni za pravokotno matriko L_{16}, pri čemer je bil vsak eksperiment izvršen pri različnih razmerah voltaže razmika, kapacitivnosti, hitrostih odvzemanja in mejnih vrednostih. Dodatno je bila uporabljena analiza variance (ANOVA) za ugotovitev najpomembnejšega faktorja. Ugotovljeno je bilo, da sta kapacitivnost in voltaža razmika najpomembnejša kontrolna faktorja, ki vplivata na uspešnost procesa obdelave.

Ključne besede: mikro-EDM, optimiranje, Taguchijeva metoda, ANOVA, siva relacijska analiza

1 INTRODUCTION

Several researchers focussed their efforts on producing micro-components and micro-systems to meet the industrial demand for miniaturisation. When producing micro-components, it is critical to achieve high form accuracy and precise dimensions. However, it is a challenge to produce complex micro-components such as micro-dies made of high-hardness materials using conventional machining methods such as micro-milling or micro-turning. This problem can be resolved with one of the methods, such as the micro-EDM. The advantage of this method is that the machining process is independent of the hardness of the workpiece. In fact, high-hardness materials are better candidates for electrical-discharge machining. Therefore, it has become one of the most important methods for machining micro- and sub-micro-components of hard, electrically conducting materials. In order to use the micro-EDM in the industries more effectively, many researchers all over the world have initiated research works to overcome all the parameters that influence the performance of the machining process.

The material-removal rate (MRR), the tool-wear ratio (TWR) and the surface roughness (SR) are the important parameters to be considered to obtain the desired machining-performance characteristics during the micro-EDM process. The gap voltage, capacitance, feed rate and threshold are the machining parameters affecting the performance measures. Among the other performance measures, the TWR and the surface roughness determining the dimensional accuracy of a machined part, the MRR determining the economics of machining and the rate of production are of the utmost importance.

The Taguchi method has been widely used in the engineering analysis, being a powerful tool to design a high-quality system. Moreover, the Taguchi method employs a special design of orthogonal array to investigate the effects of all the machining parameters through a small number of experiments. Recently, the Taguchi method was widely employed in several industrial fields and research works. Lin et al.[1] adapted the Taguchi

method to obtain the optimum machining parameter of the electrical-discharge-machining process. Prihandana et al.[2] used the Taguchi method to identify the optimum process parameters to increase the material-removal rate of a dielectric fluid containing a micro-powder in the micro-EDM using the L_{18} orthogonal array. Tosun et al.[3] used the Taguchi method to explore the effects of the MRR and the kerf of the wire-electrical-discharge machining. Their works revealed that the Taguchi method was a powerful approach used in designing an experiment. However, the Taguchi method can be used to optimize only single performance characteristics. Hence, in order to optimize any multiple performance characteristics, the researchers found the grey relational analysis to be a suitable theory.

Somashekhar et al.[4] used a new approach for the optimization of the micro-WEDM process with multiple performance characteristics based on the statistical-based analysis of variance (ANOVA) with the grey relational analysis. Chiang and Chang[5] applied the grey relational analysis to optimize the WEDM process with multiple performance characteristics such as the MRR and the maximum surface roughness.

The Taguchi method coupled with the grey relational analysis has a wide area of application in manufacturing processes as it can solve multi-response optimization problems.[6,7] Natarajan and Arunachalam[8] presented the optimization of multiple performance characteristics using the Taguchi method and grey relational analysis. With this analysis, the optimum parameters in the EDM of the 304 stainless steel were identified and the improvements in the performance characteristics were found using the grey relational analysis. Vijay Kumar Meena and Man Singh Azad[9] studied the effect of the input and output parameters of a micro-EDMed Ti-6Al-V alloy with a tungsten carbide electrode. They employed the grey relational analysis of variance to optimize the levels of input parameters and found that the MRR, the TWR and the overcut can be improved. Rajyalakshmi and Venkata Ramaiah[10] utilized the grey-Taguchi technique as a multi-objective optimizer to identify the machining parameters of Inconel 825 in the WEDM process. It has been concluded that the grey-Taguchi method is suitable for a parametric optimization of multiple performance characteristics.

Jung and Kwon[11] also employed the Taguchi method and grey relational analysis to find the optimum machining parameters to satisfy the multiple characteristics of the EDM process. Shen et al.[12] determined the optimum combination of the process parameters during the EDM process of 1Cr17Ni7 using Cu as the electrode based on the performance characteristics such as the material-removal rate, the tool-wear rate and the surface roughness. Muthu Kumar et al.[13] identified the optimum levels of the parameters with the grey relational analysis and the percentage contribution of all the parameters with ANOVA to study the optimization of machining parameters. In this paper, to solve the multiple-performance-characteristics problem of the micro-EDMed EN-24 die

steel, the Taguchi-based grey relational analysis was used.

2 EXPERIMENTAL PROCEDURE

Experiments were conducted on the CNC micro-electrical-discharge machine (die-sinking type) of a DT-110-model multi-process micro-machining tool. The workpiece material used in this study was EN-24 die steel, widely used in the tool and die industry. EN-24 die steel is a high-quality alloy steel. Silver tungsten (AgW) with the diameter of 300 μm was used as an electrode. The dielectric used in this study was the EDM oil3. A micro-electrical-discharge machine with an RC-type pulse generator was used to obtain a quality micro-hole in the EN-24 die steel.

Experiments were conducted using the L_{16} orthogonal array, in which the parameters such as the gap voltage, the capacitance, the threshold and the feed rate were varied at four levels, with the level four being the highest value of the process variable. The machining parameters and their levels are highlighted in **Table 1**.

Table 1: Machining parameters and their levels for die-sinking micro-EDM
Tabela 1: Parametri obdelave in njihove vrednosti pri mikro-EDM poglabljanju orodja

Parameters	Level1	Level2	Level 3	Level 4
Gap voltage (V)	80	100	120	140
Capacitance (nF)	0.1	1.0	10	100
Feed rate (μm/s)	2	4	6	8
Threshold (%)	20	40	60	80
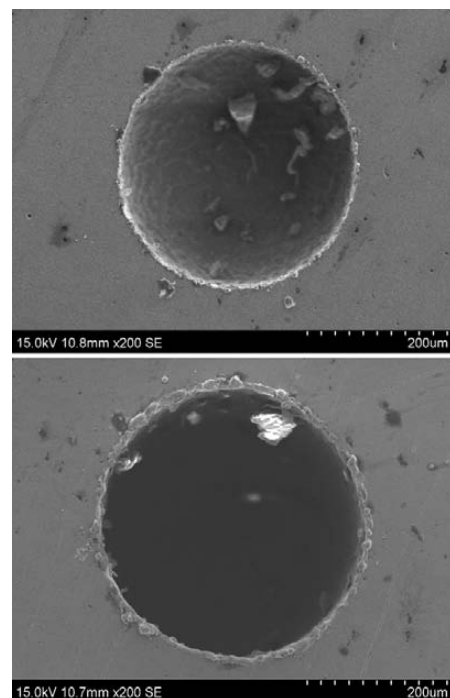
Figure 1: SEM image of a micro-hole on the workpiece
Slika 1: SEM-posnetek mikroluknje na obdelovancu
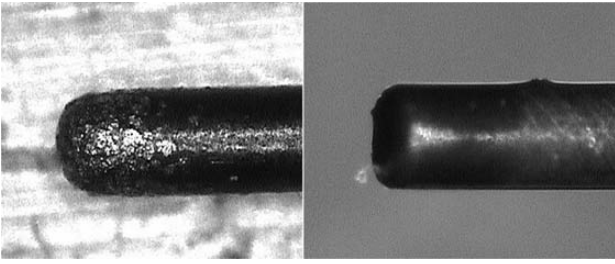
Figure 2: VMS image of the electrode after machining
Slika 2: VMS-posnetek elektrode po obdelovanju

The material-removal rate for the micro-EDM process can be calculated by dividing the total volume of the material removed by the total machining time. Assuming a nil diametral wear of the electrode, the MRR is calculated on the basis of the effective depth of the hole, divided by the respective time. The effective depth of the hole is calculated on the basis of the difference between the depth shown on the monitor of the machine and the difference between the electrode lengths before and after the machining, which can be measured using the video-measuring system (VMS). The wear ratio is defined as the ratio of the amount of the electrode to the amount of the workpiece removed. One of the most difficult output parameters to be calculated is the tool-wear ratio in the micro-EDM process. There are four methods used to measure the tool-wear ratio by means of measuring the weight, the length, the shape and the total volume, respectively.

In this study, the tool-wear ratio was calculated on the basis of the total volume. The average surface roughness (R_a) was measured using a non-contact Talysurf CCI 3000A. **Figure 1** shows a SEM (scanning electron microscope) image of a machined micro-hole and **Figure 2** shows a VMS image of the electrode after machining.

3 DESIGN AND PLAN OF THE EXPERIMENTS

To evaluate the effects of the machining parameters on the performance characteristics, a specially designed experimental procedure is required. Classical experimental-design methods are too complex and difficult to use. Additionally, a large number of experiments has to be carried out when the number of machining parameters increases.[14,15] In this study, the Taguchi method, a powerful tool for the parameter design of performance characteristics, was used to determine the optimum machining parameters for the maximum MRR, the minimum TWR and a lower surface roughness in the die-sinking micro-EDM. The methodology of Taguchi for four factors at four levels was used for the implementation of the plan of the experiments. According to the Taguchi quality-design concept, a L_{16} orthogonal-array table with 16 rows (corresponding to the number of experiments) was chosen for the experiments. The optimization of the observed values was then determined through a comparison with the Taguchi signal-to-noise (S/N) ratio. The

calculation of the value of ANOVA with the use of the full factorial design ($4 \times 4 \times 4 \times 4$) reduced the total of 256 sets of the experiments down to 16, thereby decreasing the cost, time and effort.

Data pre-processing is a process of transferring the original sequence to a comparable sequence. Hence, the experimental results are normalized in the range between zero and one. Based on the characteristics of the data sequence, various methodologies are available for data pre-processing.[16] Therefore, a linear normalization of the experimental results for the MRR, the TWR and the surface roughness were performed.

3.1 Analysis of the Taguchi method

The S/N ratio based on the larger-the-better criterion for the overall grey relational grade was calculated using the following equation:

$$\frac{S}{N} = -10 lg \frac{1}{n} \sum_{i=1}^{n} \frac{1}{y_i^2} \qquad (1)$$

The S/N ratio based on the smaller-the-better criterion for the overall grey relational grade was calculated by using the following equation:

$$\frac{S}{N} = -10 lg \frac{1}{n} \sum_{i=1}^{n} y_i^2 \qquad (2)$$

Thus, the S/N ratio is considered to evaluate the effect of the machining parameters on the MRR, the TWR and the SR.

3.2 Grey relational analysis (GRA)

The grey relational analysis is a widely used analyzing system even when a model is uncertain or the information is incomplete. It provides an efficient solution to complicated interrelationships among multiple performance characteristics.[17] Based on the normalized experimental data, the grey relational coefficient is calculated representing the correlation between the desired and actual experimental data. Then, the overall grey relational grade is determined by averaging the grey relational coefficient corresponding to the selected responses. The overall performance characteristics of the multiple response process depends on the calculated grey relational grade.[18,19] In the grey relational analysis, the normalized MRR value corresponding to the larger-the-better (LB) criterion can be calculated using:

$$x_i(k) = \frac{x_i(k) - \min x_i(k)}{\max x_i(k) - \min x_i(k)} \qquad (3)$$

and the normalized TWR and SR values corresponding to the smaller-the-better (SB) criterion can be calculated using:

$$x_i(k) = \frac{\max x_i(k) - x_i(k)}{\max x_i(k) - \min x_i(k)} \qquad (4)$$

where $x_i(k)$ is the value after the grey relational gene-ration, min $x_i(k)$ is the smallest value of $x_i(k)$ for the kth response, and max $x_i(k)$ is the largest value of $x_i(k)$ for the kth response.

The grey relational coefficient ($\xi_i(k)$) for the nor-malized S/N ratio values is computed using:

$$\xi_i(k) = \frac{\Delta_{\min} + \xi\Delta_{\max}}{\Delta_{oi}(k) + \xi\Delta_{\max}} \qquad (5)$$

where Δ is the absolute difference, $\Delta_{oi}(k) = \|x_o(k) - i(k)\|$ is the difference in the absolute values between $x_o(k)$ and $x_i(k)$, ξ is the distinguishing coefficient (0–1), $\Delta_{\min}$ is the smallest value of Δ_{oi} and $\Delta_{\max}$ is the largest value of Δ_{oi}. After averaging the grey relational coeffi-cients, the grey relational grade γ_i can be obtained:

$$\gamma_i = \frac{1}{n}\sum_{k=1}^{n}\xi_i(k) \qquad (6)$$

where n is the number of the process responses.

4 RESULTS AND DISCUSSION

The plan of the tests was developed with the aim of determining the effects of the gap voltage, the capaci-tance, the feed rate and the threshold. The values cal-culated using all the equations generated were compared with the experimental measurements to identify the optimum parameters. This study shows that the Taguchi method with the grey relational analysis can be extensively used to determine the optimum parameters in the micro-EDM process with multiple performance characteristics.

Initially, by using equations 1 and 2, the S/N ratio was calculated on the basis of the experimental data. Table 2 lists the experimental results and the S/N ratios

of the MRR, the TWR and the SR correlated with each experimental measurement for the die-sinking micro-EDM from the L_{16} orthogonal array based on the Taguchi method.

By using equations 3 and 4, the S/N ratio values were normalized to obtain the grey relational grade. The normalized data and derivative sequence Δ_{oi} for each of the responses are presented in Table 3. The grey rela-tional coefficients, given in Table 3, for each response were calculated by using equation 5. Table 3 also shows the overall grey relational grade calculated using equation 6. Thus, the multi-criteria optimization problem was transformed into a single equivalent objective-func-tion-optimization problem using the combination of the Taguchi approach and grey relational analyses. It is maintained that the higher the value of the grey relational grade, the closer to the optimum is the corresponding factor combination.[20]

The higher GRG highlighted in Table 3 shows that the corresponding experimental results are closer to the ideally normalized value. Experiment 5 has the best mul-tiple performance characteristics among 16 experiments as it has the highest GRG. In this study, the optimization of the multiple performance characteristics of the micro-EDM of EN-24 die steel was converted into an optimization of the GRG. The mean of the GRG for each level of the machining parameters and also the total mean of the GRG for 16 experiments are calculated in Table 4. Usually, the larger is the GRG, the closer will the product quality be to the ideal value. Hence, a large GRG is desired for an optimum performance. Therefore, the optimum-parameter setting, highlighted in Table 4, for a better MRR and lower TWR and SR is $A_2B_1C_4D_3$. The optimum level of the process parameters is the level with the highest GRG. Figure 3 shows the grey-rela-

Table 2: Experimental layout using the L_{16} orthogonal array and the performance results
Tabela 2: Eksperimentalna postavitev z L_{16} pravokotno matriko in uspešnost rezultatov

Exp. No	Level of parameter				Experimental result			S/N ratio (dB)		
	Gap vol-tage (V)	Capaci-tance (nF)	Feed rate (µm/s)	Threshold (%)	MRR (mm³/s)	TWR (%)	SR (µm)	MRR	TWR	SR
1	80	0.1	2	20	0.00025	13.42	0.087	−72.03	−22.55	21.21
2	80	1	4	40	0.000555	14.01	0.098	−65.11	−22.93	20.18
3	80	10	6	60	0.000555	18.29	0.113	−65.11	−25.24	18.94
4	80	100	8	80	0.000527	16.70	0.107	−65.57	−24.45	19.41
5	100	0.1	4	60	0.001271	14.06	0.094	−57.92	−22.96	20.54
6	100	1	2	80	0.000533	17.03	0.101	−65.47	−24.62	19.91
7	100	10	8	20	8.86E−05	18.31	0.126	−81.05	−25.25	17.99
8	100	100	6	40	0.000478	14.16	0.117	−66.42	−23.02	18.64
9	120	0.1	6	80	9.22E−05	16.36	0.102	−80.70	−24.27	19.83
10	120	1	8	60	0.000939	16.12	0.116	−60.55	−24.15	18.71
11	120	10	2	40	0.000202	21.50	0.132	−73.89	−26.65	17.59
12	120	100	4	20	0.000894	13.22	0.136	−60.97	−22.42	17.33
13	140	0.1	8	40	0.001335	15.81	0.112	−57.49	−23.98	19.02
14	140	1	6	20	0.001249	13.49	0.139	−58.07	−22.60	17.14
15	140	10	4	80	9.87E−05	16.97	0.163	−80.11	−24.59	15.76
16	140	100	2	60	0.000516	17.85	0.161	−65.75	−25.03	15.86

Table 3: Experimental results using the grey relational analysis
Tabela 3: Rezultati eksperimentov s sivo relacijsko analizo

Exp. No.	Normalized *S/N* ratio			Derivation sequence Δ_{oi}			Grey relational coefficient GC_{ij}			Grey relational grade γ_i
	MRR	TWR	SR	MRR	TWR	SR	MRR	TWR	SR	
1	0.3827	0.9697	1	0.6173	0.0303	0	0.4475	0.9429	1	0.7968
2	0.6765	0.8804	0.8104	0.3235	0.1196	0.1896	0.6071	0.8069	0.7250	0.7130
3	0.6765	0.3326	0.5835	0.3235	0.6674	0.4165	0.6071	0.4283	0.5456	0.5270
4	0.6571	0.5199	0.6704	0.3429	0.4801	0.3296	0.5932	0.5101	0.6027	0.5687
5	0.9818	0.8736	0.8767	0.0182	0.1264	0.1233	0.9649	0.7982	0.8022	0.8551
6	0.6612	0.4792	0.7623	0.3388	0.5208	0.2377	0.5961	0.4898	0.6778	0.5879
7	0.0000	0.3302	0.4101	1.0000	0.6698	0.5899	0.3333	0.4274	0.4588	0.4065
8	0.6210	0.8595	0.5281	0.3790	0.1405	0.4719	0.5689	0.7806	0.5145	0.6213
9	0.0148	0.5620	0.7466	0.9852	0.4380	0.2534	0.3366	0.5331	0.6637	0.5111
10	0.8703	0.5923	0.5418	0.1297	0.4077	0.4582	0.7940	0.5508	0.5218	0.6222
11	0.3039	0.0000	0.3360	0.6961	1.0000	0.6640	0.4180	0.3333	0.4295	0.3936
12	0.8523	1.0000	0.2884	0.1477	0.0000	0.7116	0.7720	1.0000	0.4127	0.7282
13	1.0000	0.6325	0.5977	0.0000	0.3675	0.4023	1.0000	0.5764	0.5541	0.7102
14	0.9754	0.9591	0.2537	0.0246	0.0409	0.7463	0.9530	0.9245	0.4012	0.7596
15	0.0397	0.4863	0	0.9603	0.5137	1	0.3424	0.4933	0.3333	0.3897
16	0.6494	0.3822	0.0197	0.3506	0.6178	0.9803	0.5878	0.4473	0.3378	0.4576

Table 4: Response table for the grey relational grade (GRG)
Tabela 4: Tabela odgovorov za sive relacijske stopnje (GRG)

Symbol	Parameter	Grey relational grade				Rank (Max–Min)
		Level 1	Level 2	Level 3	Level 4	
A	Gap voltage	0.6514	0.6177	0.5638	0.5793	4
B	Capacitance	0.7183	0.6707	0.4292	0.5940	1
C	Feed rate	0.5590	0.6715	0.6048	0.5769	3
D	Threshold	0.6728	0.6095	0.6155	0.5143	2

Total mean value of the GRG (γ_m) = 0.6030

tional-grade graph, where the dashed line is the value of the total mean of the grey relational grade. Basically, the larger the grey relational grade, the better are the multiple performance characteristics.

4.1 Analysis of variance (ANOVA)

ANOVA was used to investigate the design parameters that significantly affect the quality characteristics. Therefore, ANOVA was done by analyzing the influence of the gap voltage, capacitance, feed rate and threshold. The results of the analysis of variance (ANOVA) for the MRR, the TWR and the SR were calculated using the values of the grey relational coefficients and grey relational grades from **Table 3**. **Table 5** shows that the contribution of the capacitance and threshold were 47.44 % and 39.35 %, respectively. These two input parameters were found to be the most significant controlling parameters meaning that they controlled the MRR, TWR and SR simultaneously and very effectively.

4.2 Confirmation test

A confirmation test was carried out to predict and verify the enhancement of the quality characteristics using the optimum parametric combination. The esti-
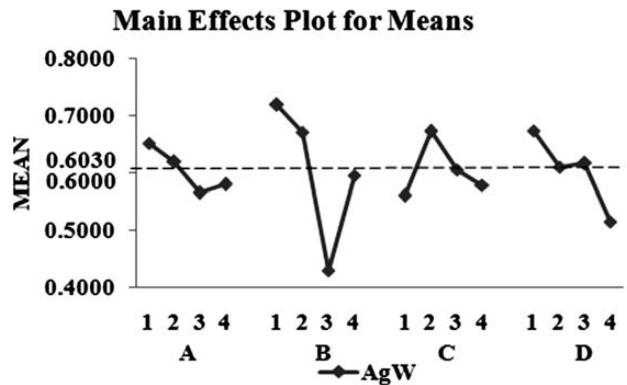
Figure 3: Main effects of the factors on the grey relational grade for AgW
Slika 3: Glavni vpliv faktorjev na razred pri sivi relaciji za AgW

Table 5: ANOVA table of grey relational analysis for AgW
Tabela 5: Tabela sive relacijske analize za AgW ANOVA

Source of variance	Sum of square	DOF	Mean square/ variance	Contri- bution (%)
Gap voltage (V)	4.66	3	1.55	6.38
Capacitance (nF)	48.17	3	16.06	65.92
Feed rate (µm/s)	7.31	3	2.44	10.01
Threshold (%)	12.93	3	4.31	17.69
Error	0	3	–	–
Total	73.06	15	4.87	100

mated grey relational grade using the optimum level of machining parameters can be calculated as:

$$\hat{\gamma} = \gamma_m + \sum_{i=1}^{p} \left(\bar{\gamma}_i - \gamma_m \right) \qquad (7)$$

where γ_m is the total mean grey relational grade, $\bar{\gamma}_i$ is the mean grey relational grade at the optimum level, and p is the number of the main designed parameters that affect the quality characteristics. Based on equation 7, the predicted grey relational grade was calculated. **Table 6** shows a comparison of the experimental results using the initial A2B1C2D3 and the optimum grey-theory-prediction-design A1B1C2D1 machining parameters. It is found that the MRR increased from 0.001271 mm³/min to 0.00132 mm³/min. The TWR decreased from 14.0579 % to 13.4671 % and the SR also decreased from 0.094 μm to 0.0907 μm. The corresponding improvement in the material-removal rate is 3.86 %, while the tool-wear ratio and the surface roughness were 4.20 % and 3.51 %, respectively. Hence, it is concluded that the grey relational analysis based on the Taguchi method for optimizing multi performance characteristics is a very useful tool for predicting the MRR, TWR and SR of the die-sinking micro-EDM.

Table 6: Micro-EDM results of L_{16} using the initial and optimum process factors
Tabela 6: Mikro-EDM-rezultati L_{16} pri uporabi začetnih in optimalnih procesnih dejavnikov

	Initial condition	Optimal factor	
		Prediction	Experiment
Level	A2B1C2D3	A1B1C2D1	A1B1C2D1
MRR	0.001271		0.00132
TWR	14.0579		13.4671
SR	0.094		0.0907
Grey relational grade	0.8551	0.905	0.9346

Improvement of the grey relational grade: 0.0795

5 CONCLUSIONS

An orthogonal array with a grey relational analysis was used to optimize the multiple response characteristics of the die-sinking micro-EDM.

The performance characteristics such as the material-removal rate, the electrode wear and the surface roughness were improved using the method proposed in this study.

According to the Taguchi L_{16} mixed orthogonal table, only 16 experiments need to be conducted to find the significant machining parameters. On the basis of an integration of the grey relational analysis and the *S/N* ratio, it is concluded from **Tables 4** and **5** that the capacitance and the threshold are the main influencing parameters followed by the gap voltage and the feed rate. More precisely, the significant machining parameters for the whole machining performance were the gap voltage of 80 V, the capacitance of 0.1 nF, the feed rate of 4 μm/s and the threshold of 20 %.

On the basis of the confirmation test, the improvement in the performance characteristics was found to be as follows: MRR 3.86 %, TWR 4.20 % and SR 3.51 %.

6 REFERENCES

[1] J. L. Lin, K. S. Wang, B. H. Yan, Y. S. Tarng, J Mater Process Technol, 102 (**2000**), 48–55

[2] G. S. Prihandana, M. Mahardika, M. Hamdi, Y. S. Wong, K. Mitsui, Int J Machine Tools Manuf, 49 (**2009**), 1035–1041

[3] N. Tosun, C. Cogun, G. Tosun, J Mater Process Technol, 152 (**2004**), 316–322

[4] K. P. Somashekar, N. Ramachandran, J. Mathew, Sixth international conference on Precision, Meso, Micro and Nano Engineering, COPEN6, 2009, C31–C36

[5] K. T. Chiang, F. P. Chang, J Mater Process Technol, 180 (**2006**), 96–101

[6] S. Datta, A. Bandyopadhyay, P. K. Pal, Int J Adv Manuf Technol, 39 (**2008**), 1136–1143

[7] U. Esme, Mater. Tehnol., 44 (**2010**) 3, 129–135

[8] N. Natarajan, R. M. Arunachalam, J Sci Ind Res, 70 (**2011**), 500–505

[9] V. K. Meena, M. S. Azad, Mat and Manuf Process, 27 (**2012**) 9, 973–977

[10] G. Rajyalakshmi, P. Venkata Ramaiah, Int. J of Adv. and Innov Res., 1 (**2012**) 3, 125–137

[11] J. H. Jung, W. J. Kwon, Journal of Mechanical Science and Technology, 24 (**2010**) 5, 1083–1090

[12] X. Shen, Z. Ning, M. Zhang, IEIT Journal of adaptive and Dynamic computing, 3 (**2012**), 26–30

[13] V. Muthu Kumar, A. Suresh Babu, R. Venkatasamy, M. Raajenthiren, CURIE, 3 (**2011**) 3–4, 79–88

[14] W. H. Yang, Y. S. Tarng, J Mater Process Technol, 84 (**1998**), 122–129

[15] T. R. Lin, Int Adv Manuf Technol, 19 (**2002**), 330–335

[16] K. Jangra, A. Jain, S. Grover, J Sci Ind Res, 69 (**2010**), 606–612

[17] J. T. Huang, Y. S. Liao, Int J Prod Res, 41 (**2003**) 8, 1707–1720

[18] K. Krishnaiah, P. Shahabudeen, Applied Design of Experiments and Taguchi methods, PHI Learning Private Limited, New Delhi, 2012

[19] Y. Kuo, T. Yang, G. W. Huang, Engineering Optimization, 40 (**2009**) 6, 517–528

[20] H. Aybin, A. Bayram, U. Esme, Y. Kazancoglu, O. Guven, Mater. Tehnol., 44 (**2010**) 4, 205–211

PREDICTION OF THE NUGGET SIZE IN RESISTANCE SPOT WELDING WITH A COMBINATION OF A FINITE-ELEMENT ANALYSIS AND AN ARTIFICIAL NEURAL NETWORK

NAPOVEDOVANJE PODROČJA PRETALITVE PRI UPOROVNEM VARJENJU S KOMBINACIJO ANALIZE KONČNIH ELEMENTOV IN UMETNIH NEVRONSKIH MREŽ

Davood Afshari[1], Mohammad Sedighi[1], Mohammad Reza Karimi[1], Zuheir Barsoum[2]

[1]School of Mechanical Engineering, Iran University of Science and Technology, Tehran, Iran
[2]Department of Aeronautical and Vehicles Engineering, KTH – Royal Institute of Technology, Stockholm, Sweden
sedighi@iust.ac.ir

The goal of this investigation is to predict the nugget size for a resistance spot weld of thick aluminum 6061-T6 sheets 2 mm. The quality and strength of spot welds determine the integrity of the structure, which depends thoroughly on the nugget size. In this study, the finite-element method and artificial neural network were used to predict the nugget size. Different spot welding parameters such as the welding current and the welding time were selected to be used for a coupled, thermal-electrical-structural finite-element model. In order to validate the numerical results a series of experiments were carried out and the nugget sizes were measured. The results obtained with the finite-element analysis were used to build up a back-propagation, artificial-neural-network model for the nugget-size prediction. The results revealed that a combination of these two developed models can accurately and rapidly predict the nugget size for a resistance spot weld.

Keywords: resistance spot weld, nugget size, finite-element analysis, artificial neural network, aluminum alloys

Cilj te preiskave je napovedati velikost področja pretalitve pri uporovno zvarjeni aluminijasti pločevini 6061-T6, debeli 2 mm. Kvaliteta in trdnost točkastega zvara določata celovitost konstrukcije, kar je odvisno predvsem od velikosti področja pretalitve. V tej študiji sta bili za napovedovanje velikosti področja pretalitve uporabljeni metoda končnih elementov in umetna nevronska mreža. Izbrani so bili različni parametri varjenja, kot sta varilni tok in čas varjenja, za skupni termično-električno-strukturni model končnih elementov. Za oceno numeričnih rezultatov je bilo izvršenih več preizkusov in izmerjena je bila velikost področja pretalitve. Rezultati, dobljeni iz analize končnih elementov, so bili uporabljeni za gradnjo modela umetne nevronske mreže za napovedovanje velikosti področja pretalitve. Rezultati so odkrili, da kombinacija teh dveh razvitih modelov lahko zanesljivo in hitro napove velikost področja pretalitve pri uporovnem točkastem zvaru.

Ključne besede: uporovni točkasti zvar, velikost področja pretalitve, analiza končnih elementov, umetna nevronska mreža, zlitine aluminija

1 INTRODUCTION

Resistance spot welding (RSW) is one of the most important and well-known methods of sheet joining in various industries, especially in the automobile and aerospace industries. The process is ideal for joining low-carbon steel, stainless steel, nickel, and aluminum or titanium alloy components with various thicknesses and it is, thus, used extensively. Although each material has its own particular place and special importance, today, aluminum alloys are the most widely used materials after steel. Though spot welding of aluminum alloys is more difficult than spot welding of steels because of their narrow plastic rang, low bulk resistance and greater thermal conductivity, aluminum alloys are still used for the bodies and chassis of many components due to their lightweight and relatively high strength resulting in a reduction of a vehicle structural weight, fuel consumption and exhaust emissions.[1,2]

Typically, a modern automotive vehicle contains 2000–5000 spot welds and the joint quality and perfor-mance can dramatically alter the structural performance of vehicles, having a critical role in durability and safety design of vehicles.[3] During a resistance-welding opera-tion, a workpiece is pressed between two electrodes and an electrical current is passed between the electrodes. Based on the Joule's law, the resistance in the electrode-worksheet and worksheet-worksheet interfaces generates the heat that locally melts and binds the sheets together. The section, where the two pieces of metal melt and then cool down to form one piece is called a nugget. In fact, the nugget is the area that actually joins the two pieces of metal together. The quality and strength of spot welds in a structure determine the performance quality of that structure, depending thoroughly on the nugget size. The nugget size should be larger than a certain volume to secure the strength of a welded joint. On the other hand, changing the parameters to obtain a very large nugget size leads to an explosion in the weld zone which redu-ces the strength of a welded joint. The nugget size is usually between 4 and 8.5 mm, completely depending on

the sheet thickness. So, a control of the welding parameters is necessary to obtain a high weld quality and to increase a vehicle's life.

Although there are many researches being carried out on the effects of welding parameters on the nugget size in a spot weld of steels and many approaches being developed and recommended for a nugget-size prediction, the studies on aluminum-alloy spot welds are scarce. Darwish et al.[4–6] completed many studies on the spot welds of commercial B. S. 1050 aluminum alloys. Khan et al.[7] and Fangjie et al.[8] used a finite-element model (FEM) to predict the nugget size for a spot weld of an aluminum alloy. Sun et al.[9] studied the failure load and the failure mode of spot welds of aluminum alloys 5182-O and 6114-T4 with a cross-tension test. Pereira et al.[1] carried out studies on the effect of process parameters on the strength of spot welds in 6082-T6 aluminum alloys with a sheet thickness 1 mm under a quasi-static tensile test and recommended a model for calculating the critical nugget size to achieve the PL failure mode. Recently, Han et al.[10] have studied the failure load in lap shear, cross tension and coach peel of resistance-spot-welded aluminum AA5754.

The use of a finite-element analysis (FEA) decreases the main costs associated with the nugget-size measurement tests; however, due to a high complexity of a spot weld, its FEA models are very time-consuming, requiring high-speed computers. The method of artificial neural networks (ANNs) is considered as an effective approach for solving non-linear problems. A quick learning ability and high-speed solutions of ANNs have led to a more extensive use of this method.[11] In recent years, the use of ANNs in modelling resistance spot welds has attracted the attention of researchers. Park[12] and Martin[13] employed these networks to predict the fatigue life and improvement in the quality of spot welds. Also, Cortez[14] used an ANN to investigate the weldability of different metals with the spot-weld process.

The joint use of an FEA and ANN can eliminate the high costs of laboratory tests and significantly shorten
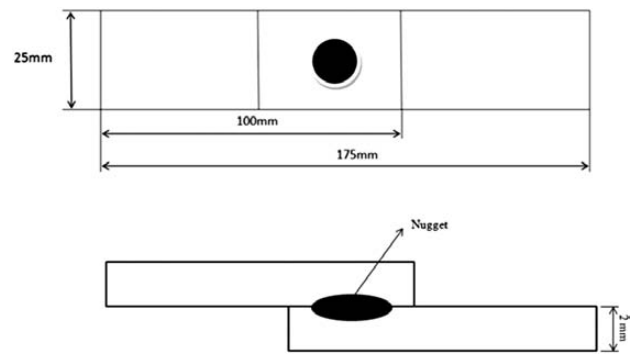
Figure 1: Dimensions of the samples (dimensions in millimeters, not to scale)
Slika 1: Dimenzije vzorcev (dimenzije v milimetrih, ni v merilu)

the time needed for a solution. This idea has been the basis of our study. In this study, a FEA model along with an ANN has been adopted to predict the nugget size for the spot welds of a thick aluminum 6061-T6 sheet 2 mm. At first, the experimental procedures utilized to prepare the spot-welded samples and the nugget-size measurement are shown. Then, the basics of the axi-symmetrically coupled, thermal-electrical-mechanical FEA are presented. The structure of an ANN model is provided in Section 4. The results are discussed in Section 5 and the conclusions are given in last section.

2 EXPERIMENTAL PROCEDURES

The thick, heat-treatable aluminum-alloy 6061-T6 sheets 2 mm were welded as a lap joint with the dimensions of 100 mm × 25 mm × 2 mm (**Figure 1**). The nominal chemical composition and mechanical properties of the base material are given in **Table 1**. Before spot welding, each sheet was cleaned mechanically with sandpaper and the welding process was performed with a NIMAK type PMP11 DGS, AC power machine with the nominal welding power of 200 kV A and copper electrodes. Nine different series of welding parameters were

Table 1: Mechanical properties and chemical composition of aluminum alloy 6061-T6 (mass fractions, w/%)
Tabela 1: Mehanske lastnosti in kemijska sestava zlitine aluminija 6061-T6 (masni deleži, w/%)

Yield strength	Tensile strength	Hardness	Al	Si	Mn	Mg	Fe	Cu	Cr
MPa	MPa	Vickers	%	%	%	%	%	%	%
276.0	310.0	107.0	97.0	0.6	0.1	1.0	0.5	0.2	0.1

Table 2: Resistance-spot-welding operations for aluminum 6061-T6
Tabela 2: Parametri točkastega varjenja aluminija 6061-T6

Sample No.	Electrical current	Welding time	Electrode force	Sample No.	Electrical current	Welding time	Electrode force
	(kA)	(cycles)	(N)		(kA)	(cycles)	(N)
1	36	4	4033	6	37	4	4033
2	36	5	4033	7	38	4	4033
3	36	6	4033	8	39	4	4033
4	36	7	4033	9	40	4	4033
5	36	8	4033	–	–	–	–

used for the welding of 27 samples (3 samples for each series of parameters). The welding conditions were based on the recommendations by AWS[15] in order to achieve the minimum nugget size and avoid an expulsion in welding.

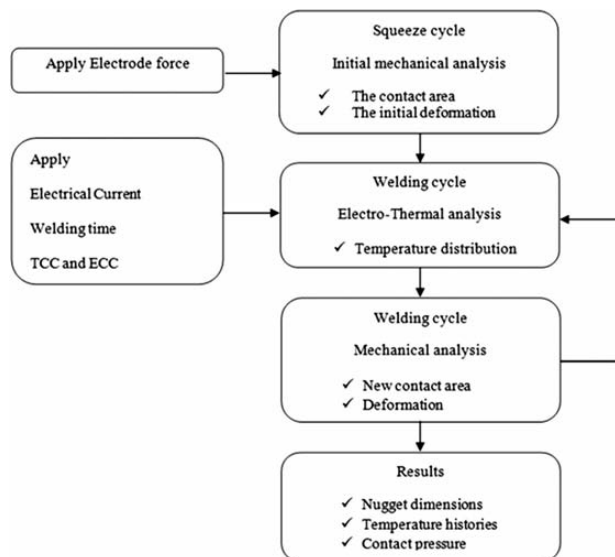**Table 2** summarizes these 9 series with the corresponding welding parameters. As seen in **Table 2**, very small expulsions occurred in welding Samples 5 and 9. To measure the nugget size, the samples were first cut along the center line and then mounted, polished and etched. The nugget-size measurements were done using an interaction of an optic microscope and special software developed for image processing.

3 FINITE-ELEMENT ANALYSIS

Different phenomena (e.g., mechanical, thermal, electrical, metallurgical, etc.) are involved in resistance-spot-welding operations. Due to a complexity of the spot-welding process and the extensive connections between these different fields, a simulation of these operations is very difficult. In this study, an axi-symmetrically coupled, thermal-electrical-mechanical FE model was used for simulating a spot weld. To create the FE model for the simulation of spot welding of aluminum 6061-T6, the commercial ANSYS12.1 software and the APDL environment were used. To achieve high accuracy, the temperature-dependent properties were defined for the material.

The solving algorithm of the finite-element model is illustrated in **Figure 2**. The first step of the welding process is the squeeze cycle. In this step, only the electrode force is applied to the model and the structural elements are used for the initial mechanical analysis to determine the initial deformation and the contact-area shape. In the welding cycle, the electrical current is

applied to the top surface of the upper electrode and by using the thermal-electrical elements the heat generation is calculated for each increment from the fully coupled model.

All the mechanical, electrical and thermal boundary conditions used in the FE model are presented in **Figure 3**. In the welding cycle, the *rms* electrical current is applied uniformly to the top surface of the upper electrode and after passing through the electrode-sheet and sheet-sheet contact areas, it reaches the bottom surface of the lower electrode, where zero electrical voltage has been applied. For all the process cycles, a constant water temperature of 25 °C was considered for the electrode's water channel. Since an exact estimation of the convection-heat-transfer coefficient for the surfaces of the sheets and electrodes that are in contact with air is very difficult as it depends on numerous factors such as the air-flow velocity and surface quality, for all the surfaces that are in contact with air, the convection-heat-transfer coefficient was determined to be constant and equal to 12 W m^{-2} K^{-1}.[16] The ambient room temperature was assumed as 20 °C. The electrode force, as a uniform compressive load, was applied to the upper electrode, as shown in **Figure 3**.

All the equations in this work are based on a two-dimensional cylindrical coordinate system. Equation 1 presents the governing equation for calculating the electrical potential φ for the whole model:

$$\frac{\partial}{\partial r}\left(C_0\,\frac{\partial\varphi}{\partial r}\right)+\frac{C_0}{r}\frac{\partial\varphi}{\partial t}+\frac{\partial}{\partial z}\left(C_0\,\frac{\partial\varphi}{\partial z}\right)=0 \tag{1}$$
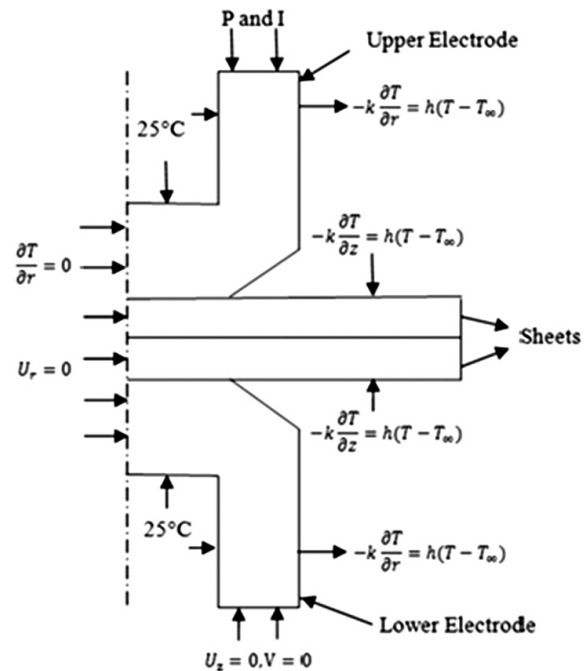

Figure 2: Flowchart of the finite-element solving algorithm
Slika 2: Shema reševanja algoritma s končnimi elementi

Figure 3: Axi-symmetric finite-element model used for a spot-weld simulation with boundary conditions
Slika 3: Osnosimetrični model končnih elementov, uporabljen za simulacijo točkastega zvara, z robnimi pogoji

where r is the radial distance, z is the distance in the axis direction and C^s is the electrical conductivity. Based on the Joule heat equation, the heat generation per unit volume, q, can be shown with equation 2:

$$q = \frac{\varphi^2 t}{R} \qquad (2)$$

where t is the time and R is the material electrical resistance. The governing equation for the transient-temperature-field distribution considering the electrical-resistance heat can be presented with equation 3:

$$\rho t \frac{\partial T}{\partial t} = \frac{\partial}{\partial r}\left(k\frac{\partial T}{\partial r}\right) + \frac{k}{r}\frac{\partial T}{\partial r} + \frac{\partial}{\partial z}\left(k\frac{\partial T}{\partial r}\right) + \dot{q} \qquad (3)$$

where ρ is the material density, C is the heat capacity, T is the temperature, $\dot{q}$ is the rate of heat generation per unit volume and k is the thermal conductivity. For a stress and strain analysis, the governing equation is described in an incremental form for the finite-element model:

$$\{\Delta\sigma\} = [D]\{\Delta\varepsilon\} + \{C\}\Delta T \qquad (4)$$

where vectors $\{\Delta\sigma\}$ and $\{\Delta\varepsilon\}$ are stress and strain increments, respectively, matrix $[D]$ is the elastic-plastic matrix and vector $\{C\}$ can be defined as:

$$\{C\} = -[D^0]\left(\{\alpha\} + \frac{\partial[D^0]^{-1}}{\partial T}\right) \qquad (5)$$

Here matrix $[D]$ is the elastic matrix and matrix $\{\alpha\}$ is the coefficient of thermal expansion.

4 ARTIFICIAL NEURAL NETWORK

A back-propagation ANN was employed to predict the nugget size for a spot weld. Structurally, every ANN is made up of three sections (**Figure 4**). The initial section corresponds to the input layer of an ANN. In the present study, the two main parameters, the welding current and the welding time, were used as the network inputs. The number of layers and neurons of the middle section, or the hidden layer, are determined with the trial-and-error method. The end section of the network is
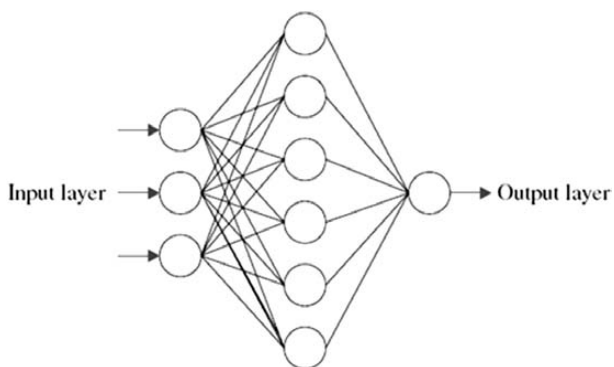
the output layer. In this study, the nugget diameter was used as the ANN output due to its significant role in the quality of the welded joint.

The training algorithm of Levenberg-Marquad was employed to train the ANN. This training algorithm has a very quick learning speed. The performance index used in the training was the mean squared error (*MSE*) defined as:

$$MSE = \frac{1}{N}\sum_{i=1}^{N}(r_i - \hat{r}_i)^2 \qquad (6)$$

where r_i is the actual variable, while $\hat{r}_i$ is the estimated variable and N is the number of data samples. In the present study, the tolerance for *MSE* was selected as 0.0001.

5 RESULTS AND DISCUSSIONS

Since the weld quality and strength are completely related to the nugget size, the metallographic analysis and microstructure studies are employed to better understand the microstructures of the weld zones and to correctly specify and measure the nugget diameter. **Figure 5** shows a typical macrostructure of a spot-welded sample. Three distinct zones are clearly observed: the base metal (BM), the heat-affected zone (HAZ) and the fusion zone (FZ) or the nugget. The microstructure investigation shows two different zones in the nugget area: the grains with columnar structure oriented in the direction of the heat flow around the nugget and a new nucleation zone in the center, as seen in **Figure 6**. The reason for the two different microstructures in the nugget zone could be a variation in the cooling rate within the nugget zone.[1]

The microstructure of the HAZ is different from that of the nugget. In the area between the nugget and HAZ, there is a thin zone with large and coarse grains; it could be attributed to an abnormal grain growth due to an extremely high temperature. However, beyond this zone, the HAZ consists of very small and fine grains, as seen in **Figure 6**.

Figure 4: Typical artificial neural network
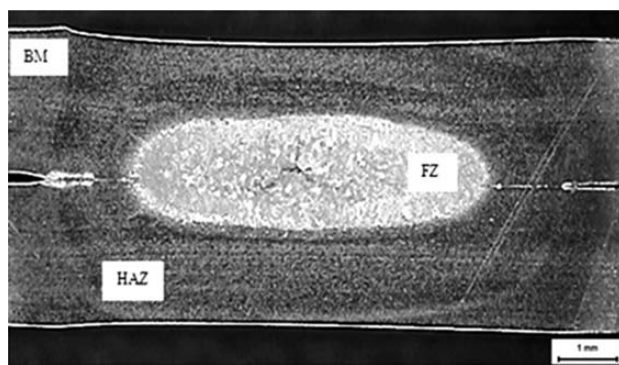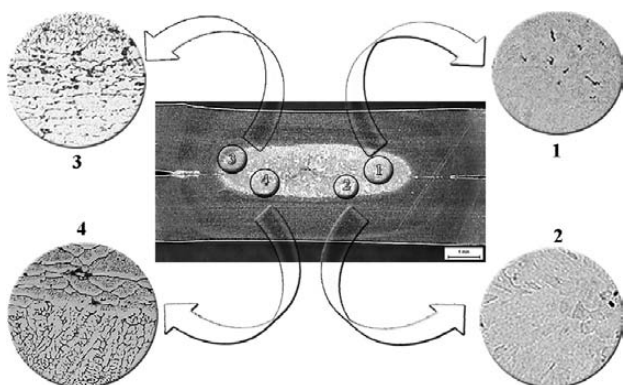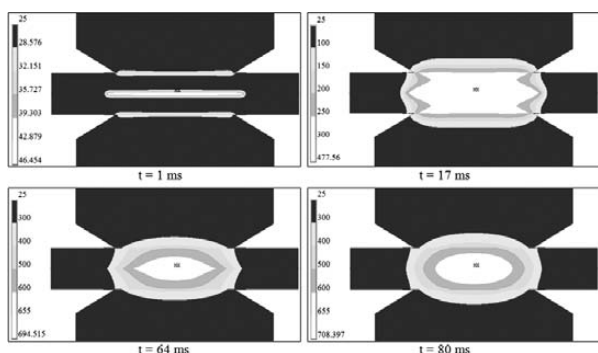**Slika 4:** Značilna umetna nevronska mreža

Figure 5: Different zones in the weld area, FZ: nugget zone, HAZ: heat-affected zone and BM: base material
Slika 5: Različna področja v zvaru, FZ: področje pretalitve, HAZ: toplotno vplivano področje in BM: osnovni material

Figure 6: Microstructure of the nugget (Sample 5)
Slika 6: Mikrostruktura v območju pretalitve (vzorec 5)

Figure 7: Nugget development in the finite-element model (welding current: 36 kA, electrode force: 4033 N), welding time: a) 1 ms, b) 17 ms, c) 64 ms and d) 80 ms
Slika 7: Rast področja pretalitve pri modelu končnih elementov (varilni tok: 36 kA, pritisk elektrode: 4033 N), čas varjenja: a) 1 ms, b) 17 ms, c) 64 ms in d) 80 ms
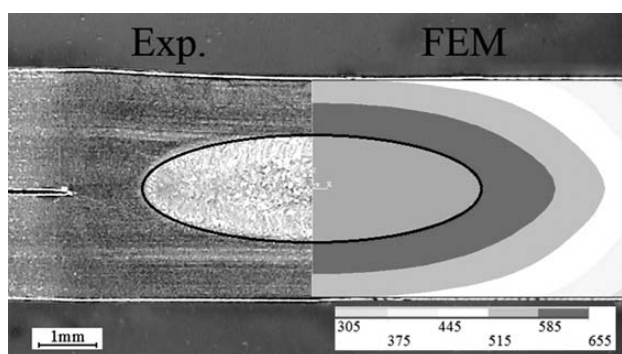
Figure 8: Comparison between the simulated nugget obtained with the FEM and the actual nugget of Sample 1
Slika 8: Primerjava med simuliranim področjem pretalitve s FEM in resnično velikostjo področja pretalitve pri vzorcu 1

Figure 7 illustrates the steps of the nugget formation in the FE model. To validate the FE model results, the model was compared with the data obtained with the nugget-size measurements. In **Figure 8**, the FEM nugget size is compared with the actual nugget size for Sample 1. **Figure 9** compares the results of the FEM and the experimental tests for all the samples presented in **Table**
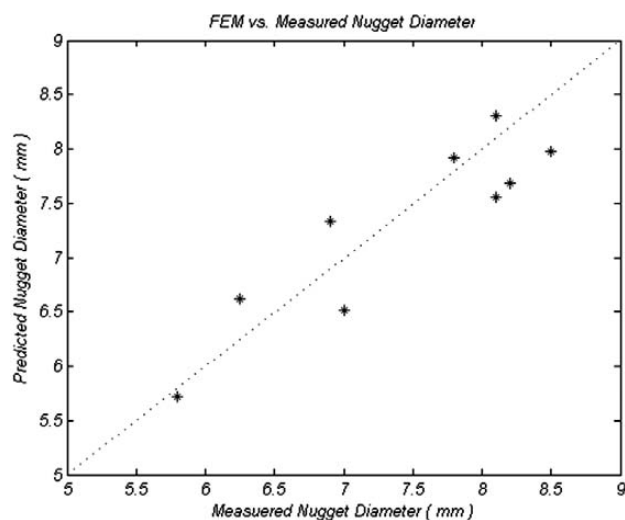
Figure 9: Comparison between the nugget diameter obtained with the FEM and the data obtained with the experimental test presented in **Table 2**
Slika 9: Primerjava med premerom pretaljenega področja, dobljenega s FEM in eksperimentalnimi podatki, prikazanimi v **tabeli 2**

1. The FEM results indicate that the presented model has a good accuracy.

As mentioned before, the welding conditions were based on the recommendations by AWS[15] in order to achieve the minimum nugget size (5.6 mm for the sheets with a thickness 2 mm) and avoid an expulsion in the welding. Considering the results obtained from a previous study,[17] for thick aluminum 6061-T6 sheets 2 mm, with a weld-nugget diameter of above 8.5 mm, the spattering of melt during a spot-welding operation is predictable. Therefore, the selection of the spot-welding parameters is based on the simulation results of the FE analysis with the aim to achieve a weld-nugget diameter between 5.6 mm and 8.5 mm. **Table 3** shows the selected spot-welding parameters obtained from the FEA for the nugget-size prediction with the ANN. Of the 54 sets of parameters presented in **Table 3**, five samples were randomly selected and used for testing the ANN, and the remaining samples (49 samples) were used for training the ANN.

Table 3: Considered spot-weld parameters for the ANN creation
Tabela 3: Parametri točkastega zvara, upoštevani pri postavitvi ANN

Electrode force (N)	Welding time (Cycles)	Welding current (kA)
4033	4, 4.5, 5, 5.5, 6, 6.5, 7 and 7.5	36
4033	4, 4.5, 5, 5.5, 6, 6.5, 7 and 7.5	36.5
4033	3.5, 4, 4.5, 5, 5.5, 6, 6.5 and 7	37
4033	3.5, 4, 4.5, 5, 5.5, 6 and 6.5	37.5
4033	3.5, 4, 4.5, 5 and 5.5	38
4033	3.5, 4, 4.5, 5 and 5.5	38.5
4033	3, 3.5, 4, 4.5 and 5	39
4033	3, 3.5, 4 and 4.5	39.5
4033	3, 3.5, 4 and 4.5	40

Figure 10: Results of the neural-network training
Slika 10: Rezultati, dobljeni z usposabljanjem nevronske mreže

Figure 11: Results of the neural-network test
Slika 11: Rezultati preizkusa nevronske mreže

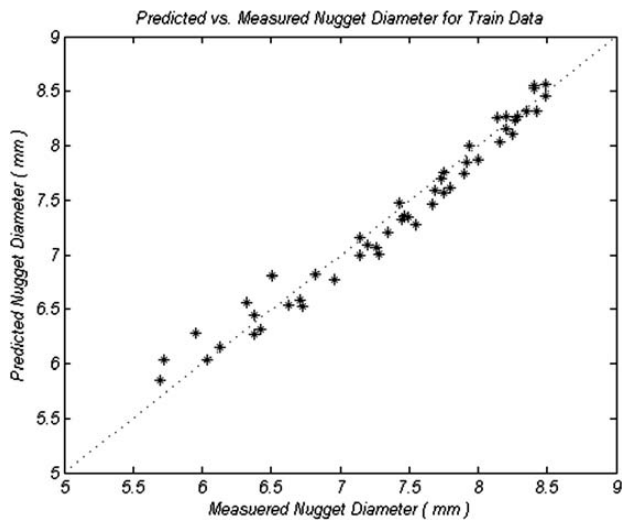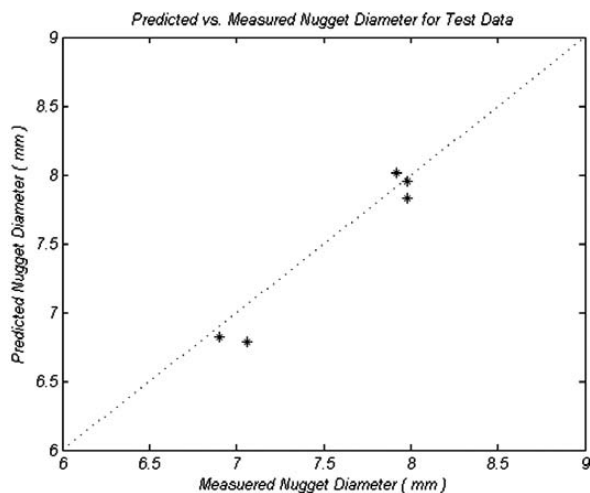By testing different structures of the ANN, it was determined that an ANN with one hidden layer and eight neurons in this layer has the lowest error in the prediction of the nugget diameter. **Figure 10** shows the results of training a developed ANN on the basis of the data obtained from the FE analysis. As this figure indicates, the presented ANN was well trained.

After training the created ANN, the network was tested by employing the five samples that had not been used in the training. The result of the testing is shown in **Figure 11**. The obtained results demonstrate that the created ANN has a good accuracy (less than 3 % of the absolute average error) in the prediction of the nugget diameter, based on the listed spot-welding parameters. So, this network can be used reliably for predicting the nugget diameter in the spot weld of thick aluminum 6061-T6 sheets 2 mm.

6 CONCLUSIONS

In this study, the nugget size for the spot weld of an aluminum 6061-T6 sheet with a thickness of 2 mm was predicted with a combination of a finite-element analysis and artificial neural network. The findings obtained from the nugget-size measurements, the FEA and the ANN can be summarized as follows:

- The comparison between the FEA results and the measured nugget size indicates that the presented model has a good accuracy in the prediction of the nugget size and that, by using this model, the nugget size for spot welds can be rapidly investigated.
- The ANN model created using the results of the FEA has a very good accuracy (less than 3 %) in the prediction of the nugget size, based on the spot-welding parameters of the welding current and the welding time.
- After a verification of FEA and ANN results, through the use of the FEA and ANN, the size of the nugget in a spot weld can be well predicted, reducing the number of the nugget-size measurements.

7 REFERENCES

[1] A. M. Pereira, J. M. Ferreira, A. J. Loureiro, D. M. Costa, P. J. Bartolo, Material and Design, 31 (**2010**), 2454–2463
[2] Y. J. Chao, Journal of Engineering Materials and Technology, 125 (**2003**), 125–132
[3] X. Sun, E. V. Stephens, M. A. Khaleel, Engineering Failure Analysis, 15 (**2008**), 356–367
[4] S. M. Darwish, S. D. Al-Dekhial, Journal of Materials Processing Technology, 91 (**1999**), 43–51
[5] S. M. Darwish, S. D. Al-Dekhial, International Journal of Machine Tools & Manufacture, 39 (**1999**), 1589–1610
[6] S. M. Darwish, International Journal of Adhesion & Adhesives, 23 (**2003**), 169–176
[7] J. A. Khan, L. Xu, Y. Chao, K. Broach, Numerical Heat Transfer Part A, 37 (**2000**), 425–446
[8] C. Fangjie, J. Zhang, S. Hu, P. Shan, Trans. Tianjin. University, 17 (**2011**), 28–32
[9] X. Sun, E. V. Davies, R. W. Khaleel, D. J. Spinella, Welding Journal, 83 (**2004**), 308–318
[10] L. Han, M. Thornton, D. Boomer, M. Shergold, Journal of Material Processing Technology, 211 (**2011**), 513–521
[11] M. S. Choobi, M. Haghpanahi, M. Sedighi, Computational Materials Science, 62 (**2012**), 152–159
[12] J. M. Park, H. T. Kang, Material and Design, 28 (**2008**), 311–325
[13] O. Martin, M. Lopez, F. Martin, Journal of Materials Processing Technology, 183 (**2007**), 226–233
[14] V. H. L. Cortez, F. A. R. Valdes, L. T. Trevino, Materials & Manufacturing Processing, 24 (**2009**), 1412–1417
[15] American welding society, Recommended practices for resistance welding, AWS C1.1M/C1.1:2000, AWS, New York, 2003
[16] X. Long, S. K. Khanna, Science and Technology of Welding and Joining, 10 (**2005**), 88–94
[17] D. Afshari, M. Sedighi, Z. Barsoum, R. L. Peng, Journal of Engineering Manufacture Part B, 226 (**2012**), 1026–1032

GEOPOLYMERIZATION OF LOW-GRADE BAUXITE

GEOPOLIMERIZACIJA REVNEGA BOKSITA

Irena Nikolić[1], Ivona Janković - Častvan[2], Jasmina Krivokapić[1], Dijana Đurović[3], Vuk Radmilović[2], Velimir Radmilović[2]

[1]Faculty of Metallurgy and Technology, University of Montenegro, Džordža Vašingtona bb, 81 000 Podgorica, Montenegro
[2]Faculty of Technology and Metallurgy, University of Belgrade, Karnegijeva 4, 11120 Belgrade, Serbia
[3]Institute of Public Health of Montenegro, Džona Džeksona bb, 81 000 Podgorica, Montenegro
irena@ac.me

In terms of quality, bauxite ore can be classified as high- or low-grade ore. High-grade bauxite ores are used for alumina extraction using the Bayer process, while low-grade bauxite ores have a limited application. In this paper we investigate the possibility of evaluating low-grade bauxite ores with the geopolymerization process. The influence of the synthesis parameters, i.e., alkali and silicate dosages and alkali cations (Na^+ and K^+) on the compressive strength of bauxite-based geopolymers is evaluated. The results show that an increase in the alkali dosage has a beneficial effect on the strength of bauxite-based geopolymers, while the strengthening of geopolymers by increasing the silicate dosage is limited by the viscosity of the geopolymer paste. Moreover, Na-geopolymers reach higher values of the compressive strength than K-geopolymers.

Keywords: geopolymerization, low-grade bauxite, alkali-cation geopolymerization degree, compressive strength

Glede na kvaliteto delimo boksitne rude na revne in bogate. Bogate se uporabljajo za pridobivanje glinice po Bayerjevem postopku, medtem ko ima revna boksitna ruda le omejeno uporabnost. V tem članku opisujemo preiskavo možnosti za oceno revne boksitne rude s postopkom geopolimerizacije. Ocenjeni so bili parametri sinteze, to je dodatek alkalij in silikatov ter alkalnih kationov (Na^+ in K^+) na tlačno trdnost geopolimera na osnovi boksita. Rezultati so pokazali, da povečanje dodatka alkalij ugodno vpliva na trdnost geopolimera na osnovi boksita, medtem ko je utrjevanje geopolimera z dodajanjem silikata omejeno z viskoznostjo geopolimerne paste. Poleg tega doseže Na-geopolimer večjo tlačno trdnost v primerjavi s K-geopolimerom.

Ključne besede: geopolimerizacija, revni boksit, stopnja alkalijske kationske geopolimerizacije, tlačna trdnost

1 INTRODUCTION

Bauxite ore is the most important Al-bearing ore, comprised of aluminium, silica, titania, iron oxides and traces of impurities. It is mainly used for alumina extraction with the Bayer process. The efficiency of aluminium extraction from bauxite ore greatly depends on the content of reactive silica. With respect to alumina and silica contents, bauxite ores can be of high (metallurgical) or low (non-metallurgical) grade. The Bayer process only utilizes the high-grade (metallurgical) bauxite with high alumina and low reactive-silica contents. On the other hand, low-grade bauxite is characterised by a higher content of reactive silica. Reactive silica includes silica phases in the form of clay or quartz, which restrict its processing with the traditional Bayer process because of a loss of soda and alumina. Effective processing of low-grade bauxite for alumina production includes a pre-treatment which renders the silica unreactive during the Bayer digestion or allows a separation of silica from bauxite.[1] The soda-sinter process or a combination of Bayer-sinter processes are mainly used to produce alumina from low-grade bauxite.[2] Nevertheless, these processes are characterised by high energy consumption which does not qualify them as efficient methods for alumina production. Chemical pre-treatments of low-grade bauxite with a selective flocculation[3] and direct or reverse flotation[4,5] are promising methods for de-silicating low-grade bauxite and hydrometallurgical processing for alumina extraction.

On the other hand, a high silica content in low-grade bauxites makes them suitable for the geopolymerization process. Geopolymerization is a relatively new technology that can transform natural or waste aluminosilicate materials, with alkali activation, into an amorphous to semi-crystalline inorganic polymer – the geopolymer.[6] The process includes several steps: dissolution of the starting material in a highly alkaline silicate solution and formation of aluminate and silicate monomeric species, formation of Si and/or Si–Al oligomers in an aqueous solution, condensation of oligomeric species in an aluminosilicate network – geopolymer, and hardening.[7] Mixtures of sodium or potassium hydroxide solutions and alkaline silicate solutions (water glass) are mainly used as activators in the geopolymerization process. The role of alkali cations in the geopolymerization process is twofold:

- the Si^{4+} and Al^{3+} cations in geopolymer gels are tetrahedrally coordinated as $[SiO_4]^{4-}$ and $[AlO_4]^{5-}$ and are linked by oxygen bridges;[8] the negative charge on the AlO_4^- group is charge-balanced by alkali cations,[9]
- alkali cations also influence the dissolution step of the geopolymerization process by acting as catalysts

in the dissolution of Al and Si from the starting materials[10].

In this paper we investigate the influence of synthesis parameters and alkali cations on the geopolymerization process.

2 EXPERIMENT

2.1 Materials and the geopolymer synthesis

Low-grade bauxite from the Paklarica deposit in Montenegro, with its granulation below 100 μm, was used for a geopolymer synthesis. Its chemical composition is given in **Table 1**.

Table 1: Chemical composition of low-grade bauxite
Tabela 1: Kemijska sestava revnega boksita

Component	w/%
SiO_2	15
Fe_2O_3	13
Al_2O_3	54
TiO_2	2
CaO	0.45
Na_2O	0.2
MgO	0.15
MnO	0.1
Cr_2O_3	0.09
K_2O	0.1
LOI*	14.9

*Loss on ignition

A mixture of sodium- or potassium-based alkaline and silicate solutions was used as an activator. The alkaline silicate solution was prepared by mixing MOH and M_2SiO_3 (M represents the Na or K ion) solutions with the mass ratios of 1, 1.5 and 2. Commercial sodium and potassium silicate solutions ($w(Na_2O) = 8.5$ %, $w(SiO_2) = 28.5$ %, the density of 1.39 kg/m³; $w(K_2O) = 13.18$ %, $w(SiO_2) = 26.38$ %, the density of 1.39 kg/m³) were used.

Geopolymer paste was prepared by mixing bauxite with the alkaline silicate solution at the solid to liquid (S/L) ratio of 2.5. The paste was cast in a closed, plastic cylindrical mould, with the dimensions of 28 mm × 60 mm and cured for 72 h at 65 °C (24 h in a closed mould, 24 h in an open mould and after the samples were removed from the moulds, they were left to cure for another 24 h). The geopolymer samples were left for 14 days at ambient temperature before any testing was performed.

2.2 Characterisation techniques

Compressive strength measurements were performed according to the MEST EN 1354:2011 standard using two cylinders of each sample and averaging the obtained experimental values.

Microstructural investigations were carried out using the FEI 235 DB focussed ion-beam system, equipped with an EDAX energy dispersive spectrometer (EDS). The SEM images were recorded with various electron detectors, including a secondary electron detector (SED) and through-the-lens back scattered detector (TLD-B).

The pore-size distribution and surface area were evaluated using N_2 adsorption/desorption isotherms that were measured with an ASAP 2020 instrument. Degassing of the geopolymer samples was performed at 100 °C for 24 h to ensure the removal of the moisture in the samples. Surface areas were calculated using the Brunauer-Emmet-Teller (BET) method,[11] while the pore-size distribution and cumulative pore volumes were determined with the Barret-Joyner-Halenda (BJH) method.[12]

The degree of geopolymerization reaction for the bauxite-based geopolymers was investigated with chemical processes using the method described by Rattanasak et al.[13]

A geopolymer powder sample (3 g) was dissolved using 30 ml of 2 M HCl and stirred for 20 min at 60 °C. After this, a separation of the solid and liquid phases was performed with filtration and the remaining solid was washed with warm water to completely remove HCl. In the final filtration step, acetone was applied to remove the water before drying the sample at 70 °C for 2 h. After this treatment, dissolution of the remaining solid with 30 ml of 3 % $w(Na_2CO_3)$ was carried out for 20 min at 80 °C. Finally, another separation of the solid and liquid phases was performed; the residual sample was washed with water and acetone and dried at 70 °C for 2 h. The mass of the solid residue (the unreacted bauxite) was determined and the geopolymerization degree (GD) was calculated using the following equation 1:

$$GD = \frac{m_{sample} - \left[m_{residue} \cdot (1 - LOI) \right]}{m_{sample}}, \% \qquad (1)$$

where m_{sample} is the mass of the powder sample in grams, $m_{residue}$ is the mass of the residual solid in grams and LOI is the loss on ignition of the powder sample of the bauxite-based geopolymer.

3 RESULTS AND DISCUSSION

3.1 Compressive strength

A change in the compressive strength of bauxite-based geopolymers as a function of synthesis parameters is given in **Figures 1** and **2**. It is evident that an increase in the NaOH concentration from 7 M to 13 M leads to an increase in the compressive strength of bauxite-based geopolymers (**Figure 1**), with the maximum value (27.36 MPa) achieved with 13 M NaOH. Additionally, this sample is characterized by the highest GD value (32.6 %). The role of NaOH in the geopolymerization process is to provide sufficient concentration of OH⁻ ions for breaking the Al–O–Si and Si–O–Si bonds in bauxite and freeing Al^{3+} and Si^{4+}, which in an alkali-silicate solution form aluminate $[Al(OH)_4]^-$ and silicate
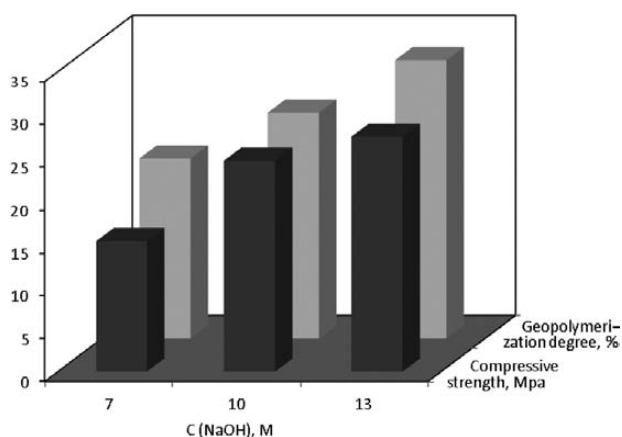
Figure 1: Change in the compressive strength of bauxite-based geopolymers as a function of the NaOH concentration with the $w(Na_2SiO_3)/w(NaOH)$ mass ratio of 1.5
Slika 1: Spreminjanje tlačne trdnosti geopolimerov iz boksita v odvisnosti od koncentracije NaOH pri masnem razmerju $w(Na_2SiO_3)/w(NaOH)$ 1,5

Figure 2: Change in the compressive strength of bauxite-based geopolymers as a function of the $w(Na_2SiO_3)/w(NaOH)$ mass ratio for the C (NaOH) of 13 M
Slika 2: Spreminjanje tlačne trdnosti geopolimerov iz boksita v odvisnosti od masnega razmerja $w(Na_2SiO_3)/w(NaOH)$; C (NaOH) je 13 M

$[(HO)_{4-x}SiO_x]^{x-}$ monomeric species.[14] An increase in the NaOH concentration from 7 M to 13 M results in a higher dissolution of Al and Si from the starting materials, a higher availability of the monomeric species for the condensation process and a formation of geopolymer oligomers (dimers, trimers) following Equation 2.[15] The increase in the NaOH concentration leads to an increase in the number of oligomers in the system which results in the formation of a gel and, consequently, a higher geopolymerization degree (**Figure 1**) as well as a higher strength of the bauxite-based geopolymers.

$$[(HO)_{4-x}SiO_x]^{x-} + [Al(OH)_4]^- \leftrightarrow$$
$$[(HO)_3AlOSiO_x(OH)_{3-x}]^{(x+1)-} + H_2O \qquad (2)$$
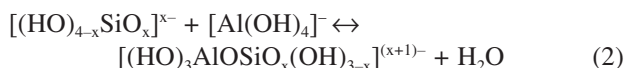
On the other hand, the compressive strength of bauxite-based geopolymers increases with an increase in the $w(Na_2SiO_3)/w(NaOH)$ mass ratio from 1 to 1.5, while a further increase leads to a decrease in the compressive strength (**Figure 2**). A change in the $w(Na_2SiO_3)/w(NaOH)$ mass ratio controls the influence of the soluble silicate dosage (the water glass dosage) on the geopolymerization process. The role of the said dosage is to provide sufficient concentration of the silicate species for the initiation of the polycondensation between silicate and aluminate species.[16]

The presence of soluble silicates in a geopolymer mixture influences both, the dissolution of Al and Si from the starting materials and the polycondensation of aluminate and silicate species. The presence of soluble silicates influences the polycondensation process by changing the nature of the silicate species present in alkaline silicate solutions. In the systems with a lower soluble-silicate concentration, monomeric chains and cyclic trimmers are the dominant silicate species, while in the systems with a higher concentration of soluble silicate, larger rings, complex structures and polymers are present, giving rise to a three-dimensional polymer
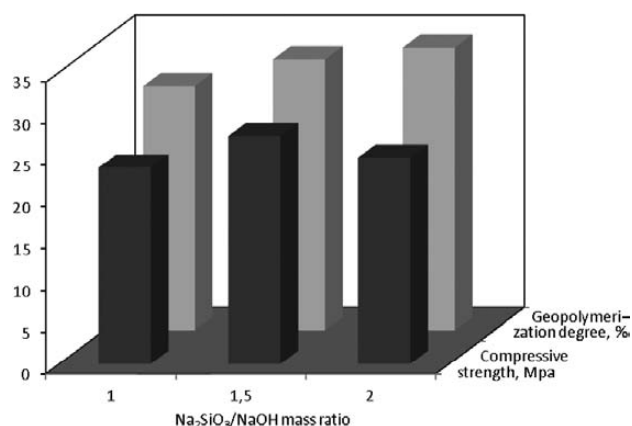
framework, leading to an increase in the mechanical properties of the resulted geopolymeric materials.[7] An increase in the compressive strength with an increase in the silicate dosage is limited by the viscosity of the geopolymer mixture. With the $w(Na_2SiO_3)/w(NaOH)$ mass ratio of 2, the geopolymer paste was extremely difficult to mould and visible cracks were observed on the surface after the curing period, resulting in a slight decrease in the compressive strength.

The investigation of the alkali-cation influence on the compressive strength of bauxite-based geopolymers was focused on the samples prepared using 13 MOH with the $w(M_2SiO_3)/w(MOH)$ ratio of 1.5, exhibiting the highest value of the compressive strength. The results have shown that Na-geopolymers are characterized by a considerably higher compressive strength and GD in comparison to K-geopolymers (**Figure 3**).
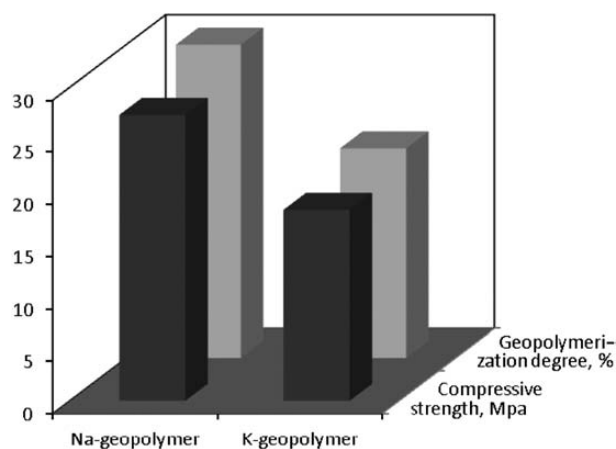
Figure 3: Compressive strength and geopolymerization degree of Na- and K-bauxite-based geopolymers
Slika 3: Tlačna trdnost in stopnja geopolimerizacije Na- in K-geopolimera na osnovi boksita

3.2 Microstructural investigations

SEM-EDS analyses were made on the broken fragments of the samples left behind after the compressive-strength tests and the results are given in **Figure 4** and **Table 2**. It is evident that the microstructure of both Na- and K-geopolymers is uniform without a distinctly separated gel phase and unreacted bauxite particles. The unreacted bauxite particles are covered with a layer of gel that forms as a result of the geopolymerization reactions. The results of the EDS microanalysis have shown that the main constituents of the bauxite-based geopolymers are Al, Si and O. The presence of Na and K is detected in the Na- and K-geopolymers, respectively. Previous investigations showed that the strength of geopolymers is strongly affected by the ratio of Si/Al in the gel phase and that an increase in the compressive strength is accompanied by an increase in the $w(\mathrm{Si})/w(\mathrm{Al})$ ratio.[17] The results presented here show that the values of the $w(\mathrm{Si})/w(\mathrm{Al})$ and $w(\mathrm{alkali\ metal})/w(\mathrm{Si})$ (or

Al) ratios for both Na- and K-geopolymers are very close, which indicates that alkali cations do not affect the values of these ratios, and the difference in the strength of Na- and K- geopolymers is not accompanied by a difference in the $w(\mathrm{Si})/w(\mathrm{Al})$ ratio.

3.3 Porosity analysis

A porosity analysis was performed on Na- and K-based geopolymers. The results are summarized in **Table 3** and the obtained adsorption/desorption isotherms are presented in **Figure 5a**. According to the IUPAC (International Union of Pure and Applied Chemistry) the classification of the adsorption/desorption isotherms,[18] both Na- and K-geopolymers may be considered as mesoporous materials (the pore size from 2 nm to 50 nm). The isotherms of Na- and K-geopolymers are the type IV isotherms with the hysteresis loops associated with the capillary condensation taking place in the mesopores. However, the initial sections of the iso-
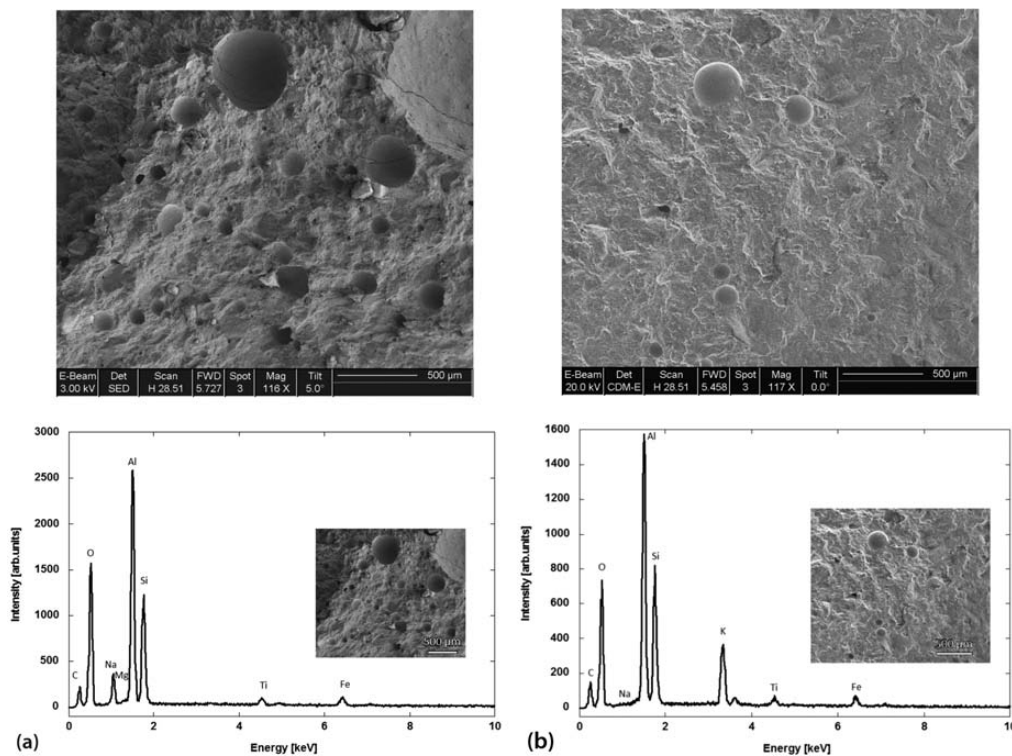
Figure 4: SEM-EDS of: a) Na- and b) K-bauxite-based geopolymers
Slika 4: SEM-EDS: a) Na- in b) K-geopolimera na osnovi boksita

Table 2: Contents of the elements ($w/\%$) and their ratios in Na- and K-geopolymers
Tabela 2: Vsebnost elementov ($w/\%$) in njihov masni delež v Na- in K-geopolimerih

Element	Element content ($w/\%$)		ratio	Na-geopolymer	K-geopolymer
	Na-geopolymer	K-geopolymer			
Al	24.62	20.3	$w(\mathrm{Na})/w(\mathrm{Al})$	0.17	–
Si	14.97	12.57	$w(\mathrm{K})/w(\mathrm{Al})$	–	0.35
Na	4.35	–	$w(\mathrm{Si})/w(\mathrm{Al})$	0.60	0.56
K	–	7.29	$w(\mathrm{Na})/w(\mathrm{Si})$	0.29	–
			$w(\mathrm{K})/w(\mathrm{Si})$	–	0.57

Figure 5: a) Adsorption/desorption isotherms and b) pore-size distribution of Na- and K-bauxite-based geopolymers
Slika 5: a) Izoterme adsorpcije/desorpcije in b) razporeditev por pri Na- in K-geopolimeru na osnovi boksita

Figure 6: t-plots of Na- and K-geopolymers
Slika 6: t-odvisnosti poroznosti Na- in K-geopolimerov

Na-geopolymer is higher than that of the K-geopolymer, indicating that more micropores contribute to the porosity of the Na-geopolymer than to the K-geopolymer. It is also indicative that the presence of microporosity in a geopolymer structure is almost eliminated by introducing K^+ instead of Na^+ in the geopolymerization reaction. Moreover, the hysteresis loop of the K-geopolymer is more pronounced than that of the Na- geopolymer (**Figure 5a**) which also indicates a development of the mesoporosity in the K- geopolymer. As the mesopores are characterized by a higher pore size, it seems reasonable that the development of mesoporosity leads to a decrease in the strength of a geopolymer structure.

The results of the porosity analysis have shown that Na-geopolymers are characterized by a higher percentage of microporosity (8.74 %) in comparison to that of K-geopolymers (0.76 %). Although K-geopolymers are characterized by a somewhat lower average pore size compared to Na-geopolymers, they are 99.24 % mesoporous materials and thus characterized by a lower compressive strength.

Moreover, as both Na- and K-geopolymers are considered as mesoporous materials, the mesopore structure is very important with respect to the geopolymer strength. It is evident that both differential curves of the pore-size distribution (**Figure 5b**) are characterized by the two peaks reflecting different pore sizes. The differential curve of the Na-geopolymer is characterized by the two close peaks, one around 14.2 nm and the other one around 22.4 nm. On the other hand, the differential curve for the K-geopolymer is characterized by two regions:

therms indicate the contributions of the micropores (the pore size less than 2 nm) to the total porosity of a geopolymer.

The results presented in **Table 3** indicate that the difference in the strength of Na- and K-geopolymers must be considered with respect to the pore structure, i.e., the contribution of the micro- and mesoporosity to the total porosity of geopolymers must be evaluated.

The method of t-plot is used to estimate the micropore volume according to the intercept at the y-axis deduced from the extension of the linear part of a t-plot. The t-plots of Na- and K-ge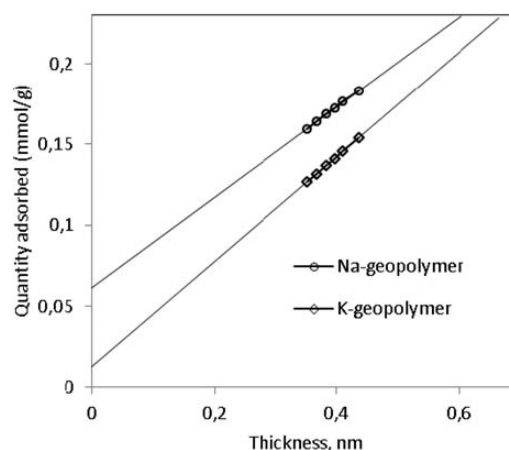opolymers are given in **Figure 6**. They are characterized by a steep slope and a small intercept, which is indicative of a high mesoporosity.[19] However, the intercept at the y-axis for the

Table 3: Porosity of bauxite-based geopolymers
Tabela 3: Poroznost geopolimerov iz boksita

C (NaOH)/(mol dm^{-3})	V_{tot}/(cm^3/g)	V_{mes}/(cm^3/g)	V_{mic}/(cm^3/g)	P_{mes}/%	P_{mic}/%
Na-geopolymer	0.056539	0.051596	0.004943	91.25	8.74
K-geopolymer	0.057570	0.057132	0.000438	99.24	0.76

V_{tot} – total porosity, V_{mes} – mesopore volume calculated by subtracting the total pore volume and micropore volume, V_{mic} – micropore volume calculated using t-plot method, P_{mes} – fraction of mesoporosity calculated as V_{mes}/V_{tot}, P_{mic} – fraction of mesoporosity calculated as $1 - V_{mes}/V_{tot}$

the narrow region with the peak corresponding to the smaller pore width of around 11.2 nm and the broad one with the peak around 48 nm. It is evident that introducing the K^+ cation to a geopolymer system leads to the development of a bimodal pore-size distribution and the development of higher pores (around 49 nm) resulting in a decrease in the geopolymer strength of K-geopolymers in comparison to the strength of Na-geopolymers.

4 CONCLUSIONS

From the results of investigating the geopolymerization of low-grade bauxite, we have drawn the following conclusions:

- The compressive strength of bauxite-based geopolymers is strongly affected by alkali and silicate dosages. Their strength may be increased with an increase in the NaOH concentration. The maximum value of the compressive strength is reached with the use of 13M NaOH.
- On the other hand, the beneficial influence of an increase in the silicate dosage is limited. In this case, the maximum value of the compressive strength was observed for the $w(Na_2SiO_3)/w(NaOH)$ mass ratio of 1.5. A decrease in the strength of a geopolymer structure with a further increase in the silicate dosage is accompanied by an increase in the viscosity of the geopolymer paste and moulding difficulties.
- Moreover, the strength of bauxite-based geopolymers is strongly affected by the nature of alkali cations. Generally, Na-geopolymers are characterized by a higher compressive strength in comparison to K-geopolymers which is influenced by their porosity.
- Alkali cations do not affect the $w(Si)/w(Al)$, $w(M)/w(Si)$ and $w(M)/w(Al)$ ratios (M represents the Na or K ion) in a gel phase of a geopolymer and the difference in the strength of Na- and K-geopolymers is not affected by the proportion of the main constituent of a gel phase.

Acknowledgements

5 REFERENCES

[1] P. Smith, The processing of high silica bauxites – Review of existing and potential processes, Hydrometallurgy, 98 (**2009**), 162–176

[2] S. Maa, Z. Wen, J. Chen, S. Zheng, An environmentally friendly design for low-grade diasporic-bauxite processing, Minerals Engineering, 22 (**2009**), 793–798

[3] C. Huang, Y. Wang, Removal of aluminosilicates from diasporic-bauxite by selective flocculation using sodium polyacrylate, Separation and Purification Technology, 59 (**2008**), 299–303

[4] Y. Wang, Y. Hu, P. He, G. Gu, Reverse flotation for removal of silicates from diasporic-bauxite, Minerals Engineering, 17 (**2004**), 63–68

[5] Z. H. Xu, V. Plitt, Q. Liu, Recent advances in reverse flotation of diasporic ores – A Chinese experience, Minerals Engineering, 17 (**2004**) 9, 1007–1015

[6] J. Davidovits, Geopolymers, inorganic polymerie new materials, Journal of Thermal Analysis, 37 (**1991**), 1633–1656

[7] D. Panias, I. P. Giannopoulou, T. Perraki, Effect of synthesis parameters on the mechanical properties of fly ash-based geopolymers, Colloids and Surfaces A: Physicochemical and Engineering Aspects, 301 (**2007**), 246–254

[8] P. Duxson, A. Fernández-Jiménez, J. L. Provis, G. C. Lukey, A. Palomo, J. S. J. van Deventer, Geopolymer technology: the current state of the art, Journal of Materials Science, 42 (**2007**), 2917–2933

[9] F. Pacheco-Torgal, J. Castro-Gomes, S. Jalali, Alkali-activated binders: A review Part 1, Historical background, terminology, reaction mechanisms and hydration products, Construction and Building Materials, 22 (**2008**), 1305–1314

[10] H. Xu, J. S. J. van Deventer, G. C. Lukey, Effect of Alkali Metals on the Preferential Geopolymerization of Stilbite/Kaolinite Mixtures, Industrial & Engineering Chemistry Research, 40 (**2001**), 3749–3756

[11] S. Brunauer, P. H. Emmett, E. Teller, Adsorption of Gases in Multimolecular Layers, Journal of the American Chemical Society, 60 (**1938**), 309–319

[12] E. P. Barrett, L. G. Joyner, P. P. Halenda, The Determination of Pore Volume and Area Distributions in Porous Substances. I. Computations from Nitrogen Isotherms, J. Am. Chem. Soc., 73 (**1951**), 373–380

[13] U. Rattanasak, K. Pankhet, P. Chindaprasirt, Effect of chemical admixtures on properties of high-calcium fly ash geopolymer, International Journal of Minerals, Metallurgy and Materials, 18 (**2011**) 3, 364–369

[14] L. Weng, K. Sagoe-Crentsil, Dissolution processes, hydrolysis and condensation reactions during geopolymer synthesis: Part I-Low Si/Al ratio systems, Journal of Materials Science, 42 (**2007**), 2997–3006

[15] T. W. Swaddle, Silicate complexes of aluminum(III) in aqueous systems, Coordination Chemistry Reviews, 219–221 (**2001**), 665–686

[16] H. Xu, J. S. J. van Deventer, The effect of alkali metals on the formation of geopolymeric gels from alkali-feldspars, Colloids and Surfaces A: Physicochemical and Engineering Aspects, 216 (**2003**), 27–44

[17] M. Komljenović, Z. Baščarević, V. Bradić, Mechanical and microstructural properties of alkali-activated fly ash geopolymers, Journal of Hazardous Materials, 181 (**2010**), 35–42

[18] K. S. W. Sing, D. H. Everett, R. A. W. Haul, L. Moscou, R. A. Pierotti, J. Rouquérol, T. Siemieniewska, Reporting physisorption data for gas/solid systems with Special Reference to the Determination of Surface Area and Porosity, Pure and Applied Chemistry, 57 (**1985**), 603–619

[19] H. Zhonghua, M. P. Srinivasan, Y. Ni, A simple method for developing mesoporosity in Activated carbon, Separation and Purification Technology, 31 (**2003**) 1, 47–52

SYNTHESIS OF α-Al$_2$O$_3$ BASED FOAMS WITH IMPROVED PROPERTIES AS CATALYST CARRIERS

SINTETIZIRANE PENE NA OSNOVI α-Al$_2$O$_3$ Z IZBOLJŠANIMI LASTNOSTMI KOT NOSILKE KATALIZATORJA

Vesna Nikolić[1], Željko Kamberović[2], Zoran Anđić[3], Marija Korać[2], Miroslav Sokić[4]

[1]Innovation Center of the Faculty of Technology and Metallurgy, University of Belgrade, Karnegijeva 4, Belgrade, Serbia
[2]Faculty of Technology and Metallurgy, University of Belgrade, Karnegijeva 4, Belgrade, Serbia
[3]Innovation Center of the Faculty of Chemistry, University of Belgrade, Studentski trg 12–16, Belgrade, Serbia
[4]Institute for Technology of Nuclear and other Raw Materials, Franše d'Eperea 86, Belgrade, Serbia
vnikolic@tmf.bg.ac.rs

This paper explores the possibility of synthesising catalyst supports with improved properties. Alumina foams were produced with the polymer replication technique. Representative high- and low-temperature sintering ceramics were selected. Suitable suspension amounts, the clay addition and sintering temperature were determined. A lower sintering temperature was used for an economic enhancement of the process. The sintering was conducted at the temperatures from 1573 K to 1773 K for 60 min. A comparative analysis of the studied systems shows that the best compressive strength of 6.2 MPa was achieved with the system based on the α-Al$_2$O$_3$–25 clay (mass fractions, w/%), polyester foam with 10 PPI, sintered at 1673 K.

Keywords: alumina, reticulated foam, sintering, mechanical properties, catalyst carrier

Članek obravnava možnosti sinteze podlage z izboljšanimi lastnostmi za katalizatorje. Izbrane so bile značilne keramike, ki se sintrajo pri visokih ali nizkih temperaturah. Določene so bile primerne vsebnosti suspenzije, dodatki gline in temperature sintranja. Za boljšo ekonomičnost postopka je bila izbrana nižja temperatura sintranja. Sintranje je bilo izvršeno pri temperaturah od 1573 K do 1773 K v trajanju 60 min. Primerjalne analize preučevanih sistemov kažejo, da je bila najboljša tlačna trdnost 6,2 MPa dosežena pri sistemu, ki temelji na α-Al$_2$O$_3$–25 gline (masni deleži, w/%), poliestrski peni z 10 PPI, sintrani pri 1673 K.

Ključne besede: glinica, mrežasta pena, sintranje, mehanske lastnosti, nosilec katalizatorja

1 INTRODUCTION

Reticulated ceramic foams are being intensely researched as catalyst carriers.[1–3] They are mostly produced with the polymer replication method, involving soaking a polymer foam into a ceramic-water suspension, drying and sintering it at the temperatures up to 1973 K.[4,5] In comparison with alumina[4] and alumina-mullite foams,[6,7] which are sintered from 1673 K to 1873 K, significantly lower temperatures are needed for the sintering of cordierite – 1573 K,[8] cordierite-mullite-alumina – 1523 K for 2 h,[9] aluminosilicate – 1523 K for 5 h [10] and porcelain – 1423 K for 5 h,[6] 1523 K for 2 h.[11] It was reported that a polyester foam is more appropriate than polyurethane due to the toxicity of the latter during combustion.[6] The production of porcelain foams involves the drying of green bodies at room temperature for 72 h and then at 373 K for 1 h,[11] instead of 24 h at room temperature.[4,6] Compressive strengths of alumina foams range from 0.27 MPa to 3 MPa.[4,12] Cordierite foams have higher compressive strengths (up to 2 MPa)[8] than alumina mullite (1.11 MPa),[7] alumina (0.59 MPa)[13] and cordierite-mullite-alumina (0.55 MPa).[9] Compressive and flexural strengths of porcelain foams can reach 23.07 MPa and 11.10 MPa, respectively.[11] Aluminosilicate[10] and fine cordierite foams (< 1 mm cell size)[1,14] achieve the pore volumes of about 90 %[10] and 80 % to 85 %,[1,14]

more than porcelain, from 77.4 % to 88.4 % for 60 PPI and 10 PPI (pores per inch) and from 26.28 % to 70.59 %.[6,11] Alumina foams have the pore volumes of 89.5 % and 86.75 % for 12 PPI[13] and between 82 % and 94 % for 5 PPI and 10 PPI,[4] more than alumina-mullite (from 83.4 % to 87.8 % for 10 PPI to 60 PPI)[7] and porcelain.[6,11]

The aim of the current study was an optimisation of the alumina-foam preparation using the polymer replication method. The production cost can be reduced by sintering the foam at a lower temperature. The preliminary results regarding the effects of adding clay were presented in the previous work of the authors.[15] In the present investigation, the polyester foam was soaked into the α-Al$_2$O$_3$ and α-Al$_2$O$_3$ clay-water suspensions. The optimum sintering temperature was determined. Sintered foams with suitable properties were proposed for an additional investigation as primary catalyst carriers.

2 EXPERIMENTAL SECTION

Initial investigations included a microstructural analysis of the starting powders, the α-Al$_2$O$_3$ and α-Al$_2$O$_3$ clay mixtures. The microstructure was analysed using a JEOL SEM JSM 5800 scanning electron microscope (SEM). The investigation of the suspensions in-

cluded a determination of the density and viscosity measured with an Ostwald viscometer. The densities of the suspensions were calculated as the ratio between the suspension mass and the volume determined with a graduated cylinder at 293 K. Viscosity measurements were conducted at the constant temperature of 293 K. The method involved a determination of the time needed for the distilled water meniscus to pass through the marked spots above and below the reservoir of the Ostwald viscometer. The procedure was repeated 10 times. Afterwards, the same procedure was applied to the suspensions. Dynamic viscosity was determined using the following equation, already presented in the previous research of the authors:[15]

$$\eta_s = \eta_w \frac{t_s \rho_s}{t_s \rho_w} \qquad (1)$$

where η is the dynamic viscosity (Pa s), t presents the value of the measured time (s) and ρ is the specific gravity (g/cm^3). Subscripts s and w represent the suspension and the water, respectively.

To identify the optimum process parameters for an alumina-foam preparation, the effects of the suspension amounts, clay addition and sintering temperature were investigated. Representative high- and low-temperature sintering ceramics were selected according to the available scientific literature and previous researches. The starting α-Al$_2$O$_3$ powder was obtained with a calcination of Al(OH)$_3$ at 1373 K for 3 h. The refractory clay was obtained from Kopovi Ub JSC, Serbia. The α-Al$_2$O$_3$ powder and α-Al$_2$O$_3$–25 clay (mass fractions, w/%) powder mixture were wet-ball milled for 40 h and 8 h, respectively. The refractory clay consisted of 35 % Al$_2$O$_3$, 60 % SiO$_2$, 3 % Na$_2$O + K$_2$O and 2 % CaO + MgO + Fe$_2$O$_3$. The suspensions consisted of α-Al$_2$O$_3$ with w = 1 % sodium carboxymethyl cellulose in water (henceforth referred to as ASCC) and α-Al$_2$O$_3$–25 clay (w/%) (henceforth referred to as A-C), with 35 % and 25 % water amounts, respectively. According to the flow sheet of the technological process of the alumina-foam preparation, presented in the previous research,[15] the polyester foam with 10 PPI was cut into cylinders and soaked in the suspensions for 3 min with constant stirring. Excess suspension was removed using gravity and shaking. The green bodies were dried for 24 h at room temperature. Sintering was conducted at (1573, 1623, 1673, 1723 and 1773) K for 60 min.

The quantity of the applied material after the soaking and drying for 24 h at room temperature was determined from the mass difference between the polymer templates and the green samples, taking into account their volumes. The pore volumes of the green and sintered bodies were examined with an image analysis using the linear intercept method. Series of 10 parallel lines were superimposed on the photographs of the foams and the porosity was determined from the ratio between the total

intercept length of the lines with pores and the total line length, using the following equation:[15]

$$P = \frac{L_p}{L_1} \cdot 100 \ (\%) \qquad (2)$$

where P is the porosity (%), L_p is the total pore-intercept length and L_1 is the total line length. The pore diameters and strut thicknesses of the polymer foams and green samples were determined from the pore- and strut-intercept lengths. Measures were conducted taking into account only the pores and struts visible on the top surface of a sample.

The pore volumes of the sintered foams were calculated using the following equation[15]:

$$P_s = \frac{\rho_r - \rho_b}{\rho_r} \cdot 100 \ (\%) \qquad (3)$$

where the real and bulk densities are ρ_r and ρ_b, respectively.

The linear shrinkage after the sintering was calculated using an equation applied in the previous research:[15]

$$S = \frac{L_g - L_s}{L_g} \cdot 100 \qquad (4)$$

where S is the linear shrinkage degree (%), L_g is the mean height of a green body (mm) and L_s is the mean height of the sintered foam (mm).

Uniaxial compression tests of the sintered foams were determined using a hydraulic testing machine INSTRON 1332 - retrofitted Fast track 8800 with 60543 static load cell (± 5 kN capacity), at a piston speed of 0.5 mm min^{-1}. The cylinder-shaped samples were set under a compression plate and the compressive strength was determined from the maximum load at failure and the cylinder base area. The procedure was repeated 3 times for each series of the samples. The microstructures of the sintered foams were analysed with SEM. The microstructure development represents a correlation between the technology and properties.

3 RESULTS AND DISCUSSION

The SEM analysis of the starting powders indicates a presence of the particle sizes below 30 μm and an irregular particle shape with a rough surface morphology in the α-Al$_2$O$_3$ sample (**Figure 1a**). In addition, the presence of clay as the binder, large surface area and energy and the effects of the attractive forces between fine particles resulted in an agglomeration in the α-Al$_2$O$_3$-clay sample (**Figure 1b**). A presence of individual particle sizes of less than 25 μm was noted.

The addition, clay as the binder significantly altered the rheological properties of the suspensions (**Table 1**). The A-C suspension had a higher density in combination with a lower viscosity and was more suitable for applying to a polymer template. The first soaking of the poly-
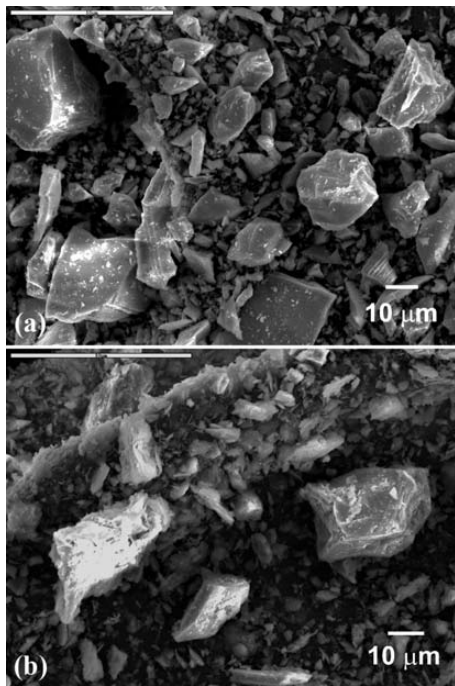
Figure 1: SEM images of starting powders: a) α-Al$_2$O$_3$ powder, b) α-Al$_2$O$_3$-clay powder mixture
Slika 1: SEM-posnetka izhodnih prahov: a) prah α-Al$_2$O$_3$, b) mešanica prahov α-Al$_2$O$_3$-glina

Table 1: Properties of the α-Al$_2$O$_3$ and α-Al$_2$O$_3$–25 clay (mass fractions, w/%) suspensions
Tabela 1: Lastnosti suspenzij z α-Al$_2$O$_3$ in α-Al$_2$O$_3$–25 gline (masni deleži, w/%)

Suspension type	ASCC	A-C
Density/(kg m^{-3})	1980	2096
Viscosity/(Pa s)	4.92×10^{-2}	2.91×10^{-2}

mer foam into the A-C suspension resulted in a complete coverage of the polymer-foam template. The characterisation of green bodies is shown in **Table 2**. The pore size and strut thickness are D and d, respectively. The samples produced using the A-C suspension had an optimum homogeneity and pore volume (78.42 %).

The pore volume decreases (**Figure 2a**) and the intensity of the linear shrinkage increases (**Figure 2b**) as the sintering temperature increases. As a measure of the system activity, the latter is the result of the formation of and an increase in the contact surface between the particles and their movement towards the interior. In the systems based on the ASCC suspension, the optimum sintering temperature of α-Al$_2$O$_3$ was not reached. With
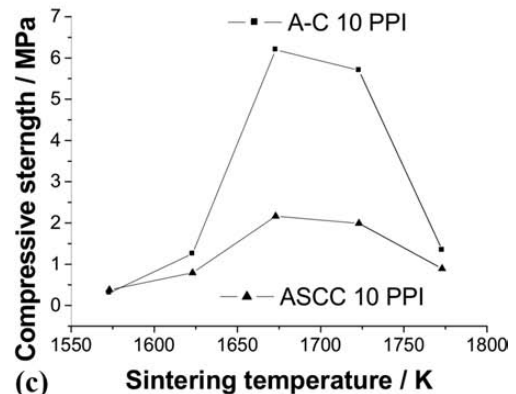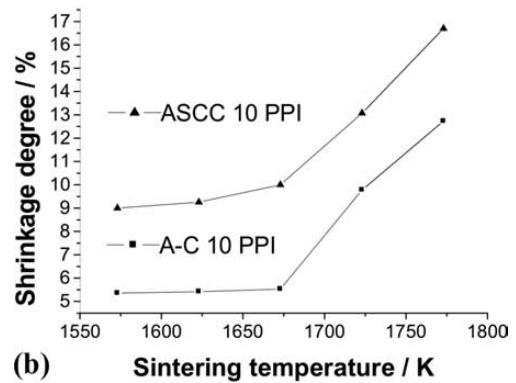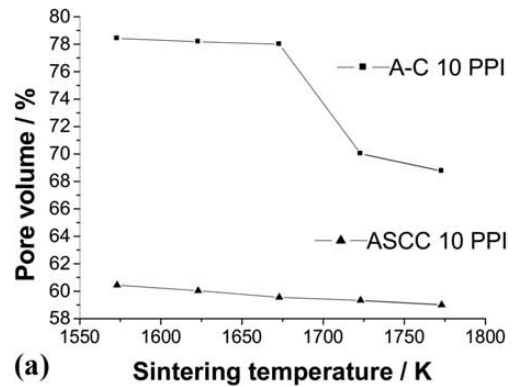
Figure 2: Dependence of: a) pore volume, b) linear shrinkage and c) compressive strength on sintering temperature
Slika 2: Odvisnost: a) volumna por, b) linearnega raztezka in c) tlačne trdnosti od temperature sintranja

the increasing sintering temperature up to 1673 K, the compressive strength increases and then declines rapidly after 1723 K (**Figure 2c** and **Table 3**). It can be concluded that the pore volume and linear shrinkage have an important influence on the values of the compressive strength.

Table 2: Characterisation of green samples
Tabela 2: Karakterizacija zelenih vzorcev

Susp.	Pore vol./%	*Mat. qty. /g cm^{-3}	D_{mean} /mm	D_{max} /mm	D_{min} /mm	Std. errs.	Std. dev.	d_{mean} /mm	d_{max} /mm	d_{min} /mm	Std. errs.	Std. dev.
ASCC	60.45	0.33	2.02	4.10	0.45	0.95	0.14	0.38	0.59	0.20	0.09	0.02
A-C	78.42	0.56	2.30	3.89	0.75	0.79	0.11	0.61	1.30	0.30	0.21	0.03

*Material quantity applied to a polymer foam

The linear shrinkage intensity, as a measure of the system activity, increases with the increasing sintering temperature. A SEM of a strut cross-section of the ASCC-suspension-based foam, sintered at 1573 K, is shown in **Figure 3a**. The gaps that remain in its central part after the polymer combustion are clearly visible. With the increasing sintering temperature, particles of irregular shapes grow from the outer surface of the struts to the interior, reducing the gaps until they are completely eliminated. The above movement of the particles causes a shrinkage of the foam, which is more intense as the sintering temperature increases, until the gaps finally disappear. A SEM of a strut cross-section of the ASCC-suspension-based foam, sintered at 1673 K, is shown in **Figure 3b**; here the gaps were not identified in the center of the struts.

Table 3: Dependence of the compressive strength on the sintering temperature
Tabela 3: Odvisnost med tlačno trdnostjo in temperaturo sintranja

Material and T/K	Max. load at failure (N)	Mean D/cm	P/MPa	Mean P/MPa	Std. err.	Std. dev.
ASCC – 1573 K	164	2.074	0.4857	0.48	0.0037	0.0064
	168		0.4975			
	166		0.4961			
ASCC – 1623 K	184	2.068	0.5480	0.55	0.0045	0.0079
	189		0.5629			
	185		0.5511			
ASCC – 1673 K	675	2.072	2.0058	2.00	0.0017	0.0030
	674		1.9999			
	676		2.0029			
ASCC – 1723 K	608	2.073	1.8023	1.80	0.0017	0.0029
	607		1.8052			
	609		1.7994			
ASCC – 1773 K	205	2.074	0.6071	0.60	0.0034	0.0059
	201		0.5953			
	203		0.6012			
A-C – 1573 K	167	2.073	0.4950	0.49	0.0017	0.0030
	166		0.4891			
	165		0.4921			
A-C – 1623 K	407	2.071	1.1969	1.20	0.0034	0.0060
	403		1.2029			
	405		1.2088			
A-C – 1673 K	2092	2.072	6.2074	6.20	0.0045	0.0079
	2093		6.2104			
	2097		6.2223			
A-C – 1723 K	1890	2.075	5.5919	5.60	0.0017	0.0030
	1892		5.5978			
	1891		5.5948			
A-C – 1773 K	477	2.075	1.4113	0.49	0.0060	0.0104
	470		1.3906			
	473		1.3994			

Figure 3: SEM images of a strut cross-section, foam based on ASCC: a) 1573 K, b) 1673 K, c) foam based on A-C, 1573 K
Slika 3: SEM-posnetki prereza opore, pena na osnovi ASCC: a) 1573 K, b) 1673 K, c) pena na osnovi A-C, 1573 K

In addition, a decrease in the volume porosity occurs. Overall, the increasing shrinking and the reduction in the volume porosity, with the increasing sintering temperature, cause an increase in the compressive strength.

A SEM of a strut cross-section of the foam based on the A-C suspension, sintered at 1573 K, is given in **Figure 3c**. No gaps are identified in its central part. It is evident that at 1573 K the contact formation between individual particles, the growth of the surface contact and the particle movement towards the interior resulted in a removal of the gaps from the central part. This led to a more intense shrinkage, a reduction in the volume porosity and a subsequent increase in the pressure strength, in comparison to the foam based on the ASCC suspensions at the same time-temperature sintering regime.

A SEM of a strut surface in the ASCC-suspension-based foam sintered at 1573 K (**Figure 4a**) clearly indicates a presence of unevenly distributed, irregularly shaped particles and a closer proximity between individual particles, while maintaining their structural inte-
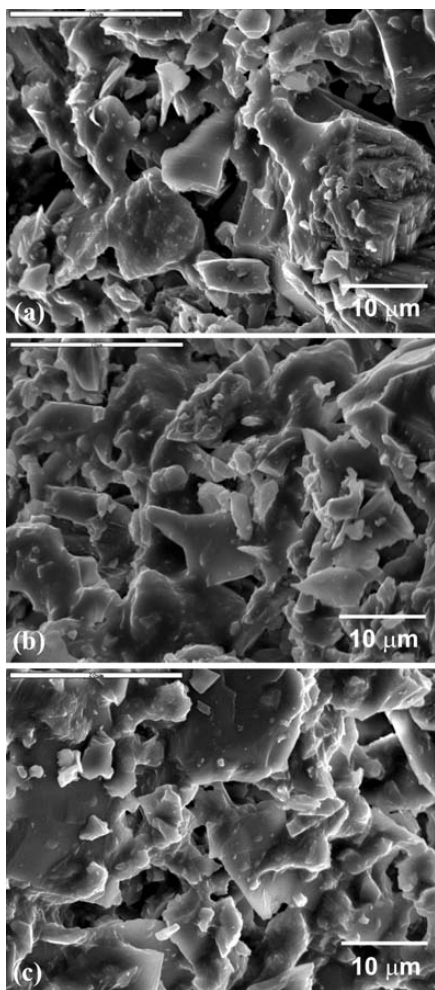
Figure 4: SEM images of a strut surface, foam based on ASCC suspension: a) 1573 K, b) 1673 K, c) 1773 K
Slika 4: SEM-posnetki površine opore, pena na osnovi ASCC-suspenzije: a) 1573 K, b) 1673 K, c) 1773 K

Figure 5: SEM images of a strut surface, foam based on A-C suspension: a) 1573 K, b) 1673 K, c) 1773 K
Slika 5: SEM-posnetki površine opore, pena na osnovi A-C-suspenzije: a) 1573 K, b) 1673 K, c) 1773 K

grity. It is evident that there was no significant increase in the surface contact, which is reflected in the values of the pressure strength. With the sintering temperature increase (**Figure 4b**), the contacts between the particles begin to develop, along with an increase in the contact surface, the latter being only between individual particles. It is noted that the particles lose their structural integrity. The increased surface contact between the particles and the growth of individual particles lead to their rearrangement and improvement of the packaging. A further increase in the sintering temperature (**Figure 4c**) shows a more rapid growth in the contact surface, as well as the individual-particle growth. Large particles grow at the expense of the small ones, found in their surroundings. The particles that appear in the growth direction and are not contiguous with the growing particles do not participate in the process. This microstructure development was causing an intense shrinkage, reducing the pore volume and increasing the compressive strength up to the specific sintering temperature, 1673 K, which was then followed by a decline. The drop in the com-

pressive strength, rapid after 1723 K, is the result of a microstructural coarsening and growth of individual particles sintered at 1773 K.

During sintering the samples based on the A-C suspension, there was an intense contact between individual particles at 1573 K (**Figure 5a**) and an increase in the surface contact with a significant reduction in the pore volume (**Figures 5b** and **5c**) at 1673 K and 1773 K. This directly influenced the linear shrinkage degree and increased the compressive strength up to the temperature of 1673 K. The samples sintered at 1723 K achieved approximately the same value of the compressive strength, followed by its significant decrease at the temperature of 1773 K, as a result of an intense microstructure coarsening due to the abnormal growth of individual particles (**Figure 5c**). The best mechanical properties were obtained with the A-C suspension sintered at 1673 K. In comparison to the system based on the ASCC suspension, this system had improved mechanical properties at lower sintering temperatures, owing to the addition of clay as the binder.

In the optimum system, A-C – 10 PPI – 1673 K, a compressive strength of 6.2 MPa was reached. This is higher than for alumina (1.4 MPa and 3 MPa for 5 PPI and 10 PPI, 1.3 MPa for 12 PPI),[4,13] cordierite (2 MPa)[8] and alumina-mullite (1.11 MPa).[7] A higher pore volume (78.42 %) was obtained, compared to porcelain, where the pore volumes were from 26.28 % to 70.59 %.[11] Although the porosity was not sufficiently open, the obtained product is still applicable as a catalyst support. In the present research, the foams with better properties were obtained by sintering at a lower temperature and for a shorter standing time (1673 K for 1h) compared to the foams sintered at 1873 K for 1 h and 5 h.[4,6] The process was shortened compared to the porcelain-foam production, where green bodies were being dried for 72 h at room temperature and additionally for 1 h at 373 K.[11]

4 CONCLUSIONS

The technological process of synthesising the alumina foam as a catalyst carrier was presented. Compared to the current production processes, higher compressive-strength values were achieved at lower sintering temperatures due to an addition of clay as the binder. The technological process was significantly simplified. The best compressive strength of 6.2 MPa was achieved with the system based on the α-Al$_2$O$_3$–25 clay (mass fractions, w/%), polyester foam with 10 PPI, sintered at 1673 K. It has been concluded that the relevant parameters controlling the process are suspension amounts, the clay addition and the sintering temperature. The presented optimisation of these parameters enables a synthesis of monolithic foams with improved mechanical properties with regard to the application and functionality of the catalyst and the quality of the final product with an increased durability and product life.

5 REFERENCES

[1] F. Ribeiro, J. M. Silva, E. Silva, M. Fatima Vaz, F. A. C. Oliveira, Catal. Today, 176 (**2011**), 93–96

[2] P. Ciambelli, V. Palma, E. Palo, Catal. Today, 155 (**2010**), 92–100

[3] A. Donazzi, B. C. Michael, L. D. Schmidt, J. Catal., 260 (**2008**), 270–275

[4] R. Faure, F. Rossignol, T. Chartier, C. Bonhomme, A. Maitre, G. Etchegoyen, P. Del Gallo, D. Gary, J. Eur. Ceram. Soc., 31 (**2011**), 303–312

[5] M. V. Twigg, J. T. Richardson, Ind. Eng. Chem. Res., 46 (**2007**), 4166–4177

[6] F. C. Buciuman, B. Kraushaar-Czarnetzki, Ind. Eng. Chem. Res., 42 (**2003**), 1863–1869

[7] S. Akpinar, I. M. Kusoglu, O. Ertugrul, K. Onel, Ceram. Int., 38 (**2012**), 6163–6169

[8] F. A. Costa Oliveira, S. Dias, M. Fatima Vaz, J. Cruz Fernandes, J. Eur. Ceram. Soc., 26 (**2006**), 179–186

[9] L. Zhang, J. M. F. Ferreira, S. Olhero, L. Courtois, T. Zhang, E. Maire, J. Chr. Rauhe, Acta Mater., 60 (**2012**), 4235–4246

[10] I. Yanase, Y. Yamakawa, H. Kobayashi, J. Ceram. Soc. Jpn., 116 (**2008**), 176–180

[11] M. Al Amin Muhamad Nor, L. C. Hong, Z. Arfin Ahmad, H. Md. Akil, J. Mater. Process. Technol., 207 (**2008**), 235–239

[12] Y. Han, J. Li, Q. Wei, K. Tang, Ceram. Int., 28 (**2002**), 755–759

[13] G. Plesch, M. Vargova, U. F. Vogt, M. Gorbar, K. Jesenak, Mat. Res. Bull., 47 (**2012**), 1680–1686

[14] M. J. Matos, S. Dias, F. A. Costa Oliveira, Adv. Appl. Ceram., 106 (**2007**), 209–215

[15] V. Nikolić, Ž. Kamberović, Z. Anđić, M. Korać, A. Vujović, M. Sokić, Proc. 44th Int. Conf. on Mining and Metallurgy, Bor, RS, 2012; http://www. irmbor.co.rs/index.php/en/, 395–400

CORROSION PROPERTIES OF DIFFERENT FORMS OF CARBON STEEL IN SIMULATED CONCRETE PORE WATER

KOROZIJSKE LASTNOSTI RAZLIČNIH OBLIK JEKEL V SIMULIRANI PORNI VODI BETONA

Aleš Česen[1], Tadeja Kosec[1], Andraž Legat[1], Violeta Bokan-Bosiljkov[2]

[1]Slovenian National Building and Civil Engineering Institute, Dimičeva 12, 1000 Ljubljana, Slovenia
[2]Faculty of Civil and Geodetic Engineering, University of Ljubljana, Jamova cesta 2, 1000 Ljubljana, Slovenia
ales.cesen@zag.si

Carbon steel, such as concrete-reinforcing steel, tends to undergo corrosion processes when exposed to certain environmental actions. These are the carbonation of concrete and the ingress of chlorides into the concrete from the environment. Many times, the carbonation and chloride contamination are simultaneous processes leading to a harsh corrosion environment and subsequent corrosion problems. Monitoring the state of corrosion is thereby a very useful and powerful tool for following and evaluating the lifetime of reinforced concrete structures. Electrochemical measurements were performed to investigate different forms of carbon steel in simulated concrete pore water at different pH values with and without the presence of chlorides. Morphological characteristics of three different types of carbon steel were studied and SEM/EDX and Raman analyses of the corrosion products were performed. It was found that steel in the form of a sheet has a higher corrosion resistivity than a steel wire and a steel rod, and that the steel rod has a higher corrosion resistivity than the steel wire. The corrosion layer on carbon steel is very diverse; several morphologies were found and analyzed.

Keywords: carbon steel, metallography, corrosion, concrete pore water

Malooglično jeklo, kot je jeklena betonska armatura, je izpostavljeno korozijskim procesom zaradi vplivov okolja. To sta karbonatizacija betona ter vdor kloridnih ionov iz okolja. Mnogokrat se karbonatizacija in vdor kloridov zgodi istočasno, kar privede do hitrega korozijskega propadanja. Spremljanje korozije na objektih je zato zelo dobro orodje za napoved in oceno preostanka trajnostne dobe nekega objekta. Elektrokemijske preiskave smo izvedli v simulirani raztopini porne vode v betonu pri različnih pH vrednostih ter brez in v prisotnosti kloridnih ionov. Določili smo mikrostrukturne značilnosti posameznih vrst ogljičnih jekel ter morfologijo korozijskih produktov z EDX/SEM-analizo ter Ramansko spektroskopijo. Ugotovili smo, da je najbolj korozijsko odporno ogljično jeklo v obliki folije, sledi palica, najslabše korozijske lastnosti pa ima žica iz ogljičnega jekla. Korozijski produkti na jeklu so različnih morfoloških oblik in sestav.

Ključne besede: ogljično jeklo, metalografija, korozija, porna voda betona

1 INTRODUCTION

The service life of a reinforced concrete structure depends on the corrosion state of the reinforcing steel that is embedded in the concrete.[1] There are numerous ways to prolong the service life of a structure, among them also the measures related to the properties of structural materials such as using high-performance concretes with improved properties[2–4] or using a more durable reinforcement material like the corrosion-resistant steel.[5–10] However, the use of the common carbon steel as a concrete reinforcement is still the most frequent and economical. Thus, reliable corrosion monitoring is essential to assess the remaining life-time of a structure, to help select an optimum rehabilitation process and evaluate its efficiency.[10–12] With a corrosion monitoring system we aim to detect the changes in the reinforcement condition, evaluate the corrosion rates and determine the types and causes of corrosion.[13–15]

It is of great importance to know the corrosion stages and mechanisms in order to evaluate the intensity of corrosion. Thereby, two extreme conditions were chosen to be studied in the present research. These are the ingress of chloride ions and the carbonation of the cement matrix. At a high alkalinity and high pH, the passive film on the carbon steel protects the metal from corrosion.[13] The oxide layer consists of firm and adherent Fe_2O_3.[13] When the same steel is subjected to a low pH, or a pore solution containing chlorides, the passivity is lost. Anodic reactions of carbon steel are dissolving iron through many possible reactions:

$$Fe \rightarrow Fe^{2+} + 2\ e^- \quad (1)$$

$$Fe^{2+} + 2\ OH^- \rightarrow Fe(OH)_2 \quad (2)$$

$$4\ Fe(OH)_2 + O_2 \rightarrow 4\ \gamma - FeOOH + 2\ H_2O \quad (3)$$

$$Fe^{2+} + 2\ Cl^- \rightarrow FeCl_2 \quad (4)$$

$$FeCl_2 + H_2O + OH^- \rightarrow Fe(OH)_2 + 2\ Cl^- + H^+ \quad (5)$$

$$4\ Fe(OH)_2 + 2\ H_2O + O_2 \rightarrow 4\ Fe(OH)_3 \quad (6)$$

$$2\ Fe(OH)_3 \rightarrow Fe_2O_3 \cdot H_2O + 2\ H_2O \quad (7)$$
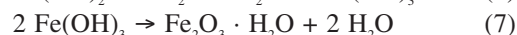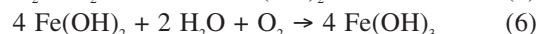
The cathodic reaction in such cases can be a reduction of the oxygen present in the electrolyte:

$$O_2 + 2\ H_2O + 4\ e^- \rightarrow 4\ OH^- \quad (8)$$
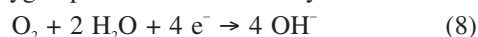
On the other hand, carbon dioxide can reduce the protective role of concrete due to a reaction with the

hydrated cement paste, leading to a pH decrease and a subsequent loss of passivity and to a corrosion initiation.[13,16] The corrosion reaction in such an environment is accelerated.

The aim of the present study is to compare the corrosion properties of different forms of carbon steel, differing by their microstructural properties. Their corrosion properties in a simulated concrete-pore-water solution are also evaluated with the presence of chloride ions. Different spectroscopic techniques are used to study morphological and mineralogical characteristics of the corrosion products on steel.

2 EXPERIMENTAL WORK

2.1 Materials and surface preparation

Three types of samples were chosen for the study, namely:
1) Carbon-steel sheets 240 μm thick with the sections of different dimensions. The wire for the electrical contact on the carbon-steel-sheet specimen was attached at the side of the sheet plates beforehand. It was protected by epoxy paint.
2) Carbon-steel rods with a diameter of 5.0 mm. The wire for the electrical contact was attached at the top of the rod prior to the measurements.
3) Carbon-steel wires with a diameter of 0.8 mm. The cross-section of the wire was exposed to the electrolyte.

Before each measurement, the wires and steel rods were abraded with the 1200-grit emery paper, degreased with acetone and then well dried.

2.2 Electrochemical measurements

The electrochemical measurements were performed in different types of the solution:
1) the 0.01 M calcium hydroxide solution, simulating the concrete pore water at pH 12.8
2) the 0.01 M sodium tetraborate solution, simulating the pore water of the carbonated concrete and a presence of chloride ions (pH 9.2, containing 0.58 % of NaCl)

A laboratory-made three-electrode corrosion cell was used with an approximate volume of 300 cm^3. The specimen was prepared in such a way that the exposed surface presented the working electrode. For the electrochemical tests a potentiostat/galvanostat PGSTAT100, the floating version, Metrohm, Netherlands, 2010, expanded with the NOVA module was used.

After the initial stabilization 2 h at the open-circuit potential (OCP), 3 subsequent linear polarization measurements at ±20 mV vs. OCP with a scan rate of 0.1 mV/s were performed. Finally, the potentiodynamic curve was measured in the range of –250 mV vs. OCP to 0.6 V at a scan rate of 1 mV/s.

2.3 SEM/EDX analysis

For the SEM/EDX analysis, a sample of the carbon-steel sheet was embedded into the cement mortar. The carbon-steel sheet was exposed to wetting and drying cycles during a 12-week exposure. During the first 6 weeks, the cycle period consisted of 2 days of wetting with distilled water and 5 days of drying the mortar specimen. During the second 6-week period, the cycles consisted of wetting the specimen with a 3.5 % NaCl solution. After the exposure, the mortar was detached from the steel-sheet sensor and the corrosion products were investigated using SEM and EDS. At the end of the exposure, the carbon-steel sheet was detached from the mortar cover, rinsed with distilled water and dried. The surface morphology was inspected and analyzed with a low-vacuum scanning electron microscope (SEM, JSM 5500 LV, JOEL, Japan) at the acceleration voltage of 20 kV. The microscope was equipped with energy dispersive spectroscopy (Inca, Oxford Instruments Analytical, UK). The EDS analysis was performed at the acceleration voltage of 20 kV.

2.4 Raman analysis

The Raman spectra were obtained with a Horiba Jobin Yvon LabRAM HR800 Raman spectrometer coupled with an Olympus BXFM optical microscope. The measurements were performed using a laser excitation line 633 nm, a 100-times objective lens and a 600-grooves per milimetre grating, which gave a spectral resolution of 2 cm^{-1} per pixel. The power of the laser was set at 0.14 mW. A multi-channel air-cooled CCD detector was used, with the integration times of between 20 s and 30 s. The spectra presented are without any baseline correction.

2.5 Metallographic examination

The samples were first grinded up to grades 2000, then they were polished up to 4000 and finally a paste 0.5 μm was used. The etching for uncovering the microstructure was performed in a 3 % mixture of HNO$_3$ in ethanol for 20 s. The samples were then immediately rinsed with ethanol and dried with air. A CARL ZEISS AXIO Imager M2m optical metallographic microscope was used to study the microstructure of the steel specimens. Metallographic specimens were prepared and investigated in the longitudinal and transverse directions of the castings. The results of the directions representing the exposed surfaces in the electrochemical study were obtained.

3 RESULTS AND DISCUSSION

In order to evaluate the corrosion properties of the three different types of carbon steel, electrochemical

experiments were conducted in a simulated concrete-pore-water solution with pH 12.8.

The comparison of the electrochemical properties at pH 12.8 and the ones in the simulated carbonated environment at pH 9.2 and with the presence of 0.58 % of chlorides is presented as well. For a further evaluation of the corrosion behavior, the samples were characterized after a 12-week exposure to the cycling conditions. After that, the surface of the exposed sensor from the carbon-steel sheet was examined with EDX/SEM and the Raman technique.

3.1 Metallographic examination

Metallographic images of the three shapes of the steel specimens are presented in **Figure 1**, namely, a longitudinal view of the steel sheet (a), the rod (b) and a cross-section of the wire (c).
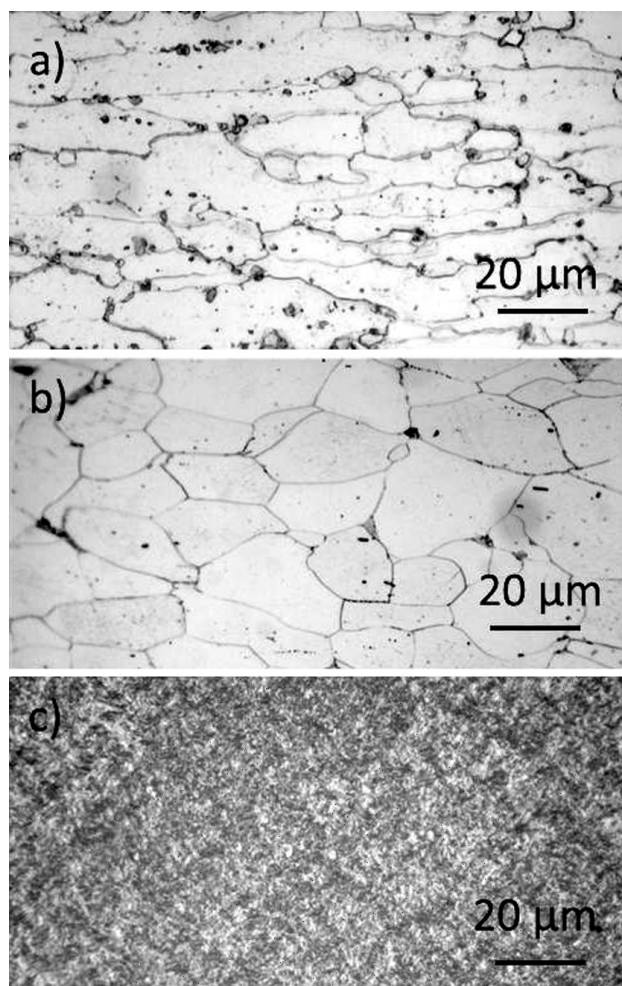
Figure 1: Metallographic images of the three forms of carbon steel: a) steel sheet – a longitudinal view, b) steel rod – a longitudinal view, c) steel wire – a cross-section
Slika 1: Metalografski posnetki treh različnih oblik ogljičnega jekla: a) vzdolžni prerez jeklene plošče, b) vzdolžni prerez jeklene palice in c) prerez žice

The steel sheet has a well-defined microstructure. It consists of ferrite crystal grains that vary in size from 20 μm to 40 μm (**Figure 1a**). Small spheroid-shaped carbides are distributed at the edges and in the crystal grains. It is assumed that the carbides might affect the corrosion properties of the steel sheet.

The microstructure of the rod in the longitudinal direction is mostly ferritic (**Figure 1b**). The amount of perlite is very small due to a low carbon content. Crystal grains are of the size of between 20 μm and 45 μm and are extremely pure towards the surface of the normalized steel rod. The content of the sulfide inclusions increases towards the core of the rod.

The cross-section of the wire has a lamellar microstructure due to the cold-worked procedure (**Figure 1c**). The microstructure consists of cementite and ferrite that were induced out of the perlite microstructure. The size of the cementite lamellas is estimated to be several nanometres.[17] The corrosion performance of the wire is expected to be more susceptible to corrosion in the cross-section than in the longitudinal direction.

3.2 Electrochemical measurements

During the stabilization process, the open-circuit potential was measured as a function of time. **Figure 2** represents the open-circuit potential curves of the three different types of the steel specimens, namely, the carbon sheet, the carbon-steel rod and the carbon-steel wire, immersed in a simulated concrete-pore-water solution with pH 12.8. All the measured curves showed a similar electrochemical behavior.

The corrosion potential, E_{corr}, in all the cases moved to more negative values. After two hours of the immersion it stabilized at –0.280 V for the carbon-steel sheet and at –0.279 V for the carbon-steel wire. The corrosion potential of the carbon-steel rod was the lowest and
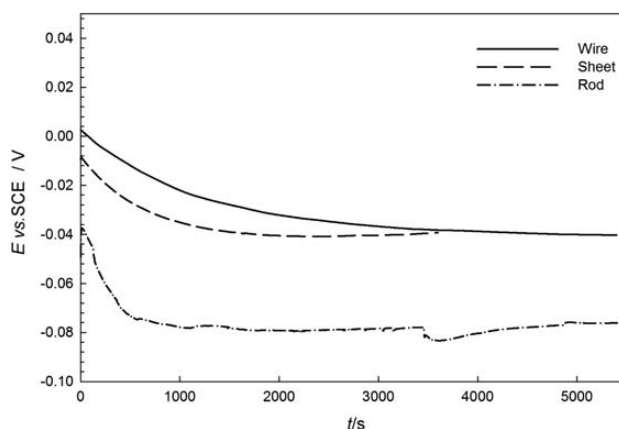
Figure 2: Open-circuit potential measurements for the three forms of carbon steel: steel sheet, steel rod and steel wire, immersed in simulated pore water, pH 12.5
Slika 2: Meritve pri potencialu odprtega kroga za jekleno ploščo, jekleno palico in prerez žice, potopljene v simulirano raztopino betona, pH 12,5

stabilized at –0.315 V after two hours of the immersion. The observed decrease in the value of E_{corr} in time might be a result of the formation of an adsorbed layer at the interface of the carbon steel/electrolyte in the simulated concrete-pore-water solution. However, the E_{corr} evolution is quite regular, indicating that a stable layer was formed on the investigated steel surfaces. The corrosion potentials, E_{corr}, are relatively high, since the corrosion potentials of corroding steels are reported to be as low as –0.7 V.[16]

At a low pH and in a chloride-contaminated environment, the corrosion potentials moved to a more negative direction (**Figure 3**). After a exposure 1 h, it was –0.5605 V for the steel sheet, –0.620 V for the wire and –0.624 V for the rod. The lower values for all the investigated samples, compared to the values at pH 12.8, point at a loss of passivity.

The exposed surfaces, as in the exposure of different types of specimens to the concrete environment, were tested in the course of the electrochemical testing. Namely, the cross-section of the wire, the outer surface of the rod and the sheet were exposed to the simulated pore water with a high alkalinity and to the pore water with pH 9.2, containing 0.58 % of NaCl in order to simu-

late a carbonated and chloride-contaminated environment.

The corrosion potential was measured until it reached a steady state, followed by a potentiodynamic linear polarization and a wide potential scan at a higher scan rate.

The corrosion potential after a exposure 2 h to the pore water with a high pH shows minimum differences among different samples. The results are presented in **Table 1**. However, when exposed to the pore water with pH 9.2, containing chlorides, the corrosion potential changes and moves towards more negative values by approximately 300 mV.

The linear-polarization technique showed that in the simulated pore water, the surface of the steel sheet shows the highest polarization resistance of 2014 kΩ cm² (**Table 1**), followed by the carbon-steel rod (1260 kΩ cm²) and the cross-section of the wire (246 kΩ cm²). With pH 9.2, the polarization resistance, R_p, for all the inve-
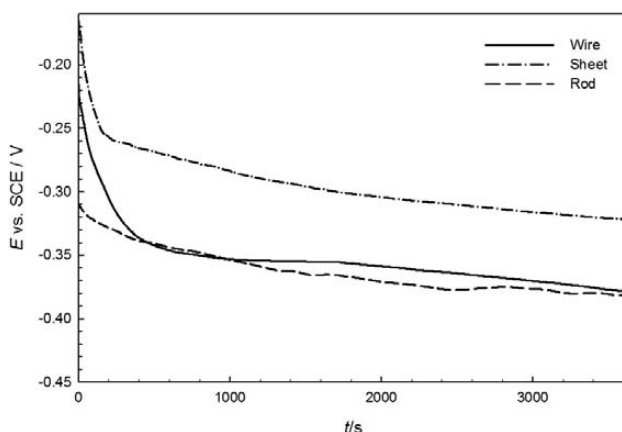
Figure 3: Open-circuit potential measurements for the three forms of carbon steel: steel sheet, steel rod and steel wire, immersed in simulated pore water with pH 9.2, containing 0.58 % of chlorides
Slika 3: Meritve pri potencialu odprtega kroga za jekleno ploščo, jekleno palico in prerez žice, potopljene v simulirano raztopino betona, pH 9,2 z 0,58 % kloridov

Table 1: Corrosion potential, polarization resistance and corrosion rates for the carbon-steel sheet, carbon-steel wire and rod. E_{corr} and E_b are the values deduced from the potentiodynamic measurements.
Tabela 1: Korozijski potencial, polarizacijska upornost in korozijska hitrost za jekleno ploščo, žico in palico. Vrednosti E_{corr} in E_b so odčitane iz potenciodinamskih meritev.

	pH = 12.8			pH = 9.2 + 0.58 % NaCl		
	wire	sheet	rod	wire	sheet	rod
E_{corr} /V	–0.279	–0.280	–0.312	–0.62	–0.56	–0.62
R_p/(kΩ cm²)	246	2014	1260	0.39	2.10	1.33
E_b/V	0.653	0.683	0.648	–0.422	–0.027	–0.099
v_{corr}/(μm/year)	1.3	0.16	0.24	773	143	227

Figure 4: Potentiodynamic measurements for the three forms of carbon steel: steel sheet, steel rod and steel wire, immersed in simulated pore water, pH 12.5, and simulated pore water with pH 9.2, containing 0.58 % of chlorides at a scan rate of 0.1 mV/s
Slika 4: Meritve linearne upornosti za jekleno ploščo, jekleno palico in prerez žice, potopljene v simulirano raztopino betona, pH 12,5 in simulirano raztopino betona, pH 9,2 z 0,58 % kloridov pri hitrosti preleta 0,1 mV/s

stigated samples became smaller, since they underwent corrosion processes. It is 595 times lower than at a high alkalinity for the steel wire, 893 times lower for the steel sheet and 840 times lower for the rod. Thereby, a lower pH and a presence of chlorides greatly affect the corrosion resistance of the exposed steel surfaces. In an aggressive environment, the aggressive species have no preferential effect on the corrosion properties of different investigated microstructures since the change in the corrosion rate is very similar for all the samples.

In **Figure 4**, the potentiodynamic curves of the three surfaces and three different microstructures (**Figure 1**) are presented. There are small, but not negligible differences in the electrochemical properties in the simulated pore water at pH 12.8 (**Figure 4a**).

The corrosion-current density is as high as j_{corr} = 0.123 µA/cm² for the rod and j_{corr} = 0.053 µA/cm² for the cross-section of the wire. The carbon-sheet sample exhibits the lowest corrosion-current density (j_{corr} = 0.017 µA/cm²). The current densities in the pseudo passive region in the anodic scans are the lowest for the steel sheet, followed by the rod, and the highest currents are found for the wire. The breakdown potentials are similar at 0.65 mV vs. SCE (the results are presented in **Table 1**).

At a lower pH, the potentiodynamic curves are different for different samples. The corrosion potentials move towards negative values, the corrosion-current densities decrease and the breakdown potentials change. The corrosion-current density is the highest for the carbon wire (j_{corr} = 19.1 µA/cm²), smaller for the rod (j_{corr} = 7.72 µA/cm²) and the smallest for the carbon sheet (j_{corr} = 3.78 µA/cm²). Also, the breakdown potentials become smaller as observed from the potentiodynamic curves and the values given in **Table 1**.

Following that, the corrosion rates were estimated. Any possible instances of crevice corrosion were elimi-

nated, so the corrosion rates were deduced from the linear polarization using an equation, where the corrosion rate, v_{corr}, in µm/year is calculated following the Faraday law[18]:

$$v_{corr} = 3.27 \cdot (j_{corr} \cdot w/M) / (d \cdot n)^{-1} \qquad (9)$$

where j_{corr} stands for the corrosion-current density in µA cm⁻², d is the density of the metal in g cm⁻³, w is the atomic mass (without units) and n is the number of exchanged electrons. The steel density is d = 7.8 g cm⁻³ and the equivalent mass is w/M = 58.

j_{corr} was calculated from the equation, using the Stern-Geary approximation of the Tafel coefficients:

$$j_{corr} = 1/2.303 \cdot R_p (\beta_A \cdot \beta_C/(\beta_A + \beta_C)) \qquad (10)$$

with β_A and β_C being 120 mV per decade.

As observed from these measurements, the corrosion rate is low at a high alkalinity and it increases immensely at a lower pH, especially when chlorides are introduced. The effect of the microstructure is reflected in the corrosion performance. The carbon-steel sheet sample has better corrosion properties than the carbon-steel rod, whereas the carbon-steel wire is the most sensitive to corrosion processes.

3.3 Surface characterization using SEM/EDX and the Raman analysis

Different morphologies of corrosion products were found on the steel surface: compact doughnut-type corrosion products (**Figure 5a**), fine rounded particles as presented in **Figure 5 b**, a compact structure with visible cracks in the surface (**Figure 5c**) and rounded particles with a greater diameter (**Figure 5 d**).

All the identified corrosion products are iron-based oxides or oxyhydroxides, some of them containing traces of chlorine (**Table 2**).

Table 2: Mass fractions ($w/\%$) of different elements in the corrosion products on the steel sheet
Tabela 2: Masni delež ($w/\%$) različnih elementov v korozijskih produktih, najdenih na jekleni plošči

product	Fe	O	Na	Cl	Al	Si
a	25.15	72.13		2.29	0.43	
b	21.42	71.78	6.58	0.22		
c	31.03	61.56		0.44	0.76	0.89
d	33.17	58.89	4.25	2.59	0.79	0.30

The Raman analysis was also conducted on the steel corrosion products. Since it is very difficult to link the morphologies, found on SEM, with the optical magnifications, it was not possible to unambiguously recognize each shape. The Raman spectra are presented in **Figure 6**.

Different types of iron oxides were identified. These are hematite, lepidocrocite, gheothite, maghemite and akaganeite. Different Raman spectra of the corrosion

Figure 5: SEM images of the corrosion products on the carbon-steel sheet after a 12-week exposure to wet and dry cycles in the mortar
Slika 5: SEM-prikaz korozijskih produktov po 12-tedenski izpostavitvi cikliranem močenju in sušenju v karbonatizirani malti
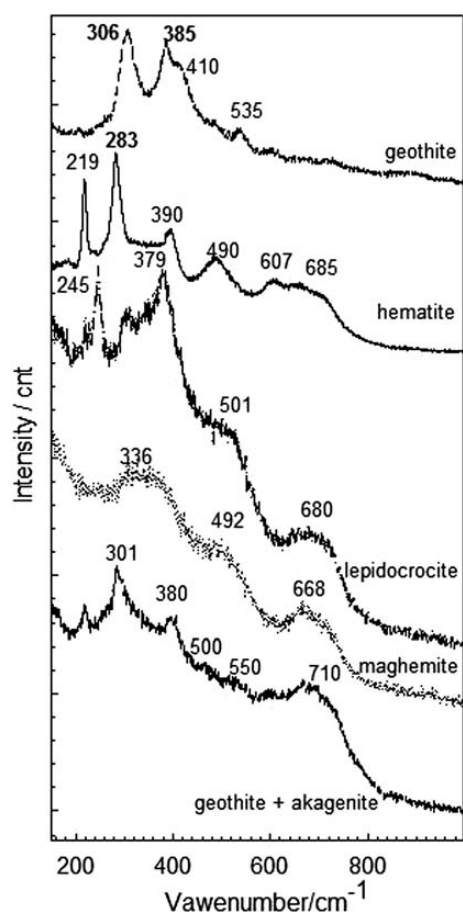
Figure 6: Raman spectra of diffrent corrosion products on the steel-sheet surface
Slika 6: Ramanski spekter različnih korozijskih produktov na jekleni pločevini

products found on the steel-sheet surface are presented in **Figure 6**.

Geothite is characterized by two strong bands at 306 cm^{-1} and 385 cm^{-1}. The latter is broadened as a shoulder of the peak at 410 cm^{-1}. There is a weak band at 535 cm^{-1}. Geothite is an α-FeOOH, iron oxyhydroxide, transparent and with an orthorombic structure. The spectra were found in the literature.[19] Hematite is defined by two strong bands at 219 cm^{-1} and 283 cm^{-1} and three weak and broad bands at (390, 490, 607 and 685) cm^{-1}. The results are similar to those reported in[19,20].

Lepidocrocite, a γ-FeOOH polymorph of iron oxyhydroxide, usually detected as a ruby-red corrosion product, was detected at several points with the characteristic bands at 245 cm^{-1}, 303 cm^{-1}, 379 cm^{-1}, 501 cm^{-1} and 680 cm^{-1}. Similar spectra were already reported.[19]

Maghemite, γ-Fe$_2$O$_3$, can be identified by broad and non-intensive bands at 336 cm^{-1}, 492 cm^{-1} and 668 cm^{-1}. This corrosion product is the most prevalent on the examined surface.

At several spots, mixtures of different corrosion products were found, for example, a mixture of geothite and akaganeite. In the Raman spectra in **Figure 6**, only the bands characteristic for akaganeite are denoted. These are (301, 380, 500, 550 and 710) cm^{-1}, whereas the most pronounced gheotite bands appear at (285, 399 and 534) cm^{-1}.

The corrosion products on the steel-carbon sheet embedded in the mortar are very versatile. They were investigated with SEM and their mineralogical nature was identified with the Raman analysis. They consist of different iron oxides and oxyhydroxides.

4 CONCLUSIONS

Corrosion properties of three different forms of carbon steel were investigated using metallography, electrochemical and surface-spectroscopic techniques.

It was found that the microstructures of the three investigated samples are different. This has an important effect on the electrochemical properties of different samples of carbon steel.

At a high alkalinity of the simulated concrete-pore-water solution with pH 12.8, the corrosion rates are low and similar, while the effect of the microstructure is still observed. The lowest corrosion rate was found for the carbon-steel sheet, followed by the carbon-steel rod and the wire, respectively. The microstructure of the wire is the most sensitive one.

In the carbonated environment, in the concrete pore water with pH 9.2, containing chlorides, the electrochemical properties of the investigated samples change immensely. The corrosion proceeds and the corrosion rate increases, causing a more expressed sensitivity of the microstructure. The highest corrosion rate was found for the wire that has the most sensitive microstructure, followed by the carbon-steel rod and the sheet, respectively.

Different and versatile corrosion products were found on the steel-carbon sheet embedded in the cement mortar after an exposure to wet and dry cycles. They were investigated with SEM and their mineralogical nature was identified with the Raman analysis. Different iron oxides and oxyhydroxides were identified, such as geothite, lepidocrocite, hematite, maghemite and akaganeite.

5 REFERENCES

[1] P. K. Mehta, P. J. M. Monteiro, Concrete: microstructure properties and materials, McGraw-Hill, New York 2006
[2] P. Dinakar, K. G. Babu, M. Santhanam, Corrosion behaviour of blended cements in low and medium strength concretes, Cement and Concrete Composites, 29 (**2007**), 136–145

[3] J. Tritthart, Transport of a surface-applied corrosion inhibitor in cement paste and concrete, Cement and Concrete Research, 33 (**2003**), 829–834

[4] L. G. Andión, P. Garcés, F. Cases, C. G. Andreu, J. L. Vazquez, Metallic corrosion of steels embedded in calcium aluminate cement mortars, Cement and Concrete Research, 31 (**2001**), 1263–1269

[5] A. Šajna, A. Legat, D. Bjegovič, T. Kosec, I. Stipanović, M. Serdar, V. Kuhar, N. Gartner, L. Pardi, L. Augustynski, Recommendations for the use of corrosion resistant reinforcement, FEHRL 79, Brussels, 2009

[6] D. Addari, B. Elsener, A. Rossi, Electrochemistry and surface chemistry of stainless steels in alkaline media simulating concrete pore solutions, Electrochim. Acta, 53 (**2008**), 8078–8086

[7] C. M. Abreu, M. J. Cristobal, R. Losada, X. R. Novoa, G. Pena, M. C. Perez, High frequency impedance study of passive films formed on 316 stainless steel in alkaline medium, J. Electroanal. Chem., 572 (**2004**), 335–345

[8] A. Bautista, G. Blanco, F. Velasco, A. Gutierezz, L. Soriano, E. J. Palomares, H. Takenouti, Changes in the passive layer of corrugated austenitic stainless steel of low nickel content due to exposure to simulated pore solutions, Corros. Sci., 51 (**2009**), 785–792

[9] M. C. Garcia-Alonso, M. L. Escudero, J. M. Miranda, M. I. Vega, F. Capilla, M. J. Correia, M. Salta, A. Bennani, J. A. Gonzales, Corrosion behaviour of new stainless steel reinforcing bar embedded in concrete, Cement Concrete Res., 37 (**2007**), 1463–1471

[10] I. Martínez, C. Andrade, Examples of reinforcement corrosion monitoring by embedded sensor in concrete structure, Cement Concrete Comp., 31 (**2009**), 545–554

[11] G. S. Duffo, S. B. Farina, Development of an embeddable sensor to monitor the corrosion process of new and existing reinforced concrete structures, Constr. Building Mat., 23 (**2009**), 2746–2751

[12] A. Legat, Monitoring of steel corrosion in concrete by electrode arrays and electrical resistance probes, Electrochim. Acta, 52 (**2007**), 7590–7598

[13] L. Bertolini, B. Elsener, P. Pedeferri, R. B. Polder, Corrosion of Steel in Concrete: Prevention, Diagnosis, Repair, Wiley-VCH Verlag GmbH & Co, Weinheim 2004

[14] A. Bentour, S. Diamond, N. S. Berke, Steel Corrosion in Concrete, E & FN Spon, an imprint of Chapman & Hall, 2-6 Boundary Row, London 1997

[15] P. Pedeferri, L. Bertolini, M. Gastaldi, T. Pastore, M. P. Pedeferri, Stainless Steel in Concrete, European Community, COST 521 Workshop, Utrecht, 1998

[16] J. P. Broomfield, Corrosion of steel in concrete: understanding, investigation and repair, Taylor & Francis, Florence 2007

[17] A. Milenin, Z. Muskalski, The FEM simulation of cementite lamellas deformation in pearlitic colony during Drawing of High Carbon Steel, 1375–1380, In: J. M. A. Cesar de Sa, A. D. Santos (eds.), Materials Processing and Design: Modeling, Simulation and Applications, Numiform 2007: Proceedings of the 9th International Conference on Numerical Methods in Industrial Forming Processes, American Institute of Physics, 2007

[18] B. Elsener, Corrosion rate of steel in concrete – Measurements beyond the Tafel law, Corros. Sci., 47 (**2005**), 3019–3033

[19] F. Dubois, C. Mendibide, T. Pagnier, F. Perrard, C. Durret, Raman mapping of corrosion products formed onto spring steels during salt pray experiment, a correlation between the scale composition and the corrosion resistance, Corros. Sci., 50 (**2008**), 3401–3409

[20] W. Chen, R. G. Du, C. Q. Ye, Y. F. Zhu, C. J. Lin, Study on the corrosion behaviour of reinforcing steel in simulated concrete pore solution using in situ Ramanspectroscopy assisted by electrochemical techniques, Electrochim. Acta, 55 (**2010**), 5677–5682

OXIDATION BEHAVIOR OF CARBON-SILICON AND CARBON-BORON-SILICON ALLOYS DERIVED FROM SOLVENT-SOLUBLE SILICON AND BORON-SILICON-DOPED COAL-TAR PITCHES

VEDENJE PRI OKSIDACIJI OGLJIK-SILICIJEVIH IN OGLJIK-BOR-SILICIJEVIH ZLITIN, PRIDOBLJENIH IZ RAZTOPIN PREMOGOVE KATRANSKE SMOLE, DOPIRANE S TOPNIM SILICIJEM IN BOR-SILICIJEM

Xiaohua Zuo[1,2], Zhijun Dong[1], Wen Li[2], Guangming Yuan[1], Zhengwei Cui[1], Yue Liu[1], Xuanke Li[1]

[1]Hubei Province Key Laboratory of Coal Conversion & New Carbon Materials, Wuhan University of Science and Technology, 430081 Wuhan, China
[2]School of Chemistry & Materials Engineering, Hubei Polytechnic University, 435003 Huangshi, China
xkli@21cn.com

The solvent-soluble silicon (Si) and boron-silicon (B-Si) doped coal-tar pitches were synthesized with the co-pyrolysis of a mixture of the toluene-soluble fraction of the coal-tar pitch (TSP), polycarbosilane and pyridine borane. The C-Si and C-B-Si alloys were obtained with a carbonization treatment of the synthetic Si and B-Si doped coal-tar pitches at 1000–1600 °C for 1 h. The physical properties of the Si and B-Si doped coal-tar pitches, such as the softening point, quinoline insolubles, the volatile content and the pyrolysis yield were determined. The influences of the pyridine-borane content in raw materials and the carbonization temperature on the composition, microstructure and oxidation resistance of the C-Si and C-B-Si alloys were investigated. The results show that the C-B-Si alloys are composed of SiC, B_2O_3 and carbon, while the silicon, boron and oxygen elements are uniformly dispersed in the carbon matrix. In most cases, the oxidation resistance of the C-B-Si alloy is better than that of the C-Si alloy, owing to the sintering-aiding action of B_2O_3 and the anti-oxidation synergism of the SiO_2 and B_2O_3 formed during oxidation. The higher the carbonization temperature, the larger is the grain size of the SiC in the C-B-Si alloy. A large grain size leads to an increase in the initial oxidation temperature of the SiC, which is unfavorable for the formation of a protective glassy film on the surface of the C-B-Si alloys. As a result, the C-B-Si alloy obtained with the carbonization at 1200 °C shows a better oxidation resistance than that obtained with the carbonization at 1600 °C under the same oxidation conditions.

Keywords: C-Si alloy, C-B-Si alloy, doped coal-tar pitch, oxidation resistance

Topila premogove katranske smole, dopirane s topnim silicijem (Si) in bor-silicijem (B-Si), so bila sintetizirana s kopirolizo mešanice v toluenu topne frakcije premogove katranske smole (TSP), polikarbonsilana in piridin borana. Zlitine C-Si in C-B-Si so bile dobljene s karbonizacijsko obdelavo premogove katranske smole, dopirane s sintetičnim Si in B-Si 1 h pri 1000–1600 °C. Določene so bile fizikalne lastnosti premogove katranske smole, dopirane s Si in B-Si, točka mehčanja, trdni delci ogljika, vsebnost hlapnih snovi in izkoristek pirolize. Preiskovan je bil vpliv vsebnosti piridin borana v surovini in karbonizacijska temperatura na sestavo, mikrostrukturo in oksidacijsko odpornost zlitin C-Si in C-B-Si. Rezultati kažejo, da so zlitine C-B-Si sestavljene iz SiC, B_2O_3 in ogljika, pri čemer so elementi ogljik, silicij, bor in kisik enakomerno razpršeni po osnovi iz ogljika. Odpornost proti oksidaciji je v večini primerov pri zlitini C-B-Si boljša od zlitine C-Si zaradi dodatnega učinka B_2O_3 in protioksidacijske sinergije SiO_2 in B_2O_3, ki nastajata med oksidacijo. Čim višja je temperatura karbonizacije, tem večja postajajo zrna zlitine SiC in C-B-Si. Večja kristalna zrna povzročijo povišanje temperature začetka oksidacije SiC, kar je neugodno za nastanek steklaste zaščitne plasti na površini zlitin C-B-Si. Rezultat tega je, da zlitina C-B-Si, dobljena pri karbonizaciji pri 1200 °C, pri enakih razmerah za oksidacijo kaže boljšo odpornost proti oksidaciji kot zlitina, pridobljena s karbonizacijo pri 1600 °C.

Ključne besede: zlitina C-Si, zlitina C-B-Si, dopirana premogova katranska smola, odpornost proti oksidaciji

1 INTRODUCTION

Carbon materials, particularly in fiber and composite forms, can have a high strength and stiffness that are maintained to the temperatures well above 2000 °C under non-oxidative conditions.[1] However, their high temperature applications are limited to the inert atmosphere or short-term exposure, as carbon is susceptible to rapid oxidation in the air at the temperatures above about 400 °C, resulting in a considerable deterioration in their mechanical properties.[2] Therefore, a number of oxida-tion-protection methods have been proposed to solve the problem and extend the service life of carbon materials. Conventional protection methods rely on refractory oxide-forming coatings as oxygen diffusion barriers on the materials, e.g., carbon fibers. This approach is only partially successful since the coatings crack during ther-mal cycling due to a thermal-expansion mismatch bet-ween the coating and the substrate unless rather com-plex, functionally graded systems are used.[3]

In order to alleviate some of the difficulties resulting from the coating microcracks, oxidation inhibitors such

as boride and silicide ceramic powders are sometimes added to the carbon matrix. Although this approach is effective in increasing a composite's overall resistance to oxidation, it is very difficult to solve the problem of homogeneous distribution of the ceramic powders in the matrix.[4]

One resultful approach to mitigating the problems of the coating and non-uniform mixing of an antioxidant powder with the matrix is to chemically dope the carbon-matrix precursor with organometallic functional groups to produce an intimate mixing of the antioxidant and the matrix.[5] Coal-tar and petroleum pitches, due to their inherent chemical properties, mesophase formation and low melting points, appear to be promising carbon-matrix precursors for doping with the organo-derivatives of silicon and boron serving both as the source of reactive C-atoms toward SiC and B_4C and the carbon matrix. In the work reported by Czosnek,[6] a typical coal-tar pitch was doped with polycarbosilane and, subsequently, carbonized at elevated temperatures to yield doped carbon materials with a homogeneous, nanoscale dispersion of the SiC particles. The resulting solids had improved oxidation-resistance characteristics.

In this work, silicon- and boron-doped carbon materials were synthesized via a co-pyrolysis and subsequent carbonization of the mixtures of the toluene-soluble fraction of the coal-tar pitch, polycarbosilane (as a silicon source) and pyridine borane (as a boron source). The main aim of this work was to develop carbon-alloy materials with a self-protection mechanism "built-in" the structure. The influence of the boron content and carbonization temperatures on the oxidation behavior of the C-Si and C-B-Si alloys was investigated. The anti-oxidative mechanism of the C-Si and C-B-Si alloys was discussed on the basis of the evolution of elemental compositions and morphology.

2 EXPERIMENTAL WORK

2.1 Preparation of Si and B-Si doped pitches and their derived C-Si and C-B-Si alloys

Polycarbosilane was purchased from Suzhou Ceramic Fiber Co. Ltd. in China. Henan Chemical Trade Co. Ltd. in China supplied pyridine borane, which was used without further purification. The coal-tar pitch was a generous gift from Wuhan Iron and Steel Co. Ltd. in China. The toluene-soluble fraction of the coal-tar pitch was obtained with a refluxing extraction using the toluene solvent and, subsequently, the removal of toluene with the distillation treatment. The toluene-soluble fraction of the coal-tar pitch was mixed with polycarbosilane at a mass ratio of 1:1 in the toluene solvent in a three-neck flask, and then a defined weight percent of pyridine borane was added to the solution. The mixture was stirred at room temperature for 2 h, heated to 180 °C and refluxed for 6 h under argon atmosphere. Then the mixture was slowly cooled to 120 °C. After removing the

toluene solvent from the mixture with a vacuum distillation, the toluene-soluble Si and B-Si doped pitches were finally obtained. The doped-pitch-sample designation and the corresponding chemical components of the raw materials used to prepare the sample are listed in **Table 1**.

Table 1: Chemical components of the raw materials used to prepare Si and B-Si doped pitches in mass fractions (*w*/%)
Tabela 1: Kemijska sestava surovin, uporabljenih za pripravo s Si in B-Si dopirane smole v masnih deležih (*w*/%)

Sample designation	Toluene-soluble fraction of coal-tar pitch (*w*/%)	Polycarbo-silane (*w*/%)	Pyridine borane (*w*/%)
B0	50.0	50.0	0
B2	42.7	42.7	14.6
B4	37.2	37.2	25.6
B6	33.0	33.0	34.0

In order to obtain C-Si and C-B-Si alloys, the doped coal-tar pitch was first semi-carbonized at 450 °C for 2 h under a 2 MPa pressure in an autoclave, and then the semi-carbonized samples were transferred to corundum crucibles and carbonized at 1000–1600 °C for 1 h in a tube furnace under a flow of argon atmosphere. The C-Si and C-B-Si alloys obtained with a carbonization at 1200 °C for 1 h of B0, B2, B4 and B6 were labeled as CB0-12, CB2-12, CB4-12 and CB6-12, respectively. The C-Si and C-B-Si alloys obtained with a carbonization at 1600 °C for 1 h of B0, B2, B4 and B6 were labeled as CB0-16, CB2-16, CB4-16 and CB6-16, respectively.

2.2 Analysis and characterization of C-Si and C-B-Si alloys

Phase compositions of C-Si and C-B-Si alloys were analyzed with X-ray diffraction (Philips X'PERT PRO MPD, made in Netherlands). The X-ray wavelength of the copper target (Cu Kα) as a radiation source was 0.15406 nm. The working-tube voltage and current were 40 kV and 30 mA, respectively. The thermal gravimetric and differential scanning calorimetry (TG-DSC) analyses of the samples were done with a comprehensive thermal analyzer (NETZSCH STA499C type, produced in Germany). For each measurement, 50–90 mg of the sample was used. The sample was heated from the ambient temperature to 1500 °C at a heating rate of 5 °C min^{-1} in dry air with a flow rate of 30 mL min^{-1}. A scanning electron microscope (TESCAN VEGA3, provided in Czech) equipped with a BRUKER 410-M energy dispersive spectrometer (EDS) was used to observe the morphology of the C-Si and C-B-Si alloys before and after the oxidation.

3 RESULTS AND DISCUSSION

3.1 Physical properties of the raw materials and Si and B-Si doped pitches

Table 2 shows physical properties of the toluene-soluble fraction of the coal-tar pitch, the Si and B-Si doped coal-tar pitches. The softening point and pyrolysis yield of the toluene-soluble fraction of the coal-tar pitch are 52.4 °C and raction 39.5 %, respectively. After the doping with silicon heteroatoms, the softening point increases to 124.3 °C and the solid yield of 60.7 % is obtained. An addition of boron-bearing additives with 2 % boron to the above Si-doped coal-tar pitch results in a further increase in the softening point and pyrolysis yield, which may be related to the residual boron and silicon in the solid. For the B-Si doped coal-tar pitch, an increase in the softening point and pyrolysis yield is observed when increasing the boron content. However, the volatile content of the toluene-soluble fraction of the coal-tar pitch decreases from 72.5 % to 45.1 % after being doped with silicon and boron (6 % boron). The doping of the toluene-soluble fraction of the coal-tar pitch with the silicon and boron heteroatoms causes a decrease in the content of the quinoline insolubles. It is worth noting that the doped coal-tar pitches synthesized in this study are completely soluble in ordinary organic solvents, such as benzene, toluene and dimethylbenzene. Owing to their high solubility, the doped coal-tar pitches could be used as impregnating agents in the fabrication of C/C composites.

Table 2: Physical properties of the toluene-soluble fraction of the coal-tar pitch (TSP), the Si and B-Si doped coal-tar pitches
Tabela 2: Fizikalne lastnosti v toluenu topne frakcije premogove katranske smole (TSP) v premogovi katranski smoli, dopirani s Si in B-Si

Sample	Softening point[a] (°C)	Quinoline insoluble[b] (w/%)	Volatile content[c] (w/%)	Pyrolysis yield[d] (w/%)
TSP	54.2	0	72.5	39.5
B0	124.3	0.12	60.4	60.7
B2	151.6	0.39	53.6	64.1
B4	165.2	0.64	47.3	69.8
B6	183.5	0.97	45.1	71.4

a) Determined using a ring-and-ball apparatus; b) Specified in the quinoline solvent; c) Specified at 900 °C for 7 min; d) Specified at 780 °C for 40 min

3.2 XRD analysis of C-Si and C-B-Si alloys

The XRD patterns of the C-Si and C-B-Si alloys obtained with a carbonization of the Si and B-Si doped coal-tar pitches at different temperatures are shown in **Figure 1**. The diffraction peaks at $2\theta = 14.6°$ and $27.8°$ in **Figures 1a** to **c** correspond to the cubic B_2O_3 phase (JCPDS Card No.00-006-0297), formed with a chemical reaction between a small amount of oxygen contained in polycarbosilane and borane produced by a decomposition of pyridine borane during the heat treatment. B_2O_3 has a low melting point (460 °C) and a good fluidity at a
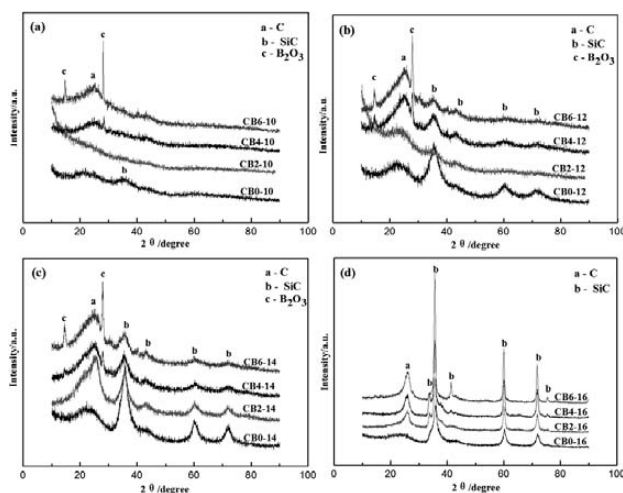
Figure 1: XRD patterns of C-Si and C-B-Si alloys obtained with a carbonization of Si and B-Si doped coal-tar pitches at: a) 1000 °C, b) 1200 °C, c) 1400 °C and d) 1600 °C for 1 h
Slika 1: XRD-posnetki zlitin C-Si in C-B-Si, dobljenih s karbonizacijo 1 h s Si in B-Si dopirane premogove katranske smole pri: a) 1000 °C, b) 1200 °C, c) 1400 °C in d) 1600 °C

temperature above 500 °C and, as a result, it can be used as a protective glassy film covering the cracks and micropores formed during the oxidation of the carbon materials, increasing the diffusion resistance to the oxygen from the air into the carbon materials and greatly retarding the oxidation of the carbon materials. The broad and weak diffraction peaks appearing at about $2\theta = 25°$ can be attributed to the (002) reflection of the pseudo-graphite carbon, which indicates a formation of the carbon with a low degree of graphitization and crystallinity in the process of carbonization. The diffraction peaks at $2\theta = (35.6°, 41.4°, 60°, 71.8°)$ in **Figures 1b** to **d** are assigned to the hexagonal β-SiC phase. Since these peaks in **Figures 1b** and **c** are broad, the SiC present in the carbon matrix formed with the carbonization treatment at 1200 °C and 1400 °C appears to be nanocrystalline. However, for the sample obtained with the carbonization treatment at 1000 °C, there is no obvious characteristic peak of the SiC phase, which shows that the SiC phase does not exist in the carbon materials or it has an amorphous structure. In addition, it can be seen from **Figure 1** that increasing the carbonization temperature to 1600 °C induces an evident increase in the relative intensity and a decrease in the full width at the half maximum (FWHM) of the characteristic peaks of the SiC, which may result from a rapid growth of the SiC crystals at a high temperature. In none of the cases did the B_4C phase occur in the carbon materials obtained with the carbonization treatment at different temperatures, which may be attributed to the non-crystalline structure of B_4C.[7] It is worth noting that the FWHM of the diffraction peaks of the SiC phase in the Si-doped carbon materials is much lower than that of the SiC phase in the B-Si doped carbon materials when the carbonization temperature is below 1600 °C (**Figures 1a** to **c**). This implies that the grain size of the SiC in the
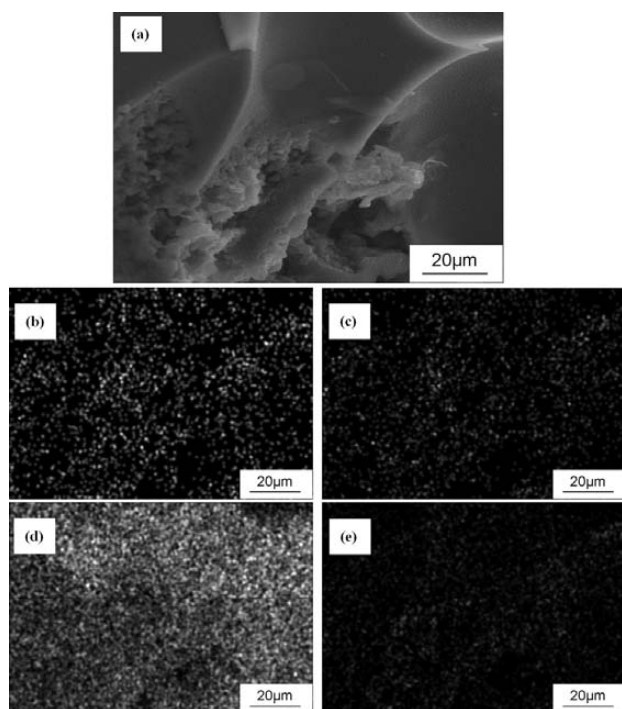
Figure 2: SEM image: a) of the C-B-Si alloy obtained with the carbonization treatment of doped coal-tar pitch B4 at 1200 °C for 1 h and the corresponding EDS elemental maps of: b) carbon, c) boron, d) silicon and e) oxygen

Slika 2: SEM-posnetek: a) zlitine C-B-Si, dobljene z 1 h karbonizacijo dopirane premogove katranske smole B4 pri 1200 °C, in EDS-posnetki razporeditve elementov: b) ogljika, c) bora, d) silicija in e) kisika

Si-doped carbon materials is larger than that of the SiC in the B-Si doped ones. When the carbonization temperature increases to 1600 °C, the diffraction peaks of B$_2$O$_3$ disappear from the carbon materials due to an intense vaporization of B$_2$O$_3$ at high temperatures. Moreover, the FWHM of the diffraction peaks of the SiC in the Si-doped carbon materials is much larger than that of the SiC in the B-Si doped ones when the carbonization temperature is 1600 °C. The converse is found in the samples obtained with the carbonization at the temperature below 1600 °C (shown in **Figures 1a** to **c**). The possible reasons still need to be further studied.

Figure 2a shows the typical morphology of the C-B-Si alloy obtained with the carbonization treatment of doped coal-tar pitch B4 at 1200 °C for 1 h. It can be seen that the resulting C-B-Si alloy is composed of many polycrystalline grains. The corresponding maps of carbon, boron, silicon and oxygen elemental distributions are shown in **Figures 2b** to **e**, revealing that carbon, boron and silicon are uniformly distributed in the alloy materials.

3.3 Oxidation behavior analysis of the C-Si and C-B-Si alloys

To investigate the influences of the pyridine-borane content in raw materials and carbonization temperatures on the oxidation resistance of the resulting C-Si and

C-B-Si alloys, the C-Si and C-B-Si alloys obtained with the carbonization treatment of B0, B2, B4 and B6 at 1200 °C and 1600 °C were put into a tube furnace, heated from room temperature to 1000 °C and kept for 1–10 h in air. The oxidation weight loss as a function of time of the C-Si and C-B-Si alloys is shown in **Figure 3**. It can be seen from **Figure 3a** that the oxidation weight loss of sample CB0-12 tends towards stability when the oxidation time exceeds 3 h. After being oxidized at 1000 °C for 10 h, its oxidation weight loss is about 10 %. On the other hand, the weight loss of samples CB2-12, CB4-12 and CB6-12 increases gradually with the prolonged oxidation time. The difference in the weight loss between the three samples is gradually diminishing. After the oxidation for 10 h, the weight losses for the three samples are very close (about 6 %). Obviously, in the case of the C-Si and C-B-Si alloys prepared with the carbonization treatment at 1200 °C, the oxidation resistance of the former is inferior to that of the latter under the same oxidation conditions. When increasing the carbonization temperature to 1600 °C, the oxidation resistances of the resulting C-Si and C-B-Si alloys drop
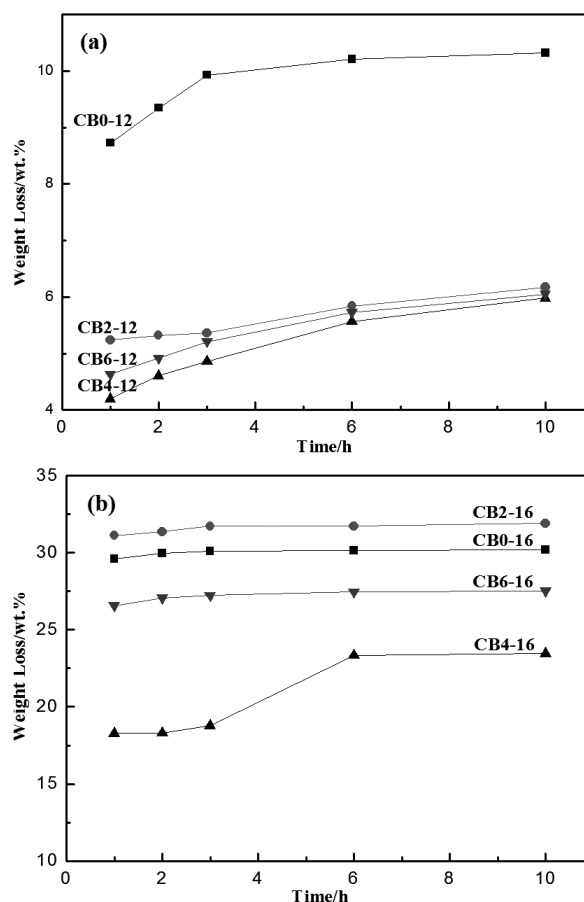
Figure 3: Oxidation weight loss at 1000 °C in the air as a function of time for the C-Si and C-B-Si alloys obtained with the carbonization treatment of B0, B2, B4 and B6 at: a) 1200 °C and b) 1600 °C for 1 h

Slika 3: Izguba mase pri oksidaciji na 1000 °C na zraku v odvisnosti od časa pri zlitinah C-Si in C-B-Si, dobljenih s karbonizacijo B0, B2, B4 in B6 1 h na: a) 1200 °C in b) 1600 °C

sharply, which can be discerned from the comparison of **Figures 3a** and **b**. After the oxidation for 10 h, the weight losses of samples CB0-16, CB2-16, CB4-16 and CB6-16 obtained with the carbonization at 1600 °C are 30 %, 32 %, 23 % and 27 %, respectively, being much higher than those of the corresponding alloys obtained with the carbonization at 1200 °C. The above results of the oxidation resistance indicate that adjusting the content of pyridine borane in the raw materials in the synthesis of the B-Si doped coal-tar pitch and selecting the appropriate carbonization temperature in the following carbonization stage play an important role in improving the oxidation resistance of the obtained C-B-Si alloy.

Figure 4 shows the XRD patterns of the C-Si and C-B-Si alloys kept in air at 1000 °C for 3 h. For the C-B-Si alloys obtained with the carbonization treatment at 1200 °C, there is no evident difference between the XRD patterns before and after their oxidation in the a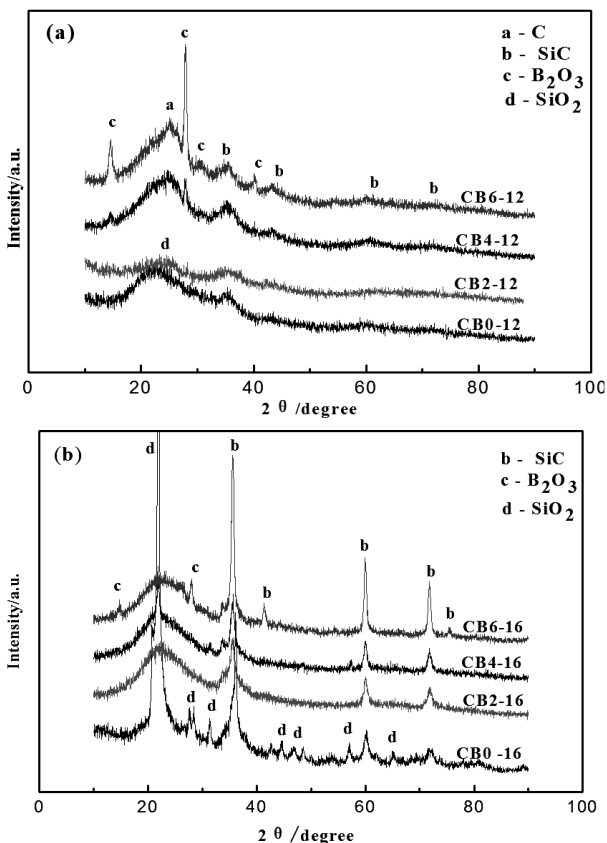ir (**Figures 1b** and **4a**) and the broad diffraction peak at $2\theta = 25°$ assigned to carbon (**Figure 4a**) is still distinct, suggesting the existence of the residual carbon in the oxidation products of CB2-12, CB4-12 and CB6-12. However, for the C-Si alloy obtained with the

Figure 4: XRD patterns of the oxidation products of the C-Si and C-B-Si alloys in air at 1000 °C for 3 h. The C-Si and C-B-Si alloys are obtained with the carbonization treatment at: a) 1200 °C and b) 1600 °C for 1 h.
Slika 4: XRD-posnetki oksidacijskih produktov po žarenju zlitin C-Si in C-B-Si 3 h na 1000 °C. Zlitine C-Si in C-B-Si so bile dobljene s karbonizacijo 1 h pri: a) 1200 °C in b) 1600 °C.

carbonization treatment at 1200 °C, there is a dramatic drop in the diffraction-peak intensity of the SiC after its oxidation in the air (**Figures 1b** and **4a**) and a broad diffraction peak appears at $2\theta = 22°$, which can be attributed to the SiO_2 formed due to the oxidation of the SiC. **Figure 4b** shows the XRD patterns of the oxidation products of the C-Si and C-B-Si alloys obtained with the carbonization treatment at 1600 °C. It can be seen from **Figures 1d** and **4b** that the diffraction peak at $2\theta = 25°$ assigned to the carbon in the C-Si and C-B-Si alloys disappears from their corresponding oxidation products, as a result of the burning up of the carbon during the oxidation of the C-Si and C-B-Si alloys. On the other hand, a very strong diffraction peak at $2\theta = 22°$ assigned to the SiO_2 phase occurs in the oxidation product of the C-Si alloy. The above XRD analysis of the oxidation products indicates that the C-B-Si alloy obtained with the carbonization treatment at 1200 °C has a better oxidation resistance than those obtained with the carbonization treatment at 1600 °C. This fact can be explained with the difference in the grain sizes of the SiC and B_4C in the C-B-Si alloy formed at different carbonization temperatures. The higher the carbonization temperature, the larger is the SiC grain size in the C-B-Si alloy. Large SiC grains are difficult to oxidize and, as a result, there is no continuous protective oxide film formed on the surface of the C-B-Si alloy during the air oxidation at 1000 °C. Oxygen from the air diffuses into the interior of the C-B-Si alloy through the cracks and holes and then reacts with carbon, which leads to a continuous combustion of carbon. However, small SiC grains are susceptible to oxidation. The SiO_2 formed with the oxidation of the SiC has a good fluidity at 1000 °C, thus forming a continuous protective oxide film sealing the microcracks and micropores in the C-B-Si alloy,[8] retarding the diffusion of the oxygen and decreasing the oxidation rate of the carbon.

In order to further understand the influence of the pyridine-borane content in the raw materials on the oxidation behavior of the C-Si and C-B-Si alloys, the morphology and structure of the C-Si and C-B-Si alloys before and after the oxidation in the air at 1000 °C for 3 h was observed with SEM. As shown in **Figure 5a**, the C-Si alloy possesses a loose structure and there are many micro-holes on its surface. Oxygen from the air diffuses into the interior through these micro-holes and reacts with the carbon in the C-Si alloy during oxidation, leading to a continuous weight loss of the C-Si alloy, as can be seen from **Figure 3a**. After the oxidation in the air at 1000 °C for 3 h, the micro-holes on the surface disappear and a smooth glassy film is formed (**Figure 5b**). The EDS spectrum of the oxidation product of CB0-12 shows that it is mainly composed of oxygen and silicon. The EDS spectrum and the above XRD analysis indicate that the main component of the glassy film is the non-crystalline SiO_2. This protective glassy film restrains the diffusion of oxygen to a great extent, and, as a result,
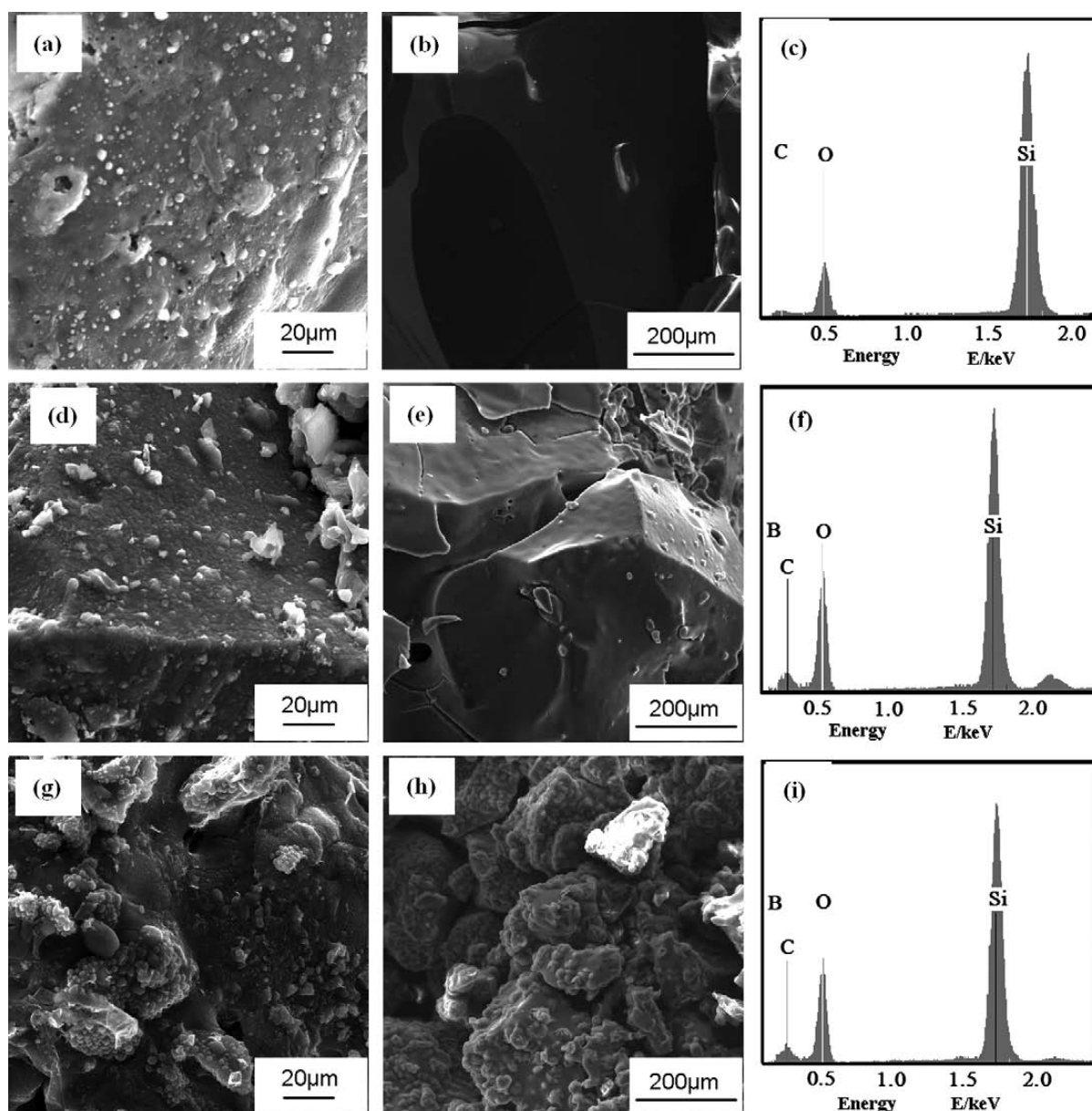
Figure 5: Typical SEM images of CB0-12, CB4-12 and CB6-12: a), c), e) before and b), d), f) after the oxidation in the air at 1000 °C for 3 h. EDS spectra of: c) CB0-12, f) CB4-12 and i) CB6-12 after the oxidation, corresponding to b), e) and h), respectively.
Slika 5: Značilni SEM-posnetki CB0-12, CB4-12 in CB6-12: a), c), e) pred oksidacijo in b), d), f) po njej 3 h na zraku na 1000 °C. EDS-spektri c) CB0-12, f) CB4-12 in i) CB6-12 po oksidaciji ustrezajo b), e) in h).

CB0-12 tends towards a constant weight loss after the oxidation for 3 h at 1000 °C (**Figure 3a**). Unlike sample CB0-12, sample CB4-12 has a relatively dense structure, as shown in **Figure 5d**. The formation of a dense structure may benefit from the sintering-aiding action of the B_2O_3 in sample CB4-12 (**Figure 1b**), which is commonly used as a flux former and can reduce the sintering temperature to obtain dense ceramics.[9,10] Moreover, the presence of B_2O_3 is beneficial for retarding the oxidation of the carbon in sample CB4-12 in the temperature range of 450–850 °C, as B_2O_3 has a low viscosity and a good mobility in this temperature range, therefore sealing the microcracks.[11] However, in the temperature range of

450–850 °C, the SiO_2 formed with the oxidation of the SiC in sample CB4-12 does not possess the function of sealing the microcracks so that no protective SiO_2 film can be formed in a short time because of its high viscosity and poor fluidity. These factors explain why the weight loss of sample CB4-12 is much lower than that of CB0-12 under the same oxidation conditions. After the oxidation for 3 h at 1000 °C, a continuous glassy film is formed on the surface of sample CB4-12, containing silicon, oxygen, carbon and boron (**Figure 5f**), consistent with the XRD pattern of the oxidation product of CB4-12 shown in **Figure 4a**. The SiO_2 formed with the oxidation of the SiC might be soluble in liquid B_2O_3

forming liquid borosilicate, which exists in the form of a B_2O_3-SiO_2 eutectic solution. The borosilicate glass has a much lower volatility and oxygen permeability so that it can inhibit the volatilization of the B_2O_3 and an oxidation of the carbon substrate. These synergistic oxidation-resistance effects have also been reported by Li et al.[12,13] The glassy film on sample CB4-12 is not perfect, however, there are some pinholes on its surface (**Figure 5e**), acting as diffusion channels for the oxygen from the air, resulting in a continuous oxidation of the carbon and a slow increase in the weight loss of sample CB4-12 (**Figure 3a**). The pyridine-borane content in the raw materials used for preparing sample CB6-12 is larger than that used for sample CB4-12. A structure comparison between CB4-12 and CB6-12, shown in **Figures 5d** and **g**, respectively, implies that a high pyridine-borane content in the raw materials is unfavorable for the formation of a dense structure during the preparation of the C-B-Si alloy. The microcracks and holes in sample CB6-12 act as diffusion channels for the oxygen from
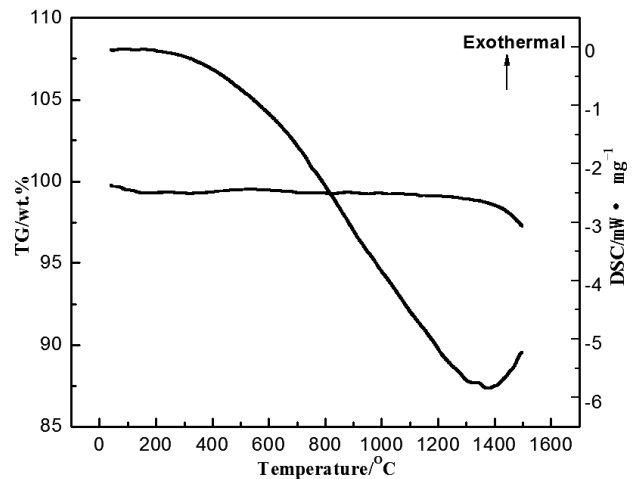
Figure 7: TG-DSC curve of CB4-12 in a dry-air flow at a heating rate of 5 °C/min
Slika 7: TG-DSC-krivulja za CB4-12 pri pretoku suhega zraka in hitrosti ogrevanja 5 °C/min
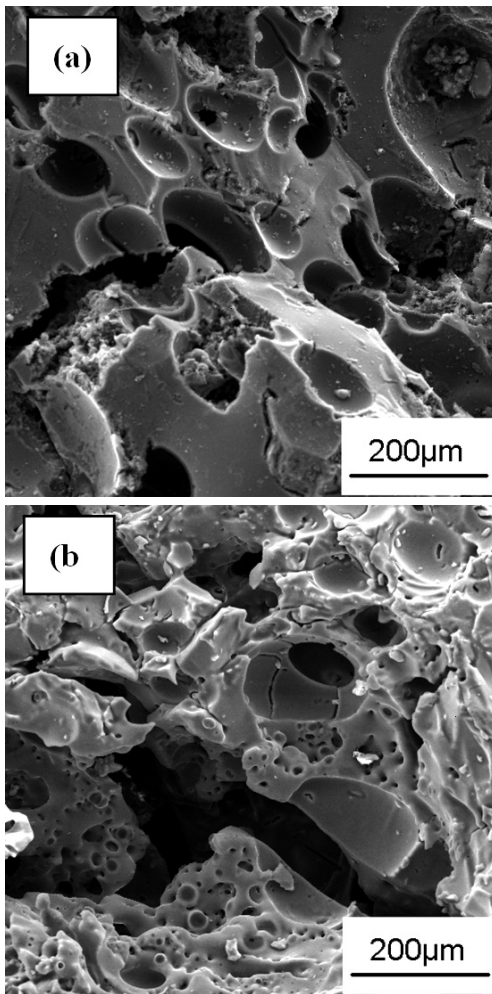
the air during the oxidation, causing a higher weight loss of CB6-12 than in the case of CB4-12 under the same oxidation conditions. After the oxidation for 3 h at 1000 °C, a discontinuous glassy film with the same element composition (**Figure 5i**) as the film shown in **Figure 5f** is formed on sample CB6-12 and many coarse particles are exposed outside the film. It can be expected that as the oxidation time increases, the thickness of the glassy film will gradually increase, and the coarse particles will finally be completely covered.

Figure 6 shows typical SEM images of CB4-16 before and after the oxidation in the air at 1000 °C for 3 h. As can be seen from **Figure 6a**, CB4-16 has a loose and porous structure, which is quite different from the dense structure of CB4-12 (**Figure 5d**). The loose and porous structure may result from an intense volatilization and escaping of B_2O_3 during the preparation of CB4-16, whose boiling point is 1500 °C at atmospheric pressure. The SEM observations indicate that too high a carbonization temperature (>1500 °C) is unfavorable for the formation of a dense structure for the C-B-Si alloy. Furthermore, the higher the carbonization temperature, the larger is the grain size of the SiC in C-B-Si alloys.[14] The growth of the SiC grains induces an increase in the initial oxidation temperature,[15] which can be confirmed with the abundance of the remaining SiC phase in the oxidation product of CB4-16 (**Figure 4b**). The volatilization loss of the B_2O_3 and the increase in the initial oxidation temperature of the SiC in CB4-16 make it very difficult to form a protective glassy film and, as a result, a great deal of carbon is oxidized. This explains the fact why the weight loss of sample CB4-16 is much higher than that of sample CB4-12 under the same oxidation conditions. After the oxidation at 1000 °C for 3 h, a large number of honeycomb-like holes occur in sample CB4-16, which may be left over during the escape of the CO and CO_2 formed by the oxidation of carbon. The

Figure 6: Typical SEM images of CB4-16: a) before and b) after the oxidation in the air at 1000 °C for 3 h
Slika 6: Značilna SEM-posnetka CB4-16: a) pred in b) po oksidaciji 3 h na zraku na 1000 °C

above SEM observations for sample CB4-16 agree with the oxidation-weight-loss curves shown in **Figure 3b**, further confirming that the oxidation resistance of CB4-16 is inferior to that of CB4-12.

To have a better insight into the dynamic oxidation behavior of the C-B-Si alloys, the TG-DSC analysis of CB4-12 was carried out on a comprehensive thermal analyzer, as shown in **Figure 7**. As the temperature increases from room temperature to about 150 °C, the mass of the sample decreases gradually and the weight loss is about 1 % when the temperature reaches about 150 °C. The weight loss in this temperature range may result from the volatilization of the moisture absorbed in the sample. In the temperature range of 150–300 °C, there is no obvious mass change, exhibiting the sample's good antioxidant ability. However, when the temperature is over 1400 °C, the mass of the sample decreases significantly, which could be attributed to a fast gasification of the protective glassy film composed of SiO_2 and B_2O_3 at a high temperature in the flowing air.[16] In addition, a strong exothermic peak appears at the temperature close to 1400 °C on the DSC curve, indicating a rapid and violent oxidation of the carbon in the C-B-Si alloy.

4 CONCLUSIONS

The solvent-soluble Si and B-Si doped coal-tar pitches were synthesized with the co-pyrolysis of a mixture of the toluene-soluble fraction of the coal-tar pitch, polycarbosilane and pyridine borane. The softening point and the pyrolysis yield of the doped coal-tar pitch increase with the increasing of the content of pyridine borane in the raw materials. The C-B-Si alloy composed of SiC, B_2O_3 and C can be obtained with the carbonization treatment of the synthetic B-Si doped coal-tar pitch at high temperatures. The boron content and the carbonization temperature have significant influences on the oxidation resistance of the resulting alloys. In most cases, the oxidation resistance of the C-B-Si alloy is better than that of the C-Si alloy, which can be attributed to the sintering-aiding action of B_2O_3 and the anti-oxidation synergism of the SiO_2 and B_2O_3 formed during the oxidation. The higher the carbonization temperature, the larger is the grain size of the SiC in the C-B-Si alloy. A large grain size leads to an increase in the initial oxidation temperature of the SiC, which is unfavorable for the formation of a protective glassy film on the surface of the C-B-Si alloy. As a result, after the oxidation at 1000 °C for 10 h, the weight loss of CB4-12 is less than 6 %, whereas it is 23 % for CB4-16. In view of the excellent oxidation resistance of CB4-12 derived from the B-Si doped coal-tar pitch, the B-Si doped pitches synthesized in this study can be used as promising impregnating agents in the fabrication of carbon/carbon composites, so as to increase their oxidation resistance at high temperatures.

5 REFERENCES

[1] S. Lu, B. Rand, K. D. Bartle, et al., Novel oxidation resistant carbon-silicon alloy fibres, Carbon, 35 (**1997**), 1485–1493

[2] A. V. K. Westwood, R. Brydson, R. Coult, et al., Carbon-boron-nitrogen alloys from borazarene-derived mesophase pitches, Carbon, 40 (**2002**), 2157–2167

[3] A. V. K. Westwood, B. Rand, S. Lu, Oxidation resistant carbon materials derived from boronated carbon-silicon alloys, Carbon, 42 (**2004**), 3071–3080

[4] C. F. Wang, F. R. Huang, Y. Jiang, et al., Oxidation behavior of carbon materials derived from a carborane- and silicon-incorporated polymer, Ceramics International, 38 (**2012**), 3081–3088

[5] P. P. Partha, T. S. Stuart, Carbon materials obtained from organometallic modification of pitch and its oxidation resistance properties, Carbon, 34 (**1996**), 89–95

[6] C. Czosnek, W. Ratuszek, J. F. Janik, et al., XRD and 29Si MAS NMR spectroscopic studies of carbon materials obtained from pyrolyses of a coal tar pitch modified with various silicon-bearing additives, Fuel Processing Technology, 79 (**2002**), 199–206

[7] A. V. K. Westwood, B. Rand, S. Lu, Oxidation resistant carbon materials derived from boronated carbon-silicon alloys, Carbon, 42 (**2004**), 3071–3080

[8] J. Y. Liu, F. Li, J. Liu, et al., Micro-analysis of high-temperature oxidation-resistance of a new kind of heat-resistant grid plate in grate-kiln, International Journal of Minerals, Metallurgy and Materials, 16 (**2009**) 6, 632–639

[9] C. K. Chang, L. Jiang, D. L. Mao, et al., Photoluminescence of 4SrO7Al2O3 ceramics sintered with the aid of B2O3, Ceramics International, 30 (**2004**), 285–290

[10] H. P. Wang, S. Q. Xuy, S. Y. Zhai, et al., Effect of B2O3 additives on the sintering and dielectric behaviors of CaMgSi2O6 ceramics, Journal of Materials Science and Technology, 26 (**2010**) 4, 351–354

[11] Y. Q. Li, T. Qiu, Oxidation behavior of boron carbide powder, Materials Science and Engineering A, 444 (**2007**), 184–191

[12] J. Li, R. Y. Luo, C. Lin, et al., Oxidation resistance of a gradient self-healing coating for carbon/carbon composites, Carbon, 45 (**2007**), 2471–2478

[13] N. Takayuki, G. Takashi, M. Makoto, et al., Oxidation of boron carbide-silicon composite at 1073 K to 1773 K, Materials Transactions, 44 (**2003**) 3, 401–406

[14] T. Sogabe, T. Matsuda, K. Kuroda, et al., Preparation of B4C-mixed graphite by pressureless sintering and its air oxidation behavior, Carbon, 33 (**1995**), 1783–1788

[15] T. Eichner, M. Braun, K. J. Huttinger, Element-substituted polyaromatic mesophases: I. Boron-substitution with the pyridine-borane complex, Carbon, 34 (**1996**), 1367–1381

[16] Z. J. Fan, Y. Z. Song, Oxidation behavior of fine-grained SiC-B4C/C composites up to 1.400 °C, Carbon, 41 (**2003**), 429–436

FAILURE-MODE TRANSITION IN RESISTANCE SPOT WELDED DP780 ADVANCED HIGH-STRENGTH STEEL: EFFECT OF LOADING CONDITIONS

PREHOD VRSTE PRELOMA UPOROVNO TOČKASTO VARJENEGA NAPREDNEGA VISOKOTRDNOSTNEGA JEKLA DP780: VPLIV RAZMER PRI OBREMENJEVANJU

Mehdi Mansouri Hasan Abadi[1], Majid Pouranvari[2]

[1]Materials Engineering Department, Najafabad Branch, Islamic Azad University, Najafabad, Iran
[2]Materials and Metallurgical Engineering Department, Dezful Branch, Islamic Azad University, Dezful, Iran
mehdi_mansouri_h@yahoo.com

Resistance spot welds of advanced high-strength steels (AHSSs) exhibit a high tendency to fail in the interfacial failure mode (i.e., a failure through the fusion zone). It is also evident that the conventional recommendations (based on the sheet thickness) for weld sizing, ensuring the pullout failure mode of welds, are not dominant in AHSS welds. Therefore, there is a need to study the failure mode of advanced high-strength-steel spot welds. This paper aims at investigating the transition from the interfacial to the pullout failure mode during various loading conditions including the tensile-shear test, cross-tension and coach-peel tests of DP780 spot welds. It was found that there is a critical fusion-zone (FZ) size ensuring the pullout failure mode in each loading condition. The results showed that the critical fusion size increased in the following order: cross-tension, coach-peel and tensile-shear test. The behaviour of the transition from the interfacial to the pullout failure mode was explained in terms of the stress state of the weld for each loading mode.

Keywords: resistance spot welding, failure mode, DP780, loading condition

Uporovni točkasti zvari naprednega visokotrdnostnega jekla (AHSS) izkazujejo nagnjenje k porušitvi med ploskvama (porušitev skozi področje zvara). Razvidno je tudi, da pri AHSS-zvarih ne veljajo navadna priporočila (glede na debelino pločevine) za velikost zvara, ki bi omogočila porušitev z iztrganjem zvara. Zato je bilo treba preučiti način porušenja točkastih zvarov pri naprednih visokotrdnostnih jeklih. Namen tega članka je opis preiskave načina porušitve od porušitve med ploskvama do porušitve z iztrganjem pri različnih obremenitvah, vključno z natezno-strižnim preizkusom točkastih zvarov DP780. Ugotovljeno je bilo, da obstaja kritična velikost FZ, ki omogoča, da se zagotovi porušitev z izpuljenjem pri vseh obremenitvah. Rezultati so pokazali, da velikost zvara narašča v naslednjem vrstnem redu: prečni natezni preizkus, natezni preizkus spojenih kotnikov (coach-peel) in natezno-strižni preizkus. Za vsako vrsto obremenitve je razložen z napetostmi prehoda iz medploskovne porušitve v porušitev z izpuljenjem.

Ključne besede: uporovno točkasto varjenje, način porušitve, DP780, način obremenitve

1 INTRODUCTION

Vehicle crashworthiness, defined as the capability of a car structure to provide adequate protection to its passengers against injuries in the event of a crash, largely depends on the integrity and mechanical performance of spot welds. Therefore, an evaluation of the spot-weld quality is a vital issue for the reliability of the vehicle and for improving the economics of the vehicle production.[1–6]

The failure mode is the manner in which a spot weld fails. Generally, the resistance spot weld (RSW) failure occurs in two modes: the interfacial failure (IF) and the pullout failure (PF).[4–6] In the interfacial mode, a failure occurs via a crack propagation, while, in the pullout mode, a failure occurs via a nugget withdrawal from one sheet. Generally, the pullout mode is the preferred failure mode due to its higher associated plastic deformation and energy absorption. Thus, vehicle crashworthiness, as the main concern in the automotive design, is dramatically reduced if spot welds fail via the interfacial

mode.[7–10] The tortuosity of the crack path in the pullout mode dissipates more energy in crash conditions and is preferable to the interfacial failure mode which does little to deflect the direction of crack propagation.[11] Therefore, it is necessary to adjust the welding parameters so that the pullout failure mode is guaranteed.

The failure mode and the failure mechanism largely depend on the complex interplay between the weld geometry and the material properties of the fusion zone (FZ)/heat-affected zone (HAZ)/base metal (BM) as well as between the test geometry and the stress state of each weld.[12,13] Therefore, the prediction of the failure mode and failure location is a challenging issue.

Spot welds in the real-service conditions experience complex loading conditions including shear, tensile, compression, bending and torsion stresses. This paper aims at investigating the failure-mode transition from the interfacial failure mode to the pullout mode under the tensile-shear (TS), cross-tension (CT) and coach-peel (CP) loading conditions.

2 EXPERIMENTAL PROCEDURE

DP780 dual-phase steel sheets 2 mm thick were used as the base metals. The chemical composition of the investigated steel is Fe-0.16C-0.24Si-0.67Mn-0.04Cr-0.01Mo (mass fractions, %). The values of the ensile strength and the elongation of the base metal are 820 MPa and 14 %, respectively. Resistance spot welding was performed using a 120 kV A AC pedestal-type resistance-spot-welding machine, controlled by a PLC operating at 50 Hz. Welding was conducted using a 45° truncated cone RWMA Class 2 electrode with an face diameter 8 mm.

To study the effects of the welding conditions on the weld performance, several welding schedules were used. The electrode force and holding time were selected on the basis of the thickness of the base material and were kept constant at 5.1 kN and 0.2 s, respectively. The welding current was increased step by step from 7 kA to 11.5 kA at the welding time of 0.5 s. The welding parameters were chosen below the expulsion limit to avoid an undesirable failure mode. Ten samples were prepared for each welding condition including three samples for the tensile-shear test, three samples for the cross-tension test, three samples for the coach-peel test and one sample for the metallographic investigation and measurement of the weld size.

The samples for the mechanical testing were prepared according to the AWS standard.[14] The mechanical tests were performed at a cross-head speed of 10 mm/min with an Instron universal testing machine. The failure modes of the spot welded specimens were determined by examining the fractured samples.

Weld-nugget (fusion zone) sizes were measured for all the samples on the metallographic cross-sections of the welds. The Vickers microhardness test was performed using an indenter load of 100 g for a period of 20 s to obtain a diagonal hardness profile from the center of the FZ to the BM. The hardness indentations were spaced 0.3 mm apart from each other.

3 RESULTS AND DISCUSSION

3.1 Microstructure-hardness characteristics

A typical macrostructure of a joint is shown in **Figure 1a** indicating three distinct zones, namely, the fusion zone (FZ), the heat-affected zone (HAZ) and the base metal (BM). A hardness profile of a joint is shown in **Figure 1b**. The hardness of the BM is averaged at 250 HV which corresponds to its ferritic martensitic microstructure (**Figure 1c**). A high hardness of the FZ can be related to the martensite formation (**Figure 1d**). The martensite formation in the FZ is attributed to the high cooling rate of the resistance-spot-welding process due to the presence of the water-cooled copper electrodes and their quenching effect as well as the short welding cycle. It was shown with the modeling that the spot welds with the thicknesses of up to 2 mm typically solidify in fewer than 3–4 cycles.[15] Gould et al.[16] developed a simple analytical model predicting the cooling rates of the resistance spot welds. According to this
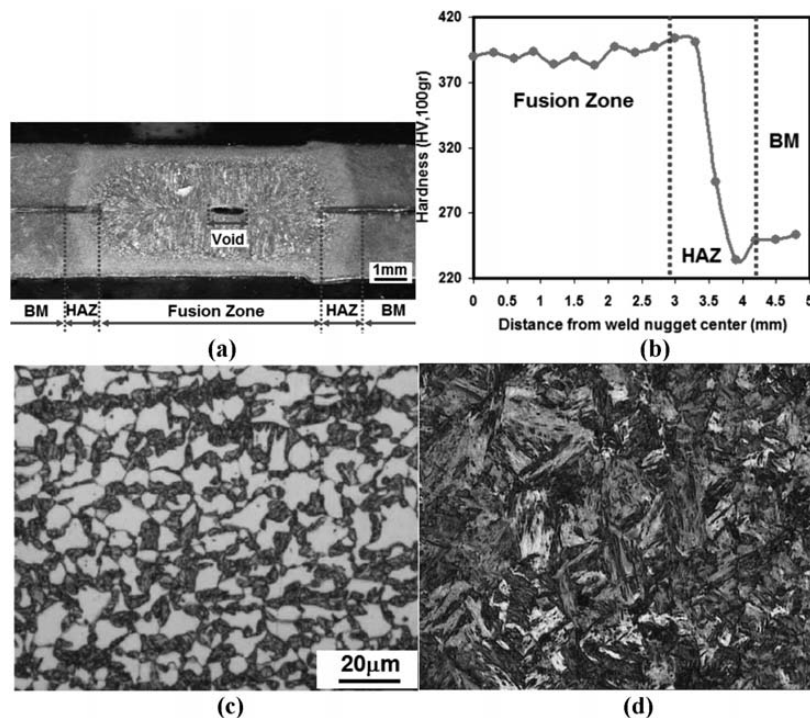
Figure 1: Typical: a) macrostructure, b) hardness profile of the resistance spot welds made on DP780, c) BM microstructure, d) FZ microstructure
Slika 1: Značilna: a) mikrostruktura, b) profil trdote uporovnega točkastega zvara na DP780, c) BM-mikrostruktura, d) FZ-mikrostruktura

model, the cooling rate for the thickness 2 mm is about 3000 K s⁻¹. For steels, the critical cooling rate required for a formation of the martensite in the microstructure can be estimated using the following equation:[17]

$$\lg v = 7.42 - 3.13\,w(C) - 0.71\,w(Mn) - 0.37\,w(Ni) - \\ - 0.34\,w(Cr) - 0.45\,w(Mo) \qquad (1)$$

where v is the critical cooling rate in K h⁻¹. The calculated critical cooling rate for the investigated steels is about 740 K s⁻¹. Since the experienced cooling rate in the FZ is higher than the critical cooling rates needed for a martensite formation, it is not surprising that a martensite structure is present in the FZ.

A reduction in the hardness (softening) with respect to the BM was observed in the sub-critical HAZ of the DP780 spot welds. The minimum hardness of the HAZ is about 235 HV (i.e., the maximum hardness reduction of 15 HV). The occurrence of the HAZ softening during the RSW of dual-phase steel is well documented in the literature.[6,18–21] This is related to the martensite tempering.

3.2 Failure-mode-transition behavior

All the DP780 spot welds failed in the interfacial mode in the TS loading condition. However, during the CT and CP tests, apart from the interfacial failure mode, the pullout mode was also observed. **Figure 2** shows typical fracture surfaces of the spot welds that failed in the interfacial mode and the pullout mode during the CT test.

The FZ size is one of the key factors in controlling the failure mode of spot welds. **Figure 3** shows the correlation among the welding current, the FZ size and the failure mode of the spot welds during the TS, CT and CP loading conditions. It is well documented that there is a critical FZ, above which the pullout failure mode is guaranteed.[4–6,11–13] The critical FZ (D_C) ensuring the pullout failure mode was determined by examining the weld-fracture surfaces. The critical FZ size (defined as the FZ size between the maximum weld size leading to the I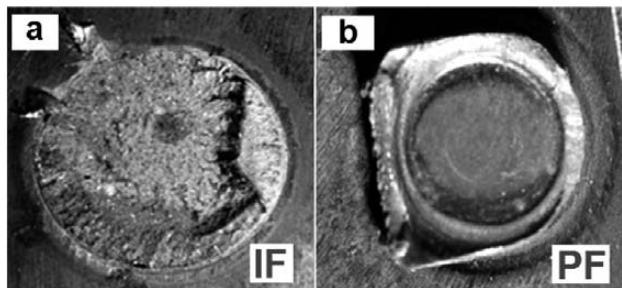F mode and the minimum weld size leading to the PF mode) was identified in **Figure 3**. In the CT test, the spot welds with the fusion-zone sizes larger than 7.1 mm

Figure 2: Typical fracture surface during the cross-tension tests: a) interfacial failure (IF) and b) pullout failure (PF)
Slika 2: Značilna površina preloma pri prečnem nateznem preizkusu: a) porušitev med ploskvama (IF) in b) porušitev z iztrganjem (PF)
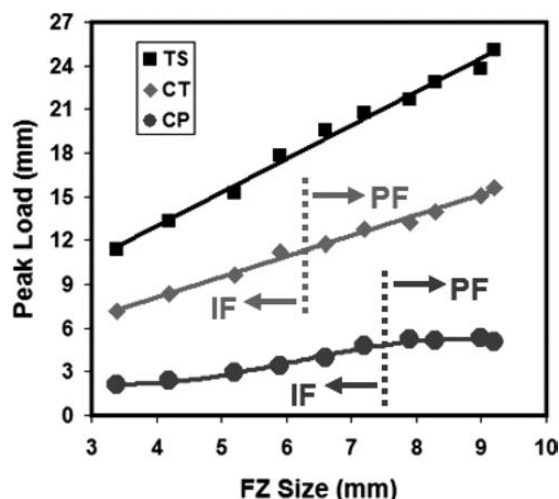
Figure 3: Effect of the fusion-zone (FZ) size on the peak load and failure mode of the spot welds during the tensile-shear (TS), coach-peel (CP) and cross-tension (CT) tests. Note that all the spot welds failed in the interfacial mode during the TS test.
Slika 3: Vpliv velikosti zvara (FZ) na konico obremenitve in način porušitve točkastih zvarov med natezno-strižnim (TS) preizkusom, preizkusom coach-peel (CP) in prečnim nateznim preizkusom (CT). Vsi zvari so se porušili med ploskvama pri natezno-strižnem TS-preizkusu.

failed in the pullout failure mode, while, during the CP test, the spot welds with the fusion-zone sizes larger than 7.9 mm failed in the pullout failure mode. All the spot welds exhibit the interfacial failure mode during the tensile-shear test. Therefore, the tendency to fail in the interfacial failure mode is increased in the following order: CT, CP and TS loading conditions. To explain the IF to PF transition behaviour, first, the stress state in these loading conditions should be briefly described. Simple models describing the stress distribution at the interface and circumference of a weld nugget during the TS,[12] CP[10] and CT tests are shown in **Figure 4**. The following points can be drawn from this figure:

(1) During the TS tests, the shear stresses are dominant at the interface. As can be seen in **Figure 4**, one leg of the lower sheet and one leg of the upper sheet are subjected to the tensile stress. In the IF mode, the shear stress at the sheet/sheet interface is the driving force of the failure. The tensile stress at the nugget circumference is the driving force for the PF mode.

(2) During the CP tests, in the IF mode, the tensile stress at the sheet/sheet interface is the driving force of the failure. The bending stress is the driving force for the PF mode during the CP test.

(3) During the CT test the notch at the sheet/sheet interface experiences the tensile stress (i.e., the opening mode, mode I of the loading condition). According to **Figure 4**, the shear stress at the nugget circumference (i.e., the HAZ) is the driving force for the PF mode during the CT test.

To explain the IF to PF transition behaviour, the following points should be considered:
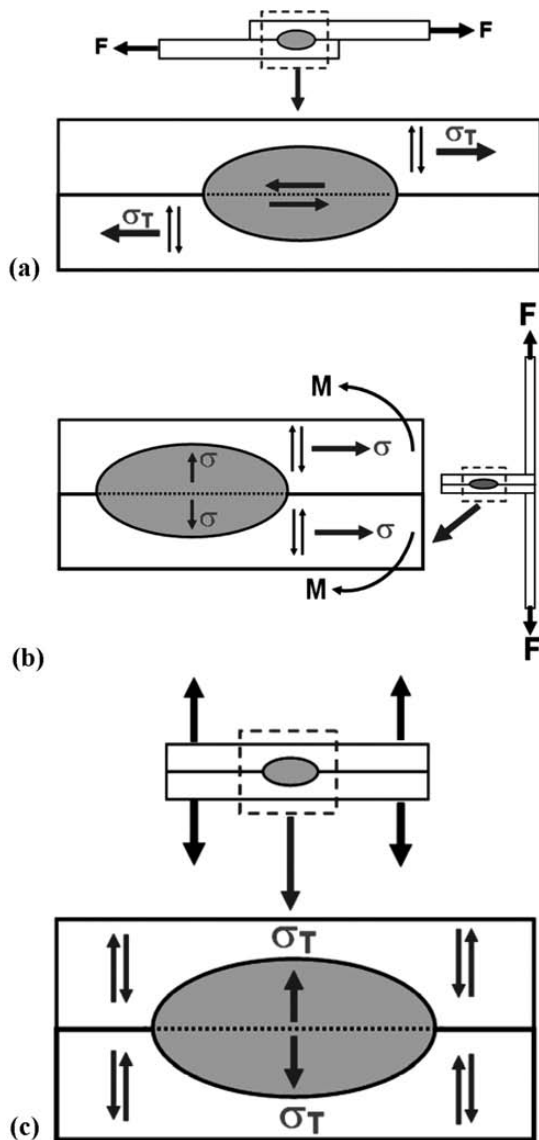
Figure 4: Simple models describing the stress distribution at the interface and circumference of a weld nugget during the: a) tensile-shear, b) coach-peel and c) cross-tension tests
Slika 4: Enostavni modeli, ki opisujejo razporeditev napetosti na stiku in okrog jedra zvara med: a) natezno-strižnim preizkusom, b) preizkusom coach-peel in c) nateznim prečnim preizkusom

(i) In the TS, the driving force for the IF mode is the shear stress at the sheet/sheet interface, while in the CT and CP tests, the tensile stress at the sheet/sheet interface is the driving force. It is well known that the shear strength of the metals is lower than their tensile strength. This point can partly explain the higher tendency of the TS samples to fail in the IF mode.

(ii) The driving force for the PF mode in the CT test is the shear stress at the nugget circumference, while in the TS and CP tests, the tensile stress is the driving force. Again, the fact that the shear strength of the metals is lower than the tensile strength can partly explain the higher tendency of the CT samples to fail in the pullout mode. Moreover, Radakovic and Tumuluru[22] showed,

with the finite-element modeling, that the location of the maximum stress is in the HAZ. This factor coupled with the softening in the HAZ of DP780 results in the strain localization in the weld circumference enhancing the pullout failure mode.

For practical purposes, it is interesting to compare the experimentally determined minimum FZ size required to obtain the PF mode with the existing industrial standards for the weld-nugget sizing. Various industrial standards recommend the minimum weld size for a given sheet thickness:

(I) AWS/ANSI/AISI,[14] a weld-button sizing, ensuring that the weld size is large enough for carrying the desired load, is expressed with equation (2):

$$D = 4t^{0.5} \tag{2}$$

where D is the weld-nugget size and t is the sheet thickness in mm.

(II) According to the Japanese JIS Z3140[23] and the German DVS2923[24] standards, the required weld size is specified according to equation (3):

$$D = 5t^{0.5} \tag{3}$$

Table 1 compares the experimentally determined critical FZ size for the spot welds made on DP780 steel 2 mm that failed under various loading conditions and the weld size determined by industrial recommendations. As can be seen, the most common weld-sizing criterion of $4t^{0.5}$ is not sufficient for producing a weld in the PF mode in all the loading conditions. Despite the fact that the sizing based on the $5t^{0.5}$ rule is sufficient for producing the PF mode during the CT test, it is not sufficient to avoid the interfacial failure during the TS and CP tests. This is due to the fact that these recommendations ignore the effect of metallurgical factors on the failure mode so that these models include only the sheet thickness for the sake of simplicity. Despite the fact that the industrial recommendation works well for obtaining the pullout mode of low-carbon steels, the sizing based on these recommendations does not guarantee the PF mode during the tensile-shear testing of the AHSS spot welds. Therefore, it seems that in addition to the sheet thickness, the metallurgical factors should be considered to precisely analyze and predict the RSW failure mode.

Table 1: Critical fusion-zone size required to ensure the pullout failure mode during the cross-tension (CT), coach-peel (CP) and tensile-shear (TS) tests along with the common industrial recommendations for spot-weld sizing
Tabela 1: Kritična velikost zvara, ki zagotavlja porušitev z izpuljenjem med prečnim nateznim preizkusom (CT), preizkusom coach-peel (CP) in natezno-strižnim (TS) preizkusom, skupaj s splošnim industrijskim priporočilom za velikost točkastega zvara

$(D_C)_{CT}$	$(D_C)_{CP}$	$(D_C)_{TS}$	$4t^{0.5}$	$5t^{0.5}$
6.6 mm	7.9 mm	N. D*	5.6 mm	7.1 mm

* N. D: Not determined – all the spot welds failed in the TS loading condition

4 CONCLUSIONS

The failure modes of the resistance spot welds made on DP780 dual-phase steels 2 mm thick were investigated under the tensile-shear, coach-peel and cross-tension tests. It was observed that the tendency to fail in the interfacial mode is the highest in the tensile-shear loading condition, while the cross-tension test exhibits a higher tendency to fail in the pullout failure mode. This was explained in terms of the stress state at the weld interface and nugget circumference during each loading mode. During the cross-tension test, a high-stress HAZ coupled with the presence of softening in the HAZ of DP780 results in the strain localization in the weld circumference enhancing the pullout-failure mode. It is shown that the industrial weld-nugget-sizing recommendation of $4t^{0.5}$ was not sufficient for producing the welds with the pullout failure mode during the mechanical testing of the DP980 resistance spot welds.

5 REFERENCES

[1] M. Pouranvari, A. Abedi, P. Marashi, M. Goodarzi, Effect of expulsion on peak load and energy absorption of low carbon resistance spot welds, Sci. Technol. Weld. Joining, 13 (**2008**), 39–43

[2] S. Simoncic, P. Podrzaj, Image-based electrode tip displacement in resistance spot welding, Meas. Sci. Technol., 23 (**2012**), 1–7

[3] P. Podrzaj, I. Polajnar, J. Diaci, Z. Kariz, Estimating the strength of resistance spot welds based on sonic emission, Sci. Technol. Weld. Joining, 10 (**2005**), 399–405

[4] P. Podrzaj, S. Simoncic, Resistance spot welding control based on fuzzy logic, Int. J. Adv. Manuf. Technol., 52 (**2011**), 959–967

[5] M. Pouranvari, S. P. H. Marashi, Failure mode transition in AISI 304 resistance spot welds, Weld. J., 91 (**2012**), 303s–309s

[6] M. Pouranvari, S. M. Mousavizadeh, S. P. H. Marashi, M. Goodarzi, M. Ghorbani, Influence of fusion zone size and failure mode on mechanical performance of dissimilar resistance spot welds of AISI 1008 low carbon and advanced high strength DP600 steels, Mater. Des., 32 (**2011**), 1390–1398

[7] M. M. H. Abadi, M. Pouranvari, Correlation between macro/micro structure and mechanical properties of dissimilar resistance spot welds of AISI 304 austenitic stainless steel and AISI1008 low carbon steel, Metall. Mater. Eng., 16 (**2010**), 134–146

[8] M. Pouranvari, S. P. H. Marashi, On the failure of low carbon steel resistance spot welds in quasi-static tensile–shear loading, Mater. Des., 31 (**2010**), 3647–3652

[9] M. Pouranvari, E. Ranjbarnoodeh, Dependence of the fracture mode on the welding variables in the resistance spot welding of ferrite-martensite DP980 advanced high-strength steel, Mater. Tehnol., 46 (**2012**) 6, 665–671

[10] M. Pouranvari, S. P. H. Marashi, Failure of resistance spot welds: tensile shear versus coach peel loading conditions, Ironmaking & Steelmaking, 39 (**2012**), 104–111

[11] M. Marya, X. Q. Gayden, Development of Requirements for resistance Spot Welding Dual-Phase (DP600) Steels Part 2: Statistical Analyses and Process Maps, Weld. J., 84 (**2005**), 197s–204s

[12] M. Pouranvari, S. P. H. Marashi, Failure mode transition in AHSS resistance spot welds, Part I: controlling factors, Mater. Sci. Eng. A, 528 (**2011**), 8337–8343

[13] M. Pouranvari, S. P. H. Marashi, D. S. Safanama, Failure mode transition in AHSS resistance spot welds. Part II: Experimental investigation and model validation, Mater. Sci. Eng. A, 528 (**2011**), 8344–8352

[14] Recommended Practices for Test Methods and Evaluation of the Resistance Spot Welding Behavior of Automotive Sheet Steels, ANSI/AWS/SAE D8.9-97

[15] M. V. Li, D. Dong, M. Kimchi, Analysis of microstructure evolution and residual stress development in resistance spot welds of high-strength steels, SAE Technical Paper 982278, SAE International, Warrendale, Pa, 1998

[16] J. E. Gould, S. P. Khurana, T. Li, Predictions of microstructures when welding automotive advanced high-strength steels, Weld. J., 86 (**2006**), 111s–116s

[17] K. E. Easterling, Modelling the weld thermal cycle and transformation behavior in the heat-affected zone, In: H. Cerjak, K. E. Easterling (eds.), Mathematical Modelling of Weld Phenomena, Institute of Materials, Minerals and Mining, 1993

[18] M. Pouranvari, S. P. H. Marashi, Key factors influencing mechanical performance of dual phase steel resistance spot welds, Sci. Technol. Weld. Join., 15 (**2010**), 149–155

[19] M. I. Khan, M. L. Kuntz, Y. Zhou, Effects of weld microstructure on static and impact performance of resistance spot welded joints in advanced high strength steels, Sci. Technol. Weld. Joining, 13 (**2008**), 294–304

[20] F. Nikoosohbat, S. Kheirandish, M. Goodarzi, M. Pouranvari, S. P. H. Marashi, Microstructure and failure behaviour of resistance spot welded DP980 dual phase steel, Mater. Sci. Technol., 26 (**2010**), 738–744

[21] M. Pouranvari, S. P. H. Marashi, On failure mode of resistance spot welded DP980 advanced high strength steel, Can. Metall. Q., 51 (**2012**), 447–455

[22] D. J. Radakovic, M. Tumuluru, An evaluation of the cross-tension test of resistance spot welds in high-strength dual-phase steels, Weld. J., 91 (**2012**), 8s–15s

[23] Japanese Industrial Standard, Method of Inspection for Spot Welds, JIS Z 3140, 1989

[24] German Standard, Resistance Spot Welding, DVS 2923, 1986

ARTIFICIAL-NEURAL-NETWORK PREDICTION OF HEXAGONAL LATTICE PARAMETERS FOR NON-STOICHIOMETRIC APATITES

NAPOVEDOVANJE HEKSAGONALNIH MREŽNIH PARAMETROV Z UMETNO NEVRONSKO MREŽO

Umit Kockan[1], Fahrettin Ozturk[2,3], Zafer Evis[1,4]

[1]Micro and Nanotechnology Department, Middle East Technical University, 06800 Ankara, Turkey
[2]Department of Mechanical Engineering, Nigde University, Nigde, Turkey
[3]Department of Mechanical Engineering, The Petroleum Institute, Abu Dhabi, United Arab Emirates
[4]Department of Engineering Sciences, Middle East Technical University, 06800 Ankara, Turkey
evis@metu.edu.tr

In this study, hexagonal lattice parameters (a and c) and unit-cell volumes of non-stoichiometric apatites of $M_{10}(TO_4)_6X_2$ are predicted from their ionic radii with artificial neural networks. A multilayer-perceptron network is used for training. The results indicate that the Bayesian regularization method with four neurons in the hidden layer with a tansig activation function and one neuron in the output layer with a purelin function gives the best results. It is found that the errors for the predicted data of the lattice parameters of a and c are less than 1 % and 2 %, respectively. On the other hand, about 3 % errors were encountered for both lattice parameters of the non-stoichiometric apatites with exact formulas in the presence of the T-site ions that are not used for training the artificial neural network.

Keywords: hydroxyapatite, crystal structure, artificial neural networks, multilayer-perceptron network

V tej študiji so z uporabo umetnih nevronskih mrež napovedani heksagonalni mrežni parametri (a in c) in prostornina osnovne celice nestehiometričnega apatita $M_{10}(TO_4)_6X_2$ iz njihovih ionskih premerov. Za učenje je bila uporabljena večplastna perceptronska mreža. Rezultati kažejo, da najboljše rezultate daje Bayesianova ureditvena metoda s štirimi nevroni v skriti plasti z aktivacijsko funkcijo 'tansig' in en nevron v zunanji plasti s 'purelin'-funkcijo. Ugotovljeno je, da je napaka pri napovedanih mrežnih parametrih a in c manj kot 1 % oziroma manj kot 2 %. Po drugi plati pa se srečamo z napako 3 % pri obeh parametrih mreže nestehiometričnega apatita z natančnimi formulami pri prisotnosti ionov na T-mestih, ki niso bili uporabljeni pri usposabljanju umetne nevronske mreže.

Ključne besede: hidroksiapatit, struktura kristala, umetna nevronska mreža, večplastna perceptronska mreža

1 INTRODUCTION

Apatite is a mineral group which normally crystallizes in the space group $P6_3/m$. Apatite is the main source of the phosphorus required by plants. Apatite-group minerals have a general formula $^{IX}M1_4{}^{VII}M2_6(^{IV}TO_4)_6X_2$ ($Z = 1$), where the left superscripts indicate the ideal coordination numbers and are isostructural with apatite. Numerous mono-, di- and trivalent cation substitutes are found in the M sites and numerous hexa-, penta- and quadravalent polyanions can occupy the TO_4 site. The X site is usually occupied by monovalent anions, however, O^{2-} and H_2O can also reside there.[1] Apatites can be substituted by various elements, but even small amounts of substitutions can make a noticeable effect on the mechanical, thermal and optical properties.[2] Recently, apatite minerals have become very important in the fields of biomaterials, sensors, detoxification of wastes and immobilization of radioactive wastes.[2–4]

Bone is a natural composite material of a mass fraction 69–80 % inorganic phase (carbonated hydroxylapatite), 17–20 % collagen (organic component) and trace amounts of water and proteins.[5] Basically, synthetic hydroxylapatite ($Ca_{10}(PO_4)_6(OH)_2$) belongs to the large chemical family of calcium phosphates (CaP). CaPs are biocompatible, non-toxic, resorbable, non-inflammatory, having an excellent osteoconductive ability and bioactive property. Therefore, it is used as a bone and dental implant and for the coatings on implants, due to its similarity to the inorganic part of the bone.[6] Stability and ion-exchange capabilities mostly depend on the lattice properties. Moreover, the residual stresses in biological apatite coatings cause serious problems. These stresses may result in the wear debris and delamination that can be lethal for the patients because of the toxic effects and biomechanical failure. One of the main reasons of these drawbacks is a structural mismatch caused by the lattice-parameter differences between the substrate and the coating.[7]

It is not easy to prepare single crystals of apatites for X-ray diffraction applications and lattice-parameter determination with other diffraction techniques as electron and neutron diffractions are time consuming and not within the reach of many researchers. Moreover, vast amounts of ion-substitution possibilities exist. Neural networks can generate lattice parameters with a variety of apatite structures using limited numbers of experimental crystal study results for training the network, so that

the experimental work can be eliminated. A neural network is set to solve a relation between the inputs and outputs, which are ionic radii and lattice parameters, respectively. Hence, it is very important to construct a suitable dataset for training the neural network and find the optimum network types and parameters that can assist in generating crystal-structure entities like the lattice parameters of apatites.[8,9]

An artificial neural network (ANN) has a wide range of applications where a large amount of data is available but no reliable physical model is present.[10] The ANN is extensively used to model complex relationships between inputs and outputs. In the program, the training is first performed using the existing experimental data. By using this method, many properties like stress, strain, hardness, toughness, residual stress[11–14] and anything else that has a complex non-linear relationship with the known input variables can be determined without extensive theoretical and experimental studies. For example, the amounts of added chemicals are the input parameters that involve vast possibilities; however, the outputs that depend on the input parameters are normally determined experimentally. Generating large numbers of experimental data may be avoided by training neural networks with small numbers of experimental data if the input variables and the values that affect the searched properties, the outputs of the neural network, are known. Alloy design is particularly efficient with this method.[15]

Pattern recognition and prediction of the lattice parameters of apatites with artificial neural networks were previously studied.[9] Hexagonal lattice parameters of stoichiometric apatites were predicted using artificial neural networks.[16] However, there is not enough detail about the learning methods used for training the network and applicability of the method to non-stoichiometric apatites. The term 'non-stoichiometric' is used to state that M/TO_4, M/X or TO_4/X ratios are different from the general formula of $M_{10}(TO_4)_6X_2$. In addition, a unit-cell-volume calculation of apatites may amplify the errors coming from the lattice-parameter predictions. The errors between the calculated and predicted unit-cell volumes of apatites were calculated. In this study, non-stoichiometric hexagonal unit-cell lattice parameters and volumes of apatites $(M_{10}(TO_4)_6X_2)$, constituted by M: Ca^{2+}, Cd^{2+}, Pb^{2+}, Sr^{2+}, Zn^{2+}, La^{3+}, Y^{3+}; T: As^{+5}, Cr^{+5}, P^{5+}, V^{5+}, Si^{+4}; and X: F^-, Cl^-, OH^-, Br^{-1}, were predicted from their elemental ionic radii using an ANN. Each ion site accepted up to three substitutions and a wide variety of coupled substitutions were investigated. In addition, mathematical formulas were derived for the calculation of the lattice parameters using average ionic radii as independent variables.

2 METHODS

In an ANN, the learning methods compare the predicted outputs with the actual results.[17] Typically 60–80 % of the data is used for training the network, while the rest is used for testing and validating the data. At the end of the training process, the test data is used to check the ability of the network to predict new data.[18] A multi-layer-perceptron (MLP) model that maps the sets of input data onto a set of appropriate output with supervised learning and batch training was used because of its high non-linear regression performance.[19] A single hidden layer with different numbers of processing units and various learning methods were experimented to achieve the highest network performance. Sigmoid transfer functions for the hidden layer and linear transfer function for the output layer were used.

Some of the frequent algorithms use a first-order derivative while others use a second-order derivative of the error functions to determine the delta value which is used to adjust the weights of the network.[20] In this study, backpropagation algorithms were used. The experimented backpropagation methods in this study were resilient backpropagation (RP), gradient descent with momentum and adaptive learning rate backpropagation (GDX), levenberg-marquardt backpropagation (LM) and scaled conjugate gradient backpropagation (SCG). In addition to these methods, bayesian regularization (BR), which is a generalization method based on LM, was used.

The backpropagation method is useful for finding a network's weight gradient $\nabla \eta(w)$ easily.[16,21] The details regarding this method were given in a previous study.[16] The performance function of most of the networks is MSE, but the generalization can be improved by modifying the performance function with the mean square of weights and biases. By using this new performance function, the weights and biases were minimized, so the network performance increased.[16,19] The performance ratio is hard to optimize. To do this, the BR method can be used. This method reveals the network parameters (weights and biases) that are being effectively used. This method is especially useful when the inputs and targets fall in the range of $[-1,1]$ or are scaled to fit this range.[19]

An MLP neural network was used for the prediction of hexagonal lattice parameters of apatites from their average ionic radii at the individual sites of M, T, and X. The average ionic radii were calculated by separately giving weight to each ion at sites M, T, and X. The weights given are the mole numbers corresponding to each ion of the apatite formula. Then, the ionic radius of each ion was multiplied by its weight and the values were added to each site. Finally, the value for each site was divided by the corresponding total weight and the average ionic radius for each site was calculated.

Lattice parameters for the training dataset were retrieved from the Joint Committee on Powder Diffraction Standards (JCPDS) database and literature[22,23] with the addition of two extra databases[24,25] and the ionic radii were found from a handbook.[26] The constructed dataset was used for training the network with a proper learning method, neuron number in the hidden layer and activation functions. After training the network, the lattice

parameters of non-stoichiometric apatites were predicted by constructing a test dataset. The outputs of the test dataset were not introduced to the software, so that the prediction accuracy could be verified by comparing the neural networks' lattice-parameter predictions with the experimental data. The formulas and lattice parameters of the apatites that were used for testing, were retrieved from the literature.[27–32] In addition, the volumes of the apatites in the test dataset were calculated using the following equation:[33]

$$V = 2.589 \times a^2 \times c \qquad (1)$$

where a and c are the lattice parameters of the hexagonal unit cell.

3 RESULTS AND DISCUSSION

After all the data were collected, several network parameters were identified such as the type of the network, the number of hidden layers, learning methods and normalization functions. The best parameters found for each learning method are given in **Table 1**. The number of neurons in the hidden layer varied between four and seven with the tangent sigmoid function in the hidden layer and pure linear function in the output layer.

The previous works showed that the lattice parameters of apatites depend strongly on the average ionic radii of the M, T and X sites,[9] so to calculate the average ionic radius of each site, the weights were given to the M, T and X sites, with each site accepting up to three ions. The datasets prepared for training the network showed that the data should be kept as small as possible to prevent large deviations of the results and overfitting. After some trial and error, a refined dataset was prepared for the neural-network application as seen in **Table 2**.

In this study, the Matlab Neural Network Toolbox, version 4, was used for training and testing the network. After experimenting with different learning types and neuron numbers for the MLP network, it was seen that all the learning types, except for the BR and the GDX, produced correlation coefficients higher than 0.99. However, their prediction results were not equally successful. The LM, SCG, and BR methods produced satisfactory results, but only the BR method was capable of giving both high-correlation coefficients and most accurate
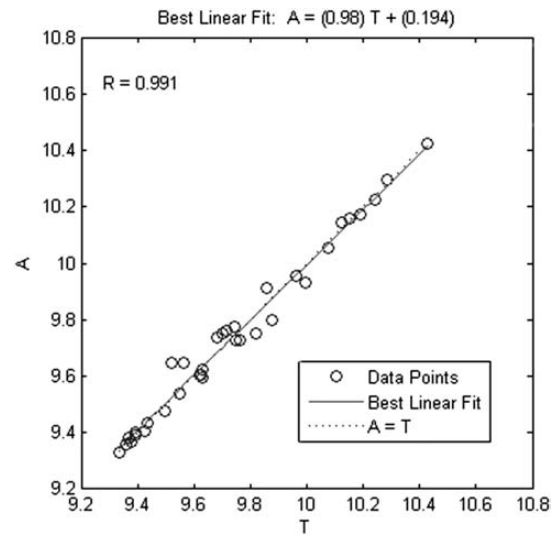
Figure 1: Linear correlation of outputs and targets for lattice parameter *a*
Slika 1: Linearna odvisnost rezultatov in ciljev za mrežni parameter *a*
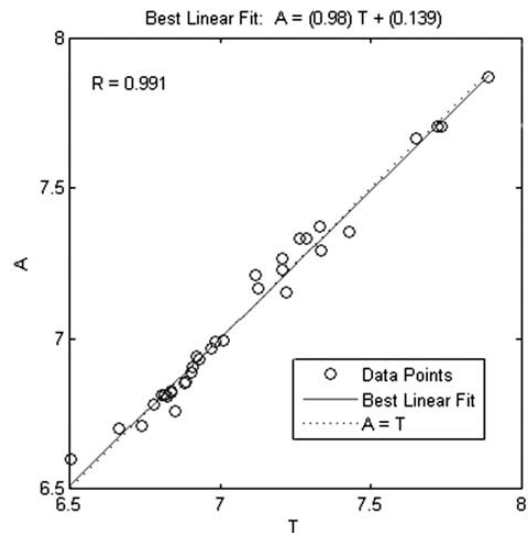
Figure 2: Linear correlation of outputs and targets for lattice parameter *c*
Slika 2: Linearna odvisnost rezultatov in ciljev za mrežni parameter *c*

prediction results, so the BR was used as the primary choice for training and testing throughout this study. The network parameters were optimized in order to obtain

Table 1: Training parameters for each learning method
Tabela 1: Parametri usposabljanja za vsako metodo učenja

Learning method	Number of neurons in the hidden layer	Activation function used for hidden layer	Activation function used for output layer	Epoch	Momentum coefficient	Learning rate	Train goal
BR	4	tansig	purelin	1000	–	–	–
GDX	7	tansig	purelin	5000	0.8	0.05	1e-3
LM	4	tansig	purelin	400	–	–	15e-4
RP	6	tansig	purelin	5000	–	–	1e-3
SCG	7	tansig	purelin	3000	–	–	177e-5 1e-3 (for *c*)

Table 2: Training dataset and percent errors for the outputs
Tabela 2: Podatki za usposabljanje in napaka rezultatov

	Apatite formula	Average radius M	Average radius T	Average radius X	$a/$ (10^{-1} nm)	$c/$ (10^{-1} nm)	a output	c output	Error (%) (a)	Error (%) (c)
1	$Ca_5 (PO_4)_3 OH$	1	0.38	1.37	9.424	6.879	9.4037	6.8499	0.215	0.423
2	$Ca_5 (VO_4)_3 (OH)$	1	0.54	1.37	9.818	6.981	9.7524	6.9889	0.668	0.113
3	$Ca_5 (CrO_4)_3 OH$	1	0.55	1.37	9.683	7.01	9.7353	6.9945	0.540	0.221
4	$Ca_5 (PO_4)_3 F$	1	0.38	1.33	9.367	6.884	9.3817	6.855	0.157	0.421
5	$Ca_5 (PO_4)_3 Cl$	1	0.38	1.81	9.52	6.85	9.6457	6.7576	1.320	1.349
6	$Ca_5 (AsO_4)_3 Cl$	1	0.46	1.81	10.076	6.807	10.057	6.8122	0.189	0.076
7	$Ca_5 (PO_4)_3 Br$	1	0.38	1.96	9.761	6.739	9.7262	6.7111	0.357	0.414
8	$Cd_5 (PO_4)_3 OH$	0.95	0.38	1.37	9.335	6.664	9.3293	6.7003	0.061	0.545
9	$Cd_5 (PO_4)_3 Cl$	0.95	0.38	1.81	9.625	6.504	9.6019	6.6	0.240	1.476
10	$Sr_5 (PO_4)_3 Cl$	1.18	0.38	1.81	9.859	7.206	9.91	7.2671	0.517	0.848
11	$Sr_5 (CrO_4)_3 Cl$	1.18	0.55	1.81	10.125	7.328	10.144	7.3722	0.188	0.603
12	$Sr_5 (PO_4)_3 Br$	1.18	0.38	1.96	9.9641	7.207	9.9553	7.2315	0.088	0.340
13	$Sr_5 (PO_4)_3 OH$	1.18	0.38	1.37	9.745	7.265	9.7731	7.3304	0.288	0.900
14	$Sr_5 (PO_4)_3 F$	1.18	0.38	1.33	9.7174	7.2851	9.7597	7.3331	0.435	0.659
15	$Pb_5 (PO_4)_3 Cl$	1.19	0.38	1.81	9.993	7.334	9.9297	7.2928	0.633	0.562
16	$Pb_5 (AsO_4)_3 Cl$	1.19	0.46	1.81	10.24	7.43	10.226	7.3553	0.137	1.005
17	$Pb_5 (PO_4)_3 OH$	1.19	0.38	1.37	9.877	7.427	9.7969	7.3545	0.811	0.976
18	$Ba_5 (PO_4)_3 OH$	1.35	0.38	1.37	10.1904	7.721	10.175	7.707	0.151	0.181
19	$Ba_5 (PO_4)_3 F$	1.35	0.38	1.33	10.153	7.733	10.159	7.7079	0.059	0.325
20	$Ba_5 (PO_4)_3 Cl$	1.35	0.38	1.81	10.284	7.651	10.296	7.668	0.117	0.222
21	$Ba_5 (CrO_4)_3 OH$	1.35	0.55	1.37	10.428	7.89	10.423	7.8724	0.048	0.223
22	$Ca_{7.684} Sr_{2.316} (PO_4)_6 (OH)_2$	1.041688	0.38	1.37	9.4955	6.9718	9.4762	6.9692	0.203	0.037
23	$Ca_{3.616} Sr_{6.384} (PO_4)_6 (OH)_2$	1.114912	0.38	1.37	9.6313	7.1246	9.6244	7.1669	0.072	0.594
24	$Ca_{8.98} Sr_{1.02} (PO_4)_6 (OH)_2$	1.01836	0.38	1.37	9.4352	6.9087	9.4345	6.9031	0.007	0.081
25	$Ca_{4.03} Cd_{0.97} (PO_4)_3 (OH)$	0.9903	0.38	1.37	9.391	6.837	9.3881	6.8215	0.031	0.227
26	$Ca_{3.98} Cd_{1.02} (PO_4)_3 F$	0.9898	0.38	1.33	9.379	6.834	9.3647	6.8252	0.152	0.129
27	$Ca_{3.475} Cd_{1.525} (PO_4)_3 F$	0.98475	0.38	1.33	9.36	6.812	9.3566	6.8103	0.036	0.025
28	$Ca_5 (PO_4)_3 F_{0.41} Cl_{0.59}$	1	0.38	1.6132	9.5485	6.8237	9.5379	6.8072	0.111	0.242
29	$Sr_6 Ca_4 (PO_4)_6 F_2$	1.108	0.38	1.33	9.63	7.22	9.5936	7.1525	0.378	0.935
30	$Sr_{7.3} Ca_{2.7} (PO_4)_6 F_2$	1.1314	0.38	1.33	9.565	7.115	9.646	7.2127	0.847	1.373
31	$Ca_{9.37} Sr_{0.63} (PO_4)_6 F_2$	1.01134	0.38	1.33	9.3902	6.9011	9.4012	6.8878	0.117	0.193
32	$Ca_5 (PO_4)_3 F_{0.17} Cl_{0.83}$	1	0.38	1.7284	9.6205	6.7761	9.6012	6.7798	0.201	0.055
33	$Ca_5 (AsO_4)_3 F$	1	0.46	1.33	9.75	6.92	9.7251	6.9385	0.255	0.267
34	$Ca_5 (AsO_4)_3 OH$	1	0.46	1.37	9.7	6.93	9.7503	6.931	0.519	0.014
					Average percent errors of outputs				0.299	0.472

Table 3: Testing the dataset and percent errors for non-stoichiometric apatites
Tabela 3: Preizkus nabora podatkov in delež napake pri nestehiometričnih apatitih

	Apatite formula	Average radius M	Average radius T	Average radius X	$a/(10^{-1}$ nm)	$c/(10^{-1}$ nm)	a output	c output	Error (%) for (a)	Error (%) for (c)
1	$Ca_{9.75} Y_{0.25} (PO_4)_6 (OH)_{1.75} F_{0.25}$	0.9975	0.38	1.365	9.406	6.874	9.3969	6.8433	0.097	0.447
2	$Ca_{9.5} Y_{0.5} (PO_4)_6 (OH)_{1.75} F_{0.25}$	0.995	0.38	1.365	9.408	6.877	9.3928	6.836	0.162	0.596
3	$Ca_{9.25} Y_{0.75} (PO_4)_6 (OH)_{1.75} F_{0.25}$	0.9925	0.38	1.365	9.384	6.86	9.3888	6.8286	0.051	0.458
4	$Ca_{9.75} Al_{0.25} (PO_4)_6 (OH)_2$	0.9885	0.38	1.37	9.4248	6.8812	9.3853	6.8162	0.419	0.945
5	$Ca_{9.5} Al_{0.5} (PO_4)_6 (OH)_2$	0.977	0.38	1.37	9.4252	6.892	9.3677	6.782	0.610	1.596
6	$Ca_{9.25} Al_{0.75} (PO_4)_6 (OH)_2$	0.9655	0.38	1.37	9.4218	6.8807	9.3509	6.7475	0.753	1.936
7	$Ca_{9.5} Mg_{0.82} (PO_4)_6 (OH)_2$	0.9778	0.38	1.37	8.8133	6.8215	9.3688	6.7843	6.303	0.545
8	$Ca_{9.5} Zn_{0.31} (PO_4)_6 (OH)_2$	0.9918	0.38	1.37	8.8972	6.8427	9.3905	6.8259	5.544	0.246
9	$Ca_{9.5} La_{0.14} (PO_4)_6 (OH)_2$	1.0004	0.38	1.37	9.3135	6.8346	9.4044	6.8512	0.976	0.243
10	$Ca_{9.5} Y_{0.23} (PO_4)_6 (OH)_2$	0.9976	0.38	1.37	8.9013	6.8548	9.3998	6.843	5.600	0.172
11	$Ca_{9.5} In_{0.17} (PO_4)_6 (OH)_2$	0.9965	0.38	1.37	8.832	6.8101	9.398	6.8397	6.409	0.435
12	$Ca_{9.5} Bi_{0.10} (PO_4)_6 (OH)_2$	1.0003	0.38	1.37	9.3442	6.8457	9.4042	6.8509	0.642	0.076
13	$Ca_{9.7} Y_{0.2} (PO_4)_6 (OH)_2$	0.9980	0.38	1.37	9.4072	6.877	9.4004	6.844	0.072	0.480
14	$Ca_{9.55} Y_{0.3} (PO_4)_6 (OH)_2$	0.9970	0.38	1.37	9.377	6.859	9.3987	6.841	0.231	0.262
15	$Ca_{9.4} Y_{0.4} (PO_4)_6 (OH)_2$	0.9959	0.38	1.37	9.399	6.8734	9.3971	6.838	0.020	0.515

16	$Ca_{9.25} Y_{0.5} (PO_4)_6 (OH)_2$	0.9949	0.38	1.37	9.388	6.8662	9.3954	6.8349	0.079	0.456
17	$Ca_{9.1} Y_{0.6} (PO_4)_6 (OH)_2$	0.9938	0.38	1.37	9.3496	6.8544	9.3937	6.8318	0.472	0.330
18	$Ca_{8.55} Y_{0.7} (PO_4)_6 (OH)_2$	0.9924	0.38	1.37	9.3384	6.8448	9.3915	6.8278	0.569	0.248
19	$Ca_{9.95}(PO_4)_{5.71}(CO_3)_{0.20} (OH)_2$	1	0.373	1.37	9.410	6.879	9.3535	6.8418	0.600	0.541
20	$Ca_{9.46}(PO_4)_5(CO_3)_{1.00} (OH)_{1.78}$	1	0.343	1.37	9.394	6.894	9.1013	6.8047	3.116	1.295
21	$Ca_{9.88}(PO_4)_{5.76}(CO_3)_{0.24}F_{1.49}(OH)_{0.51}$	1	0.3712	1.3402	9.382	6.891	9.3241	6.8432	0.617	0.694
22	$Ca_{9.34}(PO_4)_{4.79}(SO_4)_{1.04}(CO_3)_{0.16}(OH)_{1.78}$	1	0.3724	1.37	9.427	6.879	9.3491	6.8411	0.8264	0.5510
23	$La_{8.65}Sr_{1.35}(SiO_4)_6O_{2.32}$	1.0503	0.40	1.40	9.7100	7.2254	9.6257	7.012	0.8682	2.9535
24	$La_{8.65}Sr_{1.35}(GeO_4)_6O_{2.32}$	1.0503	0.53	1.40	9.9120	7.3236	9.8341	7.1225	0.7859	2.7459
25	$La_9Sr_1(SiO_4)_{5.5}(AlO_4)_{0.5}O_{2.25}$	1.045	0.4117	1.40	9.7111	7.2290	9.6746	7.0095	0.3759	3.0364
26	$La_{9.5}(SiO_4)_{5.5}(AlO_4)_{0.5}O_2$	1.03	0.4117	1.40	9.7260	7.2002	9.6509	6.967	0.7722	3.2388
27	$La_{9.33}(SiO_4)_6O_2$	1.03	0.40	1.40	9.721	7.187	9.5919	6.9546	1.3281	3.2336
28	$La_{9.33}(SiO_4)_2(GeO_4)_4O_2$	1.03	0.4867	1.40	9.870	7.257	9.8336	7.0343	0.3688	3.0688
29	$La_{9.33}(SiO_4)(GeO_4)_5O_2$	1.03	0.5083	1.40	9.902	7.276	9.8325	7.05	0.7019	3.1061
30	$La_{9.33}(GeO_4)_6O_2$	1.03	0.53	1.40	9.912	7.283	9.8124	7.064	1.0048	3.0070

Table 4: Percent errors for the calculated volumes
Tabela 4: Delež napake pri izračunanih prostorninah

	Apatite formula	V (unit cell)	V (predicted)	Error (%) volume
1	$Ca_{9.75} Y_{0.25} (PO_4)_6 (OH)_{1.75} F_{0.25}$	1574.5	1564.5	0.639
2	$Ca_{9.5} Y_{0.5} (PO_4)_6 (OH)_{1.75} F_{0.25}$	1575.9	1561.4	0.917
3	$Ca_{9.25} Y_{0.75} (PO_4)_6 (OH)_{1.75} F_{0.25}$	1564.0	1558.4	0.356
4	$Ca_{9.75} Al_{0.25} (PO_4)_6 (OH)_2$	1582.5	1554.4	1.773
5	$Ca_{9.5} Al_{0.5} (PO_4)_6 (OH)_2$	1585.1	1540.8	2.793
6	$Ca_{9.25} Al_{0.75} (PO_4)_6 (OH)_2$	1581.4	1527.5	3.406
7	$Ca_{9.5} Mg_{0.82} (PO_4)_6 (OH)_2$	1371.8	1541.7	12.387
8	$Ca_{9.5} Zn_{0.31} (PO_4)_6 (OH)_2$	1402.4	1558.4	11.123
9	$Ca_{9.5} La_{0.14} (PO_4)_6 (OH)_2$	1534.9	1568.8	2.209
10	$Ca_{9.5} Y_{0.23} (PO_4)_6 (OH)_2$	1406.2	1565.4	11.322
11	$Ca_{9.5} In_{0.17} (PO_4)_6 (OH)_2$	1375.3	1564.0	13.720
12	$Ca_{9.5} Bi_{0.10} (PO_4)_6 (OH)_2$	1547.5	1568.6	1.365
13	$Ca_{9.7} Y_{0.2} (PO_4)_6 (OH)_2$	1575.6	1565.8	0.624
14	$Ca_{9.55} Y_{0.3} (PO_4)_6 (OH)_2$	1561.4	1564.5	0.200
15	$Ca_{9.4} Y_{0.4} (PO_4)_6 (OH)_2$	1572.1	1563.3	0.555
16	$Ca_{9.25} Y_{0.5} (PO_4)_6 (OH)_2$	1566.7	1562.0	0.299
17	$Ca_{9.1} Y_{0.6} (PO_4)_6 (OH)_2$	1551.3	1560.8	0.613
18	$Ca_{8.55} Y_{0.7} (PO_4)_6 (OH)_2$	1545.4	1559.1	0.889
19	$Ca_{9.95}(PO_4)_{5.71}(CO_3)_{0.20} (OH)_2$	1577.0	1549.7	1.731
20	$Ca_{9.46}(PO_4)_5(CO_3)_{1.00} (OH)_{1.78}$	1575.1	1459.3	7.352
21	$Ca_{9.88}(PO_4)_{5.76}(CO_3)_{0.24}F_{1.49}(OH)_{0.51}$	1570.4	1540.3	1.917
22	$Ca_{9.34}(PO_4)_{4.79}(SO_4)_{1.04}(CO_3)_{0.16} (OH)_{1.78}$	1582.7	1548.1	2.188
23	$La_{8.65}Sr_{1.35}(SiO_4)_6O_{2.32}$	1763.7	1682.1	4.63
24	$La_{8.65}Sr_{1.35}(GeO_4)_6O_{2.32}$	1862.9	1783.3	4.269
25	$La_9Sr_1(SiO_4)_{5.5}(AlO_4)_{0.5}O_{2.25}$	1765.0	1698.6	3.764
26	$La_{9.5}(SiO_4)_{5.5}(AlO_4)_{0.5}O_2$	1763.4	1680.0	4.727
27	$La_{9.33}(SiO_4)_6O_2$	1758.3	1656.6	5.787
28	$La_{9.33}(SiO_4)_2(GeO_4)_4O_2$	1830.3	1761.1	3.782
29	$La_{9.33}(SiO_4)(GeO_4)_5O_2$	1847.0	1764.6	4.461
30	$La_{9.33}(GeO_4)_6O_2$	1852.5	1760.9	4.947

the best results with the BR method. Four processing elements and the tansig activation function were used in the hidden layer, while the purelin function was used in the output layer.

A training dataset constructed from thirty-four data entries was used for the prediction of non-stoichiometric apatites. This dataset was trained using the BR method with four neurons in the hidden layer. The tansig activation function was used in the hidden layer, while the purelin function was used for the output layer. The training dataset can be seen in **Table 2**. The coefficient of determination, R^2, was 0.981 for both lattice parameters as seen in **Figures 1** and **2**. In both figures the vertical axis (A) represents the predicted value, while the horizontal axis (T) represents the experimental value. In addition, the average error percentage was 0.299 % and 0.472 % for the lattice parameters a and c, respectively. The results indicate that that training was precise.

After the training of the model, a test dataset constructed from non-stoichiometric apatites was used to predict their lattice parameters. The results of the predictions can be seen in **Table 3**. The data in the first six lines from **Table 3** were not charge balanced and approximate formulas for the apatites were used for the prediction. The errors for the lattice parameters were less than 1 % for *a* and 2 % for *c*. The data in lines seven to eighteen from **Table 3**[27] contained an error of about 5 % due to the measurement errors. The predicted lattice parameters from the approximate formulas of these apatites confirmed the error in the measurements. Four of the generated results had an error of about 5 % for lattice parameter a, but the rest of the predictions were completed with an error of less than 1 % for both lattice parameters.

The data after line nineteen from **Table 3** included virtually exact formulas taken from the literature. The error margins given in these studies for certain apatite formulas were not taken into account to get the results of exact formulas. These apatites produced less accurate results compared to the previous data in the same dataset. The errors for lattice parameter *a* were generally less than or around 1 % with a maximum of 3.116 %. However, the errors for lattice parameter *c* were varying around 3 % which was significantly higher compared to lattice parameter *a*. This was probably due to the complex T sites associated with these apatites. Some of the ions at the T site used for testing the network were not included in the dataset of the training network due to the insufficient experimental data and this resulted in decreased prediction accuracy. Even under these circumstances, the errors for both lattice parameters did not get significantly higher than 3 %.

The volume calculations for the apatites given in **Table 3** are given in **Table 4**. The apatite volumes were calculated successfully except for four cases with an error of about 5 % for lattice parameter a. In addition, the results for the apatites after the nineteenth data entry in **Table 4** were varying significantly, so reliable volume calculations for the apatites with the complex T sites were not possible. These results show that if a training dataset could be improved with the apatites involving different arrangements at the T sites, even the lattice parameters of highly non-stoichiometric apatites could be predicted with high accuracies.

The predictions can be reproduced using equations 2 and 3 for lattice parameters *a* and *c*, respectively. These equations were derived using the final weights and activation functions of the network trained with the BR method:

$$a = -3.5488 \cdot F_1 + 2.0679 \cdot F_2 + 2.1481 \cdot F_3 - 4.6425 \cdot F_4 + 3.6454 \tag{2}$$

$$c = -1.8272 \cdot F_1 + 1.8272 \cdot F_2 + 2.1636 \cdot F_3 - 1.9986 \cdot F_4 + 1.7878 \tag{3}$$

$$F_1 = \frac{2}{1 + exp(-2 \cdot E_1)} \tag{4}$$

The F_i values in these equations are the activation functions of each neuron in the hidden layer, calculated with equation 4. E_i is the weighted sum and its value for the corresponding F_i can be calculated using the equations and final weights given in **Tables 5** and **6** for lattice parameters *a* and *c*, respectively. In **Tables 5** and **6**, C_1, C_2, and C_3 are the final weights of the network corresponding to the average ionic radii R_A, R_B, and R_C, respectively. C_4 is the bias for each processing element.

Table 5: Weights between the input and hidden layer for lattice parameter *a*
Tabela 5: Uteži med vnosom in skritimi plastmi za mrežni parameter *a*

i	$E_i = C_1 \times R_M + C_2 \times R_T + C_3 \times R_X + C_4$			
	C_1	C_2	C_3	C_4
1	−0.29121	−0.37429	−0.93008	−0.68189
2	2.1243	−0.84122	−0.72689	−1.3309
3	−1.0465	−2.5549	0.6731	1.4169
4	−0.075195	−4.125	−0.091451	1.1377

Table 6: Weights between the input and hidden layer for lattice parameter *c*
Tabela 6: Uteži med vnosom in skritimi plastmi za mrežni parameter *c*

i	$E_i = C_1 \times R_M + C_2 \times R_T + C_3 \times R_X + C_4$			
	C_1	C_2	C_3	C_4
1	−0.52211	−0.49087	−0.25122	0.054422
2	0.52211	0.49087	0.25122	−0.054422
3	1.0851	−0.95392	−0.34973	0.51105
4	−0.45506	−1.021	0.044623	0.29596

4 CONCLUSIONS

In this research, hexagonal lattice parameters and unit cell volumes of non-stoichiometric apatites of $M_{10}(TO_4)_6X_2$ were predicted from their ionic radii by an ANN. The results reveal that the lattice-parameter errors for the results of the apatites by the ANN were less than 1 % for *a* and 2 % for *c*, respectively. However, the non-stoichiometric apatites with virtually exact formulas generated the errors of up to around 3 % for both lattice parameters because of their complex T sites. These results indicate that the hexagonal lattice-parameter prediction of the non-stoichiometric apatites with both approximate and exact formulas were reliable, provided that their T sites do not contain large quantities of ions except for the ones used for the training dataset. It is suggested that the accuracy of the predictions could be improved if the training dataset could be modified with the apatites containing different elements at the T sites to overcome the complexity, so that a wider range of possibilities could be investigated for demanding applications where strict lattice parameters are needed for the apatites with the desired elements.

5 REFERENCES

[1] M. Kohn, J. Rakovan, J. M. Hughes, Phosphates: Geochemical, Geobiological and Materials Importance, Mineralogical Society of America, 2002

[2] B. Wopenka, J. D. Pasteris, Mater Sci Eng C, 25 (**2005**), 131–43

[3] S. Peroos, Z. Du, N. H. de Leeuw, Biomater, 27 (**2006**), 2150–61

[4] M. I. Dominguez, J. Carpena, D. Borschnek, M. A. Centeno, J. A. Odriozola, J. Rose, Journal of Hazard Mater, 150 (**2008**), 99–108

[5] J. C. Goes, S. D. Figueiro, A. M. Oliviera, A. A. M. Macedo, C. C. Silva, N. M. P. S. Ricardo, A. S. B. Sombra, Acta Biomater, 3 (**2007**), 773–8

[6] E. Pecheva, T. Petrov, C. Lungu, P. Montgomery, L. Pramatarova, Chem Eng J, 137 (**2008**), 144–53

[7] S. Zhang, Y. S. Wang, X. T. Zeng, K. Cheng, M. Qian, D. E. Sun, W. J. Weng, W. Y. Chia, Eng Fract Mech, 74 (**2007**), 1884–93

[8] J. C. Elliott, Structure and Chemistry of the Apatites and Other Calcium Orthophosphates, Elsevier, 1994

[9] P. Wu, Y. Z. Zeng, C. M. Wang, Biomater, 25 (**2004**), 1123–30

[10] S. Malinov, W. Sha, Comp Material Science, 28 (**2003**), 179–98

[11] A. Bezazi, S. G. Pierce, K. Worden, E. H. Harkati, Int J Fatigue, 29 (**2007**), 738–47

[12] R. P. Cherian, L. N. Smith, P. S. Midha, Artif Intell Eng, 14 (**2000**), 39–44

[13] M. Col, H. M. Ertunc, M. Yilmaz, Mater & Des, 28 (**2007**), 488–95

[14] C. Karatas, A. Sozen, S. Erguney, Expert Syst Appl, 36 (**2009**), 3514–21

[15] H. K. D. H. Bhadeshia, ISIJ Int, 39 (**1999**), 966–79

[16] U. Kockan, Z. Evis, J Appl Crystal, 43 (**2010**), 769–79

[17] Z. Zhang, K. Friedrich, Comp Sci Tech, 63 (**2003**), 2029–44

[18] P. A. Lucon, R. P. Donovan, Composites Part B, 38 (**2007**), 817–23

[19] H. Demuth, M. Beale, M. Hagan, Matlab Neural Network Toolbox 6, Users Guide, The Mathworks Inc., 2008

[20] S. Samarasinghe, Neural Networks for Applied Sciences and Engineering, Taylor&Francis, 2007

[21] S. I. Gallant, Neural Network Learning and Expert Systems, The MIT Press, 1993

[22] K. Boughzala, E. B. Salem, A. B. Chrifa, E. Gaudin, K. Bouzouita, Mater Res Bull, 42 (**2007**), 1221–9

[23] B. Hamdi, H. E. Feki, J. Savariault, A. B. Salah, Mater Res Bull, 42 (**2007**), 299–311

[24] http://webmineral.com/data/Svabite.shtml.

[25] http://webmineral.com/data/Johnbaumite.shtml.

[26] D. R. Lide, Handbook of Chemistry and Physics, Taylor&Francis, 2003

[27] T. J. Webster, E. A. Massa-Schlueter, J. L. Smith, E. B. Slamovich, Biomater, 25 (**2004**), 2111–21

[28] B. Basar, Z. Evis, Mater Sci Tech, 25 (**2009**), 794–8

[29] Z. Evis, J Ceram Soc Japan, 114 (**2006**), 1001–4

[30] M. Veiderma, K. Tonsuaadu, R. Knubovets, M. Peld, J Organometal Chem, 690 (**2005**), 2638–43

[31] L. Leon-Reina, J. M. Porras - Vazquez, E. R. Losilla, M. A. G. Aranda, Solid State Ionics, 177 (**2006**), 1307–15

[32] J. E. H. Sansom, A. Najib, P. R. Slater, Solid State Ionics, 175 (**2004**), 353–5

[33] Z. Evis, Ceram Inter, 33 (**2007**), 987–91

DETERMINATION OF THE NOTCH FACTOR FOR SHAFTS UNDER TORSIONAL STRESS WITH ARTIFICIAL NEURAL NETWORKS

UPORABA UMETNIH NEVRONSKIH MREŽ ZA DOLOČANJE FAKTORJA ZAREZNEGA UČINKA NA GREDEH, OBREMENJENIH S TORZIJSKIMI NAPETOSTMI

Murat Tolga Ozkan[1], Cengiz Eldem[1], İsmail Sahin[1]

[1]Gazi University, Faculty of Technology, Department of Industrial Design Engineering, 06500 Ankara, Turkey
tozkan@gazi.edu.tr, mtozkan06@yahoo.com

When designing machine equipment, geometrical figures or discontinuities such as notches, holes, steps and curves can occur. Sudden cross-section changes, discontinuities and force flows cause concentrations, particularly in the stress area. Stress concentrations may be formed due to dimensional features of a material or directions of applied forces. Such stress concentrations are considered as they have a notch effect on the material. The notch effect may lead to a breaking and distortion of a material. In this study, a mathematical model estimating the notch-factor values for a grooved round bar in torsion, a round shaft with a transverse hole in torsion and a round shaft with a shoulder fillet in torsion, using artificial neural networks (ANN) is introduced. The model estimates the notch factor using shaft dimensions, torque and corner rounding values. The ANN model developed in the study quickly and accurately estimates the notch-factor values, otherwise obtained from the catalogues with complicated analytical calculations. In this model, the uncertainties occurring in analytical calculations and the calculation errors were eliminated, thus long calculation times were saved as well. The results reviewing the performance of the ANN model developed for a grooved round bar in torsion, a round shaft with a transverse hole in torsion and a round shaft with a shoulder fillet in torsion were quite good. In the study, a multiple regression analysis of the data was also performed, but no conclusion evaluating the data was obtained.

Keywords: shafts, notch-sensitivity factor, torsion, artificial neural network, statistical analysis

Pri konstruiranju strojnih delov se pojavljajo nezvezne geometrijske oblike, kot so zareze, luknje, stopnice in krivine. Nenadna sprememba prereza, nezveznosti in potek sil povzročajo koncentracijo napetosti v napetostnem območju. Koncentracije napetosti v materialu lahko nastanejo zaradi dimenzijskih sprememb ali sprememb smeri delovanja sil. Taka koncentracija napetosti se obravnava kot zarezni učinek v materialu. Zarezni učinek lahko povzroči porušitev ali izkrivljenje materiala. V tej študiji je predstavljen matematični model umetne nevronske mreže (ANN), ki lahko obravnava faktor zareznega učinka okrogle palice z utorom, okrogle gredi s prečno odprtino, obremenjeno s torzijo, in okrogle gredi z zaokroženim prehodom. Model določa faktor zareznega učinka z uporabo dimenzij, navora in radija zaokrožitev. Razvit ANN-model omogoča hitrejše in bolj zanesljivo določanje faktorja zareznega učinka, ki ga sicer dobimo iz katalogov z zapletenimi analitičnimi preračunavanji. V tem modelu so odpravljene nezanesljivosti, ki se pojavljajo pri analitskem preračunavanju, odpravljene so računske napake in prihranjeno nam je dolgotrajno preračunavanje. Pregledane so bile zmogljivosti ANN-modela, razvitega za torzijo okrogle palice z utorom, torzijo okrogle gredi s prečno odprtino in okrogle gredi z zaobljenim prehodom. V študiji je bila izvedena tudi multipla regresijska analiza podatkov, vendar ni bilo mogoče izluščiti ugotovitve, ki bi prispevala k oceni podatkov.

Ključne besede: gred, faktor zareznega učinka, torzija, umetna nevronska mreža, statistična analiza

1 INTRODUCTION

Breaks and deformations are observed on almost all machine parts used for a power and force transmission. In order not to have these undesired effects, the notch factor is considered in the calculations. Thus, a formation of such effects is minimized or eliminated. Theoretical notch factors used in the calculations according to the change in the calculations or type of strain affecting the shafts vary. For each different type of strain, there are many table values available, but it is an inconvenient procedure to obtain the values required for the design from such tables.

Mechanical damages formed as a result of fatigue have been a subject of engineering studies for many years. One of the first studies on this subject was made by W. A. J. Albert who tested metal chains lifted up under cyclic loadings in Germany in 1828. The term "fatigue" was first used in 1839 by J. V. Poncelet.[1]

During the studies he made in 1850s in Germany, August Wöhler started to develop design strategies in order to avoid fatigue damage, testing iron, steel and other metals under torsion, bending and axial loadings. With his studies, Wöhler proved that fatigue was affected by the average stress as well as by cyclic stresses.[2]

McClintock made the first theoretical research related to the ductile damage, taking place as void growth.[3] In this research, it was concluded that the rate of void growth definitely depends on three axial stress regions as well as on the rate of hydrostatic equivalent stress. As a result of his experiments, McClintock concluded that

different samples do not always have the same unit deformation in crack formation.

The study made by Rice and Tracey took McClintock's study to a higher level. With this study, it was concluded that the rate of void growth definitely depends on three axial stress regions as well as on the rate of hydrostatic equivalent stress.[4]

With their experimental study, Hancock and Mackenzie supported the idea that the orientability of ductility for construction materials could be three-axial, and revealed that the material damage had been caused by high-degree hydrostatic pressure.[5]

By using the results of their experimental study, Bridgman, Hancock and Mackenzie revealed damage-unit-deformation and representation parameters of triaxiality in a closed damage curve.[6] Hancock and Brown examined stress-unit deformation spaces on a notched sample.[7] In the study, damage was reviewed at the centre point of the minimum cross-section where triaxiality is the highest on a cylindrical notched sample.

Ozkan made a study about the notch-sensitivity determination of shafts. He used an ANN model.[8] Ozkan et al. made a study about determining the notch factor on the shafts under tensile stress. They also used an ANN model.[9]

Recorded literature studies have revealed that notched tensile tests are commonly applied experiments. They show that notched tensile experiments include a large number of notch types. Therefore, it is obvious that modelling the data obtained from standard-experiment results and notched tensile experiments will provide an increase in the number of variables in experimental studies.

The notch-factor selection and the calculations made afterwards require long and inconvenient procedures and, consequently, a significant amount of time and labour. It is necessary to utilise computer programs to solve such problems.

The aim of this study was to develop a mathematical model that can provide for the best notch factors on a grooved round bar in torsion, a round shaft with a transverse hole in torsion and a round shaft with a shoulder fillet in torsion by considering the formal characteristics of the material affecting the notch factor and the torsional-stress effect influencing the shaft. The mathematical model was developed using a multilayer feedforward

Figure 1: Artificial neural network
Slika 1: Umetna nevronska mreža

artificial neural network (MLP). In the study, a multiple regression analysis of the data was made. Multiple-regression and ANOVA analyses were also made, but since their results did not help us interpret the data, the study was focused on ANN. The artificial-neural-network model developed within the study consisted of three inputs for the round shaft with a shoulder fillet in torsion and the grooved round bar in torsion, two inputs for the round shaft with a transverse hole in torsion, one hidden layer and one output.

2 ARTIFICIAL NEURAL NETWORKS

The concept of artificial neural networks first appeared as the idea of simulating the principle operation of the brain on digital computers. An artificial neural network is a mathematical model inspired by the functional structure of a biological neural network.[10] Artificial neural networks consist of many operation elements connected to each other. Operation elements in artificial neural networks (nodes) function like simple nerves. An artificial neural network consists of many nodes connected to each other. The main unit of an artificial neural network is an artificial nerve. An artificial nerve is much simpler than a biological nerve. In **Figure 1**, an artificial neural element is shown. All the artificial neural networks are derived from this main structure. Differences in this structure allow different classifications of artificial neural networks.

An ANN model consists of two main steps: the training and the test. The meaning of learning in artificial neural networks is to allow a neural network to produce correct outputs by establishing the right connections between the input and the output data relating to the problem. This procedure continues until the difference between the estimated output and the desired output decreases to a certain value. Artificial neural networks learn with experience just like humans. For that purpose, an experimental group is divided into two parts: the training group and the test group. During the training period, the network uses an inductive training model to train the training group.[11] The training process continues in the network until the desired output value is obtained.[12] When certain amounts of the input are entered in the network during learning, the network makes changes to itself to be able to give similar responses. Here, the error in question is the difference between the estimated output and the generated output. After training, the network is tested to find whether ANN has actually learned, instead of just memorizing, the data. In the test section, the data not used during the training is used.

The performance of a developed ANN model is determined using different error-analysis methods. In general, such methods can be ranked as the absolute fraction of variance (R^2), the root-mean-square error (RMSE) and the mean absolute-percentage error
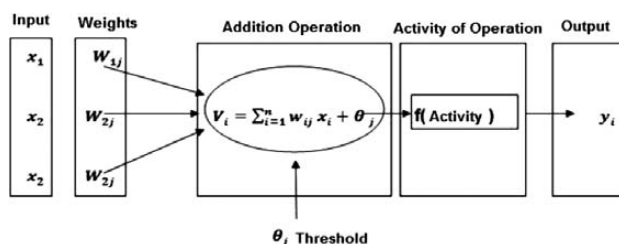
(MAPE). The best performance of an ANN model is at the highest value of R^2 and at the lowest values of RMSE and MAPE.[13] Such parameters are defined with the following equations:

$$R^2 = 1 - \left[\frac{\sum (MR_{exp,1} - MR_{ANN,i})^2}{\sum (MR_{ANN})^2} \right] \qquad (1)$$

$$RMSE = \sqrt{\frac{1}{N} \sum_{i=1}^{N} (MR_{ANN,i} - MR_{exp,1})^2} \qquad (2)$$

$$MAPE = \frac{MR_{ANN} - MR_{exp}}{MR_{ANN}} \cdot 100 \qquad (3)$$

3 STRENGTH-REDUCTION FACTORS

Resistance diagrams are obtained using standard-experiment test-bar surfaces that have been polished. Dimensional and surface features of the actual machine elements are different from the test bars. Therefore, the values taken from a permanent-resistance diagram cannot be used without considering the resistance-reduction factors.[14] The resistance limits of materials are affected by the factors such as notch, surface roughness, dimension, manufacture method, heat treatment, environmental effect, etc.[15]

In some cases, the results obtained for machine elements with experiments show the existence of the stresses much bigger than the normal stresses. The reason for that is the geometrical difference between the parts. The notch is the generally defined dimensional difference.[16]

In design of machine elements, geometric figure differences or discontinuities such as notches, holes, steps or various groove roundings and keyways can occur for certain reasons. Sudden section changes and discontinuities cause concentrations in the force flow, particularly in the stress area. Such stress concentrations cause a notch effect on the material.[17]

3.1 Stress-concentration factor (K_t) and notch-sensitivity factor (q)

The stress-concentration factor (K_t) is defined as the ratio of the biggest stress generated at bottom of the notch to the nominal stress:[18,19]

$$K_t = \frac{\tau_{max}}{\tau_n} \qquad (4)$$

In the calculation of torsional stress, the relations in equations 5 and 6 are used:

$$\tau_n = \frac{M}{W_p} \qquad (5)$$

$$\tau_n = K_t \frac{M}{W_p} \qquad (6)$$

In the machine elements, the stress that is times the calculated nominal stress is generated at the bottoms of geometric figures. If the material is brittle, the notched material is broken due to the static stress that is times lower than the nominal stress. For example, if there is a notch with a concentration factor $K_t = 3$ on a machine element made of hardened steel, such an element is three times more fragile than the unnotched one:[17–19]

$$K_c = 1 + q(K_t - 1) \qquad (7)$$
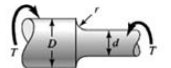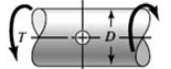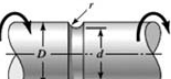
The stress-concentration factor (K_t) is a value depending on geometry. The fatigue-strength-reduction factor indicating an active reduction in the material strength is K_c. The notch factor depends on the geometrical shape of the notch and the sensitivity of the material to the notch. If the effect of the notch's geometrical shape is represented with the theoretical notch factor K_t, and the sensitivity of the material to the notch is represented with the notch-sensitivity factor q, the notch factor is calculated using the relation given in equation 7.

4 RESULTS AND DISCUSSION

The data in this study was obtained by examining the graphics relating to the notch factor from Peterson's book "Design Factors for Stress Concentration".[20,21] The

Table 1: Numbers of trainings and tests for the shafts under torsional stress
Tabela 1: Število usposabljanj in podatki za gred, izpostavljeni torzijski obremenitvi

Notch-factor values for the shafts under torsional stress			Training Data	Test Data	Total Data
Round shaft with a shoulder fillet in torsion		Torsion	590	100	690
Round shaft with a transverse hole in torsion		Torsion	130	30	160
Grooved round bar in torsion		Torsion	450	110	560

graphics were transformed to digital values, obtaining the data for the ANN learning and testing. In the notch charts, there are three basic figures for the shafts under the torsional-stress effect. These are a round shaft with a shoulder fillet in torsion, a round shaft with a transverse hole in torsion and a grooved round bar in torsion. In **Table 1**, there are the numbers of trainings and tests used for determining the notch factors for the three basic figures.

In **Table 1**, the classification and the numbers for the shafts under the torsional-stress effect are presented. The input data used in ANN includes the maximum shaft diameter (D), the minimum shaft diameter (d) and the chamfer radius (r), while the output data is the notch factor (**Table 2**).

Table 2: Input and output values for the notch factor of the shafts
Tabela 2: Vhodne in dobljene vrednosti za faktor zareze gredi

Determination input/output parameters for the shafts under torsional stress		
Symbol	Name	Input/output
D	Maximum diameter of the shaft	Input
d	Minimum diameter of the shaft	Input
r	Chamfer radius	Input
K_t	Stress-concentration factor	Output

As ANN has been generated, not all the experiment data is used in the training. After the ANN system has

been established and the training procedure finished, 10 % of the experiment data is hidden from the system to check whether ANN has given correct results. In the scope of the study, 690 pieces of data for the round shaft with a shoulder fillet in torsion, 160 for the round shaft with a transverse hole in torsion and 560 for the grooved round bar in torsion have been obtained with theoretical calculations (**Table 3**). Out of such data, 590 pieces for the round shaft with a shoulder fillet in torsion, 130 for the round shaft with a transverse hole in torsion and 450 pieces for the grooved round bar in torsion were used for the training purposes. The other data was saved for the test purposes. The test data is used to find the error rate of the ANN system estimations.

In the study, a feedforward, multiple-layer neural-learning mechanism was used as the learning mechanism. For the learning model, the Levenberg-Marquardt algorithm (LMA) was used. During the determination of the learning criteria in ANN, different network structures were tried and the network structure with the minimum error and maximum learning rate was selected. According to that, the best learning for the round shaft with a shoulder fillet in torsion took place within a 3-4-1 network structure, for the grooved round bar in torsion within a 3-3-1 structure and for the round shaft with a transverse hole in torsion it took place within a 2-3-1 network structure (**Figure 2**). In this study, a single output layer and a single hidden layer were selected for

Table 3: Input and output samples used in the ANN model
Tabela 3: Vhodni in izhodni vzorci, uporabljeni v ANN-modelu

Round shaft with a shoulder fillet in torsion				Grooved round bar in torsion				Round shaft with a transverse hole in torsion		
D	d	r	K_t	D	d	r	K_t	D	d	K_t
2	2.04	0.024	2.29	1	1.02	0.025	2.082	2	153.846	3.643
3	3.06	0.051	2.12	2	2.04	0.068	1.928	3	120.000	3.430
4	4.08	0.084	2	3	3.06	0.12	1.835	4	117.647	3.300
5	5.1	0.125	1.926	4	4.08	0.2	1.767	5	100.000	3.160
13	13.26	1.95	1.33	11	11.22	1.375	1.464	6	96.774	3.080
14	14.28	2.45	1.297	12	12.24	1.644	1.44	7	93.333	3.000
15	15.3	3	1.264	13	13.26	1.95	1.414	8	80.000	2.910
16	16.32	3.6	1.242	14	14.28	2.45	1.386	9	72.000	2.840
35	36.75	8.75	1.286	15	15.3	3	1.36	12	60.000	2.708
36	37.8	9.9	1.264	16	16.32	3.6	1.325	13	57.778	2.680
37	38.85	11.1	1.242	17	17.34	4.25	1.3	14	56.000	2.650
38	41.8	0.456	2.7	18	18.36	4.95	1.276	15	54.545	2.640
39	42.9	0.663	2.5	35	36.75	7.875	1.425	16	53.333	2.630
62	93	3.844	1.925	36	37.8	9	1.4			
63	94.5	4.725	1.8	37	38.85	10.175	1.364			
64	96	5.568	1.728	38	39.9	11.4	1.338			
65	97.5	6.5	1.66	45	67.5	3.375	2.144			
66	99	8.25	1.584	46	69	3.956	2.04			
67	100.5	10.05	1.51	47	70.5	4.7	1.94			
87	261	17.4	1.457	48	72	5.376	1.872			
88	264	19.8	1.41	53	79.5	10.6	1.574			
89	267	22.25	1.374	54	81	12.15	1.53			
90	270	24.75	1.34	55	82.5	13.75	1.486			
91	273	27.3	1.32	56	84	15.4	1.44			
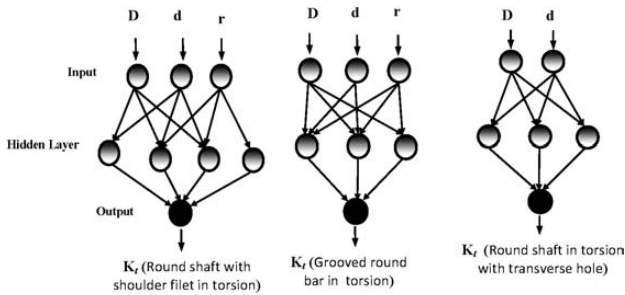
Figure 2: Suitable network structures for the notch factors of the shafts for: a) round shaft with a shoulder fillet in torsion, b) grooved round bar in torsion, c) round shaft with a transverse hole in torsion
Slika 2: Primerne strukture mreže za faktor zareznega učinka na gredi pri torziji: a) okrogla gred z zaokroženim prehodom, b) okrogla palica z utorom, c) okrogla gred s prečno odprtino

each type of the shafts. As a result of the experimental-data training, it was observed that optimum outputs were the models having eight neurons for the round shaft with a shoulder fillet in torsion, seven neurons for the grooved round bar in torsion and six for the round shaft with a transverse hole in torsion. For all of these experimental-data trainings, determination of the network structure and its optimization, the Pythia software was used.

In the software, for each different notch situation (the grooved round bar in torsion, the round shaft with a transverse hole in torsion and the round shaft with a shoulder fillet), the ANN model with the highest performance was determined. For this purpose, different variations were tried to determine the notch factor of the shafts under the torsional effect, and the model with the highest performance was selected as the ANN model (**Table 4**).

In order to test the network structure of ANN, a normalization of the inputs was implemented at first. The normalization of the inputs and outputs was made within the ranges of (–1, +1) or (0, –1). The normalization of the input (x_{nor}) is made with equation 8:

$$x_{nor} = \frac{(x_r - x_{min})}{(x_{max} - x_{min})} \qquad (8)$$

Table 4: Determination of the appropriate network design
Tabela 4: Določanje oblikovanja primerne mreže

Round shaft with a shoulder fillet in torsion	Grooved round bar in torsion	Round shaft with a transverse hole in torsion
MLP 3-15-1	MLP 3-22-1	MLP 2-3-1
MLP 3-13-1	MLP 3-19-1	MLP 2-11-1
MLP 3-23-1	MLP 3-30-1	RBF 2-9-1
MLP 3-13-1	MLP 3-5-1	MLP 2-7-1
MLP 3-20-1	MLP 3-8-1	MLP 2-7-1
RBF 3-24-1	MLP 3-32-1	RBF 2-2-1
MLP 3-30-1	RBF 3-7-1	MLP 2-5-1
MLP 3-30-1	RBF 3-18-1	MLP 2-8-1
MLP 3-20-1	RBF 3-15-1	MLP 2-4-1
MLP 3-21-1	RBF 3-22-1	RBF 2-10-1
MLP 3-47-1	RBF 3-30-1	RBF 2-5-1

Here, x_r represents the actual input value, x_{min} is the minimum input value and x_{max} is the maximum input value. The values used for the normalization are given in **Table 5**.

Table 5: Values used for normalization
Tabela 5: Vrednosti, uporabljene za normalizacijo

Shafts under torsion	Parameters	x_{max}	x_{min}
Round shaft with a shoulder fillet in torsion	D (maximum diameter of shaft)	91	2
	d (minimum diameter of shaft)	273	2.04
	r (chamfer radius)	27.3	0.024
Grooved round bar in torsion	D (maximum diameter of shaft)	57	1
	d (minimum diameter of shaft)	85.5	1.02
	r (chamfer radius)	17.1	0.025
Round shaft with a transverse hole in torsion	D (maximum diameter of shaft)	16	2
	d (minimum diameter of shaft)	153.846	53.333

Formulization of neurons was made with the Fermi-transfer function that is widely used in the ANN training (equation 9). The Fermi-transfer function is a commonly preferred function in the studies conducted in different areas:

$$F_i = \frac{1}{1 + e^{-4(\sum x_{nor} \cdot w_1 - 0.5)}} \qquad (9)$$

Here, x_{nor} represents the normalized value of the input as ($I = 1, 2, 3, ..., n$) and represents its weight value. The weights obtained in the ANN model are given in **Table 6**. The Fermi functions created for each shaft type considered in the study are given in equations 10, 11 and 12:

$$F_{i_{Shoulder\,filet\,(1-4)}} = \frac{1}{1 + e^{-4(\sum D_{nor} \cdot w_{21} + d_{nor} \cdot w_{21} + r_{nor} \cdot w_{21} - 0.5)}} \qquad (10)$$

$$F_{i_{Grooved\,(1-3)}} = \frac{1}{1 + e^{-4(\sum D_{nor} \cdot w_{21} + d_{nor} \cdot w_{21} + r_{nor} \cdot w_{21} - 0.5)}} \qquad (11)$$

$$F_{i_{Transverse\,hole\,(1-3)}} = \frac{1}{1 + e^{-4(\sum D_{nor} \cdot w_{21} + d_{nor} \cdot w_{21} - 0.5)}} \qquad (12)$$

At the end of all these calculations, the output value of the network is calculated with equation 13:

$$S_{ann} = f_i(S_{max} - S_{min}) + S_{min} \qquad (13)$$

Here, S_{max} represents the maximum output value as fi ($I = 1, 2... n$) and S_{min} represents the minimum output value.

After the training and test procedures, the results obtained from the ANN model were compared to the theoretical (actual) calculation results considering the statistical error. In the error analysis, the performance of both the training and test data is evaluated. In the study,

Table 6: Weights calculated for the shafts under the torsional-stress effect
Tabela 6: Izračunane uteži gredi pri torzijskih napetostih

Round shaft with a shoulder fillet in torsion				Grooved round bar in torsion				Round shaft with a transverse hole in torsion		
i	W_{1i}	W_{2i}	W_{3i}	i	W_{1i}	W_{2i}	W_{3i}	i	W_{1i}	W_{2i}
1	1.034673	−0.994349	1.193954	1	−1.383967	1.996118	−11.65191	1	0.576589	−1.068331
2	2.166340	−1.506025	5.954506	2	−0.228184	−1.205579	1.134065	2	0.062530	−0.394452
3	−5.204485	−3.426240	−2.290548	3	−0.626798	0.816721	−1.226995	3	−1.182488	0.407942
4	0.550379	0.391485	−1.669116							
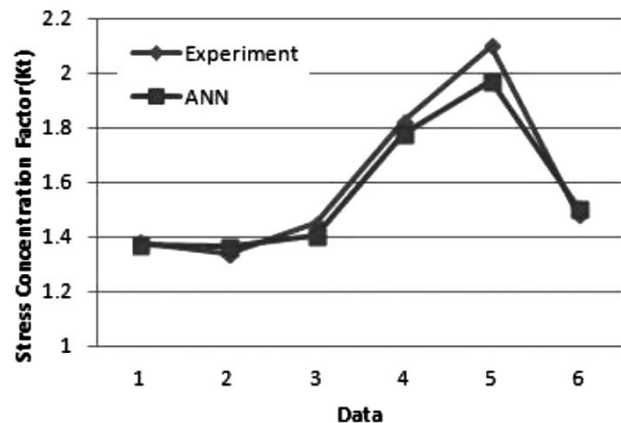
Figure 3: Comparison of the notch-sensitivity factors for a grooved round bar in torsion (ANN – the actual data)
Slika 3: Primerjava faktorja občutljivosti na zarezo pri okrogli palici z utorom (ANN – dejanski podatki)

Figure 4: Comparison of the notch-sensitivity factors for a round shaft with a shoulder fillet in torsion (ANN – the actual data)
Slika 4: Primerjava faktorja občutljivosti na zarezo pri okrogli gredi z zaokroženim prehodom pri torziji (ANN – dejanski podatki)

while statistical analyses were made with the Statistica software, the graphics were created with the MATLAB software. When **Figures 3**, **4** and **5** are reviewed, it can be seen that theoretical-calculation results and ANN results are very close. With the developed ANN model, the results determining the notch factors are very close to the actual values.

The performance of the ANN model depends on the deviation amount (the error) between the actual output values and the output values obtained with the ANN model. For the analysis of such error amounts, three statistical values were used. These are the statistical error amount (the root-mean-square error – RMSE), the absolute rate of change (and the average error rate (MAPE). If, in a model, the RMSE value is low, the value is close to one and the MAPE value is close to zero, it is concluded that the data sample was solved with the ANN model with a very low deviation. When **Figures 6**, **7**, **8** and **Table 7** are reviewed, it can be observed that the test

Figure 5: Comparison of the notch-sensitivity factors for a round shaft with a transverse hole in torsion (ANN – the actual data)
Slika 5: Primerjava faktorja občutljivosti na zarezo pri okrogli gredi s prečno odprtino pri torziji (ANN – dejanski podatki)

performance of the ANN model developed to estimate the notch factors is very good.

Table 7: Statistical values of the notch factors for a round shaft with a shoulder fillet in torsion, grooved round bar in torsion and round shaft with a transverse hole in torsion
Tabela 7: Statistične vrednosti faktorja zareze pri okrogli gredi z zaokroženim prehodom pri torziji, okrogli palici z utorom in okrogli gredi s prečno odprtino

	R^2	RMSE	MAPE
Round shaft with a shoulder fillet in torsion	0.998496193	0.00045234	0.00133894419
Grooved round bar in torsion	0.999026056	0.000929826	0.00092129141
Round shaft with a transverse hole in torsion	0.999852111	0.00048452	0.00013216197

Table 8: Statistical error amounts obtained with the regression analysis and ANN
Tabela 8: Statistična napaka, dobljena z regresijsko analizo ANN

	Multiple regression analysis		Artificial neural network (ANN)
	R^2	Adjusted R	R^2 (ANN)
Round shaft with a transverse hole in torsion	0.98972458	0.98766949	0.998496193
Round shaft with a shoulder fillet in torsion	0.65122920	0.63513208	0.999026056
Grooved round bar in torsion	0.72001774	0.69953123	0.999852111
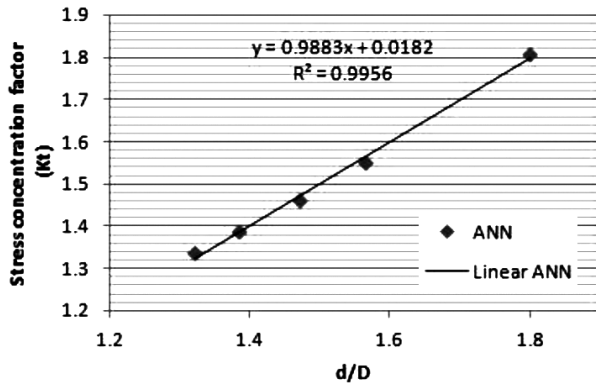
Figure 6: Notch factor for a round shaft with a shoulder fillet in torsion
Slika 6: Faktor zareze pri okrogli gredi z zaokroženim prehodom pri torziji
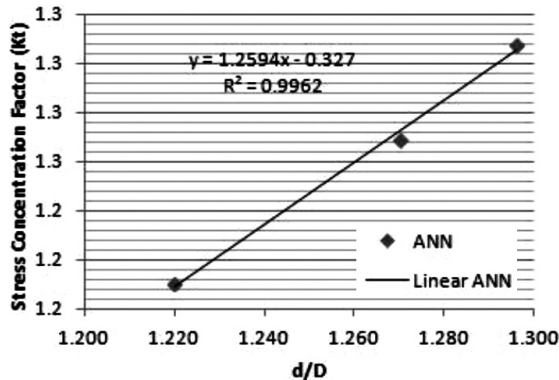
Figure 7: Notch factor for a grooved round bar under the torsional effect
Slika 7: Faktor zareze pri okrogli palici z utorom pri torziji
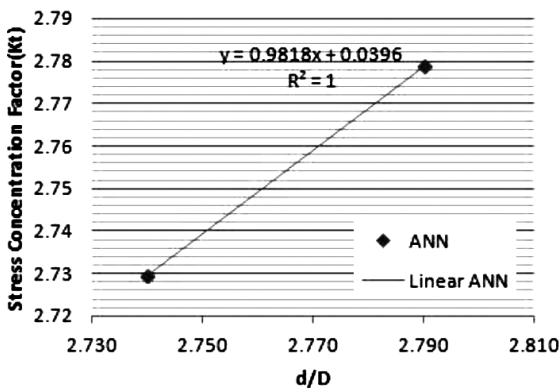
Figure 8: Notch factor for a round shaft with a transverse hole under the torsional effect
Slika 8: Faktor zareze pri okrogli gredi s prečno odprtino pri torziji

In **Figures 5**, **6** and **7**, the performance of a YSA model is available for the notch-factor estimation. Here, the closeness value between the actual values and the estimated values is graphically shown. As seen in the figures, the estimations made by the ANN model were rather close to the actual values.

In the study, a multiple regression analysis (RA) of the data was made as well and specifically adjusted R^2 values were observed. In the analysis, a suitable R^2 could

Figure 9: ANOVA analysis; notch-sensitivity factor for a grooved round bar in torsion
Slika 9: ANOVA analiza; faktor zareznega učinka pri okrogli palici z utorom pri torziji

Figure 10: ANOVA analysis; notch-sensitivity factor for a round shaft with a shoulder fillet in torsion
Slika 10: ANOVA analiza; faktor zareznega učinka pri okrogli gredi z zaokroženim prehodom pri torziji
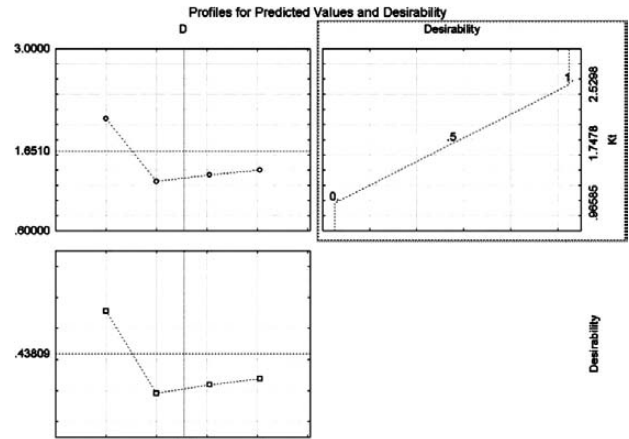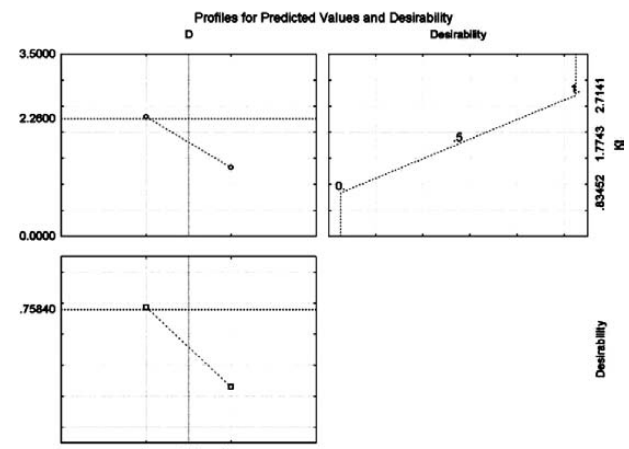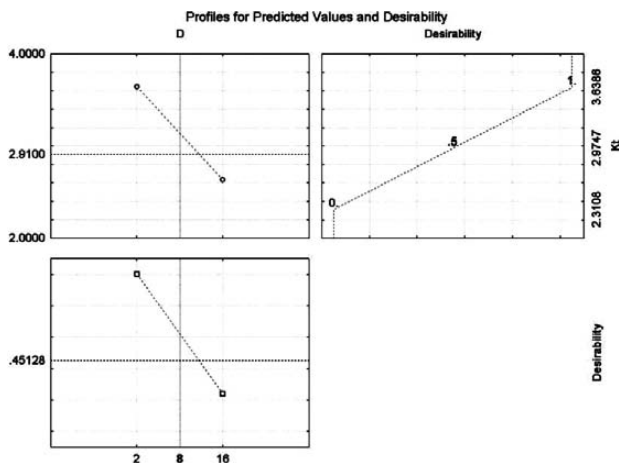
Figure 11: ANOVA analysis; notch-sensitivity factor for a round shaft with a transverse hole in torsion

Slika 11: ANOVA analiza; faktor zareznega učinka pri okrogli gredi s prečno odprtino

only be obtained for the round shaft with a transverse hole in torsion. In **Table 8**, the statistical error amounts (R^2) obtained with the regression analysis and the statistical error amounts (R^2) of the ANN test data were compared. An ANOVA analysis of the data was made as well, but no results interpreting the data were obtained (**Figures 9**, **10** and **11**). Statistically, only the parameter of the maximum diameter of the shaft affected the notch sensitivity.

5 CONCLUSIONS

In this study, an ANN model developed for estimating the notch factors of the shafts under the torsional effect has been introduced. The values trained and tested with ANN were obtained by reviewing the charts in the literature.[19,20] When comparing the notch-factor values calculated with the equations obtained from the ANN model with the experimental values, very good results were obtained. With this study, it was clearly found that the notch factors of the shafts can be estimated using ANN without the need for theoretical number crunching. With ANN, complicated and long calculations, individual chart readings and interpolation errors have been eliminated. Thus, this enabled us to obtain more correct results in a faster way. Also, in the study, the data was subject to a multiple regression analysis. At the end of this analysis, since no results interpreting the data could be obtained, the study was focused on ANN.

6 REFERENCES

[1] T. Nicholas, High Cycle Fatigue: A Mechanics of Materials Perspective, 1st ed., Elsevier, Oxford 2006, 213–238

[2] A. Doğrusadık, Çentikli Parçaların Yorulma Ömürlerinin Saptanmasında Kullanılan Yöntemlerin Deneysel Tahkiki, İstanbul Teknik Üniversitesi, İstanbul 2009, 1–2

[3] F. Mcclintock, A criterion of ductile fracture by the growth of holes, J Appl Mech, 35 (**1968**), 363–71

[4] J. Rice, D. Tracey, On the ductile enlargement of voids in triaxial stress fields, J Mech Phys Solids, 17 (**1969**), 201–17

[5] J. Hancock, A. Mackenzie, On the mechanisms of ductile failure in high-strength steels subjected to multi-axial stress-states, J Mech Phys Solids, 24 (**1976**), 69–147

[6] P. Bridgman, Studies in large plastic flow and fracture, MA Harvard University Press, Cambridge 1976, 3–5

[7] J. Hancock, D. Brown, On the role of strain and stress state in ductile Failure, Journal of the Mechanics and Physics of Solids, 31 (**1983**), 1–24

[8] M. T. Ozkan, Notch Sensitivity Factor Calculation in the Design of Shafts using Artificial Neural Network System, Energy Education Science and Technology Part A: Energy Science and Research, 30(SI) (**2012**), 621–630

[9] M. T. Ozkan, C. Eldem, E.Koksal, Notch Sensitivity Factor Determination with Artificial Neural Network for Shafts under Bending Stress, Pamukkale Üniversitesi Mühendislik Bilimleri Dergisi, 19 (**2013**) 1, 24–32

[10] M. T. Ozkan, Experimental and artificial neural network study of heat formation values of drilling&boring operations on Al 7075 T6 workpiece, Indian Journal of Engineering & Materials Science (IJEMS), 20 (**2013**), 259–268

[11] C. Elmas, Yapay Sinir Ağları, Seçkin Yayıncılık, Ankara 2003, 27–37 (In Turkish)

[12] Y. Tasdemir, Artificial neural networks for predicting low temperature performances of modified asphalt mixtures, IJEMS, 16 (**2009**) 4, 237–244

[13] T. Findik, S. Tasdemir, I. Şahin, The use of artificial neural network for prediction of grain size of 17-4 pH stainless steel powders, Scientific Research and Essays, 5 (**2010**) 11, 1274–1283

[14] X. Yao, Evolving artificial neural Networks, Proceedings of the IEEE, 1999, 87

[15] T. Menlik, M. B. Özdemir, V. Kirmaci, Determination of freeze – drying behaviors of apples by artificial neural network, Expert system with application, 37 (**2010**), 7669–7677

[16] A. Bozacı, Makine Elemanlarının Projelendirilmesi, Seç Yayın Dağıtım, İstanbul 1995, 1–6 (In Turkish)

[17] M. Akkurt, Makine Elemanları, Birsen Yayın Evi Ltd. Şti. Seç Yayın Dağıtım, İstanbul 2005, 29 (In Turkish)

[18] E. Koç, Makine Elemanları, Nobel Kitapevi, Adana 2004, 47 (In Turkish)

[19] A. C. Can, Makine Elemanları Tasarımı, Birsen Yayın Evi, İstanbul 2006, l43 (In Turkish)

[20] R. E. Peterson, Design Factors for Stress Concentration; Machine Design, 23 (**1951**) 2, 169; 23 (**1951**), 161; 23 (**1951**) 3, 159; 23 (**1951**) 6, 173; 23 (**1951**) 7, 155, Reprinted with the permission from Machine Design, a Penton Media Inc. publication

[21] R. G. Budynas, J. K. Nisbett, Shigley's Mechanical Engineering Design, McGraw-Hill, USA 2006, 1003–1005

Appendix A: Notch-determining examples for the shafts under the torsional stress using ANN mathematical formulae

Example 1: Round shaft with a transverse hole in torsion
Primer 1: Okrogla gred s prečno odprtino pri torziji

N/W	INPUT NEURONS			OUTPUT NEURON	
	N1	N2	N3	N1	2.919787
WEIGHTS (W)	−1.175518	0.574674	0.061991	N2	−2.252147
	0.405123	−1.101991	−0.384738	N3	4.610924
$Q = 1/(1+\text{Exp}(-4 \cdot (i1 \cdot w1 + i2 \cdot w2 + i3 \cdot w4 - 0.5)))$					

WEIGHTS					
N1	0.007621				
N2	0.280911	$N4$	0.09827	Q	2.7295444
N3	0.120636				

Example 2: Round shaft with a shoulder fillet in torsion
Primer 2: Okrogla gred z zaokroženim prehodom pri torziji

N/W	INPUT NEURONS					OUTPUT NEURON	
	N1	N2	N3	N4	N5	N1	−1.192632
	−0.527014	0.436152	−7.038280	0.600414	−4.732217	N2	3.673670
WEIGHTS (W)	−0.866854	0.590241	−2.128378	0.041027	−3.205369	N3	7.462569
	1.456036	−11.101250	−4.762488	−1.340877	5.252158	N4	1.609339
						N5	−6.440091
$Q = 1/(1+\text{Exp}(-4 \cdot (i1 \cdot w1 + i2 \cdot w2 + i3 \cdot w4 - 0.5)))$							

WEIGHTS					
N1	0.079370				
N2	0.005604				
N3	0.000003	$N4$	0.20223	Q	1.564021224
N4	0.147278				
N5	0.000942				

Example 3: Grooved round bar in torsion
Primer 3: Okrogla palica z utorom pri torziji

N/W	INPUT NEURONS			OUTPUT NEURON	
	N1	N2	N3	N4	
	3.759538	−1.522419	3.805108	N1	1.946942
WEIGHTS (W)	−1.108545	−1.898673	−3.206606	N2	3.777504
				N3	−1.771848
$Q = 1/(1+\text{Exp}(-4 \cdot (i1 \cdot w1 + i2 \cdot w2 + i3 \cdot w4 - 0.5)))$					
WEIGHTS					
N1	0.935048				
N2	0.280911	$N4$	0.19874	Q	1.600998225
N3	0.120636				

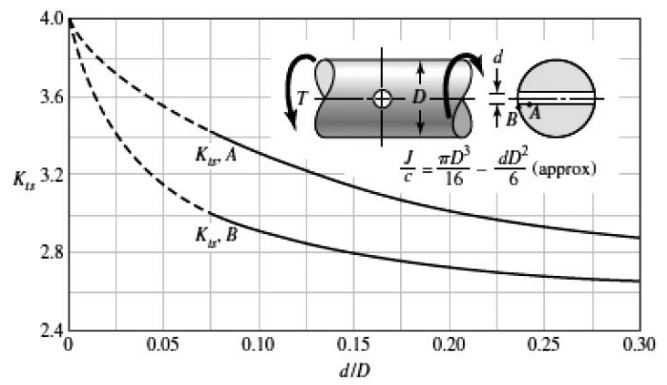## Appendix B: Stress-concentration-factor charts

Round shaft with a shoulder fillet in torsion[20,21]
$\tau_0 = Tc/J$, where
$c = d/2$ and $J = \pi d^4/32$
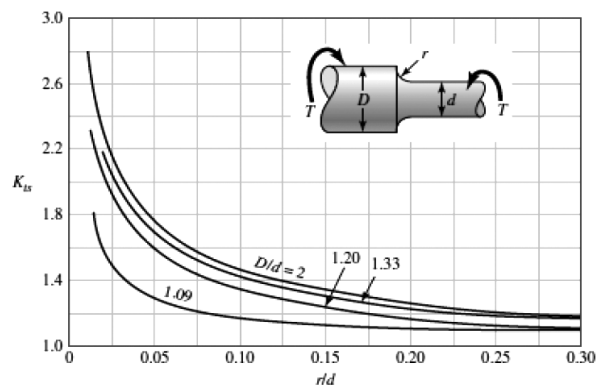
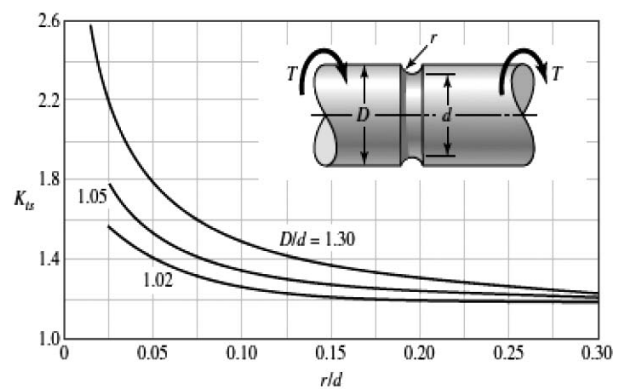Round shaft with a transverse hole in torsion[20,21]

Grooved round bar in torsion[20,21]

$\tau_0 = Tc/J$

where $c = d/2$

and $J = \tau d^4/32$

EVALUATION OF THE SURFACE ROUGHNESS AND GEOMETRIC ACCURACIES IN A DRILLING PROCESS USING THE TAGUCHI ANALYSIS

OCENA HRAPAVOSTI POVRŠINE IN GEOMETRIJSKE NATANČNOSTI POSTOPKA VRTANJA Z UPORABO TAGUCHIJEVE ANALIZE

Evren Kabakli[1], Melih Bayramoğlu[2], Necdet Geren[2]

[1]CIMSATAS, P. B. 634, 33004 Mersin, Turkey
[2]Mechanical Engineering Department, The University of Cukurova, 01330 Adana, Turkey
bayramog@cu.edu.tr

This paper presents an evaluation of the surface roughness and geometric accuracies in drilling operations performed using U-drills without a pilot hole. The surface roughness, perpendicularity and cylindricity were used as the response parameters for evaluating the effects of the feed rate, peripheral speed, hole diameter and hole depth. The performance characteristics were measured and various signal-noise ratios were calculated with the Taguchi method. An analysis of variance (ANOVA) was performed and the effects of the controlled factors at different levels were analyzed to identify the optimum drilling conditions for U-drills. The results of this study will allow an operator to select the optimum parameter values for U-drills to reduce the manufacturing costs.

Keywords: surface roughness, perpendicularity, cylindricity, U-drills, coated indexable insert drills, Taguchi method, optimization

Članek predstavlja oceno hrapavosti površine in geometrijske natančnosti operacije vrtanja, izvršene z U-svedrom brez vodilne izvrtine. Hrapavost površine, navpičnost in cilindričnost so bile uporabljene kot odgovarjajoči parametri za oceno odvzema, obodne hitrosti, premera in globine luknje. Izmerjene so bile značilnosti delovanja, razmerja signalov hrupa pa so bila izračunana z uporabo Taguchijeve metode. Izvršena je bila analiza variance (ANOVA) in analizirani kontrolni faktorji vpliva na različnih nivojih, da bi ugotovili optimalne razmere vrtanja za U-svedre. Rezultati te študije bodo omogočili operaterju, da bo izbral optimalne vrednosti parametrov za U-sveder in za zmanjšanje proizvodnih stroškov.

Ključne besede: hrapavost površine, pravokotnost, cilindričnost, U-svedri, prekriti indeksirani vložki svedrov, Taguchijeva metoda, optimizacija

1 INTRODUCTION

Drilling is usually the most efficient and economical method of cutting a hole in a solid metal and has a considerable economic importance because of its wide application in most of the manufactured components. It has been reported that drilling accounts for nearly 40 % of all the metal-removal operations in the aerospace and automobile industries.[1] Hence, achieving a required hole quality is important for the functional-behavior parts and the economics of drilling operations.

Drilling operations are not regarded as precision machining and, thus, subsequent operations are required to improve the accuracy levels. These finishing operations improve the surface finish significantly; however, eliminating the inaccuracies resulting from drilling operations is difficult.[2–5] Therefore, many researches were carried out to evaluate the surface roughness and accuracy of drilled holes. These researches were largely concentrated on finding the effects of cutting speed, feed rate, tool geometry, type of the material and rigidity of the machine tools, using twist drills.[6–10] Most of these researches were focused on the optimization of the para-

meters using the Taguchi method. However, little work has been reported on the effects of the hole depth and hole diameter on the quality of the holes obtained with U-drills.

The usual procedure for drilling large holes is that first a pilot hole is drilled to overcome the poor cutting of large drills. The hole quality is affected by several factors such as tool geometry, cutting speed, feed rate, workpiece material and rigidity of the machine tool.[11,12] The drill geometry is considered to be the most important factor affecting a drill performance. Hence, with the development of the tools featuring indexable inserts (commonly referred to as U-drills), the need for the preparatory and subsequent machining has changed drastically. Modern tools have led to the solid drilling being carried out in a single operation without any previous drilling of the centre and pilot holes, making the hole production more productive.[13]

This study aims to minimize and/or eliminate the subsequent operations needed after the drilling operations using U-drills. U-drills are generally used for roughing operations to reduce the machining time by cutting holes without any pilot drilling. Using the opti-

mum feed rate is important in this type of drilling operations. The feeds that are too low may cause an unsatisfactory surface finish due to the swaging during the initial penetration of the tool into a workpiece. On the other hand, excessive cutting forces, due to high feeds, may cause poor tolerances and damage on a workpiece and tool holder because of the fracture on the tool inserts. This study aims to minimize and/or eliminate the subsequent operations needed after the drilling operations by optimizing the process parameters such as the cutting speed, feed rate, hole diameter and hole depth using the Taguchi method. A horizontal CNC machining center was used for the drilling tests. Medium-carbon steel was used as the workpiece material. The surface roughness, perpendicularity and cylindricity were selected as the performance characteristics. Then, the optimum process parameters for the best surface finish and hole accuracy were derived from the analysis of the results. The parameters having the major effects on the hole quality and the percentage contribution of these effects were analyzed and, finally, confirmation tests were carried out comparing these results with the experimental results.

2 EXPERIMENTAL DETAILS

2.1 Design of experiments

Designs of experiment techniques, specifically orthogonal arrays (OA), are employed in the Taguchi approach to systematically vary and test different levels of each of the control factors.[14] The commonly used orthogonal arrays include L_4, L_9, L_{12}, L_{18}, and L_{27} depending upon the number of the parameters to be studied and the levels for each factor. In this work, four parameters, namely A, B, C and D, at three levels were investigated. Therefore, the L_9 (3^4) orthogonal array, shown in **Table 1**, was employed for the design of the experiments.

Specific test characteristics for each experimental evaluation are identified according to the associated row of the L_9 orthogonal-array table. L_9 means that nine experiments have been performed to study the effects of

four variables at three levels. The number of columns of an array in the table represents the maximum number of the parameters that can be studied using that array. The columns in an orthogonal array indicate the factor and its corresponding levels, and each row in the orthogonal array constitutes an experimental run performed at the given factor settings.

In this study, only a specific kind of workpiece material was considered, so the workpiece material had no effect on the variations of responses. Different diameters were considered for the desired holes using the tools with the same geometry and grade. All the experiments were performed on the same drilling machine, so the machine and the process had no effect on the variations of responses. The flank wear and crater wear were checked on the tools after every set of experiments due to their significant effects on the surface finish and cutting forces and no wear was detected on the cutting tools. Therefore, it is assumed that the chatter effect had no influence on the variations of responses.

The feed and cutting speed are two important process parameters for achieving the desired material-removal rate and productivity in drilling. The use of a better tool material with a higher strength and hot hardness and a better drill geometry design can enable a larger feed in drilling. The effect of the feed in drilling is an area that had not been studied extensively.[15] Therefore, the cutting speed and the feed rate were defined as the controlled factors. Additionally, the hole diameter and hole depth were considered as they represent the constraints in a drilling process in today's machining applications. The steps defined in **Figure 1** were followed when conducting the experiments and analyzing the results to investigate the effects of the process parameters on the surface roughness, perpendicularity and cylindricity.

A product array was used to test various combinations of the control-factor settings against all the combinations of the noise factors. Then, the mean response and the standard deviation were approximated for each run using the following equations:

$$y_{ave} = \frac{1}{n} \sum_{i=1}^{n} y_i \quad \text{is the mean response} \tag{1}$$

Table 1: L_9 orthogonal array used for the design of the experiments and controlled factors with their levels
Tabela 1: Ortogonalna postavitev L_9, uporabljena za postavitev preiskav in kontrolnih faktorjev z njihovimi nivoji

Run # /trial #	Level	Factor A Hole diameter (mm)	Level	Factor B Hole depth (mm)	Level	Factor C Feed rate (mm/r)	Level	Factor D Cutting speed (m/min)
1	1	19	1	45	1	0.06	1	140
2	1	19	2	68	2	0.09	2	160
3	1	19	3	95	3	0.12	3	180
4	2	23	1	45	2	0.09	3	180
5	2	23	2	68	3	0.12	1	140
6	2	23	3	95	1	0.06	2	160
7	3	26	1	45	3	0.12	2	160
8	3	26	2	68	1	0.06	3	180
9	3	26	3	95	2	0.09	1	140
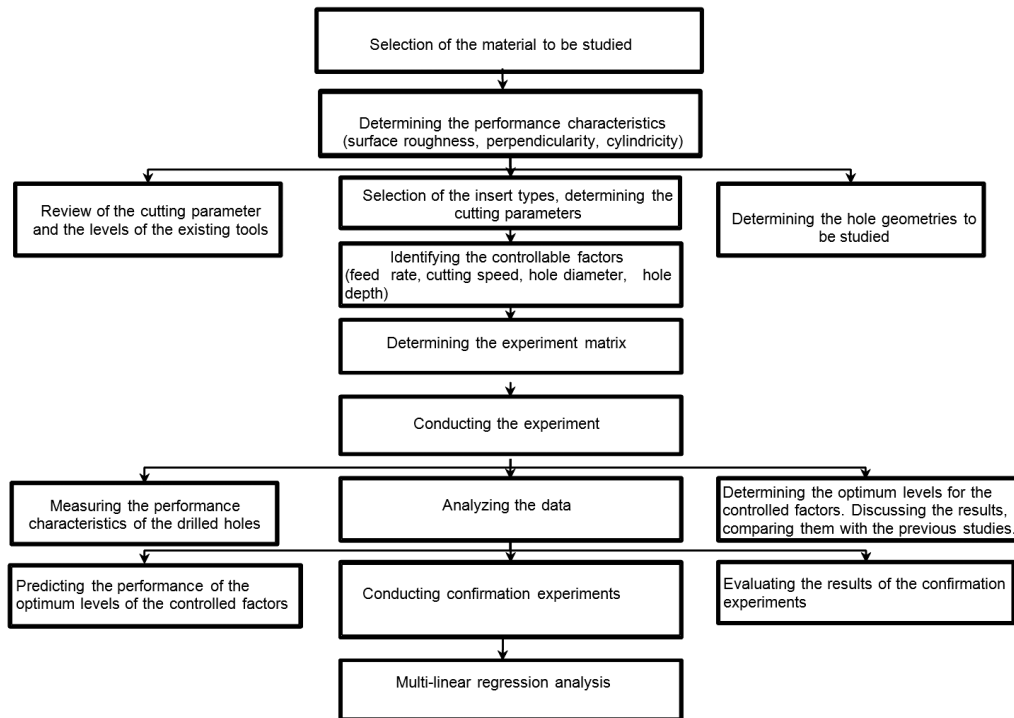
Figure 1: Flowchart of the Taguchi method employed in this study
Slika 1: Diagram Taguchijeve metode, uporabljene v tej študiji

$$S = \frac{1}{n}\sqrt{\sum_{i=1}^{n}\frac{(y_i - y_{\text{ave}})^2}{n-1}} \quad \text{is the standard deviation} \quad (2)$$

The preferred parameter settings were then determined through an analysis of the signal-to-noise (*S/N*) ratio. These *S/N* ratios were derived from the quadratic loss function and expressed with a decibel scale. After all of the *S/N* ratios were computed for each run of the experiment, a graphical approach was used to analyze the data. In the graphical approach, the *S/N* ratios and the average responses were plotted for all the factors against their levels. The graphs were then examined to select the factor level that best maximizes each *S/N* ratio. Finally, confirmation tests were conducted for the optimum setting parameters to verify that the defined performance was actually realized.

2.2 Workpiece material

In this study, hot-rolled low-alloyed medium-carbon steel of 207 HB was used as the workpiece material. This material with the chemical composition given in **Table 2** is modified from C35 and used in the automobile indu-

Table 2: Chemical composition of the workpiece material in mass fractions (*w*/%)
Tabela 2: Kemijska sestava materiala obdelovanca v masnih deležih (*w*/%)

C	Si	Mn	P	S	Cr	Mo	Ni	Al	Cu	Sn
0.37	0.57	0.97	0.013	0.055	0.16	0.01	0.12	0.017	0.22	0.014

stry. The workpieces were 250 mm in length with a square cross-section of 80 mm × 80 mm.

2.3 Cutting tools

The U-drilling tools, shown in **Figure 2**, were used in the experiments. A U-drilling tool has two internal coolant flutes and indexable central and peripheral inserts. The central inserts are made of 1044-grade, fine-grained, cemented carbide PVD coated with a bronze-colored TiAlN layer 3 μm. The peripheral inserts were of grade 4024. They had a cemented carbide substrate coated with a MT-CVD layer of TiCN ensuring the abrasive wear resistance, followed by a layer of Al_2O_3 providing a high-temperature protection.

2.4 Experimental setup

An OKUMA MA-500HB SPACE CENTER, a horizontal CNC machining center with an OSP E100M controller, was used for conducting the experiments in this

Figure 2: a) U-drill tool, b) central insert, c) peripheral insert
Slika 2: a) U-vrtalno orodje, b) centralni vložek, c) obodni vložek
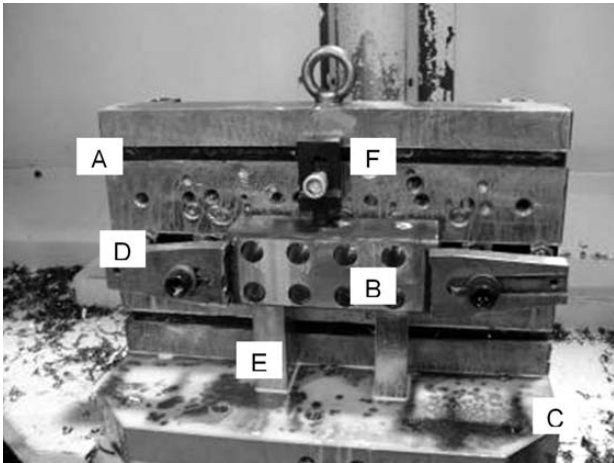
Figure 3: Fixture used during the test
Slika 3: Pritrditev, uporabljena pri preizkusu

study. During the tests, the machine spindle torque was limited by the controller to about 25 % of the maximum spindle torque of a usual application in a factory during production.

The initial start-up checks were performed before the drilling in order to minimize and eliminate the sources of variation and increase the reliability of the results. The linear positioning accuracy of the machine was checked according to ISO 230-1 at three axes and found to be about 3 μm. The repeatability of the positioning accuracy of the machine at three axes was found to be about 1 μm. The spindle speed was checked with a SCHENCK VIBRO BALANCER 42 and no deviation was detected. A torque meter was used to tighten the workpiece repeatably by applying a 220 N m torque. The radial run-out of the drilling tool was checked before every run of the experiments. The maximum total run-out of the drilling tool was detected as 0.05 mm. The workpiece surface was cleaned by milling to eliminate the effect of an angular deviation between the tool and the workpiece before the drilling process.

The fixture used during the tests is shown in **Figure 3**. The fixture consists of a support console (A), a workpiece (B), a pallet (C), the fixing arms (D), the lower supporting blocks (E) and the upper adjustable supporting blocks (F). The rear side of the workpiece was machined on a conventional milling machine before the drilling operations to eliminate the adverse effects of the tightening forces of the fixing arms.

2.5 Perpendicularity and cylindricity measurements

A CNC controlled coordinate measuring machine (CMM) was used to measure the perpendicularity and cylindricity of the holes during the experiments. The machine was ZEISS ACCURA CMM with a measuring range of 900 mm × 1500 mm × 700 mm. The machine was equipped with a multi-sensor rack for automated measuring without any manual changing of the probes for different purposes, having a passive scanning option.

The linear measuring uncertainty of CMM was (2.2 + (L/300)) μm and the form uncertainty of the roundness was 1.7 μm during the scanning with a VAST XXT scanning probe. During the experiments, the linear and scanning uncertainties of the machine were verified with the linear and round standard gauge blocks.

2.6 Surface-roughness measurements

A stylus-contact-type device, MITUTOYO SJ 301 surface roughness tester, was used to measure the surface roughness of the holes during the experiments. The roughness tests were carried out according to DIN 1990. The device was verified before the measurements using a standard roughness specimen. The Gauss filter was used while measuring the P profile. The Ra average roughness parameter was selected as the output parameter to define the geometric irregularities of the surfaces drilled at different conditions. The values of 0.8 mm and 4.0 mm were selected for the cut-off and evaluated profile lengths, respectively. Five cut-off lengths were scanned with a measuring speed of 5 mm/s and three of them were filtered.

3 RESULTS AND DISCUSSIONS

Ten holes were drilled in a single operation without any previous drilling of the centre or the pilot holes on the experiment samples for each experimental run. Then, the effects of the process parameters on the three performance characteristics – the surface roughness, the perpendicularity and the cylindricity – were analyzed using the results of the *S/N* ratios and ANOVA. The results of the experiments performed at different levels of each factor with the corresponding *S/N* ratios and the total variations and standard deviations determined for the performance characteristics are given in **Tables 3** and **4**, respectively.

3.1 Data analysis based on the S/N ratios and ANOVA

3.1.1 Surface roughness

The average *S/N* ratio of the controlled factors affecting the surface roughness were determined and given in **Table 5** and **Figure 4**. The optimum combination of the hole diameter, hole depth, feed rate and cutting speed, giving the best performance characteristics, was determined as A3 (a 26 mm hole diameter), B1 (a 45 mm hole depth), C1 (a 0.06 mm/r feed rate) and D3 (a 180 m/min cutting speed) using the distribution of the average *S/N* ratios shown in **Figure 4**.

The analysis of variance for different drilling modes, given in **Table 6**, shows that the most important variable affecting the surface roughness is the hole diameter with a percentage contribution of 70.64 %. The maximum deviation in the surface-roughness value was detected when the hole diameter was changed within the range of 19 mm and 26 mm. This was due to the changes in the

Table 3: Average surface-performance-characteristic values obtained for different configurations and the *S/N* ratios estimated for each run
Tabela 3: Povprečne vrednosti značilnosti vedenja površine pri različnih postavitvah in *S/N*-razmerjih, dobljenih pri vsaki ponovitvi
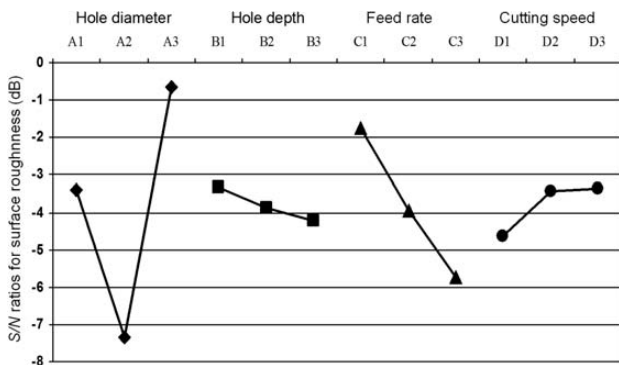
Run #	Average surface roughness (µm)	S/N ratio surface roughness (dB)	Average perpendicularity (mm)	S/N ratio perpendicularity (dB)	Average cylindricity (mm)	S/N ratio cylindricity (dB)
1	1.21	−1.693	0.0061	43.528	0.0325	29.6196
2	1.44	−3.270	0.0106	38.877	0.0727	22.5651
3	1.80	−5.279	0.0182	33.862	0.0479	26.3535
4	2.40	−6.578	0.0085	40.082	0.0278	31.0535
5	2.62	−10.174	0.0150	35.242	0.0394	18.5163
6	2.58	−5.319	0.0113	35.749	0.0265	25.0493
7	1.21	−1.748	0.0095	39.816	0.0261	31.3278
8	0.80	1.779	0.0121	37.719	0.0483	25.9372
9	1.26	−2.037	0.0259	30.409	0.0485	25.8253
S/N total		−34.319		335.283		236.248
S/N average		−3.813		37.254		26.250

Table 4: Total variations and standard deviations determined for the performance characteristics
Tabela 4: Skupni odmiki in standardna deviacija, določena pri značilni učinkovitosti

Run #	Ave. surface roughness (µm)	Total var. R_a (µm)	St. dev. R_a (µm)	Ave. perp. (mm)	Total var. perp. (mm)	St. dev. perp. (mm)	Ave. cyl. (mm)	Total var. cyl. (mm)	St. dev. cyl. (mm)
1	1.21	± 0.215	0.149	0.006 1	± 0.004	0.003	0.0325	± 0.011	0.006
2	1.44	± 0.350	0.214	0.010 6	± 0.007	0.004	0.0727	± 0.028	0.017
3	1.80	± 0.435	0.373	0.018 2	± 0.013	0.009	0.0479	± 0.008	0.004
4	2.40	± 0.565	0.320	0.008 5	± 0.009	0.005	0.0278	± 0.005	0.004
5	2.62	± 0.520	0.451	0.015 0	± 0.012	0.008	0.0394	± 0.005	0.004
6	2.58	± 0.39	0.237	0.011 3	± 0.012	0.009	0.0265	± 0.005	0.003
7	1.21	± 0.230	0.164	0.009 5	± 0.007	0.004	0.0261	± 0.012	0.008
8	0.80	± 0.225	0.152	0.012 1	± 0.008	0.005	0.0483	± 0.023	0.015
9	1.26	± 0.01	0.061	0.025 9	± 0.023	0.016	0.0485	± 0.025	0.017

power requirement for drilling different sizes of the holes. The feed rate also had a significant effect on the surface roughness with a percentage contribution of 24.97 %. This means that these two factors must be considered first when optimizing the process parameters to improve the surface finish in drilling processes.

Figure 4: *S/N* response graph of the surface roughness
Slika 4: Graf *S/N*-odgovorov na hrapavost površine

Table 5: *S/N* response table for the surface roughness
Tabela 5: Tabela *S/N*-odgovorov pri hrapavosti površine

Factor	Mean S/N ratio (dB)			
	Level 1	Level 2	Level 3	Difference N
A: hole diameter	−3.414	−7.36	−0.669	6.689
B: hole depth	−3.340	−3.888	−4.212	0.872
C: feed rate	−1.744	−3.962	−5.734	3.990
D: cutting speed	−4.635	−3.446	−3.359	1.275

Table 6: Analysis of variance for the surface roughness
Tabela 6: Analiza variance za hrapavost površine

Source of variation		Degree of freedom	Sum of squares	Mean square	Contribution %
A	hole diameter	2	67.8224	33.911	70.64
B	hole depth	2	1.1657	0.5828	1.21
C	feed rate	2	23.9766	11.988	24.97
D	cutting speed	2	3.0485	1.5243	3.18
Total		8	96.013		100

With the optimum levels of the controlled factors, the predicted *S/N* ratio for the surface roughness to be used in the verification of the experiment was found using the following equation:

$$\mu_{A3,B1,C1,D3} = [(−1.748 + 1.779 + (−2.037)) / 3 + (−1.693 + (−6.578) + (−1.748)) / 3 + (−1.693 + (−5.319) + 1.779) / 3 + (−5.279 + (−6.578) + 1.779) / 3] − (3 − 3.813) = 2.3279979 \text{ dB}$$

Using the data given in **Table 5** and **Figure 4**, a confirmation test was carried out. Ten holes were drilled on the experiment specimen using the determined parame-

ters. The *S/N* ratio of the confirmation test was calculated as:

$\mu_{A3,B1,C1,D3} = -0.71$ dB.

The predicted *S/N* ratio was 2.327 dB, but when compared with the *S/N* ratios given in **Table 3**, a significant improvement was employed. The mean *S/N* ratio of the experiments was –3.813 dB. Hence, the improvement ratio of 81.4 % was found when considering the mean value of the *S/N* ratio.

A multi-linear regression analysis was carried out for the data range given in **Table 1** to model the relationship between the factors and the performance measure. This equation gives the expected value of the surface roughness for any combination of the feed rate, cutting speed and hole diameter. The regression equation obtained with the coefficient of determination, $R^2 = 0.9207$, was as follows:

$R_a = 25.40\,f - 0.011\,V_c + 0.049\,D$ (3)

Using the range of the selected parameters of $f = 0.06–0.12$ mm/r, $V_c = 140–180$ m/min and $D = 19–26$ mm, the range of the R_a values can be computed using equation 3:

$R_a = 25.40\,(0.06–0.12) - 0.011\,(140–180) + 0.049$ (19–26)

$R_a = (1.524–3.048) - (1.54–1.98) + (0.931–1.274)$

$R_a = (0.915–2.342)$

From the absolute values for the selected parameters, the importance coefficients of the parameters for the surface roughness can be calculated as follows:
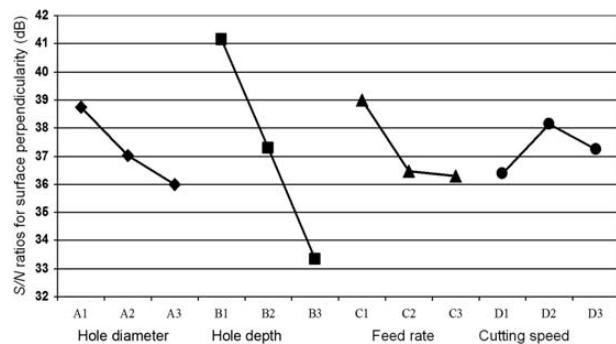
$IC_f\,/\% = [(1.524 / 3.995), (3.048 / 6.302)] = (38.15–48.37)$

$IC_{Vc}\,/\% = [(1.54 / 3.995), (1.98 / 6.302)] = (31.42–38.55)$

$IC_D\,/\% = [(0.931 / 3.995), (1.274 / 6.302)] = (23.30–20.21)$

3.1.2 Perpendicularity

The average *S/N* ratios of the controlled factors affecting the perpendicularity were determined and the results are given in **Table 7**. The average *S/N* ratios for

Figure 5: *S/N* response graph of the perpendicularity
Slika 5: Graf odgovora *S/N* na navpičnost

the perpendicularity are shown in **Figure 5**. It is evident from this figure that the optimum conditions are A1 (a 19 mm hole diameter), B1 (a 45 mm hole depth), C1 (a 0.06 mm/r feed rate) and D2 (a 160 m/min cutting speed).

Table 7: *S/N* response table for the perpendicularity
Tabela 7: Tabela odgovora *S/N* na navpičnost

		Mean *S/N* ratio (dB)			
Symbol	Factor	Level 1	Level 2	Level 3	Difference n
A	Hole diameter	38.755	37.02	35.981	2.774
B	Hole depth	41.142	37.279	33.340	7.802
C	Feed rate	38.999	36.456	36.307	2.692
D	Cutting speed	36.393	38.148	37.221	1.755

With the optimum levels of the controlled factors, the predicted *S/N* ratio for the perpendicularity was calculated from the following equation:

$\mu_{A1,B1,C1,D2} = [(43.528 + 38.877 + 33.682)/3 + (43.528 + 40.082 + 39.816)/3 + (43,528 + 35.749 + 37.719)/3 + (38.877 + 35.749 + 39.816)/3] - (3 \times 37.254) = 45.282494$ dB

Table 8: Analysis of variance for the perpendicularity
Tabela 8: Analiza variance za navpičnost

Source of variation		Degree of freedom	Sum of squares	Mean square	Contribution %
A	hole diameter	2	11.780	5.890	9.70
B	hole depth	2	91.307	45.653	75.18
C	feed rate	2	13.756	6.868	11.31
D	cutting speed	2	4.624	2.312	3.81
Total		8	121.446		100

The analysis of variance (**Table 8**) show that the most important variable affecting the perpendicularity is the hole depth with a percentage contribution of 75.18 %. The maximum deviation in the perpendicularity value was detected when the hole depth increased in the range of 45–95 mm. This could be due to an excessive deflection of the tool and a difficulty in removing the chips from the cutting zone as the hole depth was increased. Hence, the chip control should be considered carefully when the chip-removing distance increases. The hole diameter and the feed rate have significant effects on the perpendicularity with percentage contributions of 9.70 % and 11.31 %, respectively. The contribution of the cutting speed to the perpendicularity was found to be 3.81 %. Its effect is not significant compared to the other parameters studied in this work. This means that three of these four factors must be considered when an optimization is planned for the range of the parameters given in **Table 1**. The results of the analysis of variance indicate that the control of the force acting on the tool and chip becomes an important factor when the chip-removing distance increases.

Using the data obtained from **Table 7** and **Figure 5** a confirmation test was carried out. Ten holes were drilled on the experiment specimen using the selected parameters. The *S/N* ratio of the confirmation test was calculated as:

$$\mu_{A1,B1,C1,D2} = 31.90 \text{ dB}$$

The predicted *S/N* ratio was 45.282 dB. The *S/N* ratio of the confirmation test for the cylindricity was lower than the predicted value. Although the predicted *S/N* ratio value was not reached, the mean perpendicularity value (0.0240 mm) obtained under the optimum conditions shows that a 52 % improvement was achieved compared to the target perpendicularity-deviation value (0.05 mm) planned for the initial conditions of this work.

3.1.3 Cylindricity

The average *S/N* ratio of the controlled factors affecting the cylindricity were determined and given in **Table 9** and **Figure 6**. As seen in **Table 9** and **Figure 6**, the controlled factors at the levels of A3 (a 26 mm hole diameter), B1 (a 45 mm hole depth), C1 (a 0.06 mm/r feed rate) and D3 (a 180 m/min cutting speed) give the optimum performance characteristics when the *S/N* analysis is used. With the optimum levels of the controlled factors the predicted *S/N* ratio for the cylindricity was calculated using the following equation:

$$\mu_{A3,B1,C1,D3} = [(31.328 + 25.937 + 25.825)/3 + (29.620 + 31.054 + 31.328)/3 + (29.620 + 25.049 + 25.937)/3 + (26.354 + 31.054 + 25.937)/3] - (3 \cdot 26.25) = 34.265 \text{ dB}$$

A confirmation test was carried out using the data given in **Table 9** and **Figure 6**. Ten holes were drilled on
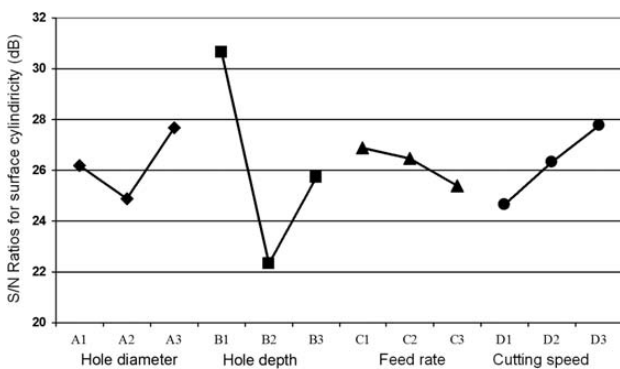
Figure 6: *S/N* response graph of the cylindricity
Slika 6: Graf odgovora *S/N* na cilindričnost

Table 9: *S/N* response table for the cylindricity
Tabela 9: Tabela odgovora *S/N* na cilindričnost

Symbol	Factor	Mean *S/N* ratio (dB)			
		Level 1	Level 2	Level 3	Difference n
A	Hole diameter	26.179	24.87	27.697	2.824
B	Hole depth	30.667	22.340	25.743	8.327
C	Feed rate	26.869	26.481	25.399	1.469
D	Cutting speed	24.654	26.314	27.781	3.128

the experiment specimen with the selected parameters for the optimum performance. The *S/N* ratio of the confirmation test was calculated as $\mu_{A3,B1,C1,D3} = 34.720$ dB.

The predicted *S/N* ratio was 34.265 dB. The *S/N* ratio of the confirmation test for the cylindricity was higher than the predicted value, but the predicted *S/N* ratio value was almost reached. The improvement ratio was 40 % when the mean *S/N* ratio of 26.520 dB was considered.

The analysis of variance for the cylindricity, given in **Table 10**, shows that the most important variable affecting the cylindricity is the hole depth with a percentage contribution of 77.72 %. After changing the hole depth in the range from 45 mm to 95 mm, the maximum deviation in the cylindricity value was detected. This can be explained with the fact that the tool deflection increases with the hole depth in drilling. Also, this fact might be a reason for the change in the chip-removing capability. The chip control becomes an important factor when the chip-removing distance increases. The hole diameter and the cutting speed also have significant effects on the cylindricity with the percentage contributions of 8.85 % and 10.86 %. This can be explained with the fact that the power requirement changes during drilling with a change in the hole diameter. In solid drilling, the depth of a cut equals half the diameter of a drilled hole. The feed rate had an insignificant effect on the cylindricity with a percentage contribution of 2.57 % under the conditions of these experiments.

Table 10: Analysis of variance for the cylindricity
Tabela 10: Analiza variance na cilindričnost

Source of variation		Degree of freedom	Sum of squares	Mean square	Contribution %
A	hole diameter	2	11.982	5.9912	8.85
B	hole depth	2	105.176	52.588	77.72
C	feed rate	2	3.480	1.7402	2.57
D	cutting speed	2	14.692	7.346	10.86
	Total	8	135.331		100

Nearly the same cylindricity values were obtained for the cutting-speed values of 140 m/min and 160 m/min. On the basis of these results, the interaction between the feed rate and the cutting speed has to be further investigated in future studies. This can be seen from the calculated R^2 value of the most suitable formulation for the cylindricity under the given conditions of this experiment. The equation is as follows:

$$Cylindricity = 0.3289\, f + 0.00016\, V_c - 0.0016\, D \qquad (4)$$

$$R^2 = 0.7258$$

Using the selected parameters of $f = 0.06-0.12$ mm/r, $V_c = 140-180$ m/min and $D = 19-26$ mm, the range of the cylindricity values can be computed using equation 4:

$$Cylindricity = 0.3289(0.06-0.12) + 0.00016(140-180) - 0.0016(19-26)$$

Cylindricity = (0.0197–0.0395) + (0.0224–0.0288) – (0.0304–0.0416)

Cylindricity = (0.0117–0.0267)

From the absolute values of the selected parameters, the importance coefficients of the parameters for the cylindricity can be calculated as follows:

IC_f/% = [(0.0197 / 0.0725), (0.0395 / 0.1099)] = (27.17–35.94)

IC_{Vc}/% = [(0.0224 / 0.0725), (0.0288 / 0.1099)] = (26.21–30.90)

IC_D/% = [(0.0304 / 0.0725), (0.0416 / 0.1099)] = (37.85–41.93)

4 CONCLUSIONS

In this study, it has been shown that the surface roughness, the perpendicularity and the cylindricity of drilled holes can be improved significantly when the target values were considered and compared at the design stage. Within the limits of the variables employed in the present experiments, the following conclusions can be drawn on the basis of the design planned with an L_9 (3^4) orthogonal array, using the Taguchi method for the solid drilling carried out with a single operation without any previous drilling of the centre or the pilot holes.

The experimental results indicated that the hole diameter and the feed rate have significant effects on the surface roughness. This shows that one of the important sources of the variation in the surface roughness is the hole diameter, as the power requirement changes during drilling when the hole diameter is changed.

The hole diameter and feed rate have significant effects on the perpendicularity with the percentage contributions of 9.70 % and 11.31 %. However, the most important variable affecting the perpendicularity was the hole depth with a percentage contribution of 75.18 %. After a change in the hole depth in the range from 45 mm to 95 mm, the maximum deviation in the perpendicularity was detected.

The percentage contributions of the hole diameter, the cutting speed and the feed rate to the cylindricity were found to be 8.85 %, 10.86 % and 2.57 %, respectively. However, the most important variable affecting the cylindricity was the hole depth with a contribution of 77.72 %. After a change in the hole depth in the range from 45 mm to 95 mm, the maximum deviation in the cylindricity was detected. The results show that the chip control should be carefully considered when the chip-removing distance increases.

The selected parameters (C1 and D3) for the minimum variation of the performance characteristics of the surface roughness, perpendicularity and cylindricity were used for drilling a hole with a 23 mm diameter and 100 mm depth on the same material and a 33.6 % reduction in the machining time was obtained compared to the usual drilling method. This test confirmed that with the optimum parameter combination selected with the Taguchi design, the desired performance characteristics can be achieved in actual drilling conditions.

5 REFERENCES

[1] J. G. Li, M. Umemoto, Y. Todaka, K. Tsuchiya, A micro structural investigation of the surface of a drilled hole in carbon steels, Acta Materialia, 55 (**2007**), 1397–1406

[2] H. C. Zhang, M. E. Huq, Tolerancing techniques: the state-of-the-art, Int. J. Production Research, 30 (**1992**) 9, 211–213

[3] E. Kilickap, Modeling and optimization of burr height in drilling of Al-7075 using Taguchi method and response surface methodology, Int. J. Advanced Manufacturing Technology, 49 (**2010**) 9/12, 911–923

[4] V. N. Gaitonde, S. R. Karnik, B. T. Achyutha, B. Siddeswarappa, J. P. Davim, Predicting burr size in drilling of AISI 316L stainless steel using response surface analysis, Int. J. Materials and Product Technology, 35 (**2009**) 1/2, 228–245

[5] A. Manna, S. Salodkar, Optimization of machining conditions for effective turning of E0300 alloy steel, Journal of Materials Processing Technology, 203 (**2008**), 147–153

[6] M. Kurt, E. Bagci, Y. Kaynak, Application of Taguchi methods in the optimization of cutting parameters for surface finish and hole diameter accuracy in dry drilling processes, Int. J. Advanced Manufacturing Technology, 40 (**2009**) 5/6, 458–469

[7] T. Kivak, G. Samtas, A. Cicek, Taguchi method based optimisation of drilling parameters in drilling of AISI 316 steel with PVD monolayer and multilayer coated HSS drills, Measurement, 45 (**2012**) 6, 1547–1557

[8] D. Kumar, L. P. Singh, G. Singh, Operational modeling for optimizing surface roughness in mild steel drilling using Taguchi technique, Int. J. Research in Management, Economics and Commerce, 2 (**2012**) 3, 66–77

[9] C. S. Deng, J. H. Chin, Hole roundness in deep-hole drilling as analysed by Taguchi methods, Int. J. Advanced Manufacturing Technology, 25 (**2005**) 5/6, 420–426

[10] N. Tosun, Determination of optimum parameters for multiperformance characteristics in drilling by using grey relational analysis, Int. J. Advanced Manufacturing Technology, 28 (**2006**), 450–455

[11] S. F. Krar, A. F. Check, Technology of machine tools, fifth edition, McGraw-Hill, New York 1998

[12] J. Z. Zhang, J. C. Chen, Surface roughness optimization in a drilling operation using the Taguchi design method, Materials and Manufacturing Processes, 24 (**2009**), 459–467

[13] Richt, Tips for improved holemaking, Metalworking World, 1 (**2011**), 16–17

[14] R. Roy, A Primer on the Taguchi Method, Van Nostrand Reinhold, New York 1990

[15] R. Li, H. Parag, A. J. Shih, High-throughput drilling of titanium alloys, Int. J. Machine Tools & Manufacture, 47 (**2007**), 63–74

COMPARISON OF NiTi ORTHODONTIC ARCHWIRES AND A DETERMINATION OF THE CHARACTERISTIC PROPERTIES

PRIMERJAVA ORTODONTSKIH LOKASTIH ŽIC NiTi IN DOLOČITEV ZNAČILNIH LASTNOSTI

Janko Ferčec[1], Matija Kos[1], Mihael Brunčko[1], Ivan Anžel[1], Branislav Glišić[2], Evgenija Marković[2], Rebeka Rudolf[1,3]

[1]Faculty of Mechanical Engineering, University of Maribor, Smetanova 17, 2000 Maribor, Slovenia
[2]School of Dentistry, University of Belgrade, Dr Subotiča 8, 11000 Belgrade, Serbia
[3]Zlatarna Celje, d. d., Kersnikova 19, 3000 Celje, Slovenia
rebeka.rudolf@um.si

The aim of this paper was to analyse the characteristic properties of six different, commercially available nickel-titanium orthodontic wires with a diameter of 0.305 mm (0.014"). The characteristic properties were determined by using semi-quantitative EDX analyses, DSC analyses for a determination of the phase temperatures, and a tensile test to obtain the mechanical properties of the wires. The investigation of the chemical composition showed an equiatomic NiTi alloy. Analyses of phase temperatures showed that the nickel-titanium orthodontic wires were, in an austenitic microstructure, exhibiting a superelastic effect in the oral environment. The uniaxial tensile stress–strain curves showed different values for the beginning and the end of the transformation range during the loading.

Keywords: NiTi wire, shape-memory alloy, phase transformation, thermal analysis, tensile test

Prispevek obravnava analizo karakterističnih lastnosti 6 komercialno dostopnih nikelj titanovih ortodontskih žic, ki imajo premer 0,305 mm (0,014") v fazi pred njihovo uporabo v ustih. V teh okvirih so bile analizirane mehanske lastnosti z enoosnim nateznim preizkusom, za določitev faznih temperatur pa je bila izvedena DSC-analiza ter semikvantitativna EDX-analiza. Dobljene enoosne krivulje napetost – raztezek so pokazale različne vrednosti začetka in konca transformacijskega območja pri obremenjevanju NiTi-žic. Analiza faznih temperatur je potrdila, da imajo ortodontske žice avstenitno mikrostrukturo, s čimer kažejo superelastični efekt, potem ko so v uporabi v ustnem okolju. Krivulja napetost-raztezek pri enoosnem nategu je pokazala različne vrednosti za začetek in konec transformacijskega območja med obremenjevanjem.

Ključne besede: NiTi-žica, zlitina s spominom oblike, fazna transformacija, termična analiza, natezni preizkus

1 INTRODUCTION

The use of the NiTi shape-memory alloy (SMA) in orthodontics began in 1970 when Andreasen started advocating their use in this field. The first orthodontic wire on the market was made by the Unitek Corporation (now 3M Unitek, Monrovia, CA, USA).[1,2] Today, NiTi wires are extensively used in orthodontics.

SMAs are unique materials with an ability to recover their shape when the temperature is increased. These materials show two special behaviours: the *Shape Memory Effect* (SME) and the *Superelastic Effect* (SE) (**Figure 1**). Both effects are characterised by a martensitic phase transformation, which is caused by changing the temperature (shape memory) or the application of stress (superelastic effect) leading to changes in the phase or microstructure. The austenite phase is stable at high temperatures and small stresses, and the martensitic phase is stable at low temperatures and high stresses. These two phases have different crystal structures. The austenitic phase has a body-centered cubic crystal structure, while the martensitic phase has a monoclinic crystal structure. The transformation from one structure to the other does not occur by diffusion of atoms. The transformation is caused by a shear lattice distortion. The martensitic transformation is known as a diffusion-less

transformation. The SME allows the alloy to return to its previous shape when it is heated above the A_f temperature. The SMA regains its original shape by transforming into the austenite phase. **Figure 1** shows the stress-strain-temperature diagram of a typical NiTi specimen tested under uniaxial loading in fully martensitic and
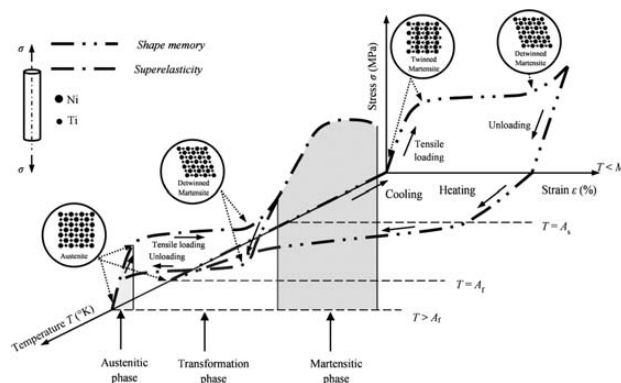

Figure 1: Stress-strain-temperature diagram exhibiting the Shape Memory and Superelastic effects of a NiTi alloy. Crystal transformation due to changing in temperature and stress.
Slika 1: Diagram napetost – raztezek – temperatura za zlitino NiTi z oblikovnim spominom in superelastičnim vedenjem. Kristalna pretvorba zaradi spremembe temperature in napetosti.

fully austenitic phases. The superelastic effect (SE) of the SMA is expressed above A_f. The SE is associated with a stress-induced transformation. **Figure 2** illustrates the superelastic effect. The SMA changes its microstructure from austenite to detwinned martensite when stress is applied. The SMA returns to its original shape when unloaded. The induced stress on unloading is less than that on loading, and the different paths between loading and unloading is referred to as hysteresis.[3–5]

The excellent biocompatibility and functional properties of SMA NiTi wires offer the possibility of their widespread use in orthodontics. In general, NiTi SMA wires show good corrosion properties. However, even though protective layers of TiO_2 are created on the surface of the wires, the release of nickel ions takes place. Biocompatibility studies suggest that SMA NiTi alloys have a low cytotoxity and genotoxicity.[6,7]

The orthodontic wire is a part of the fixed orthodontic appliance and its function is to deliver the optimal force on the tooth or the group of teeth. The optimum force used in an orthodontic treatment should be enough to produce tooth movement without tissue damage and pain. The NiTi SMA is used in the initial stage of the orthodontic treatment for teeth levelling and aligning. Low, continuous orthodontic forces are desirable, which is achieved by using wires with a low modulus of elasticity.[8–11] In this way, minimal periodontal tissue damage and maximum comfort for the patient are ensured.[12]

The objective of this paper was to analyse the functional and mechanical properties of different NiTi orthodontic wires used in orthodontic treatments. The correlation between the chemical composition and the functional properties, such as the temperatures of the phase transition and the stress-strain behaviour of wires, were investigated.
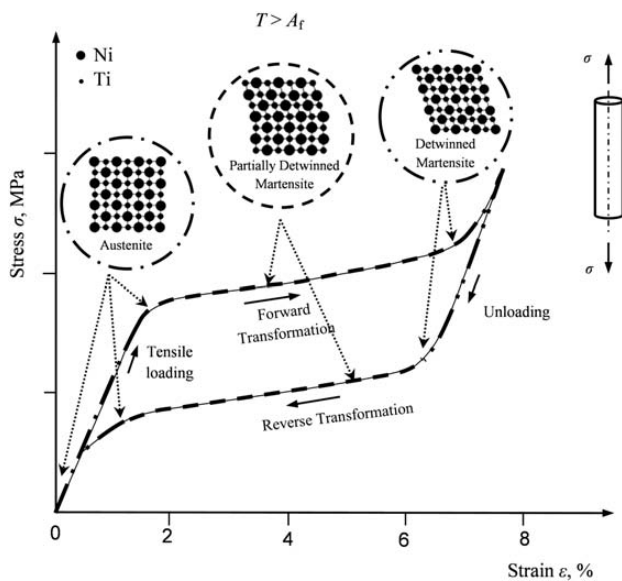
Figure 2: Schematic representation of the superelastic effect (stress-strain curve for SMA under uniaxial loading)
Slika 2: Shematski prikaz učinka superelastičnosti (krivulja napetost – raztezek za zlitine s spominom oblike pod enoosno obremenitvijo)

2 MATERIAL AND INVESTIGATION METHODS

New NiTi wires with a diameter of 0.305 mm (0.014"), taken from the original packaging, were used for the analyses (**Table 1**).

Table 1: Orthodontic wires from different producers included in the analyses
Tabela 1: Analizirane ortodontske žice različnih proizvajalcev

Orthodontic wire	Type of the wire
1	CuNiTi
2	Thermo-Active (NiTi)
3	NiTi
4	NiTi
5	Thermo (NiTi)
6	NiTi

2.1 EDX semi-quantitative chemical analysis

The SMA NiTi is characterized by an equiatomic proportion of nickel and titanium.[13] The chemical compositions of all six NiTi archwires were analysed on a longitudinal cross-section and on the surface of the wires. The electron microscope Sirion NC 400 with an energy-dispersive X-ray (EDX) detector was used to perform the semi-quantitative chemical microanalysis. The sample preparation for the EDX on the longitudinal section of wire was carried out in following way: 1) wire samples were cold mounted using the compound Varidur 200; 2) the samples were ground with SiC paper; P2500, and P4000; 3) the samples were polished with Chemomet polishing cloth with sized alumina polishing paste 0.05 μm; 4) the samples were cleaned in an ultra-sound appliance and, finally; 5) the samples were positioned in an aluminium holder with a graphite strip and inserted into the chamber of the microscope. The EDX analyses were made on 12 different sites on each wire (longitudinal cross-section and on the surface of the wire).

2.2 Phase-transformation temperature

The important temperatures of the phase transformations in the NiTi wires are M_s (martensite – start) and M_f (martensite – finish) as well as A_s (austenite – start) and A_f (austenite – finish). In some SMA materials an intermediate R-phase could be formatted with a rhombohedral crystal structure. The start of the phase formatting is known as R_s and the end as R_f[14–16].

Under stress-free conditions these temperatures are commonly measured using DSC (differential scanning calorimetry). In our experiments the specimens for the DSC analyses were cut from orthodontic wires. Each specimen for the DSC analyses consisted of approximately long piece of wire 3–4 mm. The DSC analyses were conducted on a STA 449 NETZSCH machine by using a liquid-nitrogen cooling accessory. The specimen was heated to 100 °C and then cooled to –100 °C to obtain the cooling DSC curve. After that, the specimen was heated from –100 °C back to 100 °C to obtain the heating DSC curve. The cooling rate was 10 °C/min, as normally used with SMA NiTi.

2.3 Stress-Strain Curve

NiTi alloys have specific mechanical properties. The stress-strain curve from a static tensile test depends on microstructure (austenite or martensite).[17,18] The tensile tests were performed using a Zwick/Roell ZO 10 machine (**Figure 3**) under the following conditions:

- ambient temperature of 22 °C,
- strain rate of 0.025 s⁻¹ (deformation velocity v = 1.5 mm/min),
- pre-load of 5 N.

The results are described in terms of the stress-strain (σ–ε) curve. The parameters considered as significant in describing the material behaviour of the curve are as follows: E_1 is the slope of the initial part of the loading curve (elastic modulus of austenite). E_2 is the slope of the transformation phase or region (austenite to martensite). E_3 is the slope of the final part of the curve (elastic modulus of austenite). σ_{SM} is the initial stress value of the transformation region or plateau. σ_{FM} is the final stress value of the transformation plateau. σ_f is the stress value at failure. ε_{SM} is the initial strain value of the transformation region or plateau. ε_{FM} is the final stress strain of the transformation plateau. ε_f is the strain value at failure.

One of most valuable properties of an ideal orthodontic archwire is good spring-back. This spring-back is the extent to which the activated wire is able to recover upon deactivation. In other words, wire may be deformed into loops or bends in complicated shapes employed to maximize their stored elastic energy and then return to their initial shape after deactivation.[2,19] Although SMAs can recover to their original austenitic phase, transformation and martensitic regions (up to the yield point of the material, where plastic deformation starts to fracture), orthodontic wires are almost never stressed in the mar-
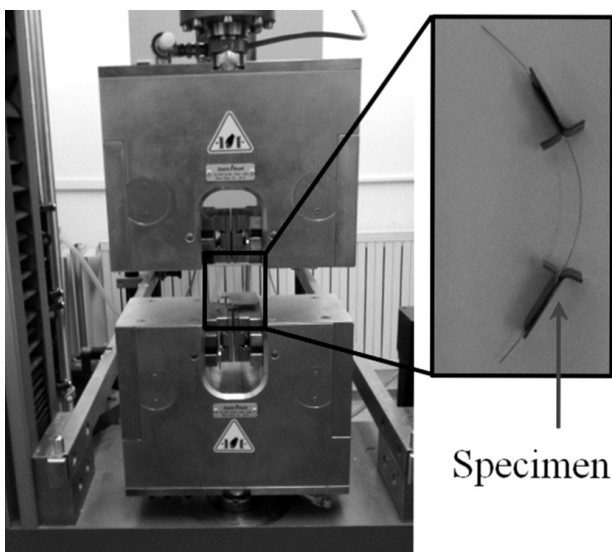
Figure 3: Tensile test for orthodontic wire with typical specimen
Slika 3: Natezni preizkus za ortodontsko žico z značilnim preizkušancem

tensitic region for orthodontic wire is just an important part, as shown in **Figure 2**[20].

3 RESULTS

3.1 EDX semi-quantitative chemical analysis

The average results of the EDX analyses are shown in **Table 2**, separately for the concentration of nickel and titanium in the longitudinal section (bulk material) and on the surface. A higher atomic fraction of nickel was found in the longitudinal section in three orthodontic wires (1, 3, 5). Moreover, in orthodontic wire 1 the atomic fraction of titanium was higher than nickel. In this wire the element Cu is added. Consequently, this alloy, when under stress, has a gentle and longer passage into the transformation area. Moreover, in wires 1 and 5 a difference in the content of Ni in the longitudinal section and on the surface was found, with a lower value of Ni. The manufacturing processes for the fabrication of NiTi wires is different and this is probably the reason for such findings. The other wires did not show any noticeable differences (max. about mole fraction x = 0.6 %).

Over 50 % of Ni was found in all wires, except in wire 1, where the Ni content is reduced by the presence of Cu. The Ni content in percentages is similar on the surface and in bulk (the noticeable difference is only visible in wire 2).

**Table 2:** Chemical composition on surface layer and bulk material of several NiTi wires in mole fractions, x/%
Tabela 2: Kemijska sestava površine in osnove Ni-Ti žic v molskih deležih, x/%

Ortho-dontic wire	Surface Layer			Bulk Material (longitudinal cross-section)		
	x(Ni)/% (± 0.1)	x(Ti)/% (± 0.1)	x(Cu)/% (± 0.1)	x(Ni)/% (± 0.1)	x(Ti)/% (± 0.1)	x(Cu)/% (± 0.1)
1	44.3	48.2	7.5	46.2	47.9	5.9
2	50.9	49.1	-	50.7	49.3	-
3	50.3	49.7	-	50.9	49.1	-
4	50.6	49.4	-	50.6	49.4	-
5	48.1	51.9	-	50.4	49.6	-
6	50.0	50.0	-	50.3	49.7	-

3.2 Phase-transformation temperature

Figure 4 presents the DSC plots for both the heating and cooling curves for separate orthodontic wires. All the curves on heating presented with temperatures A_f lower than 37 °C (body temperature), indicating an expression of the superelastic effect during an orthodontic treatment.

The temperatures of the phase transformation are presented in **Table 3**. The temperatures where there is full austenite stability are in the range from 14.3 °C to 26.8 °C. The R-phase appeared in the orthodontic wire 6. The temperatures where there is full martensite stability are in the range from –14.58 °C to –71.3 °C. Orthodontic wires 1, 4 and 6 begin their transition into the R phase or, respectively, into martensite, above 0 °C, while the temperature of the food consumed has the final influence
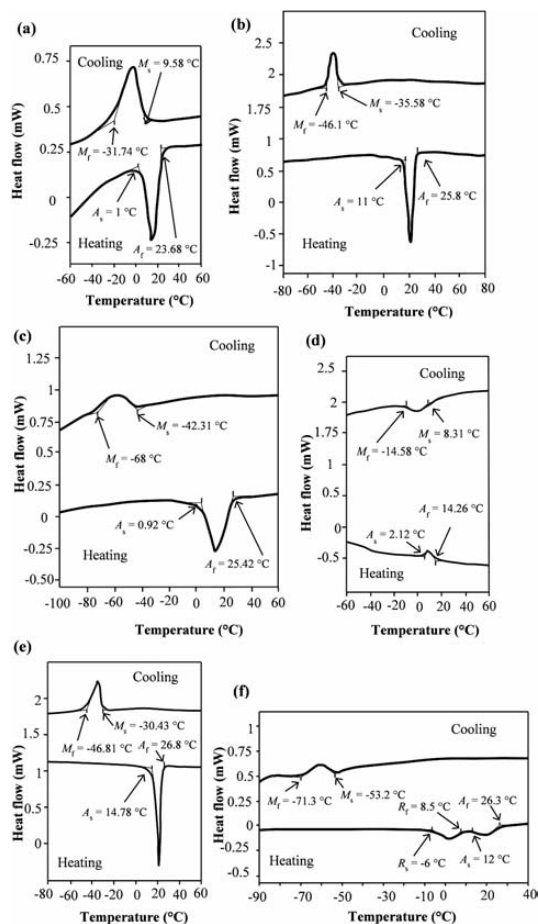
Figure 4: DSC curves and phase-transition temperatures for the orthodontic wire: a) orthodontic wire 1, b) orthodontic wire 2, c) orthodontic wire 3, d) orthodontic wire 4, e) orthodontic wire 5, f) orthodontic wire 6

Slika 4: DSC-krivulja in temperature faznih prehodov za ortodontsko žico: a) ortodontska žica 1, b) ortodontska žica 2, c) ortodontska žica 3, d) ortodontska žica 4, e) ortodontska žica 5, f) ortodontska žica 6

on the phase changes. This leads to changes of the SMA properties. Namely, these alloys, in the martensitic phase, show a lower modulus of elasticity, expressing higher forces on the teeth. In contrast to this, the consumption of food that warmer than body temperature causes the phase to change back to austenite, which is a consequence of stress increasing the passage into the transformation area (in accordance with the increasing temperature).

**Table 3:** Temperatures of phase transformation
Tabela 3: Temperature faznih prehodov

Ortho-dontic wire	M_f/°C	M_s/°C	R_s/°C	R_f/°C	A_s/°C	A_f/°C
1	−31.74	9.58	-	-	1.00	23.68
2	−46.10	−35.58	-	-	11.00	25.80
3	−68.00	−42.31	-	-	0.92	25.42
4	−14.58	8.31	-	-	2.12	14.26
5	−46.81	−30.43	-	-	14.78	26.80
6	−71.30	−53.20	−6.00	8.50	12.00	26.30

3.3 Stress-Strain Curve

Figure 5 shows the stress strain curve for each orthodontic wire. The results are presented in **Table 4**.

In **Figure 6a** the modulus of elasticity for the austenite, transformation and martensite phase is presented. The orthodontic wire 4 has the largest modulus of elasticity in the austenitic phase. The modulus of elasticity in the transformation phase of all the orthodontic wires is approximately at the same level varying from 3800 MPa to 6800 MPa. In an orthodontic treatment the desirable mechanical properties of the wires are changeable with regard to the treatment level. At the beginning of the treatment a low stiffness is important. At the end of orthodontic treatment, when the levelling stage is over and extensive tooth movement is needed, the stiffness of
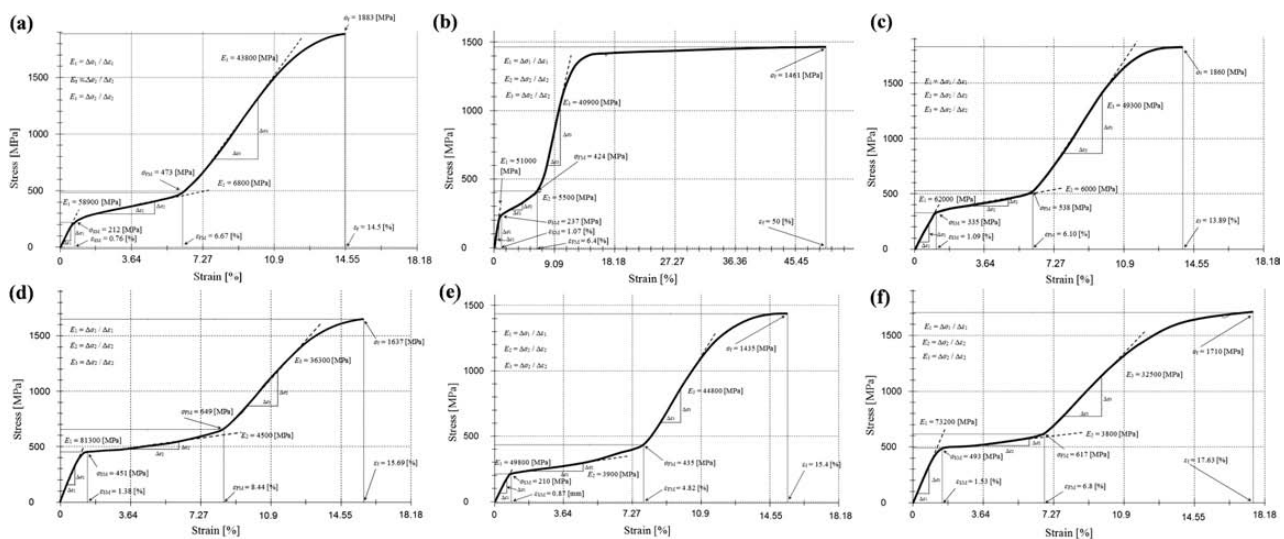
Figure 5: Characteristic parameters to describe material response, for a static-tensile test up to failure for the orthodontic wire: a) orthodontic wire 1, b) orthodontic wire 2, c) orthodontic wire 3, d) orthodontic wire 4, e) orthodontic wire 5, f) orthodontic wire 6

Slika 5: Značilni parametri za opis materialnega odziva pri nateznem preizkusu do porušitve ortodontske žice: a) ortodontska žica 1, b) ortodontska žica 2, c) ortodontska žica 3, d) ortodontska žica 4, e) ortodontska žica 5, f) ortodontska žica 6

Table 4: Comparison of mechanical properties of different, commercially available orthodontic wires during tensile test up to failure
Tabela 4: Primerjava mehanskih lastnosti različnih komercialno dostopnih ortodontskih žic med nateznim preizkusom do porušitve

| Orthodontic wire	E_1/MPa	E_2/MPa	E_3/MPa	σ_{SM}/MPa	σ_{FM}/MPa	σ_f/MPa	ε_{SM}/%	ε_{FM}/%	ε_f/%
1	58900	6800	43800	212	473	1883	0.76	6.27	14.5
2	51000	5500	40900	237	424	1461	1.07	6.4	50
3	62000	6000	49300	335	538	1860	1.09	6.10	13.89
4	81300	4500	36300	451	649	1637	1.38	8.44	15.69
5	49800	3900	44800	210	435	1435	0.87	7.82	15.4
6	73200	3800	32500	493	617	1710	1.53	6.8	17.63

the wire must be higher. For this reason, it is clear that the optimal mechanical properties of orthodontic wires are different during the course of an orthodontic treatment.

It is important for orthodontic wires to have a low modulus of elasticity in the initial stage of treatment, when low forces are needed. This is one of the reasons why SMA NiTi wires are used in the initial stage of an orthodontic treatment.

Another important factor in orthodontic treatment is to ensure the application of continuous forces. The SMA NiTi provides nearly continuous force in the transformations plateau. **Figure 6b** shows the initial strain value for the transformation ε_{SM} and the value of the final strain ε_{FM} of the transformation. The wires 4 and 5 show a wide range of transformation plateau or strain and a good spring-back.

Figure 6c shows a comparison of the initial stress value of the transformation plateau σ_{SM} and the final stress value of the transformation plateau σ_{FM}. The orthodontic wire 6 shows the largest stresses. The orthodontic wire 1 shows the lowest stress σ_{SM}.
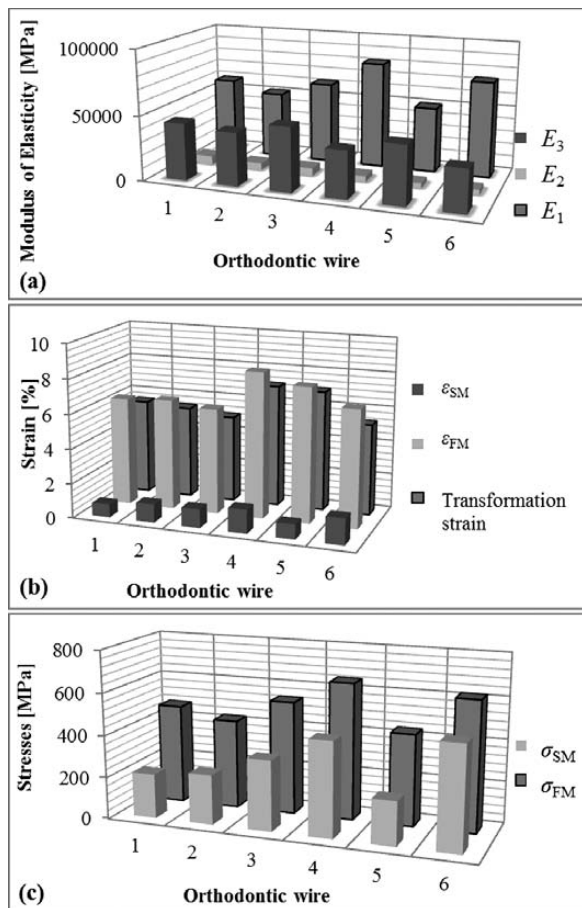
Figure 6: Comparison of orthodontic wires: a) modulus of elasticity for austenite E_1, transformation E_2 and martensitic E_3 phase; b) strain ε_{SM}, ε_{FM} and total transformation strain; c) experimental results for stress σ_{SM} and σ_{FM}
Slika 6: Primerjava ortodontskih žic: a) modul elastičnosti za avstenitno E_1, transformacijsko E_2 in martenzitno E_3 fazo; b) raztezek ε_{SM}, ε_{FM} in celotni transformacijski raztezek; c) eksperimentalni rezultati za napetost σ_{SM} and σ_{FM}

4 DISCUSSION

NiTi orthodontic wires have a complex metallurgical nature. The results of this paper show a correlation between the chemical composition, the phase transformation and the stress-strain curve of NiTi archwires used in orthodontic treatment. The investigation of the chemical composition showed a typical (equiatomic) composition for the nickel and the titanium in the SMA NiTi. The analysis of the phase-transformation temperatures of all six orthodontic wires showed that the temperature A_f, when the austenite phase is present, were below body temperature. All the wires exhibited a superelastic effect when they were used in the mouth. During the tensile test, the wires showed different elastic modulus, different slopes in the transformation phase and different martensite modulus. All of the wires showed the typical transformation plateau for SMA. Orthodontic wire 4 showed the maximum transformation plateau or strain (7.06 %). Whereas orthodontic wire 6 showed the least modulus of transformation plateau ($E = 3800$ MPa), which indicated the application of the lowest force on the teeth during orthodontic treatment.

The modulus of elasticity for the investigated wires was in the range between 49900 MPa and 81300 MPa in the austenitic phase, while in the transformation phase their values were between 3800 MPa and 6800 MPa. The modulus of elasticity for martensite phase are in the range between 40900 MPa and 49300 MPa.

In NiTi SMAs the influence of the chemical composition of the alloy is very important for the transformation temperatures and the connection between the transformation temperatures and the mechanical properties. Namely, the transformation temperature in the NiTi SMA depends on the content of nickel and titanium: increasing the nickel content decreases the A_f temperature. The values of A_f temperature in the NiTi

SMA change from 120 °C at 50 % Ni down to –40 °C at 51 % Ni[3]. A small change in the nickel content alters the A_f transformation temperature, above at which the SMA exhibits a superelastic behaviour.

The A_f temperature in orthodontic wire should be as similar as possible to body temperature (37 °C), namely, the SMA at this temperature shows a minimum stress (σ_{SM}) for the start of martensite transformation for the superelastic behaviour (wire 5 had the smallest difference between A_f and body temperature and minimum stress σ_{SM}). Decreasing the A_f temperature according to the body temperature increases the stress at which the SMA enters into the transformational plateau (wire 4 has the largest difference between A_f and body temperature and shows a large stress σ_{SM}).

In order to approach the necessary A_f temperature in the SMA for orthodontic wires it is necessary to have an accurate amount of nickel and titanium ($x = 50.3$ % up to 50.9 % Ni). Our uniaxial tensile tests were performed at ambient temperature (22 °C). The values for stress (σ_{SM}, σ_{FM}) increase with body temperature, while the modulus of elasticity stays unchanged.

The transformation strain decreases with temperature growing from the A_f temperature. Therefore, these are the greatest at the A_f temperature (wire 4 has a transformation strain of 7.06 % at room temperature 8 °C above the A_f temperature).

While the A_f temperatures of the other wires are higher than the temperature at which the tensile test has been performed, the transformation-induced strains are slightly different from those at body temperature. In **Table 4** we have listed the stress and strain at the rupture of the material; however, in orthodontic practice, such high stresses and strains are never achieved with the deformation of wires.

The rupture of the orthodontic wires is caused by the sudden changes of temperature in the mouth and, consequently, increasing stresses in the wire. The rapid changes of temperature in the mouth are provoked due to the ingestion of hot or cold foods or drinks. These temperatures can range from 2 °C to 60 °C. If the actual temperatures are below A_f, the stresses at which the martensitic transformation occurs are reduced and, therefore, the forces on the teeth are smaller. In contrast to this, at elevated temperatures (60 °C) the stress for the martensitic transformation (σ_{SM}) increases, which can lead to increased forces on the teeth. Temperature shocks in the mouth cannot be avoided, since they are part of everyday life in humans. In the orthodontic NiTi SMA wire it is important to minimize these shocks so that the wire is at its most effective to perform its function. For this, the mechanical properties, especially the superelasticity, are the most important.

5 CONCLUSIONS

In this work, for the first time, a combination of EDX, DSC and tensile-test analyses were used to deter-mine the correlation between the chemical composition, the phase temperatures and the stress-strain curves of different orthodontic wires. The result of this investigation are reflected in a determination of the functional property (super-elasticity), which is the most important property of orthodontic wires. Based on the obtained results, it could be concluded that such a complex review is especially useful for the users of wires (i.e., orthodontists), because it reduces the chances of making a decision about the wrong wire material for special orthodontics problems.

A connection between clinical dentistry and a knowledge of materials science is necessary in order to achieve a better understanding of the orthodontic wire's behaviour.

6 REFERENCES

[1] A. W. Brantley, T. Eliades, Orthodontic Materials: Scientific and Clinical Aspects, Georg Thieme Verlag, Stuttgart 2001, 77

[2] P. R. Kusy, Angle. Orthod., 67 (**1997**), 197–207

[3] D. C. Lagoudas, Shape Memory Alloy: Modelling and Engineering Applications, Springer, Texas (USA) 2008

[4] S. A. Thompson, Inter. End. J., 33 (**2000**), 297–310

[5] J. D. Fernandes, R. V. Peres, A. M. Mendes, C. N. Elias, ISRN Dent, 2011 (**2011**), 132408

[6] Mohammed Es-Souni, Martha Es-Souni, H. Fischer-Brandies, Anal. Bional. Chem., 381 (**2005**), 557–567

[7] G. Rahilly, N. Price, J. of Orthod., 30 (**2003**), 171–174

[8] Y. Ren, J. C. Maltha, A. M. Kuijpers-Jagtman, Angle. Orthod., 73 (**2003**), 86–92

[9] R. P. Kusy, A. M. Stush, Dent. Mater., 3 (**1987**), 207–217

[10] K. Reitan, P. Rygh, Current principles and techniques, Mosby, St. Louis 1994, 96

[11] J. Ferčec, B. Glišić, I. Šćepan, E. Marković, D. Stamenković, I. Anžel, J. Flašker, R. Rudolf, A. Phys. P. A, 122 (**2012**), 659–665

[12] M. A. Darendeliler, O. P. Kharbanda, E. K. Chan, P. Srivicharnkul, T. Rex, M. V. Swain, A. S. Jones, P. Petocz, Orthod. Craniofac, 7 (**2004**), 79–97

[13] K. Otsuka, X. Ren, Progress in Mat Science, 50 (**2005**), 511–678

[14] Y. Shen, H. M. Zhou, Y. F. Zheng, L. Campbell, B. Peng, M. Haapasalo, J. End., 37 (**2011**), 1566–1571

[15] W. A. Brantleya, M. Iijimaa, T. H. Grentzerc, Am. J. Orthod. Dentofacial. Orthop., 124 (**2003**), 387–394

[16] J. A. Shaw, C. B. Churchill, M. A. Iadicola, Exp. Tech., 33 (**2009**), 55–62

[17] J. Kłaput, AFE, 10 (**2010**), 155–158

[18] M. Arrigoni, F. Auricchio, V. Cacciafesta, L. Petrini, R. Pietrabissa, J. Phys., 11 (**2001**), 509–514

[19] A. Valiathan, S. Dhar, Artif. Organs., 20 (**2006**), 16–19

[20] W. R. Proffit, Contemporary Orthodontics, 4rd ed., Mosby, Elsevier, St. Louis 2007

APPLICATION OF FLAME RETARDANT MICROCAPSULES TO POLYESTER AND COTTON FABRICS

NANOS MIKROKAPSUL Z ZAVIRALCEM GORENJA NA POLIESTRNO IN BOMBAŽNO BLAGO

Barbara Golja[1], Boštjan Šumiga[2], Bojana Boh[2], Jožef Medved[3], Tanja Pušić[4], Petra Forte Tavčer[1]

[1]University of Ljubljana, Faculty of Natural Sciences and Engineering, Department of Textiles, Aškerčeva 12, 1000 Ljubljana, Slovenia
[2]University of Ljubljana, Faculty of Natural Sciences and Engineering, Department of Chemical Education and Informatics, Aškerčeva 12, 1000 Ljubljana, Slovenia
[3]University of Ljubljana, Faculty of Natural Sciences and Engineering, Department of Materials and Metallurgy, Aškerčeva 12, 1000 Ljubljana, Slovenia
[4]University of Zagreb, Faculty of Textile Technology, Pierottijeva 6, 10000 Zagreb, Croatia
barbara.golja@ntf.uni-lj.si

A microencapsulated fire retardant was used with the intention to produce fire retardant textiles. Melamine-formaldehyde polymer-wall microcapsules with a triphenyl phosphate core were applied to both a cotton woven and a polyester nonwoven fabric using impregnation and screen printing. The samples were observed with a scanning electron microscope (SEM). The combustion performance of the textile samples was examined with the limiting oxygen index (LOI) and the vertical burning test. The thermal properties of the microcapsules and fabrics were examined using TGA and DSC analyses. The mass per unit area, rigidity and air permeability of the treated fabrics were tested. The results show that the microcapsules with triphenyl phosphate can be successfully applied to cotton and polyester fabrics using screen printing and impregnation methods, but the fire retardation was successful only at the highest concentration of the microcapsules. At this concentration, the mechanical properties of the starting materials appear to deteriorate.

Keywords: polyester, cotton, textile, microcapsules, fire retardant, triphenyl phosphate

V raziskavi je bil uporabljen mikrokapsuliran zaviralec ognja z namenom ustvariti ognjevarno tekstilijo. Mikrokapsule z melamin-formaldehidno ovojnico in trifenil fosfatnim jedrom so bile uporabljene na bombažni tkanini in poliestrni vlaknovini z impregnacijo in filmskim tiskom. Vzorci so bili pregledani z elektronskim mikroskopom (SEM). Gorenje tekstilnih vzorcev je bilo preučeno z vrednostjo kisikovega indeksa (LOI) in vertikalnega preizkusa gorenja. Termične lastnosti mikrokapsul in blaga so bile preiskane z uporabo TGA- in DSC-analize. Pri obdelanih vzorcih je bila izmerjena ploščinska masa, togost in zračna prepustnost. Iz rezultatov je razvidno, da se da mikrokapsule s trifenil fosfatom uspešno aplicirati na bombaž in poliester z impregniranjem in tiskanjem, vendar pa je bilo zaviranje gorenja uspešno le pri najvišji koncentraciji mikrokapsul. Pri tej koncentraciji pa se mehanske lastnosti začetnih materialov očitno poslabšajo.

Ključne besede: poliester, bombaž, tekstil, mikrokapsule, zaviralec gorenja, trifenil fosfat

1 INTRODUCTION

There are many factors that influence the flammability of textiles. These factors are the composition of fibres; the construction of the yarn; the presence of certain finishes, dyes, impurities or detergent residues; the geometry or position of the material; the temperature; the relative humidity; the air flow; and the presence of oxygen. Various fibres react differently to a flame exposure.

To guarantee human safety, textiles can be treated with different fire retardants (FR). These are chemicals that reduce the flammability of the material to which they are applied.[1] Fire-retardant materials do not burn; however, these materials show certain physical and chemical changes after the removal of a flame source.[2]

Synthetic fibres may be rendered flame retardant during their production, thereby creating a degree of inherent flame retardancy. The retardant additives can be incorporated in the polymer melt/solution prior to extrusion or retardant molecules can be grafted onto the main polymeric chain.[3] The other way of protecting synthetic fibres, and the only way of protecting natural fibres, from burning is by applying suitable flame retardant finishes. The best and the most durable FRs for cellulose are those based on phosphorus (P) and nitrogen (N) that can react with the fibres or create a cross-linked structure on the fibres. Phosphorus and/or halogen compounds are among the fire retardants that confer good protection to polyester. Phosphorus compounds are therefore effective for use with both cotton and polyester fibres.[4] One such compound is triphenyl phosphate (TPP) (**Figure 1**).

TPP is widely used as a non-solvent plasticiser for cellulose acetate films, giving flexibility and toughness to the films; it is also an excellent FR agent and plasticiser for synthetic resins based on phenolics and phenylene oxide as well as formaldehyde in the production of
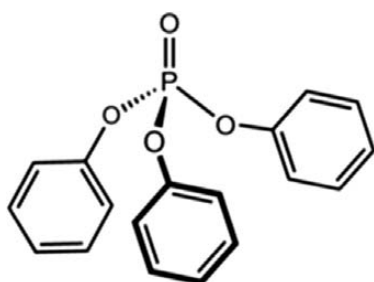
Figure 1: Structure of triphenyl phosphate
Slika 1: Struktura trifenil fosfata

stencil blanks, dopes, films, varnishes, plastics, lacquers, etc.[5] TPP breaks down in the flame to produce chemical species such as P_2, PO, PO_2 and HPO_2. These reactions reduce the hydrogen atom concentration in the vapour phase, thus extinguishing the flame.[6]

The techniques used for the flame retardant finishing of fabrics are mostly padding and coating. The disadvantages of applying retardants this way include the stiffness of the treated fabrics and negative effects on the colouring. One way to resolve this problem may be the use of microencapsulation. Microencapsulation is defined as "a technology of packaging solids, liquids or gaseous materials in miniature sealed capsules that can release (or not) their contents at controlled rates under the influence of specific conditions."[7] In this way, the active compounds are safely stored inside the capsules, isolated from their surroundings, and they are protected from any degrading factors.[8–11] In the last few years, there have been reports of applying microcapsules loaded with a fire retardant to textiles to provide a reliable protection from burning. Di-ammonium hydrogen phosphate (DAPH) is the compound used most often as a FR in such researches.[12–16] However, no paper describing the use of encapsulated TPP to protect textiles from burning was found.

The goal of our work was to prepare microcapsules with a triphenyl phosphate core and melamine-formaldehyde wall using the *in-situ* polymerisation method and to apply these microcapsules to cotton woven (CO) and polyester nonwoven fabrics (PES) (both are highly flammable) using screen printing and impregnation methods. The objective of the research was to determine whether the chosen fire retardant acts successfully on these two materials when encapsulated and whether the printing and impregnation methods of the microcapsule application provide a good fire retardant protection. The intention was to determine the optimum concentration of the microcapsules in the printing paste and in the impregnation bath. The flame retardancy of the samples was determined with a vertical burning test and a LOI analysis. The thermal behaviours of the microcapsules and fabrics were examined with thermogravimetric (TGA) and differential scanning calorimetry (DSC) analyses. The distribution, dimensions and form of the microcapsules on the printed and impregnated fabrics were observed using SEM. The fabric properties of the treated materials were tested with standardised methods.

2 EXPERIMENTAL WORK

2.1 Material

A bleached and mercerised 100 % cotton woven fabric (124 g/m² in mass, supplied by Tekstina, d. d., Slovenia) and a 100 % polyester nonwoven fabric (184 g/m² in mass, obtained from Filc, d. d., Škofja Loka, Slovenia) were used for the study. A suspension of the microcapsules (MC) with a size of 1–7 μm, a pressure-sensitive melamine-formaldehyde wall and a solid triphenyl phosphate core was prepared with an *in-situ* polymerisation of melamine-aldehyde prepolymers.[17] The suspension was added to the printing paste, composed of a synthetic polyacrylate thickener, Tubivis DRL 300, and a polyacrylate binder, Tubifast AS 30, both obtained from CHT, Germany. Padding binder FM/N (acrylic polymer solution from Minerva, Italy), in combination with an ammonium sulphate catalyst (Sigma Aldrich, Germany), dispersing agent Sinergil BT/N (Minerva, Italy) and an MC suspension, was used in the preparation of the impregnating baths.

2.2 Printing and impregnation

Table 1 presents the recipes for four printing pastes with an increasing quantity of MCs. Paste P4 was prepared with the highest concentration of microcapsules (600 g/kg) that still allowed its formulation. It was not possible to prepare a more concentrated paste due to the other required ingredients. The printing, drying and curing conditions are presented in **Table 2**.

Table 1: Printing paste recipes
Tabela 1: Recepture tiskarskih past

Component	Quantity (g/kg)			
	P1	P2	P3	P4
Polyacrylate thickener	34	34	34	34
Polyacrylate binder	150	150	150	150
MCs	0	200	400	600
Distilled water	816	616	416	216

Table 2: Printing, drying and curing conditions for the flat screen printing
Tabela 2: Razmere pri tiskanju, sušenju in fiksiranju pri ploskem filmskem tisku

Phase	Condition
Printing	Flat screen stencil: mesh of 43 threads/cm Printing speed: 80 % Squeegee diameter: 8 mm Magnet pressure: level 5 No. of passes: 2
Drying	Air drying
Thermal curing	Ernst Benz TKF 15-M500 drier, $T = 150$ °C, $t = 5$ min

Flat screen printing was performed on a laboratory magnetic printing machine, MINI MDF R 390, Johannes Zimmer AG (Austria). The area coverage of the printing paste on the cotton and felt cloth was approximately 25 cm × 35 cm.

Impregnation baths with an increasing quantity of MCs were prepared according to **Table 3**. Impregnation bath I4 was prepared with the maximum possible concentration of microcapsules (800 g/kg), which means that no distilled water was added. It was not possible to prepare a more concentrated bath due to the other required ingredients. The impregnation, drying and curing conditions are presented in **Table 4**.

The impregnation was performed on the Mathis 2-roll horizontal laboratory foulard (Switzerland).

Table 3: Impregnation bath formulas
Tabela 3: Recepture impregnirnih kopeli

Component	Quantity (g/kg)			
	I1	I2	I3	I4
Binder	140	140	140	140
Catalyst (water-to-catalyst ratio 2:1)	10	10	10	10
Dispersing agent	50	50	50	50
MCs	0	200	400	800
Distilled water	800	600	400	0

Table 4: Impregnation, drying and curing conditions
Tabela 4: Razmere pri impregniranju, sušenju in fiksiranju

Phase	Condition
Padding	Wet pick up of 100 % – cotton fabric Wet pick up of 330 % – polyester felt No. of passes between rolls: 1
Drying	Air drying
Thermal curing	Ernst Benz TKF 15-M500 drier, $T = 150$ °C, $t = 3$ min

The abbreviations of all the samples used in this study are listed in **Table 5**.

Table 5: Abbreviations of the samples
Tabela 5: Okrajšave oznake vzorcev

Abbr.	Sample	Abbr.	Sample
PES	PES fabric – untreated	CO	CO fabric – untreated
PESp0	PES printed without MC	COp0	CO printed without MC
PESi0	PES impregnated without MC	COi0	CO impregnated without MC
PESp200	PES printed with 200 g/kg MC	COp200	CO printed with 200 g/kg MC
PESi200	PES impreg. with 200 g/kg MC	COi200	CO impreg. with 200 g/kg MC
PESp400	PES printed with 400 g/kg MC	COp400	CO printed with 400 g/kg MC
PESi400	PES impreg. with 400 g/kg MC	COi400	CO impreg. with 400 g/kg MC
PESp600	PES printed with 600 g/kg MC	COp600	CO printed with 600 g/kg MC
PESi800	PES impreg. with 800 g/kg MC	COi800	CO impreg. with 800 g/kg MC

2.3 Analysis

2.3.1 Washing

The samples were laundered for 30 min at 40 °C according to the ISO 105-C01:1989 (E) standard, using a soap solution (5 g/l of soap) with pH 7 and a liquor-to-fabric ratio of 50 : 1.

2.3.2 SEM observations

The uniformity of the deposit, size and morphological characteristics of MCs on the finished fabrics were observed with a scanning electron microscope (Jeol JSM 606). The samples were coated with gold.

2.3.3 Combustion test

The combustion performance was studied with the LOI and the vertical burning test. The LOI was measured using a limiting oxygen index chamber (Dynisco, USA) according to standard ASTM D 2863. The vertical burning test was performed in the burning chamber according to the DIN 53906 standard.

2.3.4 Thermal properties of microcapsules and the fabrics treated with microcapsules – TGA and DSC analyses

The samples were examined with a 449c Jupiter instrument (NETZSCH). The samples were placed on Al_2O_3 carriers. They were heated in a protective atmosphere (air) and the measurements were performed from 35–650 °C at a heating rate of 10 K/min. The samples were then cooled at 10 K/min to room temperature.

2.3.5 Fabric properties

The fabric mass per unit area was determined according to the SIST EN 12127:1999 standard, and the fabric air permeability was determined according to the SIST EN ISO 9237:1999 standard.

3 RESULTS AND DISCUSSION

3.1 SEM micrographs

There are differences in the structure between the cotton woven fabric and polyester nonwoven fabric because of different ways, in which they are made. The cotton woven fabric is made in a weaving process, where the yarns are packed close together with high forces and the fabric is therefore thin, smooth and compact, with the structure in good order. The polyester nonwoven fabric is made in a process of needle-punching directly from the fibres, with less tension during the production and it is therefore thicker, more porous and hairy, having a disordered structure. These structural differences influence the absorption and retention of added substances.

The micrographs in **Figure 2** present the impregnated and printed cotton and polyester samples. Many microcapsules are present on the fabrics; they are round in shape and not damaged. The microcapsules are more evenly distributed on the woven CO samples (**Figures**
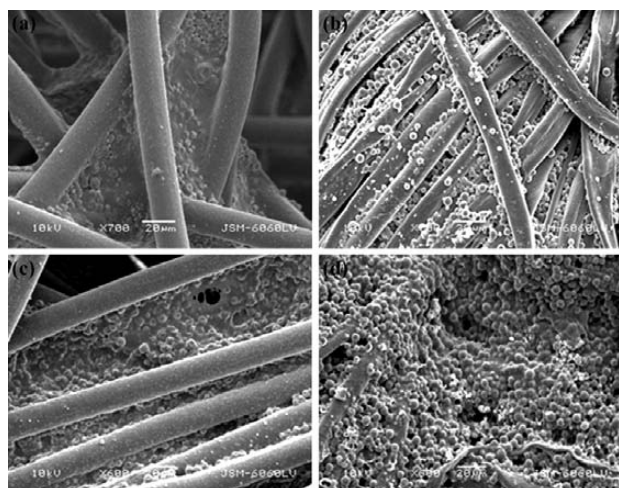
Figure 2: SEM micrographs of: a) PESi400, b) COi400, c) PESp400 and d) COp400
Slika 2: SEM-posnetki vzorcev: a) PESi400, b) COi400, c) PESp400 in d) COp400

2b and **d**) than on the nonwoven PES samples (**Figures 2a** and **c**). Because of the porous structure of the non-woven PES, the microcapsules are captured in the nooks among the fibres and only a few microcapsules are located on the fibres. The printed CO sample (**Figure 2d**) is almost completely covered with microcapsules, while the impregnated CO sample has fewer micro-capsules on the surface (**Figure 2b**). This effect is due to the printing process (the paste was applied onto the fabric horizontally with a squeegee) and the rheological properties of the paste (thixotropy), which prevented the capsules passage through the yarn during printing. Impregnating, on the other hand, is a mechanical process that allows the products to pass through a yarn, so it seems that most of the microcapsules are located in the inner part of the yarn of the impregnated fabric.

3.2 Combustion tests (the vertical burning test and LOI)

The results of the vertical burning test and LOI are shown in **Tables 6** and **7**, respectively. **Figure 3** repre-sents the untreated and treated PES and CO samples after the burning test.

The upward burning behaviour shows that the PES samples burn longer than the CO samples and do not glow, whereas the CO samples glow longer than they burn. An addition of TPP microcapsules prolongs the burning time of the PES samples, while it has no influ-ence on the burning time of the cotton samples with less than 800 g/kg of microcapsules. The samples of cotton burned through their whole length, so that there was no residual cloth left, only some ash. In the case of PES, the flame did not spread over the whole length of the sample, so that there was some unburned fabric. Neither material burned when impregnated with 800 g/kg of microcapsules (PESi800, COi800), as they were both

self-extinguishing (**Figure 3**). These samples were tested for the LOI. Both had an LOI of 25, meaning that the ignition and burning were slowed down. The LOI should be at least 26 to consider the samples to be flame retardant. The washed samples had a lower LOI of 24, most likely due to the removal of some microcapsules during the washing process.

Table 6: The results of the vertical burning test of the printed and impregnated samples with different quantities of the applied micro-capsules
Tabela 6: Rezultati vertikalnega preizkusa gorljivosti tiskanih in impregniranih vzorcev z različno količino nanesenih mikrokapsul

Sample	Burning time (s)		Glow time (s)	
	unwashed	washed	unwashed	washed
PES	14	15	0	0
PESp0	50	44	0	0
PESi0	44	33	0	0
PESp200	90	114	0	0
PESi200	50	43	0	0
PESp400	80	117	0	0
PESi400	50	37	0	0
PESp600	50	33	0	0
PESi800	0	5	0	0
CO	12	9	20	7
COp0	5	3	20	30
COi0	7	6	25	20
COp200	5	5	40	44
COi200	8	9	20	10
COp400	19	9	9	15
COi400	16	11	3	8
COp600	15	10	10	13
COi800	0	9	0	0
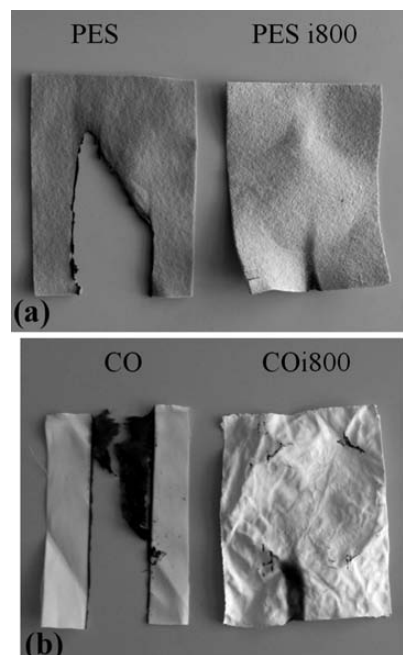
Figure 3: Samples of the untreated and impregnated fabrics after the vertical burning test: a) PES and b) CO
Slika 3: Neobdelani in impregnirani vzorci po vertikalnem preizkusu gorenja: a) PES in b) CO
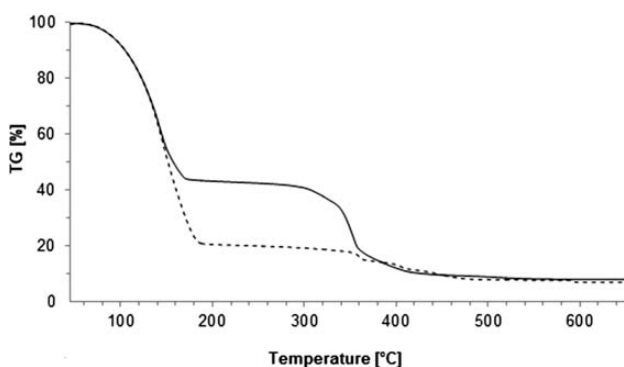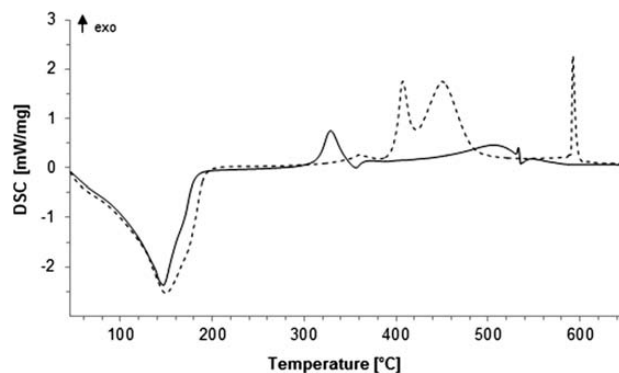
Table 7: Results of the LOI test of the unwashed and washed samples impregnated with the maximum concentration of microcapsules
Tabela 7: Rezultati preizkusa LOI neopranih in opranih vzorcev, impregniranih z najvišjo koncentracijo mikrokapsul

Sample	LOI (%)	Time of burning (s)
PESi800	25	180
PESi800 washed	24	120
COi800	25	60
COi800 washed	24	70

3.3 TGA and DSC analyses

Figures 4 and **5** represent the TGA and DSC curves of the suspensions of the microcapsules with and without a TPP core, composed only of melamine resin (a blend). The TGA curves reveal that both suspensions show a substantial weight loss, starting at 80 °C, due to water evaporation. The decrease in the weight stops at approximately 180 °C for both suspensions, indicating additional polycondensation reactions of the melamine-formaldehyde resin in the walls of the microcapsules and, most likely, an evaporation of formaldehyde along with the water. The weight loss at this temperature is much higher for the microcapsules without a core because the suspension with TPP microcapsules is more concentrated than the suspension with blind microcapsules; consequently, more water evaporated from the second sample. TPP microcapsules start to degrade at 320 °C, whereas blind microcapsules start to degrade later, at 360 °C. The decomposition finishes, for both MC types, at approximately 420 °C. A further increase in the temperature does not change the weight of the samples.

The DSC diagram (**Figure 5**) shows an endothermic peak at 150 °C, confirming the evaporation of water and formaldehyde from the suspensions of microcapsules. Blind MCs show high exothermic peaks at (410, 450 and 590) °C, indicating different degrading products of the melamine-resin wall material. TPP microcapsules have a small exothermic peak at 330 °C and no other exothermic peak arises with the increasing temperature. The released heat is, therefore, much lower with TPP than with blind microcapsules. We also assume that the degra-
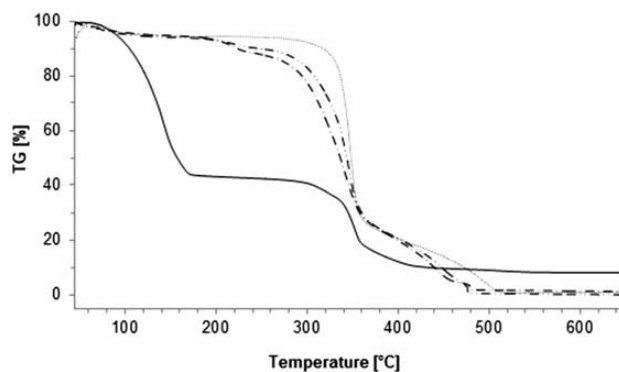

Figure 5: DSC curves of the samples: TPP MCs (——), MCs without a core (- - -)
**Slika 5:** DSC-krivulje vzorcev: TPP MC (——), MC brez jedra (- - -)

dation at 330 °C releases the flame retarding products, hindering further burning or oxidation of the surroundings.

In **Figures 6** to **9**, we can see the TGA and DSC curves of the untreated cotton and polyester and also both samples printed or impregnated with TPP MC. All the diagrams also present a curve of the TPP MC suspension.

At first glance, we can see that the TGA curves for all of the textile samples are very similar. The curve of the suspension deviates from dry samples because of the evaporation of water at the temperatures below 180 °C. All of the CO samples lost their weight at the lower temperatures (330 °C) than the PES samples (400 °C). The printed samples degrade earlier than the raw materials, and the impregnated ones that carry more MCs degrade even earlier. The TPP MCs start to degrade at lower temperatures than the surrounding material, and the degradation products such as P_2, PO, PO_2 and HPO_2 in the vapour phase extinguish the flame. Consequently, if there are more microcapsules on the material, the degradation starts earlier and the flame retardancy is stronger.

The DSC curves in **Figures 7** and **9** confirm that the presence of MCs on the textile materials changes their

Figure 4: TG curves of the samples: TPP MCs (——), MCs without a core (- - -)
Slika 4: TG-krivulje vzorcev: TPP MC (——), MC brez jedra (- - -)

Figure 6: TG curves of the samples: TPP MC (——), CO (······), COi800 (–··–), COp400 (–··–)
Slika 6: TG-krivulje vzorcev: TPP MC (——), CO (······), COi800 (–··–), COp400 (–··–)
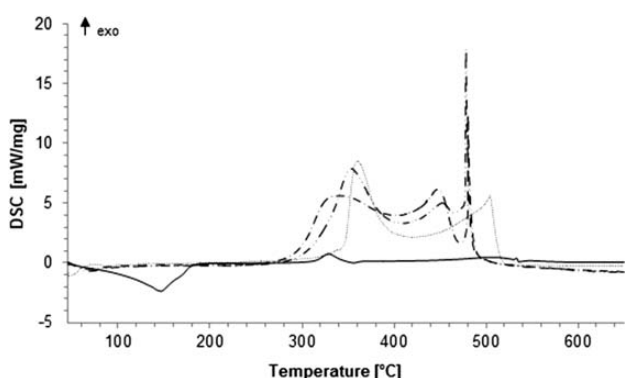
Figure 7: DSC curves of the samples: TPP MC (——), CO (······), COi800 (–·–), COp400 (–··–)
Slika 7: DSC-krivulje vzorcev: TPP MC (——), CO (······), COi800 (–·–), COp400 (–··–)

Figure 9: DSC curves of the samples: TPP MC (——), PES (······), PESi800 (–·–), PESp600 (–··–)
Slika 9: DSC-krivulje vzorcev: TPP MC (——), PES (······), PESi800 (–·–), PESp600 (–··–)

properties. The printed cotton fabric has lower exothermic peaks, starting at lower temperatures than the raw cotton fabric; even lower are the exothermic peaks of the impregnated samples with more MCs on their surfaces. The microcapsules decrease the heat released from the cotton fabric. A similar picture is seen for the PES fabrics. The exothermic peak is the highest for the untreated PES. The PES samples impregnated or printed with MCs have lower peaks than the untreated sample. Both are very similar. The microcapsules decrease the heat release from the PES fabric as well.

A comparison of **Figures 7** and **9** also demonstrates how different the behaviours of cotton and polyester fibres are at high temperatures. Natural CO fibres degrade gradually in several oxidation reactions, represented by several broad peaks on the DSC curve, whereas synthetic PES fibres degrade almost instantly at higher temperatures. The DSC curve shows one high, sharp peak at approximately 520 °C.
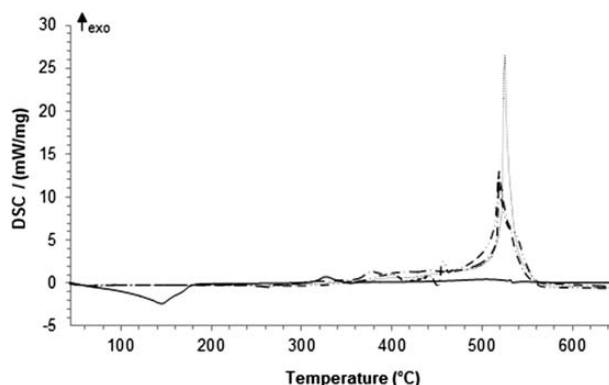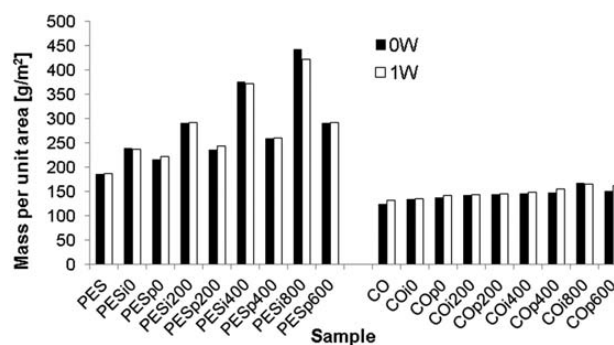
3.4 Fabric properties

The mass per unit areas of raw, printed, impregnated and washed samples are presented in **Figure 10**. The

differences in the structure between the woven and nonwoven fabrics influence different absorption and retention parameters of the added substances.

The mass per unit area of the untreated PES samples (184 g/m^2) is higher than that of the untreated CO samples (124 g/m^2). The higher mass and more porous structure of PES enable a greater absorption of the microcapsules from the printing paste and an even higher absorption from the impregnation bath. The highest addition of MCs can be observed on the impregnated PES samples, which also show the best flame retardancy. The compact cotton fabric does not enable a high accumulation of MCs. The mass per unit area increases with the increasing amount of the microcapsules in the impregnating baths and/or printing pastes and it is more pronounced in the PES samples than in the CO samples.

The air permeability (**Figure 11**) of the polyester samples is much higher than that of the cotton samples. The permeability of both evidently decreases with higher amounts of the applied microcapsules. Again, there are larger differences among the polyester samples than among the cotton samples due to higher deposits from the impregnation and/or the printing system on the polyester. For both materials, PES and CO, the impregnated samples have a better air permeability than the printed

Figure 8: TG curves of the samples: TPP MC (——), PES (······), PESi800 (–·–), PESp600 (–··–)
Slika 8: TG-krivulje vzorcev: TPP MC (——), PES (······), PESi800 (–·–), PESp600 (–··–)

Figure 10: Mass per unit areas of impregnated, printed, unwashed and washed PES and CO samples
Slika 10: Ploščinska masa impregniranih, tiskanih, nepranih in pranih PES- in CO-vzorcev
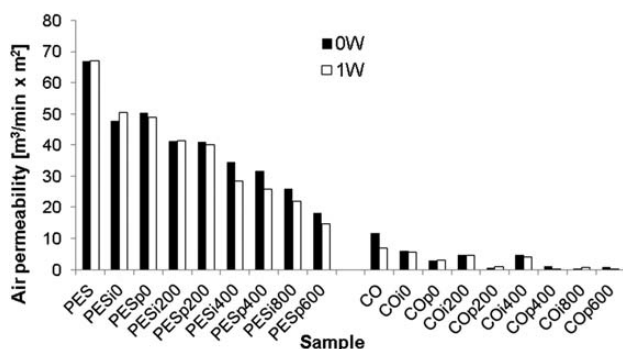
Figure 11: Air permeability of impregnated, printed, unwashed and washed PES and CO samples
Slika 11: Zračna prepustnost impregniranih, tiskanih, nepranih in pranih PES- in CO-vzorcev

ones. Printing on the polymer created a relatively impermeable layer on the samples, while a large quantity of the MCs applied on them led to further impermeability.

All the printed and impregnated samples had a very high rigidity; the rigidity of the impregnated samples was so high that it could not be accurately measured in this study.

4 CONCLUSIONS

Fire retardant triphenyl phosphate was encapsulated via an *in-situ* polymerisation method. The produced microcapsules were round in shape, undamaged and 1–7 μm in size, and they were successfully applied to cotton woven and polyester nonwoven fabrics using screen printing and impregnation techniques.

An addition of TPP microcapsules prolongs the burning time of the PES samples, while it has no influence on the burning time of the CO samples with less than 800 g/kg of the microcapsules. Neither of the materials burned when impregnated with the maximum concentration of microcapsules, 800 g/kg. The LOI of these samples (25) showed that the ignition and burning decreased, but they were not sufficiently disabled for these materials to be considered fire retardant.

The TGA analysis shows that with more microcapsules on the material the degradation starts earlier and the flame retardancy is stronger. The DSC curves reveal that on both PES and CO samples the microcapsules decrease the heat release from the fabric.

Structural differences between the cotton woven fabric and the polyester nonwoven fabric influenced different absorptions of the microcapsules and their contributions. The mass per unit area increased with the increasing amount of the microcapsules in the impregnating baths and/or the printing pastes and was more pronounced in the PES samples than in the CO samples. The impregnated PES samples absorbed the highest amount of MCs and showed the best flame retardancy. The air permeability of both samples decreased with the application of the microcapsules and the rigidity increased drastically.

The results show that the investigated processes are not yet appropriate for practical use and that more research is needed to improve the fire-retardant properties of triphenyl phosphate microcapsules and their influence on the textile properties of the treated fabrics.

5 REFERENCES

[1] D. Katović, S. Flinčec Grgac, S. Bischof - Vukušić, A. Katović, Fibres & Textiles in Eastern Europe, 20 (**2012**) 1, 94

[2] A. R. Horrocks, JSDC, 99 (**1983**), 191

[3] A. R. Horrocks, D. Price, Advances in fire retardant materials, Woodhead Publishing Limited, Cambridge 2008, 25

[4] K. H. Pawlowski, B. Schartel, Polymer International, 56 (**2007**), 1404

[5] P. Forte Tavčer, E. Magovac, B. Šumiga, B. Boh, S. Bischof Vukušić, Treatment of cotton fabric with encapsulated flame-retardant triphenylphospate, Book of abstracts of the 42nd Symposium on Novelties in Textiles, Ljubljana, 2011, 40

[6] A. R. Horrocks, D. Price, Fire retardant materials, Woodhead Publishing Limited, Cambridge 2001, 50

[7] A. K. Anal, W. F. Stevens, C. Remuñán-López, International Journal of Pharmaceutics, 312 (**2006**), 166

[8] G. Nelson, International Journal of Pharmaceutics, 242 (**2002**), 55

[9] M. M. Miró Speco, S. G. Escobar, P. Marino, C. Puggia, M. V. Defain Tesoriero, L. Hermida, Journal of industrial textiles, 40 (**2010**) 1, 13

[10] B. Ocepek, B. Boh, B. Šumiga, P. Forte Tavčer, Coloration technology, 128 (**2012**), 95

[11] R. Badulescu, V. Vivod, D. Jaušovec, B. Vončina, Carbohydrate polymers, 71 (**2008**), 85

[12] S. Giraud et al., Journal of Industrial Textiles, 31 (**2001**), 11

[13] S. Giraud et al., Polymer degradation and Stability, 77 (**2002**), 285

[14] S. Giraud et al., Polymer degradation and Stability, 88 (**2005**), 106

[15] S. Giraud, F. Salaun, I. Vroman, S. Bourbigot, Polymer degradation and Stability, 95 (**2010**), 315

[16] I. Vroman, S. Giraud, S. Bourbigot, Polymer degradation and Stability, 95 (**2010**), 1716

[17] B. Šumiga et al., Patent SI 23760 A, Aero, d. d., 2012

ISOTHERMAL SOLIDIFICATION DURING TRANSIENT LIQUID-PHASE BONDING OF GTD-111/Ni-Si-B/GTD-111

IZOTERMNO STRJEVANJE MED SPAJANJEM GTD-111/Ni-Si-B/GTD-111 S PREHODNO TEKOČO FAZO

Majid Pouranvari

Young Researchers and Elite Club, Dezful Branch, Islamic Azad University, Dezful, Iran
mpouranvari@yahoo.com

A prediction of the required time to ensure the completion of isothermal solidification (t_{IS}) can serve as a first step toward the optimization of a transient-liquid-phase (TLP) process to achieve a eutectic-free joint. The objective of this study is to estimate the required bonding time to obtain an intermetallic-free joint centerline during the TLP bonding of a cast GTD-111 nickel-based superalloy using a Ni-4.5Si-3.2B (mass fractions, $w/\%$) amorphous interlayer. Considering the solidification behaviour of the residual liquid, t_{IS} could be predicted by a mathematical solution of the time-dependent diffusion equation based on Fick's second law.

Keywords: transient-liquid-phase bonding, isothermal solidification, superalloy, GTD-111

Napovedovanje potrebnega časa za zagotavljanje poteka izotermnega strjevanja (t_{IS}) se lahko uporablja kot prvi približek za optimizacijo postopka spajanja s prehodno tekočo fazo (TLP) za doseganje spojev brez evtektika. Namen te študije je ugotoviti potreben čas spajanja za doseganje srednje linije spoja brez intermetalnih faz med TLP-spajanjem nikljeve GTD-111 super-zlitine s strjevalno strukturo z uporabo Ni-4,5Si-3,2B (masni deleži, $w/\%$) amorfne vmesne plasti. Z upoštevanjem vedenja preostale taline pri strjevanju je mogoče t_{IS} napovedati z matematično rešitvijo časovne odvisnosti difuzijske enačbe, ki temelji na drugem Fickovem zakonu.

Ključne besede: spajanje s prehodno tekočo fazo, izotermno strjevanje, superzlitina, GTD-111

1 INTRODUCTION

Nickel-based superalloys are used extensively in modern industry due to their excellent high-temperature tensile strength, stress rupture and creep properties, fatigue strength, oxidation and corrosion resistance, and microstructural stability at elevated temperature.[1–3]

Transient-liquid-phase (TLP) bonding is considered as an interesting repairing/joining process for nickel-based superalloys due to its ability to produce near-ideal joints.[4–12] The TLP process nominally involves three stages: (i) when heated, the braze melts and begins to dissolve the substrate; (ii) the liquid composition reaches the liquidus and isothermal precipitation of the equilibrium solid begins; (iii) the liquid is eliminated by diffusion of the melting-point modifiers into the substrate (i.e., isothermal solidification).[13,14]

The typical microstructure of a TLP bonded joint of a nickel-based precipitation-hardened superalloy such as GTD-111 using a boron-containing interlayer, consists of three distinct microstructural zones, before completion of the isothermal solidification (**Figure 1**):[6–9]

- the Athermally Solidified Zone (ASZ), which usually consists of an intermetallic formed during a eutectic reaction. This zone is formed due to there being insufficient time for completion of the isothermal solidification. Cooling is the main driving force for athermal solidification (i.e., non-isothermal solidification).

- the Isothermally Solidified Zone (ISZ), which usually consists of a solid-solution phase. A compositional change induced by interdiffusion between the substrate and the interlayer during holding at a constant bonding temperature is the driving force for the isothermal solidification. As a result of the absence of solute rejection at the solid/liquid interface during isothermal solidification under equilibrium, the formation of a second phase is basically prevented.[7,8]

- the Diffusion Affected Zone (DAZ), which consists of boride precipitates due to boron diffusion into the base metal (BM) during the TLP bonding.

For the commercial application of TLP bonding, the appropriate holding time required for complete isothermal solidification (t_{IS}) should be determined to obtain
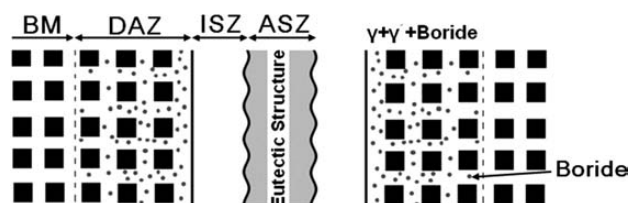
Figure 1: Schematic representation of various microstructural zones in a TLP-bonded γ'-strengthened nickel-based superalloy before isothermal solidification completion
Slika 1: Shematski prikaz mikrostrukture v različnih območjih v TLP spajani superzlitini na osnovi niklja z γ'-delci za utrjevanje pred koncem izotermnega strjevanja

the proper bond microstructure. When the holding time is lower than t_{IS}, athermal solidification of the residual liquid phase may lead to intermetallic formation, which in turn degrades the mechanical strength, service temperature and corrosion resistance of the bonds compared to the base metal.[4–10]

In this paper a diffusion model based on a migrating interface is used to predict the isothermal solidification completion time during the TLP bonding of a GTD-111 nickel-based superalloy and the predicted value was compared with experimental data.

2 EXPERIMENTAL PROCEDURE

The GTD-111 superalloy, as the base metal, was used in the standard heat-treatment condition in this investigation. The chemical composition of the GTD-111 was Ni-13.5 Cr-9.5 Co-4.75 Ti-3.3 Al-3.8 W-1.53 Mo-2.7 Ta-0.23 Fe-0.09 C. A commercial Ni-4.5Si-3.2B alloy (MBF30), in the form of amorphous foil with 25.4 μm thickness, was used as the interlayer. Coupons of 10 mm × 5 mm × 5 mm were sectioned using an electro-discharge machine. To remove the oxide layer, contact surfaces were ground using 600-grade SiC paper and then cleaned ultrasonically in an acetone bath. The

(a)

(b)

Figure 2: a) Microstructure gradient in TLP-bonded GTD-111 using Ni-Si-B filler alloy at 1100 °C for 30 min, b) fracture surface of the TLP bonded sample after partial isothermal solidification
Slika 2: a) Spreminjanje mikrostrukture v TLP-spoju GTD-111 z uporabo Ni-Si-B-zlitine polnila 30 min pri 1100 °C, b) površina preloma s TLP spojenega vzorca po delnem izotermnem strjevanju

interlayer was then inserted between two base metal coupons. A stainless-steel fixture was used to fix the coupons in order to hold the sandwich assembly and reduce the metal flow during the TLP operation. The liquidus and solidus temperatures of the interlayer are 1054 °C and 894 °C, respectively.[15] The bonding was carried out at 1100 °C for (30, 45, 60 and 75) min under a vacuum of approximately 1.33×10^{-4} mbar in a vacuum furnace.

The bonded specimens were sectioned perpendicular to the bond. The microstructure of the joints was studied using an optical microscope and a scanning electron microscope (SEM). For the microstructural examinations the specimens were etched using two etchants. The Murakami etchant (10 g KOH, 10 g $K_3[Fe(CN)_6]$, 100 ml H_2O) preferentially etches the Cr-rich phases and can therefore be used to reveal precipitates adjacent to the joint/base metal interface. The molybdenum-acid etchant (0.5 g MoO_3, 50 ml HCl, 50 ml HNO_3, 200 ml H_2O), which preferentially etches the γ'-phase, was used to indicate the γ-γ'-microstructure of the joints. Semi-quantitative chemical analyses of the phases formed in the joint region were conducted on a Cam Scan scanning electron microscope, equipped with a beryllium-window energy-dispersive spectrometer (EDS) system using INCA software.
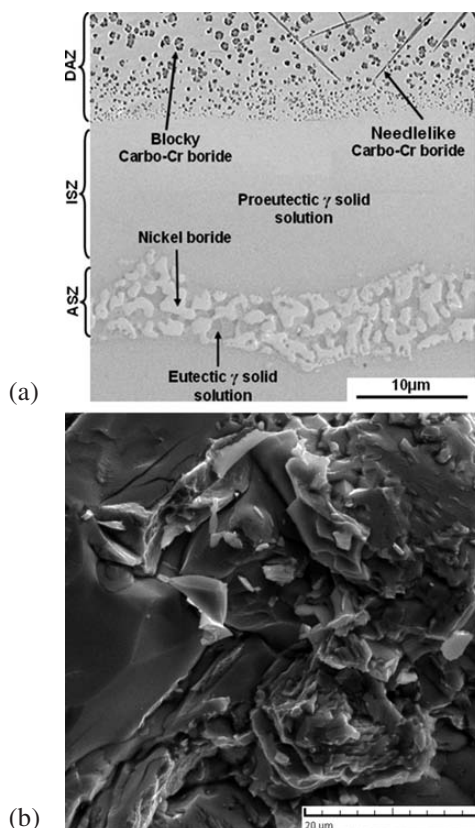
3 RESULTS AND DISCUSSION

3.1 Microstructure of the bond

The microstructure of the TLP-bonded GTD-111/ Ni-Si-B/GTD-111 is detailed elsewhere.[4,6] In this section a summary of the results is presented. **Figure 2a** shows an SEM image of the bonds made at 1100 °C for 30 min, indicating three distinct microstructural zones in the bond region including (i) an isothermal solidification zone (ISZ), (ii) a diffusion-affected zone (DAZ) and (iii) an athermal solidification zone. The formation of these zones can be explained as follows:

Since the bonding temperature (i.e., 1100 °C) is higher than the liquidus temperature of the Ni-Si-B filler alloy (i.e., 1055 °C), the interlayer melts. Three transportation phenomena occur during the TLP bonding of the IN718/Ni-4.5Si-3.2B/IN718, including the following:

- Dissolution of the BM,
- Diffusion of MPD elements (Si and B) from the molten interlayer into the BM,
- Diffusion of Cr, Co, Mo, W, Ta, Al and Ti from the BM into the bond region.

All of these phenomena govern the chemical composition of the liquid phase, which in turn dictates the liquidus temperature of the liquid phase. The effect of alloying elements on the liquidus temperature depends on the distribution coefficient (k). Two phenomena help to increase the liquidus temperature of the liquid phase including:

- Depletion of the liquid phase from the MPD elements that have a k value less than unity significantly increases the liquidus temperature of the liquid phase.
- Co and W content of the liquid is increased gradually as a result of the BM dissolution phenomenon and the diffusion of Co and W from the BM into the bond region during the bonding process. The presence of Co and W, which exhibit a k value larger than unity,[16] increase the liquidus temperature.

As a consequence of both phenomena, the liquidus temperature of the liquid phase increases gradually during holding at the bonding temperature. Once the liquidus temperature increased to the bonding temperature, isothermal solidification starts. As a result of the absence of any solute rejection at the solid/liquid interface during isothermal solidification, the formation of the second phase is prevented. The microstructure of this zone consists of a pro-eutectic nickel-rich γ solid-solution phase. The average hardness of this zone was 310 HV.

If the sample is cooled down before completion of the isothermal solidification, the residual liquid would solidify under a different mechanism. The morphology of the product suggests that the structure is formed via a eutectic-type transformation during cooling. During solidification induced by cooling, B is rejected to the liquid in the middle of the joint due to the low solubility of B in the solidifying γ phase. Continuous solute enrichment of the liquid could cause the solute concentration to exceed the solubility limit of the solute in the γ phase. Consequently, any residual liquid could transform into eutectic-type solidification products during cooling from the bonding temperature.[7–10] The microstructure of the ASZ consists of two distinct phases: a nickel-rich solid-solution phase and an intermetallic phase. The average hardness of this zone was 570 HV. The EDS analysis showed[6] that the intermetallic phase is a nickel-rich boride. The solidification sequence can be summarized as follows:

$$L \rightarrow \gamma + L \rightarrow \gamma + \text{Nickel Boride} \qquad (1)$$

The diffusion-affected zone (DAZ) consists of second-phase particles with two different morphologies: particles with a blocky morphology and particles with a needle-like morphology. Boron and carbon were detected in both types of precipitates using an EDS analysis. The EDS compositional analysis of the metallic elements showed that both precipitates are Cr-rich carbo-boride.[4] The diffusion of boron from the liquid phase into the base metal, coupled with the fact that boron can reduce the solubility of carbon in an austenitic matrix, and the presence of Cr (which is a strong boride former) can explain the formation of Cr-rich carbo-borides.

It is of interest to note that due to the spatially non-continuous distribution along the joint/base-metal interface and the lower hardness compared to that of the eutectic microconstituents, the Cr-rich boride precipita-tes in the DAZ have a less detrimental effect on the joint strength compared to the ASZ. However, the interme-tallic-containing solidification products can serve as the preferential failure source for the brazed joint due to the inherently high hardness and brittleness of the interme-tallic phases. Consequently, they can significantly reduce the mechanical properties and creep strength of the joint, especially when the intermetallics are spatially conti-nuous.[8–10] The shear strength of this bond was 310 MPa, which is about 40 % of that of the base metal (780 MPa). A fracture-surface examination showed that the crack propagated along the joint centerline. **Figure 2b** shows a fracture surface of these bonds, indicating a semi-clea-vage/intergranular fracture. Therefore, in a situation where isothermal solidification has not been accompli-shed completely, eutectic micro-constituents that usually have the highest hardness in the bond region and form an interlinked network are the preferential failure source. Therefore, it is necessary to eliminate the eutectic pro-ducts in order to improve the strength of the joints. The experimental results showed that for a bonding time of 75 min at 1100 °C, in which the eutectic products are completely removed, bonds with a shear strength of 530 MPa (i.e., a joint efficiency of 68 %) were achieved.
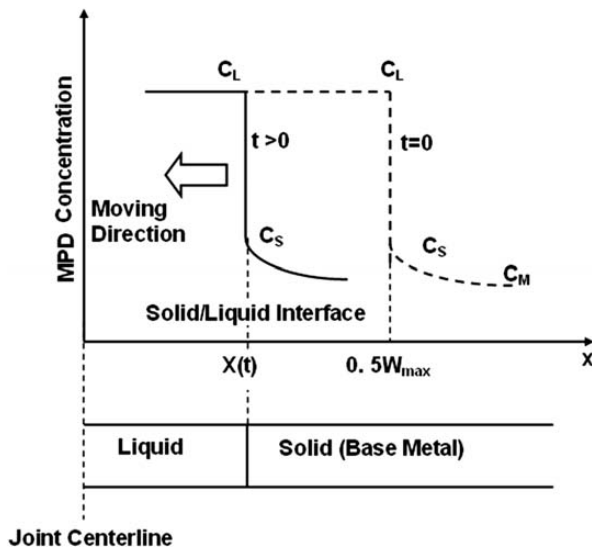
3.2 Prediction of the isothermal solidification time

When considering TLP bonding for commercial applications, an important bonding parameter is the hold-ing time required to complete the isothermal solidifica-tion (t_{IS}). Isothermal solidification is a prerequisite for obtaining a proper bond microstructure during the TLP bonding. If the holding time is lower than t_{IS}, athermal solidification of the residual liquid phase will lead to intermetallic formation, which in turn degrades the shear strength of the bond. Therefore, in this section, consi-dering the solidification behaviour of residual liquid, a diffusion model based on a migrating interface was used to predict the isothermal solidification's completion time.

Conventional analytical models of TLP bonding are based on binary systems; one of these models is used to estimate t_{IS} for the GTD- 111/Ni-Si-B/GTD-111 multi-components system. Migrating the solid/liquid interface modelling approach was used by several researchers.[17,18] This approach treats the system as two, semi-infinite phases with a coupled diffusion-controlled moving solid/ liquid interface (**Figure 3**). Isothermal solidification can be characterized by the motion of the solid-liquid interface, resulting from solid-state diffusion of the melting-point depressant (MPD) into the base metal. Interface motion can be determined by applying conser-vation of mass at the interface in conjunction with Fick's first law:[18]

$$(C_L - C_S)\frac{dX(t)}{dt} = D_S \frac{\partial C_S}{\partial x} - D_L \frac{dC_L}{dx} \qquad (2)$$

$$X(t) = K\sqrt{4Dt} \qquad (7)$$

Equation (7) suggests a linear relationship between the eutectic structure width (ASZ size) and the square root of the bonding time.

At the end of the isothermal solidification, two solid/liquid interfaces meet at the centerline (i.e., $X(t)$ reaches half of the maximum liquid width (W_{max})). Therefore, the completion time for isothermal solidification during TLP bonding can be calculated using the following equation:

$$t_{IS} = \frac{W_{max}^2}{16K^2D} \qquad (8)$$

where the constant K will be determined by mass conservation at the moving interface. The derivatives of the concentration profile and the interface position can then be substituted into Equation (3) to solve for K:

$$(C_L - C_S)K\sqrt{\frac{D}{t}} = D_S \frac{C_S - C_M}{1 + erf(K)} \cdot \frac{2}{\sqrt{4\pi DT}} exp(-K^2) \qquad (9)$$

Rearrangement of Equation (9) leads to:

$$\frac{C_L - C_M}{C_L - C_S} = K\sqrt{\pi}\ exp(K^2)(1 + erfK) \qquad (10)$$

Since the calculation of K needs numerical solving, a linear approximation of the right-hand side of Equation (9), when $K < 0.1$, was obtained by MATLAB software:

$$\frac{C_L - C_M}{C_L - C_S} = 2K \qquad (11)$$

A combination of Equation (7) and Equation (10) leads to:

$$t_{IS} = \frac{W_{max}^2}{4D}\left(\frac{C_L - C_S}{C_S - C_M}\right)^2 \qquad (12)$$

The theoretical maximum width of the liquid can be obtained by a simple mass conservation:[18]

$$W_{max}C_L = W_0 C_{FM} \qquad (13)$$

where C_M is the MPD concentration of the filler metal.

3.3 Model validation

In this section the described model is used to estimate t_{IS} for the investigated system. For GTD-111/Ni-Si-B/GTD-111, however, the involved materials are quite complex and there is a lack of detailed diffusion and phase-diagram data. In order to apply the migrating solid/liquid interface and compare it with the experimental results for GTD-111/Ni-Si-B/GTD-111, the following assumptions were taken into consideration:

1. Since Ni is the main element in GTD-111 nickel-based superalloy, the base metal was considered as pure nickel.
2. The solidification behaviour of the ternary Ni-Si-B interlayer could be considered similar to the solidi-

Figure 3: Schematic showing solute distribution during isothermal solidification stage during TLP bonding process
Slika 3: Shematski prikaz razporeditve koncentracij med izotermno fazo strjevanja pri TLP-postopku spajanja

Where C_L and C_S are the equilibrium liquidus and solidus, respectively, and $X(t)$ is the liquid/solid interface position. Because of the orders of magnitude difference in the diffusivity of solid and liquid, interface motion is separated into two distinct regimes. During the dissolution stage, the right-hand side of Equation (2) is dominated by the second term containing D_{liquid} and the interface moves into the solid until local equilibrium is achieved at the liquid/solid interface. At this point the dissolution ceases. Once the gradient in the liquid reaches zero, the liquid term becomes negligible and the interface begins to move back into the liquid and the isothermal solidification starts. In this condition the kinetics of the TLP process is dominated by Equation (3):[17,18]

$$(C_L - C_S)\frac{dX(t)}{dt} = D\left(\frac{\partial C(x,t)}{\partial t}\right)_{x=X(t)} \qquad (3)$$

The concentration profile of the MPD element in the solid can be calculated by applying Fick's second law in the solid and can be satisfied by a general error function solution:

$$C(x,t) = A + Berf\left(\frac{x}{\sqrt{4Dt}}\right) \qquad (4)$$

where A and B are constants determined by the following boundary conditions:

$$C(\infty, t) = A + B = C_M \qquad (5)$$

$$C(X(t), t) = A + Berf\left(\frac{x}{\sqrt{4Dt}}\right) = C_S \qquad (6)$$

where C_M is the MPD concentration of the base metal. Since Equation (6) has to be satisfied for all values of t, $X(t)$ must be proportional to $t^{1/2}$, hence:

fication behaviour of the binary Ni-B interlayer. Two reasons for this assumption are:

- For multi-component TLP systems, the kinetics of the solid/liquid interface movement is controlled by a faster solute,[19] which is boron in the case of the GTD-111/Ni-Si-B/GTD-111 system. The diffusion coefficient of boron in nickel is about 10^4 times greater than that of the silicon in the nickel substrate.
- As mentioned above, the eutectic type structure resulting from non-equilibrium solidification of the residual liquid consists of a γ-solid solution and nickel boride, and no silicide was observed in the ASZ microstructure. Indeed, the low solubility of boron in the nickel-based substrates resulted in the formation of intermetallic phases in the eutectic structure of the ASZ.

The thermodynamic data that were used for prediction of t_{IS}, are:

$x(C_S)$ = 0.3 % B (based on Ni-B binary phase diagram[20])

$x(C_L)$ = 13.16 % B (based on liquidus composition for Ni-Si-B filler[21])

$x(C_M)$ = 0

$x(C_{FM})$ = 13.6 % B (based on the initial composition of interlayer) (mole fractions x)

The diffusion coefficient of boron in GTD-111 will be needed to calculate the t_{IS}. Unfortunately, there is little data for the diffusion coefficient of boron in nickel-based superalloys. The diffusion coefficient of boron out of a Ni-Cr-Si-B filler metal in a nickel-based substrate at a temperature of 1100 °C was determined by Kukera et al.[22] to be 6.22×10^{-11} m²/s.

Figure 4 shows a plot of ASZ size (or eutectic width) vs. square root of the bonding time. The eutectic width decreases linearly with the square root of bonding time. Therefore, the migrating interface model is applicable for the system that is used in this study. Also, solving equation (9) numerically with these data yields 12.96
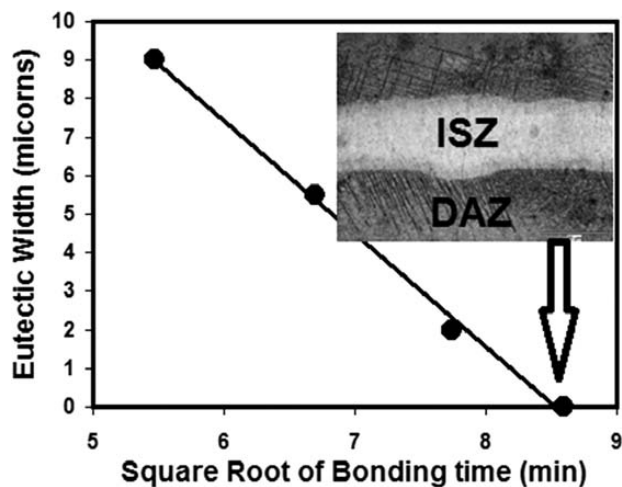
$\times 10^{-3}$ for K, which is considerably less than 0.1, supporting the applicability of Equation (12) in the present work.

According to the above data and using Equation (12) the resulting value for t_{IS} is 89 min. Experimental results showed that at bonding temperatures of 1100 °C, bonds free from the centerline eutectic were obtained after 75 min. **Figure 5** shows the typical microstructure of the bonds made at 1100 °C for 75 min, indicating a eutectic-free joint. The absence of a eutectic-type structure in the joint centerline suggests the completion of isothermal solidification under this bonding condition. As can be seen, this model can predict t_{IS} with a reasonable accuracy. A good agreement between the time calculated for t_{IS} (89 min) and that experimentally observed (75 min) was obtained. This difference can be attributed to the liquid penetration into the grain boundaries of the base metal, grain-boundary migration, loss of liquid metal by the squeezing-out action[23,24] and the simplified assumptions of the model. It should be noted that the accuracy of the t_{IS} predication is largely dependent on the diffusion data. Despite some discrepancy between the experimental and predicted values, this modelling can be considered as the first step for the designing and optimization of process parameters to achieve an appropriate TLP bond microstructure.

Finally, it is interesting to note that isothermal solidification completion prevents the formation of a eutectic structure in the bond region; however, significant amounts of Cr-rich carbo-boride were still present in the DAZ (**Figure 5**). The high Cr content of these precipitates leads to a significant depletion of Cr around this region. Because of the fact that Cr is the key element for the corrosion resistance of the superalloy,[25] its depletion can reduce the local corrosion resistance of the matrix.[26–28] It has been reported previously that the corrosion resistance of a brazed superalloy was impaired by the precipitation of Cr-rich particles within the braze/base-alloy interface.[29] Therefore, in order to restore the corrosion resistance of the substrate, it is necessary to design a proper post-bond heat treatment (PBHT) to eliminate the boride precipitates in the DAZ via a break-up and dissolution processes.
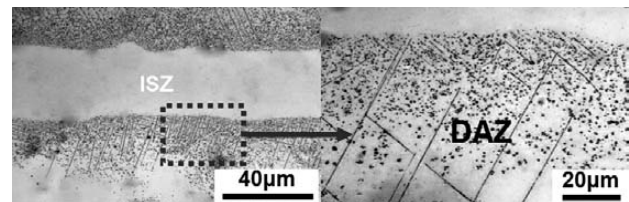

Figure 4: The width of eutectic-type micro-constituents versus square root of bonding time for TLP bonding of GTD-111/Ni-Si-B/GTD-111
Slika 4: Širina evtektičnih faz v odvisnosti od kvadrata časa spajanja za TLP-spajanje GTD-111/Ni-Si-B/GTD-111

Figure 5: Microstructure of TLP bonded GTD-111 at 1100 °C for 75 min showing eutectic-free joint centerline. Extensive boride precipitates are present in the diffusion-affected zone (DAZ).
Slika 5: Mikrostruktura TLP-spoja GTD-111 po 75 min na 1100 °C prikazuje srednjo linijo brez evtektika. Številni izločki borida so prisotni v difuzijsko vplivanem področju (DAZ).

4 CONCLUSIONS

The isothermal solidification process during the TLP bonding of the GTD-111 nickel-based superalloy using an amorphous Ni-Si-B interlayer was studied. The following conclusions can be drawn from this study:

1. When the bonding time is not sufficient to complete the isothermal solidification (i.e., a bonding time of less than 75 min at bonding temperatures of 1100 °C), the residual liquid phase after an incomplete isothermal solidification at the bonding temperature was transformed to a eutectic type structure consisting of the γ-solid-solution phase and the boride intermetallic. According to the solidification behaviour and the ASZ microstructure, boron is main controlling MPD element of the isothermal solidification.

2. It was found that there is a linear relationship between the eutectic width and the square root of the bonding time, suggesting that the isothermal solidification process is governed by solid-state diffusion.

3. The time required for the completion of isothermal solidification during the TLP bonding of the GTD-111 superalloy could be predicted with fairly good accuracy using a mathematical solution of the time-dependent diffusion equation based on Fick's second law.

5 REFERENCES

[1] A. Milosavljevic, S. Petronic, S. Polic-Radovanovic, J. Babic, D. Bajic, The influence of the heat treatment regim on a fracture surface of nickel-based superalloys, Mater. Tehnol., 46 (**2012**) 4, 411–417

[2] R. Sunulahpašić, M. Oruč, M. Hadžalić, M. Rimac, Optimization of the mechanical properties of the superalloy Nimonic 80A, Mater. Tehnol., 46 (**2012**) 3, 263–267

[3] A. Semenov, S. Semenov, A. Nazarenko, L. Getsov, Computer simulation of fatigue, creep and thermal-fatigue cracks propagation in gas-turbin blades, Mater. Tehnol., 46 (**2012**) 3, 197–203

[4] M. Pouranvari, A. Ekrami, A. H. Kokabi, Microstructure development during transient liquid phase bonding of GTD-111 nickel-based superalloy, J Alloys Comp, 461 (**2008**), 641–647

[5] M. Pouranvari, A. Ekrami, A. H. Kokabi, TLP bonding of cast IN718 nickel based superalloy: Process–microstructure–strength characteristics, Mater. Sci. Eng. A, 568 (**2013**), 76–82

[6] M. Pouranvari, A. Ekrami, A. H. Kokabi, Microstructure-properties relationship of TLP-bonded GTD-111 nickel-base superalloy, Mater. Sci. Eng. A, 490 (**2008**), 229–234

[7] D. S. Duvall, W. A. Owczarski, D. F. Paulonis, TLP Bonding: A new method for joining jeat resistant alloys, Weld. J., 53 (**1974**), 203–214

[8] O. A. Ojo, N. L. Richards, M. C. Charturvedi, Effect of gap size and process parameters on diffusion brazing of Inconel 738, Sci. Technol. Weld. Joining, 9 (**2004**), 209–220

[9] M. Pouranvari, A. Ekrami, A. H. Kokabi, Effect of bonding temperature on microstructure development during TLP bonding of a nickel base superalloy, J Alloys Comp., 469 (**2009**), 270–275

[10] W. F. Gale, D. A. Butts, Transient liquid phase bonding, Sci. Technol. Weld. Joining, 9 (**2004**), 283–300

[11] F. Jalilian, M. Jahazi, R. A. L. Drew, Microstructural evolution during transient liquid phase bonding of Inconel 617 using Ni-Si-B filler metal, Mater. Sci. Eng. A, 447 (**2007**), 125–33

[12] M. Pouranvari, A. Ekrami, A. H. Kokabi, Effect of the Bonding Time on the Microstructure and Mechanical Properties of a Transient Liquid Phase Bonded IN718 using a Ni-Cr-B Filler Alloy, Mater. Tehnol., 47 (**2013**) 5, 593–599

[13] N. R. Philips, Microstructural Evolution and Ductile Phase Toughening in Brazed Joints, Phd Thesis, University of California, 2008

[14] I. Tuah-Poku, M. Dollar, T. B. Massalski, A study of the transient liquid phase bonding process applied to a Ag/Cu/Ag sandwich joint, Metall. Trans. A, 9 (**1988**), 675–686

[15] G. Humpston, D. M. Jacobson, Principles of soldering and brazing, ASM International, Metals Park, Ohio 1993

[16] O. A. Ojo, N. L. Richards, M. C. Chaturvedi, Microstructural study of weld fusion zone of TIG welded IN 738LC nickel-based superalloy, Scripta Materialia, 51 (**2004**), 683–688

[17] O. A. Ojo, N. L. Richards, M. C. Chaturvedi, Isothermal solidification during transient liquid phase bonding of Inconel 738 superalloy, Sci. Technol. Weld. Joining, 9 (**2004**), 532–540

[18] Y. Zhou, W. F. Gale, T. H. North, Modelling of transient liquid phase bonding, Int. Mater. Rev., 40 (**1995**), 181–196

[19] C. W. Sinclair, G. R. Purdy, J. E. Morral, Transient liquid-phase bonding in two-phase ternary systems, Metall. Trans. A., 31A (**2000**), 1187–1192

[20] T. B. Massalski (ed.), Binary alloy phase diagrams, ASM International, Metals Park, OH 1986, 366–371

[21] S. Omori, Y. Hashimoto, K. Shoji, K. Hidaka, Y. Kohira, J. Jpn Soc. Powder metal., 18 (**1972**), 316–320

[22] J. Kukera, A. Buchal, A. Rek, K. Stransky, Kovove Mater., 22 (**1984**), 250–262

[23] T. Padron, T. I. Khan, M. J. Kabir, Modelling the transient liquid phase bonding behaviour of a duplex stainless steel using copper interlayers, Mater. Sci. Eng. A, 385 (**2004**), 220–228

[24] W. D. MacDonald, T. W. Eagar, Isothermal solidification kinetics of diffusion brazing, Metall. Matter.Trans A, 29 (**1998**), 315–32

[25] J. Lippold, S. D. Kiser, J. N. DuPont, Welding Metallurgy and Weldability of Nickel-Base Alloys, Wiley publishing, 2009

[26] M. Pouranvari, A. Ekrami, A. H. Ekrami, Solidification and Solid State Phenomena during TLP bonding of IN718 Superalloy Using Ni-Si-B Ternary Filler Alloy, J Alloys Comp, 563 (**2013**), 143–149

[27] M. Pouranvari, A. Ekrami, A. H. Kokabi, Transient Liquid Phase Bonding of Wrought IN718 Nickel Based Superalloy Using Standard Heat Treatment Cycles: Microstructure and Mechanical Properties, Materials & Design, 50 (**2013**), 694–701

[28] O. A. Idowu, O. A. Ojo, M. C. Chaturvedi, Microstructural Study of Transient Liquid Phase Bonded Cast INCONEL 738LC Superalloy, Metall Mater Trans A, 37A (**2006**), 2787–2796

[29] B. Jahnke, J. Demny, Microstructural investigations of a nickel-based repair coating processed by liquid phase diffusion sintering, Thin Solid Films, 110 (**1983**), 225–35

A NEW METHOD FOR DETERMINING WATER ADSORPTION PHENOMENA ON METAL SURFACES IN A VACUUM

NOVA METODA ZA DOLOČANJE ADSORPCIJE VODNE PARE NA KOVINSKIH POVRŠINAH V VAKUUMU

Makfir Sefa[1,2], Janez Šetina[2], Bojan Erjavec[2]

[1]Lotric Metrology, Selca, Slovenia
[2]Institute of Metals and Technology, Lepi pot 11, 1000 Ljubljana, Slovenia
makfir.sefa@lotric.si

A new method for measuring the amount of adsorbed water vapor on different technical metal surfaces in vacuum systems after exposure to water vapor has been developed. The method is based on a measurement of the pressure – time response after the sudden introduction of a constant gas flow into the vacuum chamber. For non-adsorbing gases the pressure approaches the equilibrium value with a time constant τ that is equal to $\tau = V/S$, where V is the volume of the system and S is the effective pumping speed for a given gas. For adsorbing a gas like water vapor the approach of the pressure to the equilibrium value is delayed due to the adsorption of molecules on the surfaces of the vacuum system. The method was evaluated using aluminum foils with different surface areas. The measured data were modeled using the Langmuir, Freundlich and Temkin isotherms. The measured water coverage on the stainless-steel and aluminum surfaces was less than one monolayer for pressures ranging from 8×10^{-5} mbar to 1×10^{-2} mbar. The best fit to the measured coverage was obtained when using the Freundlich isotherm.

Keywords: water vapor, adsorption, surface coverage, adsorption isotherm

Razvita je bila nova metoda merjenja adsorbirane količine vodne pare na različnih tehničnih površinah v vakuumskih sistemih. Metoda temelji na merjenju časovnega odziva tlaka po nenadnem uvajanju konstantnega toka plina v vakuumsko komoro. Za pline, ki se ne adsorbirajo, se tlak približa ravnotežni vrednosti s časovno konstanto τ, ki je enaka $\tau = V/S$, kjer je V volumen sistema in S efektivna hitrost črpanja za dani plin. Pri plinu, ki se adsorbira, kot je na primer vodna para, je bližanje tlaka ravnotežni vrednosti zadržano zaradi adsorpcije molekul na površini vakuumskega sistema. Metoda je bila ocenjena s folijami iz aluminija, ki so imele različne velikosti površine. Izmerjeni podatki so bili modelirani z Langmuirjevo, Freundlichovo in Temkinovo izotermo. Za tlake od 8×10^{-5} mbar do 1×10^{-2} mbar je bilo izmerjeno pokritje z vodo na površini nerjavnega jekla in na površini aluminija manj kot ena monoplast. Najboljše ujemanje izmerjenega povprečja je bilo doseženo s Freundlichovo izotermo.

Ključne besede: vodna para, adsorpcija, pokritje površine, adsorpcijska izoterma

1 INTRODUCTION

Water vapor adsorption on the inner surfaces of vacuum systems after exposure to the ambient atmosphere is one of the major problems for most processes carried out in an unbaked vacuum system, and frequently determines the pump-down time to reach ultra-high-vacuum conditions. When a vacuum system is exposed to the ambient atmosphere the water vapor can be adsorbed in several monolayers[1]. The amount of adsorbed water vapor on the surfaces of vacuum systems depends on the characteristics and treatment of the material surface, the partial pressure of the water vapor in the atmosphere and the exposure time. A better knowledge of the amount adsorbed and the behavior of the water vapor on the material surface is one of the main contributions to solving the problem of the pump-down time. The amount of adsorbed water vapor on the surfaces of different materials has been studied by several authors using different methods. Minxu Li and H. F. Dylla[2–4] measured the amount of adsorbed water vapor on an electro-polished stainless-steel surface after exposure to

various water vapor pressures and duration times. They calculated the amount of adsorbed water vapor by integrating the desorption flux. Another interesting method, known as the radioactive tracer technique, was also used to determine the amount of adsorbed water vapor on the technical surfaces of metals.[5–7] On the other hand, P. A. Redhead[8,9] studied the effect of adsorption-desorption processes on the pump-down behavior for both monolayer and multilayer adsorption. He reported that the amount of adsorbed water vapor can be expressed as a function of the pressure using a suitable adsorption isotherm.

We have developed a special method for measuring water vapor adsorption on the inner surfaces of vacuum systems with the amount of adsorbed water vapor being less than one monolayer. We made the first measurements in an empty chamber, and then in the same chamber loaded with samples of aluminum foil that had different surface areas. The amount of adsorbed water vapor on the sample surface was calculated by subtracting the amount adsorbed on the walls of the empty chamber from the amount adsorbed in the

chamber with the sample. The measured data were analyzed according to the surface-area dependence of the adsorbed amount. The measured results of the amount of adsorbed water vapor on the surfaces of the vacuum chamber after exposure to various water vapor pressures are compared to the modeling results using several different adsorption isotherms (i.e., the Langmuir isotherm, Freundlich isotherm, and Temkin isotherm).

2 EXPERIMENTAL

2.1 Measurement setup

A schematic of the experimental setup is shown in **Figure 1**. The sample chamber (SC) has a volume of 0.66 L and an inner surface area of 760 cm^2. It is equipped with a capacitance diaphragm gauge (CDG1) and a spinning rotor gauge (SRG). The SC is connected through a vacuum valve V_0 to a turbomolecular pump (TMP) that has a pumping speed of 60 L s^{-1} for N$_2$. Between the SC and the valve V_0 there is an orifice that is made by drilling a hole in a blank Cu gasket for a CF40
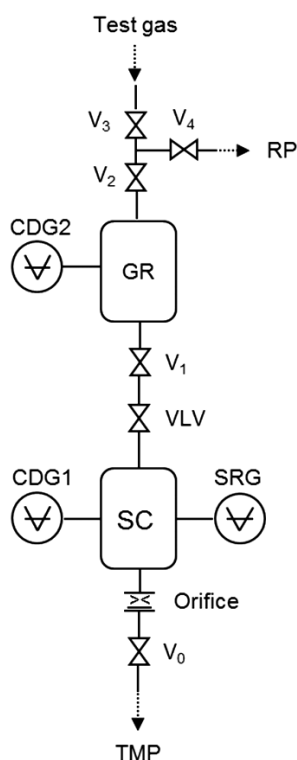
Figure 1: Measurement system for studies of the adsorption of water vapor on metal surfaces in a vacuum: CDG1 – capacitance diaphragm gauge (0.1 mbar FS), CDG2 – capacitance diaphragm gauge (100 mbar FS), SRG – spinning rotor gauge, GR – gas reservoir, SC – sample chamber, TMP – turbo molecular pump, RP – rotary pump, VLV – variable leak valve, V_0, V_1, V_2, V_3, V_4 – all-metal valves

Slika 1: Merilni sistem za študij adsorpcije vodne pare na površino kovin v vakuumu: CDG1 – kapacitivni membranski merilnik tlaka (0,1 mbar FS), CDG2 – kapacitivni membranski merilnik tlaka (100 mbar FS), SRG – viskoznostni merilnik z lebdečo kroglico, GR – rezervoar plina, SC – komora z vzorcem, TMP – turbomolekularna črpalka, RP – rotacijska črpalka, VLV – ventil s spremenljivim pretokom, V_0, V_1, V_2, V_3, V_4 – kovinski ventili

flange. The dimensions of the orifice are diameter 5.3 mm and thickness 2 mm. On the other side, the SC is connected to a gas reservoir (GR) through a vacuum valve (V_1), and a variable leak valve (VLV). The GR is equipped with a capacitance diaphragm gauge (CDG2) and connected to both a rotary pump (RP) and a gas source through the valves V_2, V_3 and V_4. All the chambers are made of austenitic stainless steel AISI 304L. All the joints are based on Conflat flanges and Cu gaskets. The valves are bakeable all-metal type. The inner surfaces have the standard finish of commercial Conflat-type fittings.

2.2 Measurement method

The SC was pumped by TMP1 for several minutes to reach a pressure of 1×10^{-6} mbar. The pressure was measured by the SRG. The previously evacuated GR was filled with nitrogen gas to a pressure in the range from 10 mbar to 20 mbar. A conductance of the VLV was adjusted to an appropriate value to get a desired pressure in the SC. After that the GR was evacuated again with the valve V_1 opened. Then V_1 was closed and GR was filled with water vapor (or another gas) through V_2 and V_3. After that the V_2 was closed and the valve V_1 was quickly opened.

The pressure rise within the SC after the sudden introduction of gas was measured by CDG1 and SRG. For the inert gas, which has no interaction with the surface, the pressure rise of gas within the SC can be calculated from the basic quantities: volume of the SC, effective pumping speed, and gas flow into the SC.

By applying the ideal gas law and assuming that the gas temperature remains constant, the flux balance yields the basic differential equation:[10,11]

$$V \frac{\mathrm{d}P}{\mathrm{d}t} = Q_{\mathrm{m}} - SP \qquad (1)$$

where Q_{in} is the gas flow into the SC, S is the effective pumping speed, t is the time, and V is the volume of the SC. If Q_{in} and S are constant (independent of pressure and time), then the solution of Eq. (1) gives a simple expression for the pressure rise $P(t)$ in the SC:

$$P(t) = \frac{Q_{\mathrm{m}}}{S} \left(1 - s^{-\frac{V}{S}t} \right) \qquad (2)$$

The pressure rise in the SC is characterized by the time constant τ which is only a function of the SC volume V and the effective pumping speed S (it is independent of the gas flow Q_{in}):

$$\tau = \frac{V}{S} \qquad (3)$$

Since τ depends only on the system parameters V and S, it can be called the system time constant. The gas flow together with the effective pumping speed determines the equilibrium pressure P_{eq} in the SC:

$$P_{eq} = \frac{Q_{in}}{S} \qquad (4)$$

By introducing Eq. (3) and Eq. (4) into Eq. (2), the latter can be rewritten as:

$$P(t) = P_{eq}\left(1 - e^{-\frac{t}{\tau}}\right) \qquad (5)$$

Eq. (5) represents the pressure rise until the volume of the SC becomes filled with gas up to the equilibrium pressure. For a gas, which can adsorb on the surface, the pressure rise in the SC cannot be described by Eq. (5) because a certain number of gas molecules from the gas flow Q_{in} can be trapped on the inner surface of the SC and do not exit through the orifice. The amount adsorbed depends on the equilibrium pressure and the inner surface area of the SC. Therefore, the system time constant of gases that have an interaction with the surface will be prolonged to an actual time constant τ'. This τ' is not only a function of the SC volume and the effective pumping speed, since it is also influenced by the adsorption of gas molecules on the inner surface of the SC. Equilibrium is achieved when the surface becomes saturated with adsorbing molecules and the flux of the adsorbed and the flux of the desorbed molecules equalize.

Figure 2 shows the normalized measured pressure rise in the case of a sudden introduction of water vapor at a constant flow rate into the SC. It can be compared to the normalized estimated pressure rise for the case of non-adsorbing gas having the same flow rate, which can be calculated by Eq. (5). The area between the two curves in **Figure 2** represents the number of adsorbed molecules in the SC that did not exit through the orifice. This area can be calculated as the difference between the
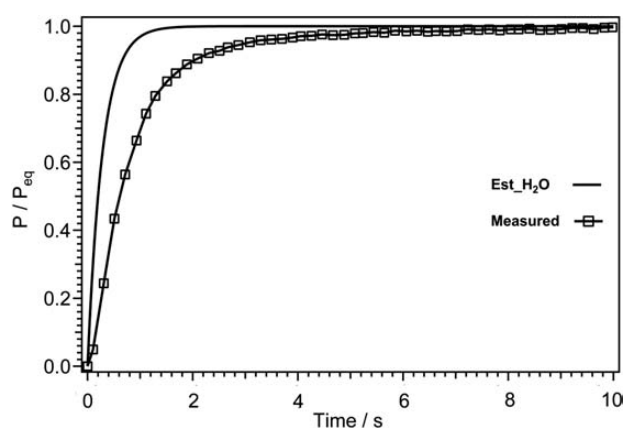
Figure 2: Example of normalized pressure rise until the volume becomes filled to an equilibrium pressure for water vapor. Measured pressure rise is compared to the estimated pressure rise (Est_H2O) with the assumption that the H_2O has no interaction with the surface.
Slika 2: Primer naraščanja normaliziranega tlaka, dokler se ne napolni volumen do ravnotežnega tlaka vodne pare. Izmerjeno naraščanje tlaka je primerjano z ocenjenim naraščanjem tlaka (Est_H2O) s predpostavko, da H_2O nima interakcije s površino.

two integrals, $(I_1 - I_2)$, where I_1 is the time integral of the estimated pressure rise given by:

$$I_1 = P_{eq}\int_0^t (1 - e^{-\frac{t}{\tau}})\mathrm{d}t \qquad (6)$$

and I_2 is the time integral of measured pressure rise $P_m(t)$ within the SC given by:

$$I_2 = \int_0^{t_{eq}} P_m(t)\mathrm{d}t \qquad (7)$$

Integration starts from the time when the V_1 is opened and needs to be continued over a sufficiently long period t_{eq} until the equilibrium of the measured pressure in the SC is reached. The number of adsorbed molecules N_{ad} on the inner surface area of the SC is calculated according to:

$$N_{ad}kT = S(I_1 - I_2) \qquad (8)$$

where k is the Boltzmann constant, T is the absolute temperature and S is the effective pumping speed.

To evaluate this measurement method a measurement with water vapor in the empty SC was performed. In this way the adsorption on the chamber walls was determined. After that the sample of aluminum foil (99.6 % Al, 0.19 % Fe, 0.17 % S) was inserted into the SC. Measurements were performed on three samples that were cut from the same sheet of foil but having a different surface area, being 5, 10 and 25 times larger than the inner surface area of the SC.

The total number of adsorbed molecules is the sum of the adsorbed molecules on the inner surface of the SC (background) N_{ad}^b and the adsorbed molecules on the aluminum foil surface N_{ad}^{Al}:

$$N_{ad}^t = N_{ad}^b + N_{ad}^{Al} \qquad (9)$$

N_{ad}^b and N_{ad}^t are calculated from the measured pressure rise using Eq. (8). The surface coverage of water vapor on the geometric area can be calculated according to:

$$\theta = \frac{N_{ad}}{n_{mono}A} \qquad (10)$$

where θ is the surface coverage, n_{mono} is the surface density of water molecules for a monolayer coverage on a flat surface ($\approx 10^{15}$ cm^{-2}) and A is the geometrical surface area.

2.3 Adsorption isotherms

The measured results were modeled using the Langmuir, Freundlich and Temkin adsorption isotherms, which are discussed in detail by Redhead[8]. The Langmuir isotherm is based on the simplest model, which assumes that the rate of adsorption is proportional to the number of empty adsorption sites, and the heat of adsorption is constant $q = q_0$. The relationship between pressure and coverage in this isotherm can be described by equation:

$$\theta = \frac{(ap)^{\frac{1}{n}}}{1+(ap)^{\frac{1}{n}}} \qquad (11)$$

where p is the pressure, $n = 1$ for non-dissociative molecules, and $n = 2$ for dissociative molecules, and a is a constant that can be described as follows:

$$a = \frac{s_0 v \tau_0}{N_m} \exp \frac{q}{RT} \qquad (12)$$

where s_0 is the sticking probability on an empty adsorption site, τ_0 is the period of oscillation of the molecule normal to the surface ($\approx 10^{-13}$ s), v is the specific arrival rate of molecules at the surface, N_m is the number of molecules for a monolayer coverage, q is the heat of adsorption and R is the universal gas constant.

The Freundlich isotherm can be derived by taking Langmuir assumptions and using a logarithmic variation of the heat of adsorption with the coverage as $q = -q' \ln\Theta$. The relation between the pressure and the coverage can be described by equation:

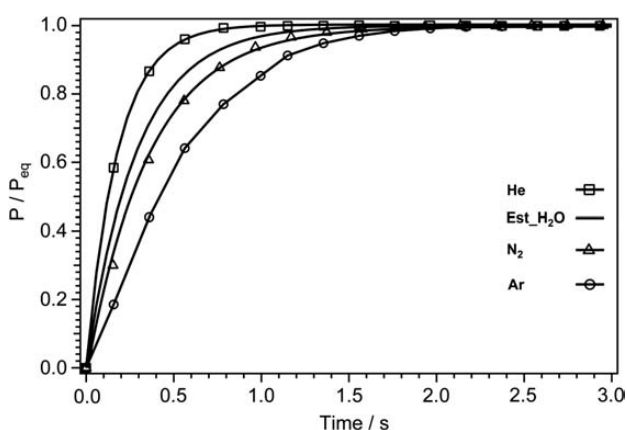$$\theta = kp^{\beta} \qquad (13)$$

where k and β are constants.

The Temkin isotherm may be derived using the Langmuir isotherm, which assumes that the heat of adsorption decreases linearly with increasing coverage as $q = q_0 (1 - \alpha\Theta)$, where α is a constant. The relationship between pressure and coverage can be described by the equation:

$$\theta = A \ln(\beta p) \qquad (14)$$

where A and β are constants:

$$A = \frac{RT}{q_0 - q_1}, \quad \beta = \frac{1 + \frac{p}{p'} \exp \frac{q_0}{RT}}{1 + \frac{p}{p'} \exp \frac{q_1}{RT}} \qquad (15)$$

Figure 3: Normalized pressure rise until the volume becomes filled to an equilibrium pressure for gases: He, N$_2$, Ar and estimated pressure rise for water vapor (Est_H$_2$O) with the assumption that H$_2$O has no interaction with the surface
Slika 3: Normaliziran tlak narašča, dokler se volumen ne napolni do ravnotežnega tlaka za pline: He, N$_2$, Ar in ocenjeni tlak vodne pare (Est_H$_2$O) narašča s predpostavko, da H$_2$O nima interakcije s površino

where $p' = N_m/s_0\tau_0 v$, q_0 is the heat of adsorption at $\theta = 0$ and q_1 is the heat of adsorption at $\theta = 1$.

3 RESULTS AND DISCUSSION

The measurement method was validated with non-adsorbing gases: He, N$_2$ and Ar. **Figure 3** shows the normalized measured pressure rise for helium, nitrogen and argon as a function of time. Also added is the normalized estimated pressure rise of H$_2$O that would be observed when no water molecules are adsorbed on the surfaces. The normalized pressure is equal to the measured or estimated pressure divided by the equilibrium pressure: $P(t)/P_{eq}$.

The calculated system time constants τ_{gas} for the gases He, N$_2$ and Ar are shown in **Table 1**. The constants were obtained by fitting Eq. (5) to the measured values. The system time constant for a given gas depends on the effective pumping speed (Eq. (3)), which is gas dependent. Since the orifice conductance is significantly smaller than the pumping speed of the turbo-molecular pump, the effective pumping speed is mainly determined by the orifice conductance.

Table 1: Measured time constants t_{gas} for different gases, time constants ratio t_{gas}/t_{N2} and square root of the ratio of molecular masses
Tabela 1: Izmerjena časovna konstanta t_{gas} za različne pline, razmerje časovnih constant t_{gas}/t_{N2} in kvadratnega korena razmerja molekulskih mas

Gas	t_{gas}/s	t_{gas}/t_{N2}	$(M_{gas}/M_{N2})^{1/2}$
He	0.17	0.49	0.38
N$_2$	0.35	1.00	1.00
Ar	0.43	1.23	1.20

In the molecular regime, the orifice conductance is inversely proportional to the square root of the molecular mass of the gas. Therefore, the ratio of the system time constants τ_{gas}/τ_{N2} should be equal to:

$$\frac{\tau_{gas}}{\tau_{N2}} = \sqrt{\frac{M_{gas}}{M_{N2}}} \qquad (16)$$

where t_{N2} is the system time constant for nitrogen, M_{N2} is the molecular mass for nitrogen, and M_{gas} is the molecular mass of the gas. **Table 1** shows that τ_{Ar}/τ_{N2} is close to the expected value. There is an enlarged difference for τ_{He}/τ_{N2}. The main reason for this deviation is the very fast pressure rise in the case of He, so that the time response of CDG1 is too slow for an accurate measurement. Close agreement for the ratio of the system time constants for N$_2$ and Ar with Eq. (16) justifies the use of Eq. (16) to estimate the system time constant for H$_2$O for the hypothetical case of non-adsorbing water molecules.

The normalized measured pressure rises in the SC as a function of time at various equilibrium pressures of water vapor P_{eq} are shown in **Figure 4**. The normalized estimated pressure rise is also added in **Figure 4**. The
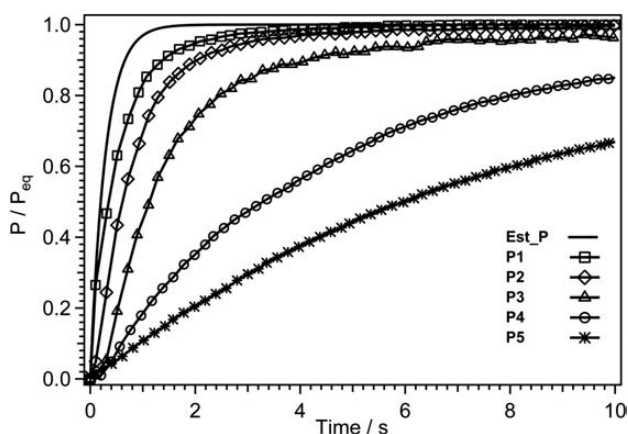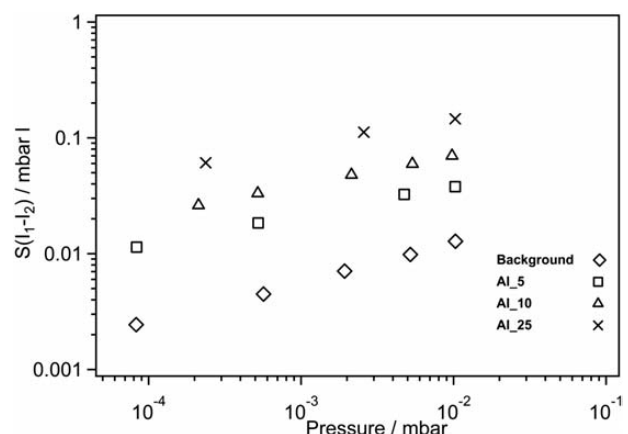
Figure 4: Normalized measured pressure rise until the volume becomes filled with water vapor to the equilibrium pressure P_{eq} ($P1 = 1.03 \times 10^{-2}$ mbar, $P2 = 5.21 \times 10^{-3}$ mbar, $P3 = 1.93 \times 10^{-3}$ mbar, $P4 = 5.67 \times 10^{-4}$ mbar and $P5 = 8.29 \times 10^{-5}$ mbar), and H_2O estimated pressure rise (Est_P) with the assumption that H_2O has no interaction with the surface

Slika 4: Normaliziran izmerjeni tlak narašča, dokler se volumen ne napolni z vodno paro do ravnotežnega tlaka P_{eq} ($P1 = 1,03 \times 10^{-2}$ mbar, $P2 = 5,21 \times 10^{-3}$ mbar, $P3 = 1,93 \times 10^{-3}$ mbar, $P4 = 5,67 \times 10^{-4}$ mbar in $P5 = 8,29 \times 10^{-5}$ mbar) in ocenjen tlak H_2O (Est_P) raste s predpostavko, da H_2O nima interakcije s površino
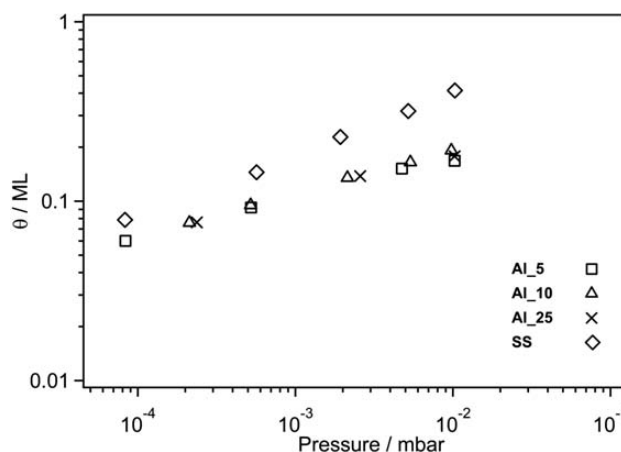
estimated pressure rise $P_e(t)$ is calculated by Eq. (5) using the estimated system time constant for water vapor that would be observed if there was no adsorption of water molecules on the chamber walls. **Figure 4** shows that the $P(t)/P_{eq}$ curves are different for different P_{eq} and it is evident that the actual time constant τ' increases with decreasing P_{eq} in the SC.

The adsorbed amount of water vapor $N_{ad}kT$ on the inner surface area of the empty SC (background) for different equilibrium pressures, calculated using Eq. (8),
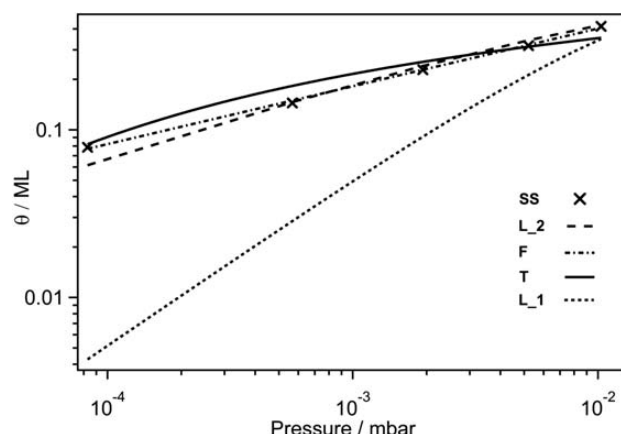

Figure 6: Surface coverage vs. H_2O equilibrium pressure for samples (Al_5, Al_10 and Al_25) having different surface areas, and for the chamber's inner surface (SS)

Slika 6: Pokritje površine v odvisnosti od ravnotežnega tlaka H_2O za vzorce (Al_5, Al_10 in Al_25) z različno velikostjo površine in za notranjo površino komore (SS)

is shown in **Figure 5**. The same procedure was then repeated in cases when samples of aluminum foil with different surface areas, being 5, 10 and 25 times larger than the chamber's inner surface area (A(Al_5) = 3800 cm^2, A(Al_10) = 7600 cm^2, and A(Al_25) = 19000 cm^2), were sequentially placed in the SC. The calculated adsorbed amounts of water vapor for each of these cases are also shown in **Figure 5**.

Figure 5 shows that the amount of adsorbed water vapor on the surface of the SC increases with increasing equilibrium pressure and also with increasing sample surface in the SC. It is expected that the amount adsorbed is proportional to the sample surface. The amount

Figure 5: Adsorbed amount of water vapor (in mbar l) vs. H_2O equilibrium pressure, in the case of an empty chamber with an inner surface area 760 cm^2 (background) and the chamber filled with samples of aluminum foil having different surface areas (A(Al_5) = 3800 cm^2, A(Al_10) = 7600 cm^2 and A(Al_25) = 19000 cm^2)

Slika 5: Adsorbirana množina vodne pare (mbar l) proti ravnotežnemu tlaku H_2O v prazni komori z notranjo ploščino površine 760 cm^2 (ozadje) in komorami, napolnjenimi z vzorci folije iz aluminija z različno velikostjo površine (A(Al_5) = 3800 cm^2, A(Al_10) = 7600 cm^2 in A(Al_25) = 19000 cm^2)

Figure 7: Surface coverage vs. H_2O equilibrium pressure for stainless-steel (SS) and model curves using Langmuir isotherm (L_2, for dissociative adsorption $n = 2$), Freundlich isotherm (F), Temkin isotherm (T) and Langmuir isotherm (L_1, for non-dissociative adsorption $n = 1$)

Slika 7: Prekritje površine v odvisnosti od ravnotežnega tlaka H_2O za nerjavno jeklo (SS) in krivulje modela z Langmuirjevo izotermo (L_2, za disociativno adsorpcijo $n = 2$), Freundlichovo izotermo (F), Temkinovo izotermo (T) in Langmuirjevo izotermo (L_1, za nedisociativno adsorpcijo $n = 1$)
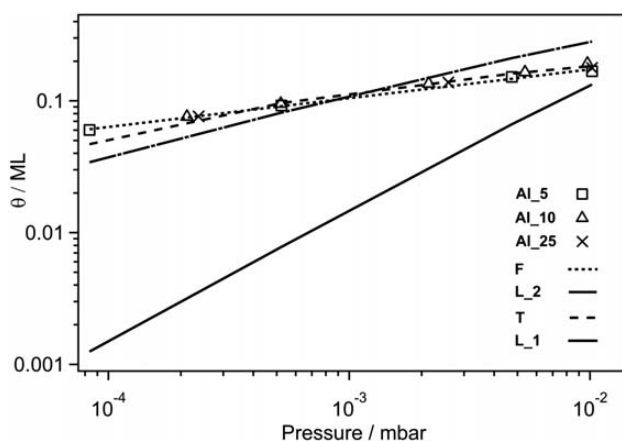
Figure 8: Surface coverage vs. H_2O equilibrium pressure for samples (Al_5, Al_10 and Al_25) having a different surface area and model curves using Langmuir isotherm (L_2, for dissociative adsorption $n = 2$), Freundlich isotherm (F), Temkin isotherm (T), and Langmuir isotherm (L_1, for non-dissociative adsorption $n = 1$)

Slika 8: Prekritje površine v odvisnosti od ravnotežnega tlaka H_2O za vzorce (Al_5, Al_10 in Al_25) z različno velikostjo površine in krivulje modela z Langmuirjevo izotermo (L_2, za disociativno adsorpcijo $n = 2$), Freundlichovo izotermo (F), Temkinovo izotermo (T) in Langmuirjevo izotermo (L_1, za nedisociativno adsorpcijo $n = 1$)

adsorbed on the Al samples can only be calculated by subtracting the background amount that is adsorbed on the chamber's inner surface (Eq. 9).

From the adsorbed amount and the known surface area the surface coverage can be calculated using Eq. (10). The surface coverage of the walls of the SC and the Al samples is shown in **Figure 6**. The values of the measured coverage of the samples of the same material, but with a different surface area are independent of the area. This proves the correctness of our measurement method. From **Figure 6** it can be derived that the surface coverage of the Al samples is on average 1.7 times lower than that of the SC.

The calculated surface coverage for each water vapor exposure pressure is modeled with the adsorption isotherms. **Figures 7** and **8** compare the measured surface coverage for the case of the stainless-steel surface of the SC and Al foils with a different surface area, with different adsorption isotherms (Eqs. (11), (13), and (14)). **Figures 7** and **8** show that the best fitting to the calculated surface coverage is the Freundlich isotherm, whereas the Temkin isotherm and the Langmuir isotherm

(for $n = 2$, dissociative adsorption) show a slightly larger deviation from the calculated surface coverage. There is a large deviation when fitting the Langmuir isotherm for the case of non-dissociative adsorption ($n = 1$).

4 CONCLUSIONS

We developed a special method for measuring the amount of adsorbed water vapor on metal surfaces. The method was tested with Al samples that have different surface areas. The measured amount of adsorbed water was proportional to the area. The results can be modeled with Langmuir, Freundlich and Temkin isotherms (in a rather narrow pressure range). The surface coverage curve of our measurement vs. H_2O exposure pressure had the best fit with the Freundlich isotherm. Fitting with the Langmuir isotherm ($n = 2$) suggested that we have a dissociative adsorption of water molecules.

5 REFERENCES

[1] A. Berman, Vacuum, 47 (**1996**), 327–332
[2] H. F. Dylla, D. M. Manos, P. H. LaMarche, JVST A, 11 (**1993**), 2623–2636
[3] L. Minxu, H. F. Dylla, JVST A, 11 (**1993**), 1702–1707
[4] L. Minxu, H. F. Dylla, JVST A, 12 (**1994**), 1772–1777
[5] R. Dobrozemsky, JVST A, 5 (**1987**), 2520–2521
[6] R. Dobrozemsky, Vacuum, 46 (**1995**), 789–792
[7] R. Dobrozemsky, S. Menhart, K. Buchtela, JVST A, 25 (**2007**), 551–556
[8] P. A. Redhead, JVST A, 13 (**1995**), 467–475
[9] P. A. Redhead, JVST A, 14 (**1996**), 2680
[10] J. M. Lafferty, Foundations of Vacuum Science and Technology, John Wiley & Sons, Inc, New York 1998, 509
[11] R. A Outlaw, H. G. Tompkins, Ultrahigh Vacuum Design and Practice, AVS, New York 2009, 48

ASSESSING THE STRESS FIELDS IN AN INJECTION-MOULDED UNDERCUT GEOMETRY DURING EJECTION SUPPORTED BY NEURAL NETWORKS

MODEL NAPOVEDOVANJA NAPETOSTI V OBMOČJU ZASKOČNE GEOMETRIJE TERMOPLASTIČNEGA IZDELKA Z NEVRONSKIMI MREŽAMI

Blaž Florjanič[1], Uroš Božič[1], Boštjan Zafošnik[2]

[1]University of Ljubljana, Faculty of Mechanical Engineering, Aškerčeva 6, 1000 Ljubljana, Slovenia
[2]School of Technologies and Systems, VITES, Na Loko 2, 8000 Novo mesto, Slovenia
info@imold.si

The continuous demand for cost optimization in the manufacturing of thermoplastic polymer products leads to the design trend of minimizing the number of assembly parts, which consequentially increases their geometrical complexity. This trend directly influences the manufacturing process of injection-moulded thermoplastic polymer parts. Parts designed in accordance with this design trend have many undercut-geometry features, which usually cannot be ejected from the mould without complex mould kinematics. A typical case of undercut geometry is represented by an annular snap joint, which can be released from the mould core by stripping it off. Stripping it off can be applied if the undercut geometry is deformed within the material's elasticity limits during ejection. When the stripping-off principle is used, an analysis of the stress field in the area of the product's undercut geometry should be carried out. Finite-element methods are commonly applied for determining the stress field. These methods offer a single point solution that requires lots of engineering effort and has to be repeated for any geometry modification. This study is focused on developing an artificial-neural-network response model that properly describes the relationships between the input factors (geometrical features) and the corresponding responses (maximum stress) in an undercut area. To overcome the necessity of carrying out numerical simulations for all the input-factor combinations the Taguchi design of experiment was used. Both the analysis of variance preformed within the Taguchi design of experiment and the artificial neural network model validation confirmed that the most influential geometrical input factor is the draft angle. For the artificial-neural-network model validation a virtual full-factorial design of experiment was used and the response surfaces were generated based on the obtained experimental results. Although the model solution is developed for a specific undercut geometry, the presented paper offers a generalized approach for assessing the stress field of the undercut-geometry features.

Keywords: thermoplastic polymers, injection moulding, finite-elements method, design of experiments, artificial neural networks

Stalna zahteva globalne ekonomije po optimizaciji stroškov v proizvodnji izdelkov iz termoplastičnih polimerov potiska v ospredje zahtevo po zmanjševanju števila montažnih delov, kar posledično pomeni povečanje njihove geometrijske kompleksnosti. Ta usmeritev neposredno vpliva tudi na proizvodni proces injekcijskega brizganja termoplastičnih polimerov. Sestavni deli, konstruirani v skladu s to usmeritvijo, imajo veliko geometrijskih področij z negativnimi snemalnimi koti, zaradi katerih je treba v orodjih uporabiti mehanizme s kompleksno kinematiko. Eden osnovnih primerov je cilindrična zaskočna geometrija, ki jo je mogoče izmetati s prisilnim snemanjem. Princip prisilnega snemanja geometrije izdelka je mogoče uporabiti kadar se geometrija z negativnimi snemalnimi koti med izmetavanjem poda v okviru meja elastične deformacije. Pri apliciranju prisilnega snemanja je priporočljivo izvesti analizo napetosti, za kar se navadno uporablja metoda končnih elementov. Ta metoda je časovno potratna, zahteva veliko inženirskih in procesorskih virov ter jo je treba ponoviti ob kakršni koli spremembi vhodnih podatkov. Predstavljena raziskava obravnava razvoj modela z uporabo umetnih nevronskih mrež, ki ustrezno obravnava odnose med vhodnimi spremenljivkami (geometrijske karakteristike) in pripadajočim odzivom (maksimalno napetostjo) v območju geometrije z negativnimi snemalnimi koti. Da bi se odpravila potreba po izvajanju obsežnega števila analiz z metodo končnih elementov, je bilo izvedeno načrtovanje eksperimenta po Taguchijevi metodi. Tako analiza variance rezultatov eksperimenta, kot tudi validacija modela, podprtega z nevronsko mrežo, sta potrdili, da je najbolj vplivna geometrijska spremenljivka snemalni kot izdelka. Za presojo vplivnosti posamezne vhodne spremenljivke modela, podprtega z nevronsko mrežo, je bilo izvedeno virtualno načrtovanje eksperimenta, pridobljeni rezultati pa so bili podlaga za oblikovanje odzivnih površin. Predstavljena raziskava ponuja generaliziran način za hitro oceno napetostnega polja v polimernih izdelkih, ki je bil preverjen pri značilnem primeru zaskočne geometrije.

Ključne besede: termoplastični polimeri, injekcijsko brizganje, metoda končnih elementov, načrtovanje eksperimentov, nevronske mreže

1 INTRODUCTION

Undercuts can be defined as the geometrical features on an injection-moulded part whose projection lines in the direction of a mould-opening vector overlap the geometry of the same part. Undercuts prevent the moulded parts from being removed from the cavity in an axial direction and are said to create a die-lock situation.[1]

These require the use of special mould features such as side cores, split cavities, collapsible cores, unscrewing devices, or stripper plates.[2] Some undercuts, like the snap rings on many container caps, can be stripped off the core forming it.[2] This means pushing the thermoplastic material out of the grooves that prevent the product from easily pulling off the core. This method is very

common but depends on the shape of the grooves and the types of thermoplastic material.[3] The allowable deformation should not be exceeded during the ejection of the part from the mould.[4] Only somewhat elastic thermoplastic polymer materials can be stripped, typically polyethylene (PE) and polypropylene (PP). Occasionally, even thermoplastic materials with a lower elasticity such as polystyrene (PS) can be stripped, if the amount of deformation during stripping is within the elastic limit at the temperature given at the moment of ejection.[3]

In this study the special case of an undercut geometry, called an annular snap joint, was observed (**Figure 1**). The following geometrical features were observed as the input factors: draft angle (β), inner radius (R), and thickness (t). The thermoplastic polymer material used for the observed part is polyester-based grade BASF Elastollan® C85A.

Artificial neural networks (ANNs) are recognized as universal function approximators and can be efficiently used to model high-dimensional and nonlinear relations.[5] In order to generate and validate the ANN model the research was carried out with the following steps:

1. Definition of the observed input factors
2. Taguchi Design of Experiment (DOE) preparation
3. Numerical simulations of stress field using finite-element methods (FEMs) and retrieval of the maximum stress
4. Experiment result analysis
5. ANN modelling and response validation
6. Deploying virtual full-factorial DOE on ANN model and response surface generation

2 EXPERIMENT PREPARATION

The experiment preparation includes the input variable definition, the Taguchi DOE, and the CAD model generation.

The correct approach to dealing with several factors is to conduct a factorial experiment.[6] For three observed
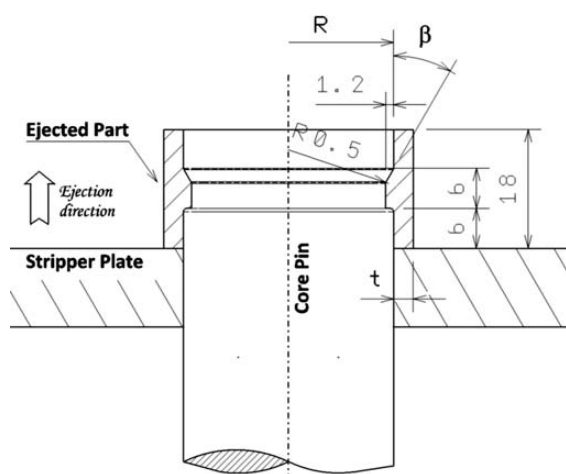

Figure 1: Annular snap joint
Slika 1: Cilindrična zaskočna nerazstavljiva zveza

factors (β, R, and t) four levels were defined, as shown in **Table 1**. To cover all the variable combinations on all levels $4^3 = 64$ runs would be carried out. This represents a full-factorial DOE. Since the FEM requires extended engineering resources, a reduced optimized number of runs was achieved by using the L16 Taguchi Orthogonal Array DOE, as shown in **Table 2**.

Table 1: DOE controllable factor levels
Tabela 1: Nivoji spremenljivk za načrtovani eksperiment

Controllable factors	Level 1 (Low)	Level 2 (Middle)	Level 3 (High)	Level 4 (High+)
Draft Angle β/°	30	40	50	60
Inner radius R/mm	10	13	16	19
Thickness t/mm	2.5	3	3.5	4

The product CAD data was generated with CATIA V5 R19 software.

3 FEM NUMERICAL SIMULATIONS AND RETRIEVAL OF THE MAXIMUM STRESS

This study deals with several nonlinearities: contact, material, and geometrical.[7] All the mentioned nonlinearities can be captured with the finite-element method (FEM). It was considered that the ejection of a moulded part is performed at 100 °C, and that there is a good lubrication between the ejected part and the core pin, which reduces the coefficient of friction to ≈ 0. Due to the high temperature the strain rate has a very small influence on the stress-strain behaviour of the BASF Elastollan® C85A. This property was determined with extra experimental testing using a high-speed testing device. The Marlow constitutive model[8] was used to model the stress-strain behaviour during ejection. The annular snap joint in **Figure 1** presents a cylindrical geometry, and so

Table 2: Experiment results, L16 Taguchi DOE
Tabela 2: Rezultati eksperimenta, L16 Taguchijeva metoda

Run No.	Controllable factors			FEM Response Maximum Stress	S/N-value
	β/°	R/mm	t/mm	σ_{max}/MPa	
1	30	10	2.5	1.707	−4.645
2	30	13	3	1.722	−4.721
3	30	16	3.5	1.754	−4.881
4	30	19	4	1.718	−4.700
5	40	10	3	2.205	−6.868
6	40	13	2.5	1.908	−5.612
7	40	16	4	2.020	−6.107
8	40	19	3.5	1.770	−4.959
9	50	10	3.5	2.595	−8.283
10	50	13	4	2.408	−7.633
11	50	16	2.5	1.869	−5.432
12	50	19	3	1.895	−5.552
13	60	10	4	2.813	−8.983
14	60	13	3.5	2.528	−8.056
15	60	16	3	2.233	−6.978
16	60	19	2.5	1.880	−5.483

an axisymmetric numerical model can be used. The stripper plate and the core pin (**Figure 1**) were modelled as analytical rigid parts because they have a much higher stiffness than the ejected part, which was discretized with 4-noded, bilinear, axisymmetric quadrilateral elements using hourglass control and reduced integration. The calculation was made using an Explicit solver.[8] The core pin was fixed and the stripper plate was controlled with a constant velocity of 20 mm/s.

Table 2 presents the results for the maximum von Mises stress that occurs in the undercut geometry during ejection.

The results in **Table 2** show that the highest von Mises stress occurs for Run No.13, where $\beta = 60°$, $R = 10$ mm and $t = 4$ mm.

The results in **Figure 2** show that the highest stress in the ejected part occurs below the surface in the region of contact between the fillets of the ejected part and the core pin.

Figure 2: Stress field ($\beta = 40$ mm, $R = 10$ mm, $t = 3$ mm)
**Slika 2:** Napetostno polje ($\beta = 40$ mm, $R = 10$ mm, $t = 3$ mm)

4 ANALYSIS OF THE EXPERIMENTAL RESULT

Design of experiments is an effective approach to optimizing the throughput in various manufacturing-related processes.[9] In this study the Taguchi DOE was used (**Table 2**). Three geometry variables, β, R, and t, were studied at four levels. MINITAB 16 software was used to design the simulations and to model and analyse the results. The summary statistics *S/N* signal-to-noise ratios were calculated based on the following equation:

$$S/N_i = -10 \lg \sigma_i^2 \tag{1}$$

where σ_i^2 is the square stress value of the *i*-th dataset. The dataset combinations that were numerically analysed with the computed stress values and *S/N* statistics are shown in **Table 2**.

The effect of the factor is defined as the response change from the overall mean due to a change in the
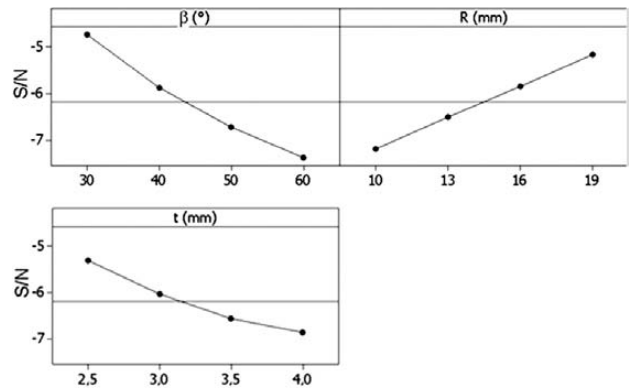
Figure 3: Main separate effects plot for each factor *S/N* values
Slika 3: Diagram vplivnosti *S/N*-vrednosti posameznega faktorja

level of that factor. The main effect plot was used to analyse the importance of the factors in **Figure 3**.

The important goal in the matrix experiment is to find the optimum level for each factor. The Taguchi methodology defines three types of quality characteristics, which are the-smaller-the-better, the-larger-the-better, and the-nominal-the-best. The design of the injection-moulding geometry should take steps towards reducing the stress values inside the moulding during ejection. Therefore, a smaller-the-better quality characteristic is implemented in this study, which means that we should maximize the *S/N* values because of a decreasing function – log. It was determined in **Figure 3** by observing the optimum level for each factor at the highest value of S/N. Thus, the optimum draft angle is β (30°), the optimal inner radius is R (19 mm), and the optimal thickness is t (2.5) mm. The predicted best setting does not correspond to one of the runs in the matrix, which is normal. The average *S/N* for each level of the three factors is listed in **Table 3**. These averages, known as main effects, are also shown in **Figure 3**.

Table 3: Average *S/N* ratio by factor levels with an overall mean of –6.18
Tabela 3: Povprečni *S/N* za posamezni nivo spremenljivke (skupno povprečje –6,18)

Controllable factors	Average S/N ratio			
	Level 1	Level 2	Level 3	Level 4
Draft Angle β/°	–4.74	–5.89	–6.73	–7.37
Inner radius R/mm	–7.19	–6.51	–5.85	–5.17
Thickness t/mm	–5.29	–6.03	–6.54	-6.86

4.1 Analysis of variance

The purpose of ANOVA is to determine the relative importance of the geometry factors on the process output. **Table 4** shows the ANOVA results. The sum of squares due to the factors β, R, t are, respectively, 15.33, 9.03, and 5.42. Thus, the factor β represents a major portion of the total variation of the *S/N*. In other words, factor β is responsible for (15.33/30.64) × 100 = 50.03 % of the *S/N* variation. This result is followed by two other

factors, factor R with next largest portion, i.e., 29.47 %, and factor t with 17.69 % of the variation in *S/N*. The smallest portion of the variation goes to the error term that explains 2.84 % of the variation. The ANOVA also indicates that all three factors are highly significant since their F values (35.17, 20.72, and 12.43) are high compared to $F_{0.05,3,15} = 3.29$.

Table 4: Analysis of Variance
Tabela 4: Analiza variance

Source	DF	SS	MS	F
Draft Angle $\beta/°$	3	15.33	5.11	35.17
Inner radius R/mm	3	9.03	3.01	20.72
Thickness t/mm	3	5.42	1.81	12.43
Residual Error	6	0.87	0.15	
Total	15	30.64		

NOTES: DF… Degrees of freedom, SS… Sum of squares, MS… Mean squares, F… statistic

4.2 Prediction of S/N under optimal conditions

The principal goal of conducting Robust Design experiments is to determine the optimum level of each factor. In this study the optimum condition is β (30°), R (19 mm), and t (2.5) mm. The additive model[10] to predict the value of the *S/N* ratio under the optimum conditions was used:

$$\frac{S}{N_{opt}} = m + b_i + R_j + t_k + e$$

$$\frac{S}{N_{opt}} = -6.18 + (-4.74 + 6.18) + (-5.17 + 6.18) + (-5.29 + 6.18) \quad (2)$$

$$\frac{S}{N_{opt}} = -2.84$$

where m is the overall mean of the S/N for the experimental region, and β_i, R_j, t_k are deviations from m caused by the factors β, R, and t, respectively. The term e indicates the error. Since the sum of squares due to the error is small, the corresponding contribution was removed in the prediction of the *S/N* under optimum conditions. The values in Eq. (2) are taken from **Table 3**.

Using Eq. (1) the stress value under the optimum conditions was predicted as:

$$\sigma = \sqrt{10^{\frac{-S/N_{opt}}{10}}} = \sqrt{10^{0.284}} = 1.387 \text{ MPa} \quad (3)$$
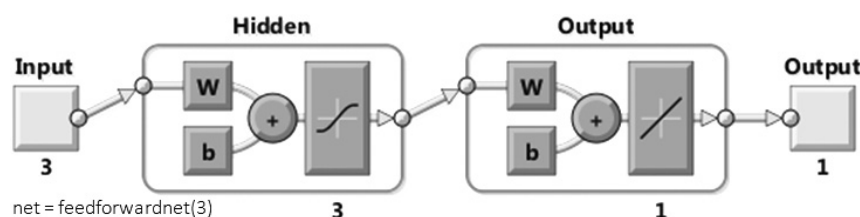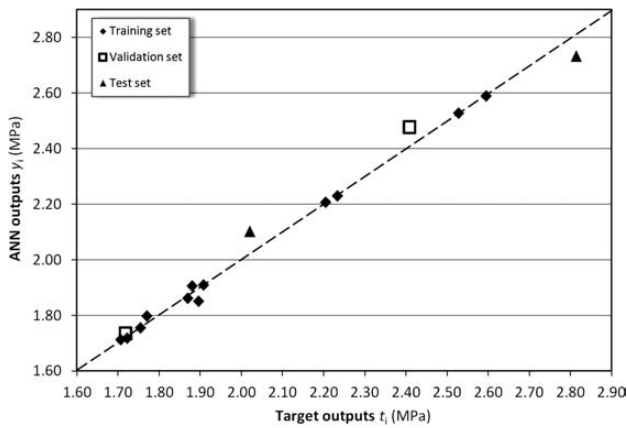
4.3 Confirmation simulation

After the calculation of the optimal conditions a numerical simulation with optimum parameter settings was performed. The simulation output with the prediction was compared. The simulation output under β (30°), R (19 mm), and t (2.5 mm) yields 1.399 MPa, which is very close to the predicted stress of 1.387 MPa, as calculated in Eq. (3). Having simulated and predicted values close to each other, it can be concluded that the additive model is adequate for describing the dependence of the *S/N* ratio on the various parameters.

5 ANN MODEL FOR ASSESSING THE MAXIMUM STRESS

ANNs provide non-parametric, data-driven, self-adaptive approaches to information processing.[11] To model a multivariable relation between the selected variable factors and the corresponding maximum stress a multi-layer, feed-forward network was used. The multi-layer feed-forward neural networks are usually applied for function-fitting problems. For ANN model generation a MATLAB 7.11.0.584 (R20130b) software environment was used. In order to avoid over fitting a simple, two-layer, feed-forward network was created using the Neural Network Toolbox™. Feed-forward networks often have one or more hidden layers of sigmoid neurons followed by an output layer of linear neurons. Multiple layers of neurons with nonlinear transfer functions allow the network to learn nonlinear relationships between the input and output vectors. The linear output layer is most often used for function fitting (or nonlinear regression) problems.[12] There are several training algorithms that can be used, from among which the Levenberg-Marquard back-propagation algorithm was adopted. It is a method that is normally used for small and medium-sized feed-forward neural networks.[12]

As a performance function for feed-forward networks a mean square error (*MSE*) was used, which defines the average squared difference between the network outputs and the target responses.

Through an iteration process of testing several feed-forward ANN architectures an optimised solution was chosen, as shown in **Figure 4**. It has 3 units in the input layer, 3 neurons with a sigmoid activation function in the hidden layer, and a single output neuron with a linear activation function.

Figure 4: ANN architecture generated with MATLAB
Slika 4: Arhitektura nevronske mreže, generirane v programskem okolju MATLAB

Figure 5: Scatter plot of ANN outputs vs. target outputs
Slika 5: Diagram raztrosa odzivov modela, podprtega z nevronsko mrežo

The ANN model results are shown in **Table 5**. The training set returned a root mean square error (*RMSE*) of 0.017 MPa and a mean absolute percentage error (*MAPE*) of 0.07 %. Both the validation set and the test set show an acceptable root mean square error (*RMSE*) of 0.052 MPa and 0.082 MPa, and also low mean absolute percentage errors (*MAPE*) of 2.06 % and 0.67 %. These results show an acceptable level of ANN model performance. Confirmation of this conclusion is also a low scatter between the target value and the corresponding ANN response, shown in **Figure 5**. All the datasets show high correlation coefficients.

Table 5: ANN model results
Tabela 5: Odziva modela

	Training set	Valida- tion set	Test set	All
RMSE/MPa	0.017	0.052	0.082	0.037
MAPE/%	0.07	2.06	0.67	1.14
Correlation coefficient	0.99829	1	1	0.99442

$$RMSE = \sqrt{\frac{1}{N}\sum_{i=1}^{N}(t_i - y_i)^2} \qquad (4)$$

Table 7: Analysis of Variance for σ_{max}/MPa
Tabela 7: Analiza variance za napetost σ_{max}/MPa

Source	DF	Seq SS	Adj SS	Adj MS	F	P
Draft Angle β/°	3	3.46610	3.46610	1.15537	620.96	0.000
Inner radius R/mm	3	2.15679	2.15679	0.71893	386.39	0.000
Thickness t/mm	3	1.38575	1.38575	0.46192	248.26	0.000
$\beta * R$	9	0.07428	0.07428	0.00825	4.44	0.001
$\beta * t$	9	0.00542	0.00542	0.00060	0.32	0.960
$R * t$	9	0.00304	0.00304	0.00034	0.18	0.994
Residual Error	27	0.05024	0.05024	0.00186		
Total	63	7.14161				
S = 0.0431350 R-Sq = 99.30 % R-Sq(adj) = 98.36 %						

NOTES: DF… Degrees of freedom, Seq SS… Sequential sums of squares, Adj SS… Adjusted sums of squares, Adj MS… Adjusted mean squares, F… statistic, P… Probability, S… Estimate of the variance, R-Sq… Coefficient of determination, R-Sq(adj)… Modified R-Sq that has been adjusted for the number of terms in the model

$$MAPE = \frac{1}{N}\sum_{i=1}^{N}\left|\frac{t_i - y_i}{t_i}\right| \qquad (5)$$

In the above equations t_i and y_i denote the target and the ANN response and N denotes the number of input samples.

Because of the small sample set a further ANN model verification was carried out on an additional three test samples, which were not included in neural network generation. The test sample data is shown in **Table 6**. The ANN model responses were observed and compared with the FEM responses. The calculated relative percentage error (*RPE*) confirms that the ANN responses are within an acceptable accuracy.

Table 6: ANN model verification
Tabela 6: Ovrednotenje odziva modela

Verifica- tion Run No.	Controllable factors			Response σ_{max}/MPa		*RPE*/%
	β/°	R/mm	t/mm	FEM	ANN	
1	35	17	3.2	1.798	1.731	−3.75
2	42	14	3.7	2.229	2.186	−1.91
3	53	12	2.8	2.290	2.333	−1.87

RMSE = 0.052 MPa   *MAPE* = 1.62 %

6 VIRTUAL DOE AND RESPONSE SURFACE GENERATION

To identify the significance of the input factors (β, R and t) and their interactions ($\beta*R$, $\beta*t$ and $R*t$) in the ANN model a full-factorial DOE ($4^3 = 64$ runs) was carried out, with the levels defined in **Table 1**. A full-factorial design was used, because the virtual environment in this case does not represent resource limitations, and there was no necessity to use any of the fractional factorial design at disposal. The analysis of variance shown in **Table 7** indicates that all the input factors can be considered significant, because their P-value is below a threshold of 0.05. On the other hand, their interactions cannot be considered as significant except for $\beta*R$.

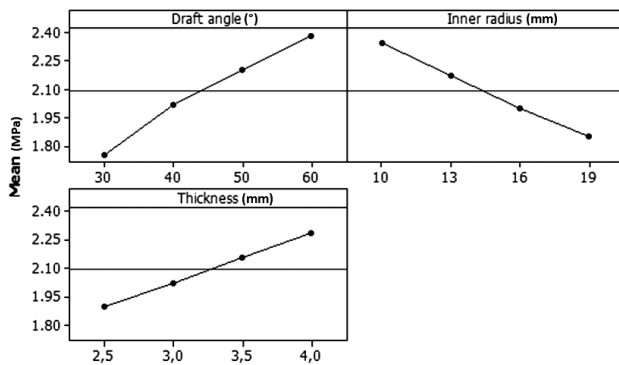To analyse the importance of the input factors in the ANN model, the main effect plot was generated as

Figure 6: Main effects plot for σ_{max}/MPa
Slika 6: Diagram vplivnosti faktorjev na napetost σ_{max}/MPa
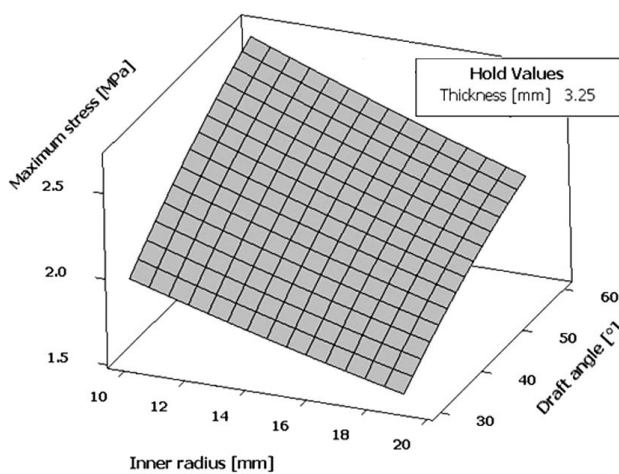

Figure 7: Response-surface plot for σ_{max}/MPa
Slika 7: Diagram odzivne površine za napetost σ_{max}/MPa

shown in **Figure 6**. From the plot it can be concluded that the most significant input factor is the draft angle (β), followed by the inner radius (R) and the thickness (t). While the draft angle (β) and the thickness (t) have positive gradients, the inner radius (R) shows that with increasing value the maximum stress decreases.

To properly visualize the effect of the two most influential input factors' responses, surface modelling was applied to the developed ANN model. **Figure 7** shows the predicted maximum stress at a fixed thickness of 3.25 mm. As expected, the surface response confirms the already observed gradients in the main effect plot as shown in **Figure 6**.

7 DISCUSSION AND CONCLUSIONS

This paper proposes an implementation and evaluation of an ANN-based model for assessing the stress field in an injection-moulded undercut geometry during ejection at an acceptable accuracy level. The stress field

in the injection-moulded undercut geometry was determined with a finite-element model, where besides contact also material and geometrical nonlinearities were considered. Both the analyses of variance preformed on the Taguchi DOE and ANN model validation, carried out through separate statistical analyses, confirmed that all the observed input factors draft angle (β), inner radius (R), and thickness (t) can be considered statistically significant. While an increased draft angle (β) or thickness (t) means a higher maximum stress, an increased inner radius (R) reduces it.

The following benefits can be expected by applying the proposed approach:

- Structured methodology for generating and evaluating an ANN-based stress-assessment model;
- Reduction of engineering efforts for maximum stress assessment when high geometrical variability is considered;
- Better understanding of input factors influence on the maximum stress.

The proposed solution for generating and evaluating an ANN-based stress-assessment model can be used as a generalized solution approach and expanded to similar cases.

8 REFERENCES

[1] G. Boothroyd, P. Dewurst, W. A. Knight, Product Design for Manufacture and Assembly, Third Edition, CRC Press, Boca Raton 2011

[2] T. A. Osswald, L. S. Turng, P. Gramann, Injection Molding Handbook, 2nd Edition, Hanser Gardner Publications, 2008

[3] H. Rees, Mold Engineering, 2nd Edition, Hanser Gardner Publications, 2011

[4] Snap-Fit Joints for Plastic – A Design Guide, Bayer Material Science, MS 00062550, Edition 02 / 2013, www.plastics.bayer.com

[5] S. Cavalier, P. Maccarone, R. Pinto, Parametrical vs. Neural Network Models for Estimation of Product Costs: A Case Study in the Automotive Industry, International Journal of Production Economics, (**2004**) 91, 165–177

[6] D. C. Montgomery, Design and Analysis of Experiment, 8th Edition, John Wiley & Sons, 2013

[7] NAFEMS, Introduction to Nonlinear Finite Element Analysis, Glasgow, 1991

[8] ABAQUS, Version 6.12-1 documentation, 2012

[9] B. Ozcelik, T. Erzurumlu, Comparison of the Warpage Optimization in the Plastic Injection Molding using ANOVA, Neural Network Model and Genetic Algorithm, Journal of Materials Processing Technology, 171 (**2006**), 437–445

[10] M. S. Phadke, Quality Engineering Using Robust Design, AT&T Bell Laboratories, USA, 1989

[11] X. Shi, P. Schillings, D. Boyd, Applying Artificial Neural Networks and Virtual Experiment Design to Quality Improvement of Two Industrial Processes, International Journal of Production Research, 42 (**2004**) 1, 101–118

[12] M. H. Beale, M. T. Hagan, H. W. Demuth, MATLAB, Neural Network Toolbox™ 7, User's Guide, online edition, The MathWorks, Inc., 2010

TEM STUDY OF DISLOCATIONS IN DUPLEX STAINLESS STEEL

ŠTUDIJA DISLOKACIJ V DUPLEKSNEM NERJAVNEM JEKLU S PRESEVNO ELEKTRONSKO MIKROSKOPIJO

Darja Jenko[1], Stan Mandziej[2], Caroline Toffolon-Masclet[3], Borivoj Šuštaršič[1], Monika Jenko[1]

[1]Institute of Metals and Technology, Lepi pot 11, 1000 Ljubljana, Slovenia
[2]Advanced Materials Analysis, POB 3751, 7500 DT Enschede, The Netherlands
[3]Commissariat à l'Energie Atomique, DMN/SRMA, 91191 Gif-sur-Yvette, Sacley, France
darja.jenko@imt.si

Specimens of duplex stainless steel (DSS, the 258-alloy type) were isothermally annealed (aged) at 300 °C and 350 °C for 10000 h and 30000 h. Spinodal decomposition of the solid solution in ferrite occurs during the thermal ageing of this material with a redistribution of mainly Cr and Ni and a formation of nanocellular domains. This causes significant changes in the mechanical properties (the hardness and the tensile strength increase, while the ductility and the notch toughness decrease). The change in the mechanical properties may be related to the changes in the material's internal structure (stacking faults, the morphology and density of dislocations) or/and internal stresses. Therefore, non-aged and aged specimens were studied using transmission electron microscopy (TEM).

Keywords: duplex stainless steel, ferrite, austenite, spinodal decomposition, transmission electron microscopy, dislocations

Vzorci dupleksnega nerjavnega jekla (DSS, tip zlitine 258) so bili izotermno žarjeni (starani) pri temperaturah 300 °C in 350 °C v trajanju 10000 h in 30000 h. Med toplotnim staranjem naj bi se v materialu pojavil spinodalen razpad trdne raztopine v feritu, predvsem s prerazporeditvijo Cr in Ni ter oblikovanjem nanoceličnih domen. To povzroča znatne spremembe mehanskih lastnosti (povečanje trdote in natezne trdnosti ter zmanjšanje razteznosti in zarezne žilavosti). Sprememba mehanskih lastnosti je lahko povezana s spremembo notranje strukture materiala (napak zloga, morfologije in gostote dislokacij) in/ali notranjih napetosti. Zato je bila izvedena študija s presevno elektronsko mikroskopijo (TEM) nestaranih in staranih vzorcev.

Ključne besede: dupleksno nerjavno jeklo, ferit, avstenit, spinodalni razpad, presevna elektronska mikroskopija, dislokacije

1 INTRODUCTION

Many metallic alloys, including duplex stainless steels (DSSs), consist of austenite (γ-Fe) and ferrite (α-Fe). The two phases have different crystal lattices, austenite having a face-centred cubic lattice (fcc) and many slip-plane systems that prevent cleavage, and ferrite having a body-centred cubic lattice (bcc) that is more easily deformable than austenite, with a propensity for cleavage. The susceptibility to cleavage is greater at lower temperatures, increasing with an addition of certain alloying elements such as chromium, silicon, phosphorus, etc., and it is higher for a coarse-grained microstructure.

Nowadays, DSSs are used in a wide range of industries, especially in the oil and gas, petrochemical, paper and nuclear industries, because of their excellent combination of mechanical properties and corrosion resistance. Austenitic Fe-NiCrMo alloys have high toughness and good resistance to oxidation and scaling.[1] An addition of Ni, Cr and Mo to iron alloys suppresses the polymorphic austenite (γ) $\Leftrightarrow$ ferrite (α) transformation. In the alloys containing high amounts of Cr, the solid solution of Cr and Ni or Co in α-Fe is not stable[2] and it decomposes with a spinodal process up to 750 °C.[3,4] The ferritic-austenitic DSS possesses a specific microstructure, where austenite and ferrite may create internal stresses during the deformation due to their elastic and plastic differences.[5]

The localization of the plastic strain is a typical feature of the fatigue of metallic materials. One of the basic classes of crystal defects is the linear defect, consisting of dislocations, where the rows of atoms are in irregular positions. There are two general types of dislocation: the edge (the Burger vector is perpendicular to the dislocation line) and the screw (the Burger vector is parallel to the dislocation line) dislocations. In 1934 Taylor and Polanyi confirmed dislocations as the carriers of plastic deformation.[6,7] Dislocations have the strain fields arising from the distortions at their cores – the strain drops radially with the distance from the dislocation core. Edge dislocations introduce compressive, tensile and shear lattice strains. Screw dislocations introduce the shear strain only. According to Roters, Raabe and Gottstein[8], there are three dislocation classes: the density of mobile dislocations travelling through a cell structure (ρ_m), the immobile dislocation density inside the cells (ρ_i), and the density of immobile dislocations in the cell walls (ρ_w).

The aim of our research was to investigate ferrite and austenite grains using transmission electron microscopy

Table 1: Average chemical composition in mass fractions (*w*/%) of duplex stainless steel (DSS), 258-alloy type
Tabela 1: Povprečna kemijska sestava v masnih deležih (*w*/%) dupleksnega nerjavnega jekla (DSS); tip zlitine 258

Average chemical composition in mass fractions (*w*/%)											
C	Cr	Ni	Mo	Mn	Si	Cu	Co	Nb	P	S	N
0.033	22.28	9.92	2.34	0.91	0.86	0.26	0.06	0.051	0.031	0.003	0.051

(TEM) or high-resolution TEM (HRTEM) with energy-dispersive X-ray spectrometry (EDXS) and to observe dislocations (the kind of dislocations and their locations in the specimens) in austenitized (non-aged) and annealed (aged at 300 °C and 350 °C for 10000 h and 30000 h) DSS, the 258-alloy type.

2 EXPERIMENTAL WORK

The specimens of DSS (the 258-alloy type) were austenitized at 1100 °C for 6 h, water quenched and then isothermally annealed (aged) at 300 °C and 350 °C for 10000 h and 30000 h. Thin foils of specimens were prepared using argon ion slicing with a JEOL EM-09100IS Ion Slicer[9,10] or electrochemical thinning with the final application of jet electropolishing.

The preparation of thin foils by means of argon ion slicing using an ion slicer is a novel method that enables a quick preparation of high-quality specimens for TEM. The specimens with a thicknesses of around 500 μm were cut out from the bulk material, having a rectangular shape of (0.5–1.0) mm × 2.8 mm (a bulk cross-section preparation), then thinned to less than 100 μm with the grinding paper SiC 800 (the grain size of around 22 μm), and further thinned with an argon ion beam. The thinning process started at the pressure of 10^{-5} Pa or 10^{-4} Pa and alternated between the front and backside of the rotating specimens. The beam was tilted between 1.0° to 2.5°. The accelerating voltage between 4.0 kV and 6 kV, the argon-gas-flow rate between 7.1 and 7.5 (arbitrary units) and the side change interval of 30 s or 60 s were chosen. After a large thin area of the specimens up to (300–500) μm × 700 μm was obtained, a small hole was made in the thinnest region of the specimens. Polishing was done at the tilt angle of 0.5°, at the accelerating voltage of 2 kV and the side change interval of 15 s or 40 s for 7 min, 10 min or 15 min. The total time of thinning was up to 9 h and 40 min.

The other method of thin-foil preparation consisted of diamond-saw cutting of about slices 0.3 mm, mechanical grinding, electrochemical thinning, punching out diameter 3 mm thin disks and final jet electropolishing with a Struers Tenupol-5 device.

After the thin-foil preparations, the non-aged and aged specimens were examined with TEM (JEOL JEM-2100) at the electron accelerating voltage of 200 kV using conventional TEM (CTEM), high-resolution TEM (HRTEM), electron diffraction (ED), and an energy-dispersive X-ray spectrometer (EDXS, JED-2300T).

The results of the inductively coupled plasma atomic emission spectroscopy (ICP-AES) bulk average chemical composition in mass fractions (*w*/%) of the starting (non-aged) material of DSS, the 258-alloy type, are shown in **Table 1**. The base metal is iron.

3 RESULTS AND DISCUSSION

Thin foils for the investigations of non-aged and aged DSS (the 258-alloy type) were studied by means of TEM in order to define ferrite and austenite phases and to observe dislocations.

Dislocations in the non-aged DSS are shown in **Figure 1**. An HRTEM image and EDXS spectra of ferrite and austenite in the same material are shown in **Figures 2** and **3**, respectively. The insets are fast Furier transforms (FFTs). The disorientation that is slightly less evident in **Figure 2** (the α-phase) may be an indication of the size of the spinodal domain. This is yet to be investigated. The elemental composition of the non-aged DSS determined with the TEM/EDS analysis is shown in **Table 2**. Ferrite has a higher content of Cr than austenite and austenite has a higher content of Ni than ferrite. The CTEM bright-field images of dislocations in the aged (annealed) DSS are shown in **Figure 4**.

An example of the interactions of electrons and elastic stresses at the grain boundary between ferrite and austenite in one of the aged DSS specimens (350 °C for 30000 h) is shown in **Figure 5**. The elemental composition of the small areas of the specimen determined with the TEM/EDS analysis is shown in **Table 3**. Compared to the non-aged specimen (**Table 2**), the aged specimen
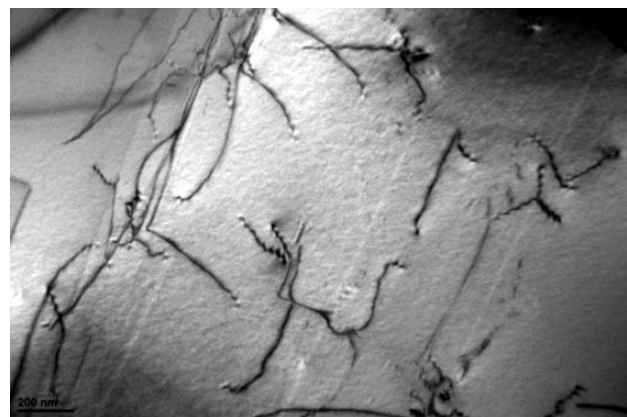
Figure 1: CTEM bright-field image of dislocations in the non-aged DSS, 258-alloy type
Slika 1: Posnetek CTEM v svetlem polju prikazuje dislokacije v nestaranem DSS, tip zlitine 258
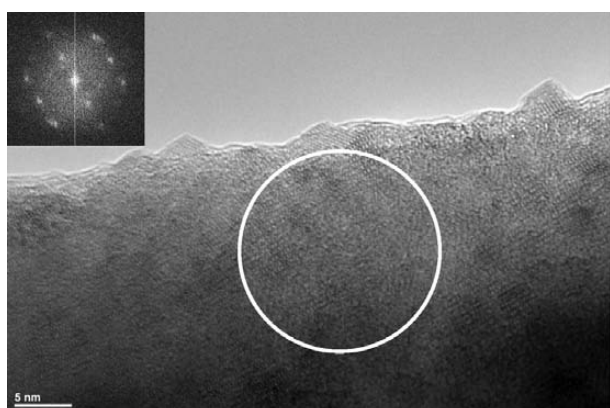
Figure 2: HRTEM image and EDXS spectrum of the indicated area of ferrite in the non-aged DSS, 258-alloy type. The inset is the fast Fourier transform (FFT).
Slika 2: Posnetek HRTEM in rentgenska spektroskopija (EDXS) označenega področja v feritu, nestaranega vzorca DSS, tip zlitine 258. Vstavljena slika prikazuje hitro Fourierjevo transformacijo (FFT).

Table 2: Elemental composition of ferrite and austenite in the non-aged DSS, 258-alloy type, determined with the TEM/EDXS analysis
Tabela 2: Elementna sestava ferita in avstenita v nestaranem DSS, tip zlitine 258, določena z rentgensko spektroskopijo (TEM/EDXS)

Element	Energy (keV)	ferrite		austenite	
		Mass (%)	Error (%)	Mass (%)	Error (%)
Si K	1.739	0.35	0.13	0.69	0.17
Cr K	5.411	27.75	0.00	21.16	0.01
Mn K	5.894	0.38	0.20	0.69	0.28
Fe K	6.398	61.58	0.00	59.87	0.00
Ni K	7.471	5.35	0.02	14.85	0.02
Cu K	8.040	1.68	0.07	0.43	0.66
Mo L	2.293	2.90	0.06	2.30	0.20
Total		100.00		100.00	

has a slightly different composition: its ferrite has a slightly higher content of Mn, Ni, Mo and Si, and a lower content of Cr and Cu, while the austenite has a slightly higher content of Mn and Cu, and a lower content of Ni, Cr, Mo and Si.
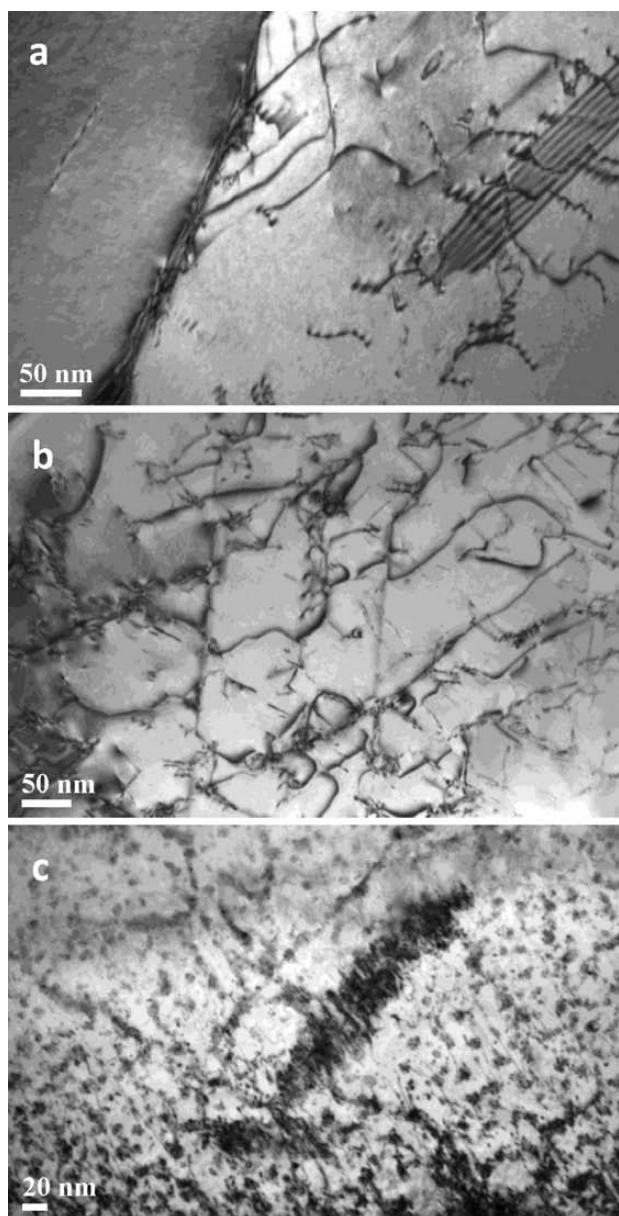

Figure 3: HRTEM image and EDXS spectrum of the indicated area of austenite in the non-aged DSS, 258-alloy type. The inset is the fast Fourier transform (FFT).
Slika 3: Posnetek HRTEM in rentgenska spektroskopija (EDXS) označenega področja v avstenitu, nestaranega vzorca DSS, tip zlitine 258. Vstavljena slika prikazuje hitro Fourierjevo transformacijo (FFT).

Spinodal decomposition occurs during thermal ageing of this type of material. It is characterized by the formation of a nanocellular microstructure of ferrite domains with the austenite regions enriched with Cr and the other alphagene alloying elements as well as the regions enriched with Co, Ni and the other gammagene alloying elements. Because of the difference in the local chemical composition, the lattice parameters are modified and their accommodation creates elastic stresses that increase the hardness and change the mechanical properties (the tensile strength increases, while the ductility and toughness decrease). The change in the mechanical properties may also be related to the changes in the material's internal structure (stacking faults, the morphology and density of dislocations). It has been established that the density of dislocations may have increased during the ageing at 300 °C and that these dislocations appeared in different configurations with many of them being substantially mobile (numerous side trails and traces of dislocations escaping to the foil surface) (**Figure 4**), while many other dislocations became immobile
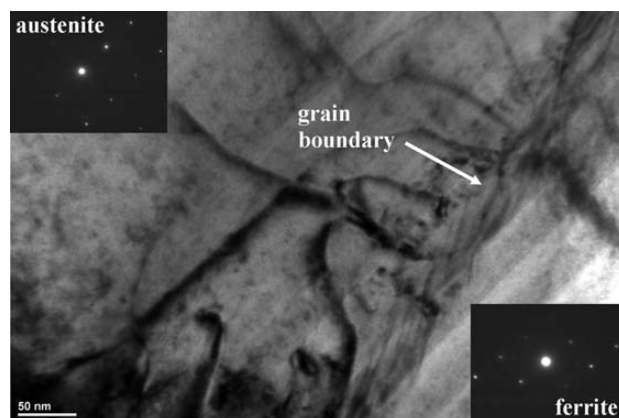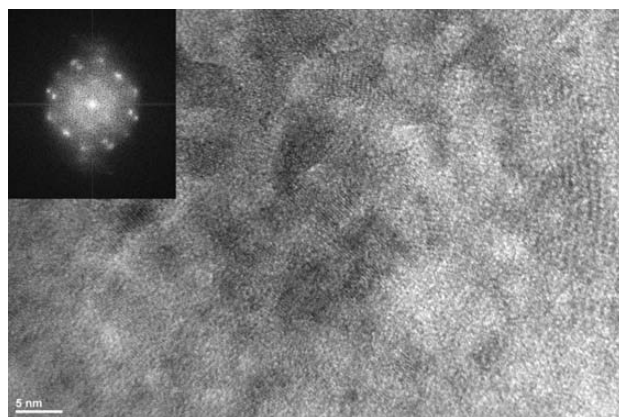
Figure 5: CTEM image of an accumulation of dislocations at the grain boundary between ferrite and austenite in the aged DSS specimen, 258-alloy type (annealed at 350 °C for 30000 h). The insets are electron-diffraction patterns of ferrite (bcc – body-centred cubic structure) and austenite (fcc – face-centred cubic structure).
Slika 5: Posnetek CTEM kopičenja dislokacij na meji zrn med feritom in avstenitom v staranem (350 °C, 30000 h) DSS, tip zlitine 258. Vstavljeni sliki prikazujeta uklonska posnetka ferita (bcc – telesno centrirana kubična struktura) in avstenita (fcc – ploskovno centrirana kubična struktura).

Table 3: Elemental composition of ferrite and austenite in the aged (annealed at 350 °C for 30000 h) DSS, 258-alloy type, determined with the TEM/EDXS analysis
Tabela 3: Elementna sestava ferita in avstenita v staranem (žarjenem pri 350 °C, 30000 h) DSS, tip zlitine 258, določena z rentgensko spektroskopijo (TEM/EDXS)

Element	Energy (keV)	ferrite		austenite	
		Mass (%)	Error (%)	Mass (%)	Error (%)
Si K	1.739	0.55	0.31	0.46	0.25
Cr K	5.411	27.13	0.01	20.31	0.01
Mn K	5.894	2.28	0.12	1.40	0.14
Fe K	6.398	59.85	0.00	63.77	0.00
Ni K	7.471	6.27	0.05	11.67	0.02
Cu K	8.040	0.63	0.64	0.56	0.48
Mo L	2.293	3.29	0.20	1.82	0.24
Total		100.00		100.00	

Figure 4: CTEM bright-field images of dislocations in the aged (annealed) DSS, 258-alloy type: a) 300 °C for 10000 h, b) 350 °C for 10000 h, c) 350 °C for 30000 h
Slika 4: Posnetki CTEM v svetlem polju prikazujejo dislokacije v staranem (žarjenem) DSS, tip zlitine 258: a) 300 °C in 10000 h, b) 350 °C in 10000 h, c) 350 °C in 30000 h

Figure 6: HRTEM image of the matrix of the aged DSS specimen, 258-alloy type (annealed at 350 °C for 30000 h). The inset is the fast Fourier transform (FFT).
Slika 6: Posnetek HRTEM matrice staranega (žarjenega pri 350 °C, 30000 h) vzorca DSS (tip zlitine 258). Vstavljena slika prikazuje hitro Fourierjevo transformacijo (FFT).

(or at least slowed down in their movements) after the ageing at 350 °C (**Figure 4**) when the transformation of the matrix occurred (**Figure 6**), leading to a virtually equilibrium state according to the effect of the ageing temperature on the change in the Charpy notch sharpness. Spinodal decomposition is faster at a higher temperature because of a greater diffusion rate. Due to spinodal decomposition, elastic stresses are generated at the austenite/δ-ferrite phase boundary. Dislocations may be slowed down in their movements or become immobile because of the grain (phase) boundary or obstacles. However, until now, we have not been able to detect such

obstacles (inclusions) with TEM/EDXS. This should also be studied, in detail, in the future, possibly with a better TEM resolution. Further investigations (TEM/EDXS) will enable a better understanding of the characteristics of spinodal decomposition and the change in the compositions of both domains. They will allow us to explain the real rearrangement of the alloying elements and the formation of the eventual new phases during spinodal decomposition. As a result, we will be able to calculate the extent of the internal stresses.

4 CONCLUSIONS

A small difference caused by the change in the ageing temperature was observed. The density of dislocations in the specimens of the non-aged and aged duplex stainless steel (DSS, the 258-alloy type) increased after the ageing at 300 °C and these dislocations appeared in different configurations with many of them being substantially mobile. After the ageing at 350 °C the dislocation configurations changed and many dislocations became immobile (or at least slowed down in their movements) when the transformation of the matrix occurred.

5 REFERENCES

[1] S. S. Ordan'yan, L. G. Maskhuliya, I. B. Panteleev, V. A. Zhukov, Poroshkovaya Metallurgiya, 243 (**1983**) 3, 45–49

[2] J. Vojvodič Tuma, B. Šuštaršič, R. Celin, F. Vodopivec, Mater. Tehnol., 43 (**2009**) 4, 179–187

[3] F. Vodopivec, M. Pristavec, J. Žvokelj, D. Gnidovec, F. Greškovnik, Z. Metallkd., 79 (**1988**), 648–653

[4] B. Šuštaršič, B. Podmiljšak, P. McGuiness, J. V. Tuma, Mater. Tehnol., 43 (**2009**) 3, 129–135

[5] W. Zieliński, W. Świątnicki, M. Bartsch, U. Messerschmidt, Materials Chemistry and Physics, 81 (**2003**) 2–3, 476–479

[6] G. I. Taylor, Proc. Roy. Soc. (London), A145 (**1934**) 855, 362–387

[7] M. Polanyi, Z. Physik., 89 (**1934**) 9–10, 660–664

[8] F. Roters, D. Raabe, G. Gottstein, Acta mater., 48 (**2000**) 17, 4181–4189

[9] A. Yasuhara, JEOL News, 40 (**2005**) 1, 46–49

[10] D. Jenko, Mater. Tehnol., 45 (**2011**) 4, 303–310

HOT ROLLING OF THE SUPERAUSTENITIC STAINLESS STEEL AISI 904L

VROČE VALJANJE SUPERAVSTENITNEGA NERJAVNEGA JEKLA AISI 904L

Franc Tehovnik, Borut Žužek, Boštjan Arh, Jaka Burja, Bojan Podgornik

Institute of Metals and Technology, Lepi pot 11, 1000 Ljubljana, Slovenia
franc.tehovnik@imt.si

The AISI 904L superaustenitic stainless steel has a narrow processing window. In this work the hot rolling of steel, specifically the hot deformation behavior, is investigated. Specimens of steel were hot rolled at temperatures from 1000 °C to 1250 °C with 50 °C increments and the rolling loads were measured and recorded. Microstructural changes were examined, with the accent on the recrystallization. From changes of the hot-rolling loads and microstructure it is concluded that the recrystallization begins at temperatures around 1050 °C and three passes of 20 % deformation at the deformation rate of 5 s^{-1}. In order to avoid over loads of rolling stand at equal deformation rate and degree, the recommended temperature was 1100 °C. The upper hot-working temperatures were not as clearly determined, it is considered to be around 1250 °C.

Keywords: hot rolling, superaustenitic stainless steel, microstructure evolution, segregation bands

Superavstenitno nerjavno jeklo AISI 904L ima ozko temperaturno območje vročega preoblikovanja. V tem delu je preiskovano vroče valjanje oziroma vedenje jekla med vročim preoblikovanjem. Vzorci jekla so bili valjani pri temperaturah med 1000 °C in 1250 °C s koraki po 50 °C in izmerjene ter zabeležene so bile sile valjanja. Preiskovane so bile spremembe mikrostrukture s poudarkom na rekristalizaciji. Iz spremembe velikosti sil vročega preoblikovanja in mikrostrukturnih sprememb je bilo ugotovljeno, da se rekristalizacija začne pri temperaturi okoli 1050 °C po treh prevlekih z 20 % deformacijo in pri hitrosti deformacije okoli 5 s^{-1}. Zaradi izogibanja velikim obremenitvam valjavskega ogrodja je spodnja priporočljiva meja preoblikovanja pri tej hitrosti deformacije postavljena pri 1100 °C. Za zgornjo mejo procesnega okna je bila predlagana temperatura okrog 1250 °C.

Ključne besede: vroče valjanje, superavstenitno nerjavno jeklo, razvoj mikrostrukture, segregacija

1 INTRODUCTION

The high-alloyed austenitic grades of stainless steels exhibit greater corrosion resistance and higher strength compared with standard stainless steel grades, e.g., ferritic or austenitic grades.[1] Compared to standard austenitic stainless steels, superaustenitic stainless steels have a similar microstructure, but a higher content of some elements, such as chromium, nickel, molybdenum, copper and nitrogen, that increase the strength and corrosion resistance. As the content of alloying elements increases, problems of industrial processing become more severe. The high-temperature strength increases and the softening rate is minimal at temperatures below 950 °C.[2]

To avoid excessive mill loading, hot working is often carried out at a high rolling temperature.[3] The presence of some alloying elements, e.g., molybdenum, has a negative influence on the hot ductility of austenitic steels.[4] Upper hot working temperatures are limited, because of the hot shortness, which results from segregation of alloying elements during casting.[5,6] Segregations at grain boundaries melt at high temperatures and the steel cracks during hot working. However, when properly heated, segregation-rich bands are elongated by hot rolling. The brittle sigma phase, which is the most common intermetallic precipitate in austenitic stainless

steels,[7] precipitates within these bands and affects the mechanical properties.[8,9] Therefore, the processing window of superaustenitic steels is quite narrow, often just 150–200 °C and is related to a series of complex processes taking place during deformation.[10] Austenite has a low stacking-fault energy (SFE) and both dynamic recrystallization (DRX) and static recrystallization (SRX) play an important role in the evolution of the microstructure during and after hot deformation.[11] It was frequently reported that DRX is the dominant restoration mechanism during the hot deformation of austenitic stainless steels.[12–15] DRX depends on the processing temperature and deformation rate.[16,17]

The present work is aimed at investigating a part of the complex processes that take place in the narrow processing window of AISI 904L, an industrially important superaustenitic stainless steel.

2 EXPERIMENTAL

For hot-rolling tests, flat specimens of AISI 904L, with the chemical composition in **Table 1**, were used. The specimens were cut from a thick hot-rolled plate 20 mm and had a length of 145 mm and a width of 46 mm. The soaking temperatures were (1000, 1050, 1100, 1150, 1200 and 1250) °C, the soaking time was 30 min. The deformation per pass was 20 % and three passes were

Table 1: Chemical composition of AISI 904L in mass fractions (*w*/%)
Tabela 1: Kemijska sestava AISI 904L v masnih deležih (*w*/%)

Chemical composition (*w*/%)									
C	Si	Mn	P	S	Cr	Ni	Mo	Cu	N
0.006	0.22	1.41	0.019	0.0005	19.61	26.1	3.9	1.4	0.0686

made for each specimen. The deformation rate during rolling was calculated to be 5 s^{-1}. The rolled specimens were then air cooled and prepared for light microscopy (LOM) examinations. The rolling loads were measured with a measurement system with 2000 recordings per second. A specimen with an initial microstructure was isothermally annealed at 950 °C for 30 min and examined with light and electron microscopy.

3 RESULTS AND DISCUSSION

Figure 1 shows the initial microstructure of AISI 904L. The initial grain size was 110 μm, with a large number of annealing twins in austenite grains typical for alloys with a low SFE[13].

The rolling loads measured at six different temperatures during three passes are shown in **Figure 2**. The loads decrease with an increasing temperature. The rolling loads at 1000 °C are the highest, and in the range from 1100 kN to 1300 kN. The loads at 1250 °C are the lowest, and increase from about 500 kN measured during the first pass to over 800 kN in the third pass. The average load rises with each pass, which can be attributed to the fall of temperature in the rolling specimen and to incomplete DRX. It is supposed that the peaks in load at the start or the end of the pass (**Figure 2**) are the result of temperature differences due faster cooling at the specimens' edges.

While the edged surfaces of the measurements of loads at lower temperatures 1000 °C to 1100 °C are attributed to the measurement system, the problem becomes more serious at higher loads. The most drastic change in load was observed after the second pass at 1100 °C. Based on the jump of the load it is evident that the temperature of hot deformation for this steel should not be lower than 1100 °C. Therefore, it can be concluded that the lower temperature of the processing window at the deformation rate of 5 s^{-1} is 1100 °C. The LOM analysis of the microstructure confirmed a significant change at 1100 °C, where the DRX becomes most evident (**Figure 3**).

The austenite microstructure obtained after hot rolling with 3 × 20 % deformation at different temperature is shown in **Figure 3**. The serrated boundaries of highly elongated grains and local bulges are clearly observed in the microstructure with a rolling temperature of 1050 °C (**Figure 3b**). The initial stages of DRX appear on the grain boundaries.

The first recrystallized grains were visible after rolling at 1050 °C. The extent of the recrystallization increased with temperature and was 100 % at 1200 °C. The changes of microstructure show that the most significant rise of DRX occurs at 1150 °C, as shown by a comparison of **Figures 3c** and **3d**. In both cases the existence of equiaxed grains confirms the occurrence of DRX already during the hot rolling. The presence of deformed austenite grains are a clear sign of incomplete DRX. The recrystallization process here includes distinct nucleation and growth stages of new grains at the interface of the recrystallized and non-recrystallized regions.[12–14] This process goes on until all the stored energy is used.[18] Once DRX is completed, the steady state is established as a result of a dynamic balance
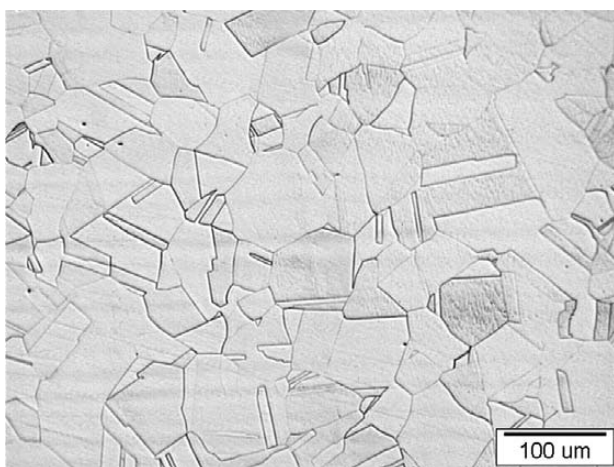
Figure 1: Initial steel microstructure after solution annealing
**Slika 1:** Začetna mikrostruktura jekla po raztopnem žarjenju
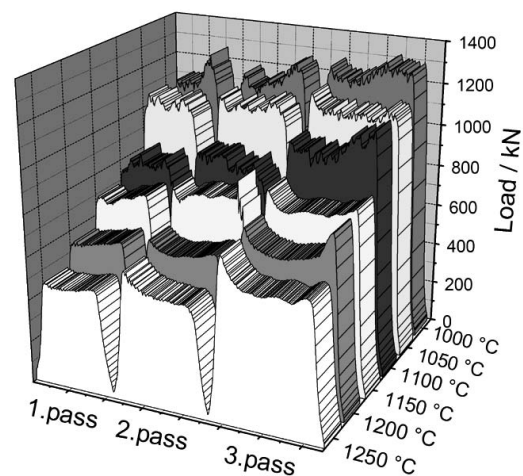
Figure 2: Rolling load per pass at different temperatures during hot rolling
Slika 2: Sile valjanja pri posameznem prevleku pri različnih temperaturah vročega valjanja

between recrystallization and work hardening.[16–18] There are no recrystallized grains in the samples rolled at 1000 °C, which indicates that no DRX has taken place. An apparently fully dynamically recrystallized microstructure is present at 1200 °C and 1250 °C and at this temperature a greater grain growth than at 1200 °C is observed. Therefore, 1250 °C is supposed to be the upper processing temperature for a fine-grained microstructure. The presence of a few twin boundaries is also found in the DRX grains. These newly formed twin boundaries are reported to be active nucleation sites for continuing DRX during straining[13].

As shown in **Figures 3b** and **3c**, recrystallization nuclei appear on the grain and twin boundaries, thus confirming the necklace DRX mechanism. The new recrystallized grains nucleate on the deformed grain boundaries and form a necklace around it.[18–20]

The segregation of alloying elements occurs during the solidification of AISI 904L. The sigma phase (σ-phase) forms from the austenite, because the solidification is primarily austenitic for all austenitic stainless steels with the $w(\mathrm{Cr_{eq}})/w(\mathrm{Ni_{eq}}) < 1.5$[21], AISI 904L $w(\mathrm{Cr_{eq}})/w(\mathrm{Ni_{eq}}) = 0.9$ and in interdendritic areas the contents of chromium and molybdenum are increased. **Figure 4** shows the σ-phase precipitates also within austenite grains as a consequence of segregations. During rolling the segregations are elongated and are observed as dark bands in etched metallographic
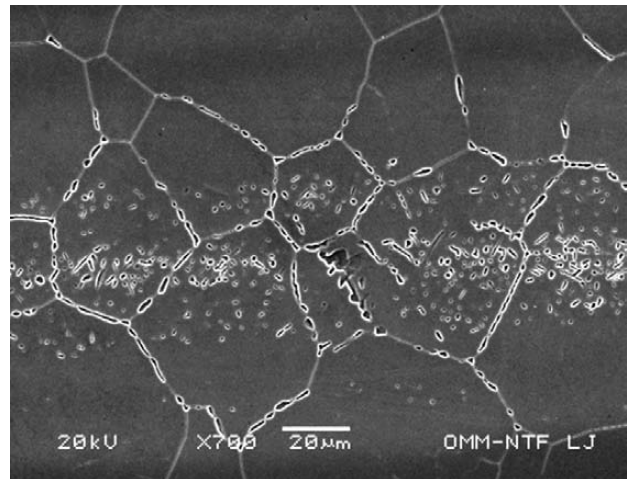
Figure 4: σ-phase precipitates at 950 °C
**Slika 4:** Izločanje σ-faze pri 950 °C

samples. An EDS analysis did not reveal a greater change in the concentration of the alloying elements because the area of sampling is too large. But after isothermal annealing at 950 °C larger σ-phase precipitates can be observed (**Figure 4**), confirming the existence of the segregations.

Dendrite segregations occur because of the high content of chromium and molybdenum and are possible because the ratio between the ferrite and austenite
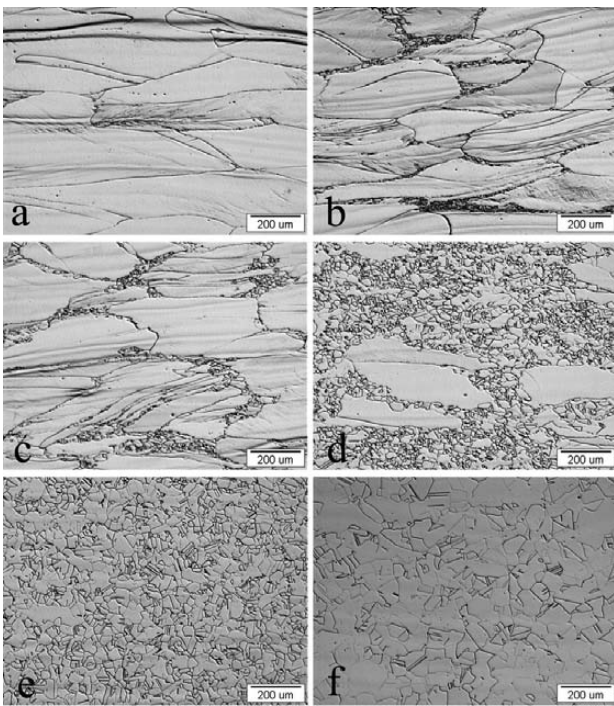
Figure 3: Microstructure of specimens after three rolling passes at different temperatures: a) 1000 °C, b) 1050 °C, c) 1100 °C, d) 1150 °C, e) 1200 °C, f) 1250 °C
Slika 3: Mikrostruktura vzorcev po treh prevlekih pri različnih temperaturah valjanja: a) 1000 °C, b) 1050 °C, c) 1100 °C, d) 1150 °C, e) 1200 °C, f) 1250 °C
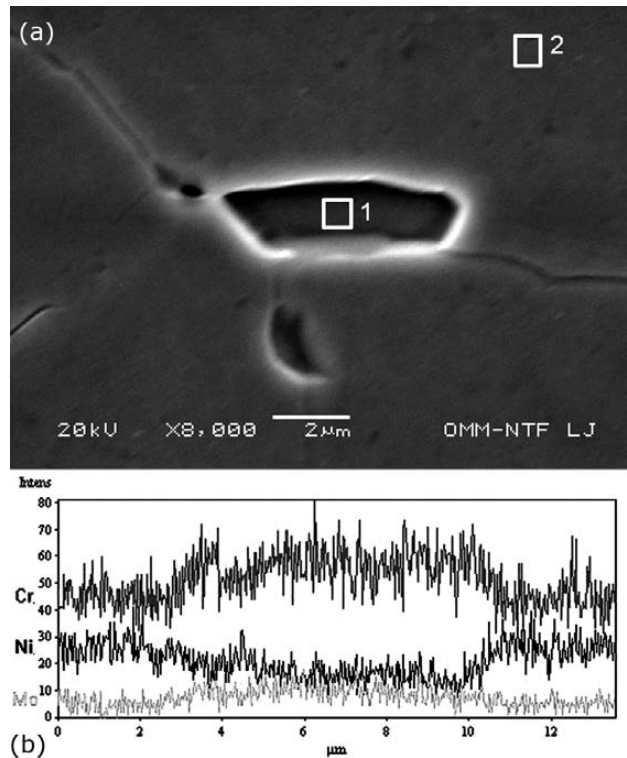
Figure 5: SEM image of σ-precipitate with marked points of EDS analysis, b) line scan analysis acros σ-phase precipitate
Slika 5: a) SEM-posnetek izločka σ-faze z označenimi mesti EDS analiz, b) linijska analiza porazdelitve elementov preko σ-fazi

forming elements changed in the austenite grains. At 950 °C σ-phase precipitates at the grain boundaries and in the segregation band in the form of lamellas or irregular shapes. The chromium contents in the σ–phase can reach up to 30 %, molybdenum contents are from 15 % to 20 %, nickel contents are below 14 %, as can be seen in the EDS analysis of the σ-phase in **Figure 5**, the results of the analysis are given in **Table 2**. Alloying elements, such as chromium, molybdenum and silicon, promote the formation of the σ-phase, while nickel and nitrogen retard it. The σ-phase mostly forms at the austenite grain boundaries, triple junctions and incoherent twin borders.

A line scan of a sperodised σ-phase on the austenite grain boundaries shows higher contents of chromium and molybden and lower contents of nickel. The line scan is shown in **Figure 5**.

Table 2: Chemical composition of σ-phase and matrix from **Figure 5**
Tabela 2: Kemijska sestava σ-faze in matrice s **slike 5**

Chemical composition (w/%)							
Spectrum	Si	Mn	Cr	Ni	Mo	Cu	Fe
1	0.54	1.26	30.47	10.70	19.02	0.00	38.00
2	0.27	1.52	19.92	22.99	4.75	2.55	48.00

4 CONCLUSIONS

The microstructure of the superaustenitic stainless steel AISI 904L after hot rolling consists only of austenite. With three 20 % rolling passes with a deformation rate of 5 s^{-1} the first recrystallized grains appear at the rolling temperature of 1050 °C and the degree of recrystallization increases with higher temperatures. Recrystallization nuclei were found to form on the grain boundaries, triple junctions and at incoherent twin boundaries. The newly formed recrystallized grains form the so-called "necklace" recrystallization mechanism as a clear sign of DRX. Across the segregation areas with high chromium and molybdenum contents the σ-phase precipitates intragranulary and intergranularly.

Acknowledgment

5 REFERENCES

[1] L. Tan, K. Sridharan, T. R. Allen, R. K. Nanstad, D. A. McClintock, Microstructure tailoring for property improvements by grain boundary engineering, J. Nucl. Mater., 374 (**2008**), 270–280

[2] B. Bradaškja, B. Pirnar, M. Fazarinc, P. Fajfar, Deformation Behaviour and Microstructural Evolution During Hot Compression of AISI 904L, Steel Res. Int., 82 (**2011**) 4, 346–351

[3] M. Mukherjee, T. Pal, Role of microstructural constituents on surface crack formation during hot rolling of standard and low nickel austenitic stainless steels, Acta Metall. Sin. (Engl. Lett.), 26 (**2013**), 206–216

[4] F. Tehovnik, D. Steiner Petrovič, F. Vode, J. Burja, Influence of Molybdenum on The Hot-Tensile Properties of Austenitic Stainless Steels, Mater. Tehnol., 46 (**2012**) 6, 649–655

[5] F. Tehovnik, F. Vodopivec, B. Arzenšek, R. Celin, The effect of lead on the hot workability of austenitic stainless steel with a solidification structure, Metalurgija, 49 (**2010**), 49–52

[6] M. Torkar, Effect of Trace and Residual Elements on The Hot Brittleness, Hot Shortness and Properties of 0.15–0.3 % C Al-Killed Steels with a Solidification Microstructure, Mater. Tehnol., 44 (**2010**) 6, 327–333

[7] M. Vach et al., Evolution of secondary phases in austenitic stainless steels during long-term exposures at 600, 650 and 800 °C, Mater. Charact., 59 (**2008**), 1792–1798

[8] R. W. Fonda, E. M. Lauridsen, W. Ludwig, P. Tafforeau, G. Spanos, Two-Dimensional and Three-Dimensional Analyses of Sigma Precipitates and Porosity in a Superaustenitic Stainless Steel, Metall. Mater. Trans. A, 38 (**2007**), 2721–2726

[9] A. C. Stauffer, D. A. Koss, J. B. Mckirgan, Microstructural Banding and Failure of a Stainless Steel, Metall. Mater. Trans. A, 35A (**2004**), 1317–1327

[10] R. M. Forbes Jones, L. A. Jackman, The structural evolution of superalloy ingots during hot working, JOM, 51 (**1999**), 27–31

[11] A. Belyakov, H. Miura, T. Sakai, Dynamic recrystallization in ultra fine-grained 304 stainless steel, Scr. Mater., 43 (**2000**), 21–26

[12] A. Momeni, K. Dehghani, H. Keshmiri, G. R. Ebrahimi, Hot deformation behavior and microstructural evolution of a superaustenitic stainless steel, Mater. Sci. Eng. A, 527 (**2010**), 1605–1611

[13] A. Hoseini Asli, A. Zarei-Hanzaki, Dynamic Recrystallization Behavior of a Fe-Cr-Ni Super-Austenitic Stainless Steel, J. Mater. Sci. Technol., 25 (**2009**), 603–606

[14] R. Puli, G. D. Janaki Ram, Dynamic recrystallization in friction surfaced austenitic stainless steel coatings, Mater. Charact., 74 (**2012**), 49–54

[15] P. Fajfar, B. Bradaškja, B. Pirnar, M. Fazarinc, Determination of hot workability and processing maps for AISI 904L stainless steel, RMZ – Materials and Geoenvironment, 58 (**2011**), 383–91

[16] M. Tikhonova, R. Kaibyshev, X. Fang, W. Wang, A. Belyakov, Grain boundary assembles developed in an austenitic stainless steel during large strain warm working, Mater. Charact., 70 (**2012**), 14–20

[17] Z. Yanushkevich, A. Mogucheva, M. Tikhonova, A. Belyakov, R. Kaibyshev, Structural strengthening of an austenitic stainless steel subjected to warm-to-hot working, Mater. Charact., 62 (**2011**), 432–437

[18] A. Momeni, K. Dehghani, Microstructural Evolution and Flow Analysis during Hot Working of a Fe-Ni-Cr Superaustenitic Stainless Steel, Metall. Mater. Trans. A, 42 (**2010**), 1925–1932

[19] H. Mirzadeh, A. Najafizadeh, Hot Deformation and Dynamic Recrystallization of 17-4 PH Stainless Steel, ISIJ Int., 53 (**2013**), 680–689

[20] Y. Han, G. Liu, D. Zou, R. Liu, G. Qiao, Deformation behavior and microstructural evolution of as-cast 904L austenitic stainless steel during hot compression, Mater. Sci. Eng. A, 565 (**2013**), 342–350

[21] N. Suutala, Effect of solidification conditions on the solidification mode in austenitic stainless steels, Metall. Trans. A, 14A (**1983**), 191–197

THE EFFECT OF HEAT TREATMENTS ON THE SOLID-PARTICLE EROSION BEHAVIOR OF THE ALUMINUM ALLOY AA2014

VPLIV TOPLOTNE OBDELAVE ZLITINE AA2014 NA VEDENJE PRI EROZIJI S TRDNIMI DELCI

Sedat Karabay

Mechanical Engineering Department of Engineering Faculty of Kocaeli University, Kocaeli, Turkey
sedatkarabay58@gmail.com

In this study the solid-particle erosion behaviour of solutionised, artificially aged (T6) and annealed specimens prepared from an extruded aluminium alloy AA2014 was investigated and an intercomparison was made. The samples were eroded in specially designed, solid-particle erosion test equipment at a 45° impingement angle and 75 m/s impingement velocity by using 180-mesh garnet erodent particles. Microstructures of the solutionised, artificially aged and annealed samples from the AA2014 were obtained using a light microscope. Moreover, the Vickers hardness of the samples exposed to different heat treatments was measured in order to evaluate the erosion rates with respect to the ductility changes in the material. Additionally, the surface morphology images of the samples were taken before and after the erosion test using a scanning electron microscope (SEM). The results showed that the heat treatments dramatically affected the erosion rates of the samples. However, artificially aged samples caused decrease reduction of the erosion resistance of the AA2014 aluminium alloy. The solutionised alloy showed the best erosion resistance compared to the precipitation hardening (T6) and annealed samples. The effects of the microstructures and the hardness on the erosion behaviour of the different heat-treated specimens were discussed. Finally, SEM images of the samples were analyzed in detailed and the erosion mechanism occurring on the surfaces of the samples was discussed.

Keywords: AA2014, impingement angle, erosive loss, erodent particle, flake, craters

V tej študiji je bila izvršena preiskava in primerjava vzorcev, izdelanih iz ekstrudirane aluminijeve zlitine AA2014, raztopno žarjenih, umetno staranih (T6) in mehko žarjenih, na vedenje pri eroziji s trdnimi delci. Vzorci so bili erodirani v posebno konstruirani napravi za preizkušanje erozije s trdnimi delci pri naklonu udarca 45° in hitrosti udarca 75 m/s, pri uporabi delcev granulacije 180. S svetlobno mikroskopijo je bila pregledana mikrostruktura raztopno žarjenih, umetno staranih in popuščanih vzorcev iz AA2014. Izmerjena je bila tudi trdota po Vickersu vzorcev, izpostavljenih različnim toplotnim obdelavam, da bi opredelili hitrost erozije glede na spremembe plastičnosti materiala. Z vrstičnim elektronskim mikroskopom (SEM) smo dodatno napravili tudi posnetke morfologije površine vzorcev pred preizkusom erozije in po njem. Rezultati so pokazali, da toplotna obdelava vzorcev močno vpliva na hitrost erozije. Vendar pa je umetno staranje vzorcev povzročilo zmanjšanje odpornosti proti eroziji zlitine AA2014. Raztopno žarjena zlitina je pokazala najboljšo odpornost proti eroziji v primerjavi z izločevalno utrjenimi (T6) in mehko žarjenimi vzorci. Komentiran je tudi vpliv mikrostrukture in trdote različno toplotno obdelanih vzorcev na vedenje pri eroziji. SEM-posnetki vzorcev so detajlno analizirani in opisani so mehanizmi erozije, ki so se pojavili na površini.

Ključne besede: AA2014, naklon udarca, izgube pri eroziji, erozijski delec, luske, kraterji

1 INTRODUCTION

Applications for the 2*xxx* series alloys include the internal and external structures of aircraft, the structural beams of heavy dump and tank trucks and trailer trucks, the fuel tanks and booster rockets of the space shuttle and internal railroad car structural members. AA2014 is the most popular type of 2xxx series group for producing mechanical constructions. It is obvious that all of these parts are exposed to various types of particle erosion following the completion of the construction.[1] Erosion is described as the progressive loss of original material from a solid surface due to a mechanical interaction between the surface and a fluid, which may be a multi-component fluid or impinging solid or liquid particles. It is common that the materials used in pipes, bends and tanks, etc., in industries like chemical, cement, mining and mineral processing and thermal power plants encounter erosion-related problems. Pulveriser mill components, multiple port outlet, orifice, PF (packet filter) bends, elbow, burner assembly, pressure parts, ID (induced draft) fan blade and coal ash slurry pipes are the main components affected by erosion in thermal power stations. There has always been an attempt to reduce the material loss due to erosion as it incurs a huge loss of the material. In the past few decades, researchers have focused on the study of material loss in order to conserve both material and energy.[2] A wide variety of methods were adopted to protect materials from the problems of wear, including the use of efficient materials,[3] processing techniques,[4] surface treatments[5,6] of the exposed components and the use of engineering skills leading to a reduced impact of wear on the material, such as an appropriate impingement angle of the erodent and the velocity of the slurry. The methodology to be followed for the protection of the material is adopted from the conclusions drawn from the simulated test carried out for the purpose. Investigations and studies

provide an insight into the mechanisms of material removal during the wear process of the material.[7,8] There are a number of methods to evaluate the erosion wear of materials using equipment, such as small feed rate erosion test equipment,[9] particle jet erosion test equipment,[10] coriolis erosion tester[11] and slinger erosion test equipment.[12] In this study, the solid-particle erosion behaviour of solutionised, artificially aged and annealed condition of AA2014 aluminium alloy has been investigated and compared to each other. The samples were eroded in specially designed solid-particle erosion test equipment. The equipment was designed using ideas presented for different test conditions and materials in the literature.[9–12] In performing the experiments, the particle-impingement angle, the velocity and the pressure were kept constant and different heat-treated samples were eroded in same test conditions for the test equipment. Furthermore, aluminium alloys exhibit ductile erosion behaviour by showing maximum erosion rates at acute angles (15°–45°). Hence, a 45° impingement angle was used in order to erode the samples effectively. The 75 m/s impingement velocity with 3 bar gas pressure was selected for the optimum erosion of ductile materials by using 180-mesh garnet erodent particles.[5–7,9–12] Increasing the velocity may cause the breaking of the garnet erodent particles owing to impacting on the metal surfaces. The test set up has versatile properties and all the parameters are also changeable with the special mechanisms to perform different test conditions. The microstructures of the solutionised, artificially aged and annealed AA2014 specimens were obtained using a light microscope and an SEM. Moreover, the erosion rates of the samples versus the thermal treatment grades of the AA2014 were calculated and the surface morphologies of the samples were presented by interpreting before and after the erosion tests.

2 EXPERIMENTAL

2.1 Material and Applied Heat Treatments

Initially, the diameter 152 mm (6 inch) AA2014 extrusion billet, with the chemical composition presented in **Table 1**, was produced by an industrial vertical air slip DC casting unit and homogenised at 480 °C for 12 h. The billet was subsequently heated to 430 °C and extruded into a diameter bar 100 mm.

Table 1: The chemical composition of the alloy AA2014 for particle erosion tests in mass fractions, *w/%*
Tabela 1: Kemijska sestava zlitine AA2014 za preizkus erozije z delci v masnih deležih, *w/%*

Al	Si	Fe	Cu	Mn	Mg	Zn	Cr	Ti	Pb
92.92	0.35	0.56	4.56	1.06	0.28	>0.15	0.01	0.02	0.01

Samples from a square cross-section of AA2014 alloy from the extruded bar were cut out (transverse section of extruded bar) with a size of 40 mm × 40 mm ×
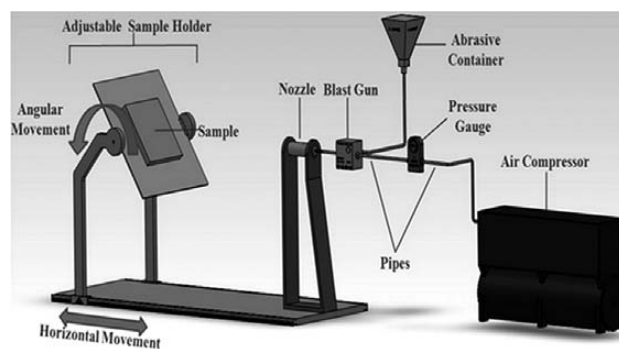
Figure 1: Solid particle erosion test equipment
Slika 1: Naprava za preizkušanje erozije s trdnimi delci

3 mm. The samples were divided into three separate groups. The first group was soaked at 570 °C for 2 h to achieve the solution heat-treated state and water quenched. The second group was additionally soaked at 160 °C for 12 h to achieve T6 precipitation. Finally, the last group, after T6, was soaked at 410 °C for 3 h to achieve annealing. All the heat treatments were carried on in an electronically operated Severn heat-treating furnace.

2.2 Erosion test

The erosion tests were performed in a horizontal sand-blast type erosion test equipment. **Figure 1** shows a schematic illustration of the erosion test equipment. Garnet particles with a size of 180-mesh driven by a static air pressure of 3 bar were accelerated along a nozzle 50 mm of diameter 5 mm. The velocity of the particles under 3 bar pressure was 75 m/s measured using the double-disc method. All the erosion experiments were run at a 75 m/s particle-impingement velocity and a 45° angle of impingement (angle of highest wear rates achieved) by using 180-mesh garnet particles. The samples were cleaned with air blasting before and after the erosion tests in order to remove the sand and dust particles, and then the samples were weighed in an electronic balance with an accuracy of ± 0.1 mg.

2.3 Hardness

The hardness of heat-treated samples was measured with a Shimazdu HMV Vickers hardness setup. The test load 300 g and the dwell time 20 s were applied and reported as the average of a minimum 5 readings (HV 0.3). The hardness results were evaluated by generating the hardness graph versus the mass loss.

2.4 Scanning electron microscope

To characterize the morphology of the eroded surfaces and in order to understand the material-removal mechanism, the eroded surfaces of the samples were
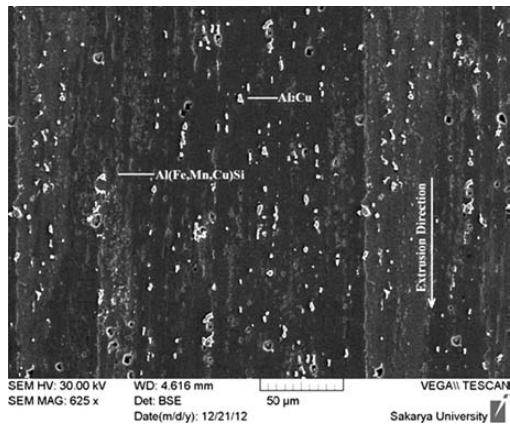
Figure 2: SEM image of longitudinal section of hot-extruded AA2014
Slika 2: SEM-posnetek vzdolžnega prereza vroče ekstrudiranega AA2014

examined using a scanning electron microscope Tescan Vega Sbu–II (Bruker EDS).

3 RESULTS AND DISCUSSION

3.1 Microstructure

Elongated α-Al grains and intermetallic precipitates were settled in the hot-extruded AA2014 bar (**Figure 2**). In the analysis of the structure by SEM, two different types of intermetallic particles with different contrasts were observed at the α-Al grain borders. These are the light- and dark-gray intermetallic particles. The EDS analysis of the light-gray particles reveals a reflection of the Al and Cu signals. However, dark-grey particles additionally reflected the Si, Mn and Fe signals. According to the XRD spectrum, the light- and dark-grey particles are the soluble Al_2Cu and the insoluble cubic α_c-Al_{12}(Fe, Mn, Cu)$_3$Si, respectively, as seen in **Figure 3**. The lack of evidence for recrystallisation across the section of the hot-extruded bar implies that the deformation introduced during the extrusion process is restricted by the pinning effect of the Al_2Cu.

According to the EDS analysis (**Figures 4b** to **6b**) of the grain boundaries of the solutionised sample, it was clearly detected that there was no response of the Al_2Cu signals. Heating the samples at 570 °C for 2 h resulted in a fully solutionised structure and the dissolution of the soluble eutectic Al_2Cu into the matrix. Also, the remaining of intermetallics verify the insolubility of α_c-Al_{12}(Fe,
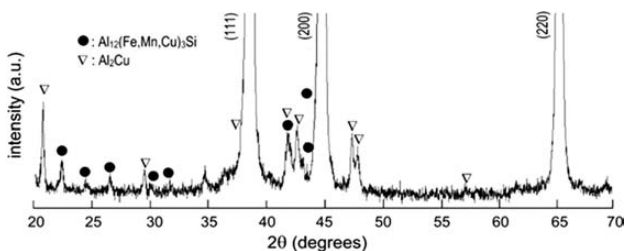

Figure 3: XRD spectrum of as-received AA2014
Slika 3: XRD-spekter dobavljenega AA2014
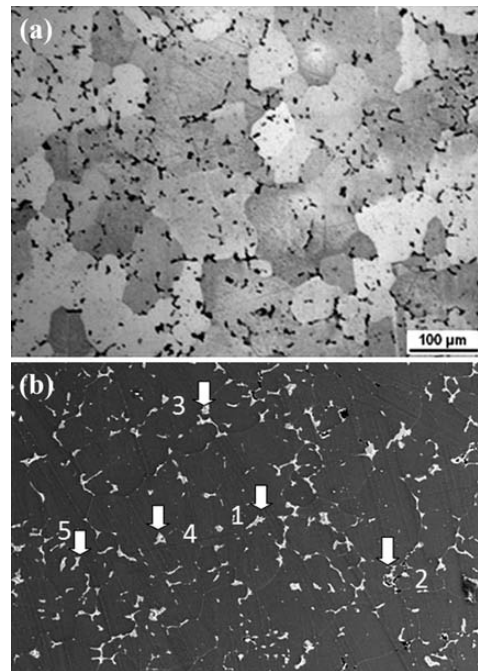
Point 1: Al 58.8, Cu 20.0, C 11.2, Mn 5.2, Fe 4.7, **Point 2:** Al 72.8, Cu 11.7, Mn 6.8, Fe 5.6, Si 3.1, **Point 3:** Al 59.5, C 28.8, Cu 8.0, Si 3.6, **Point 4:** Al 90.1, Cu 8.0, Mn 1.9, **Point 5:** Al 51.4, C 43.6, Cu 5.0 (mass fractions, w/%)
Figure 4: a) Light-microscope view of the solution heat-treated sample, b) indicated points of EDS analysis of solution heat-treated sample
Slika 4: a) Mikrostruktura raztopno žarjenega vzorca, b) označena mesta EDS-analiz raztopno žarjenega vzorca
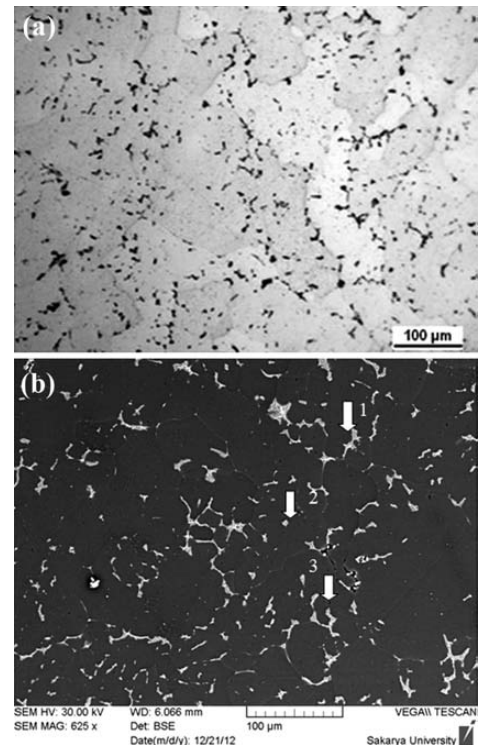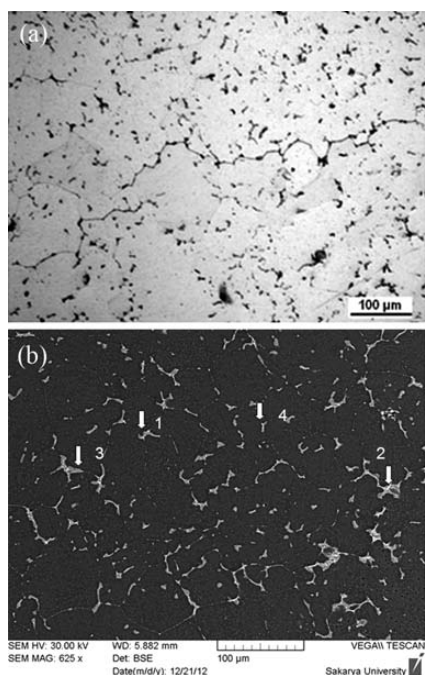

Point 1: Al 58.5, Cu 31.8, C 8.9, Si 0.8; **Point 2:** Al 62.0, Cu 38.0; **Point 3:** Al 56.1, Cu 3.9 (mass fractions, w/%)
Figure 5: a) Light-microscope view of T6 sample, b) indicated points of EDS analysis of T6 treated sample
Slika 5: a) Mikrostruktura vzorca po T6 toplotni obdelavi, b) označena mesta EDS-analiz vzorca po T6 toplotni obdelavi

Point 1: Al 80.6, Cu 15.7, Si 3.7; **Point 2:** Al 47.8, Cu 19.2, Mn 11.5, Fe 9.8, Si 1.0; **Point 3:** Al 71.5, C 16.9, Mn 5.1, Fe 3.5, Si 2.9; **Point 4:** Al 85.5, C 10.0, Cu 4.5 (mass fractions, *w*/%)
Figure 6: a) Light-microscope view of annealed sample, b) indicated points of EDS analysis of annealed sample
Slika 6: a) Mikrostruktura mehko žarjenega vzorca, b) označena mesta EDS-analiz mehko žarjenega vzorca

Mn, Cu)$_3$Si. A light-microscope view of the solutionised sample was presented in **Figure 4a**.

Holding the sample at an elevated temperature assists in the segregation of the Si from the matrix to the grain boundary. Thus, the chemical composition of the grain boundary becomes closer to the Al-Si-Cu ternary eutectic. Also, it forces the grains to coarsen. Especially during the annealing stage, the precipitates, which occurred for T6 indicated in **Figure 5a**, start to coarsen and settle on the grain boundary, also become detectable by EDS analysis, as seen in the **Figure 6b**. A light-microscope view of the annealed sample is presented in **Figure 6a**.
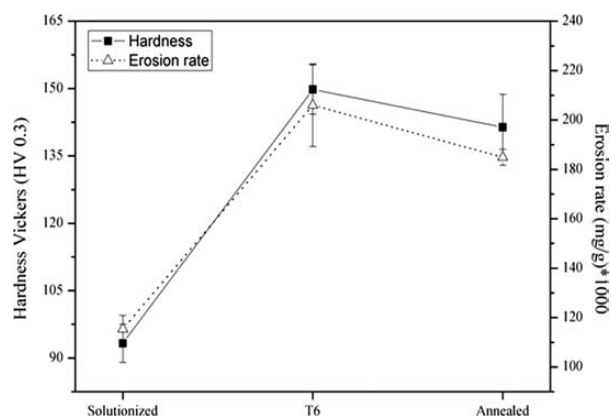
3.2 Erosion rate

Samples prepared under three different heat-treatment conditions were exposed to erosive wear in the test
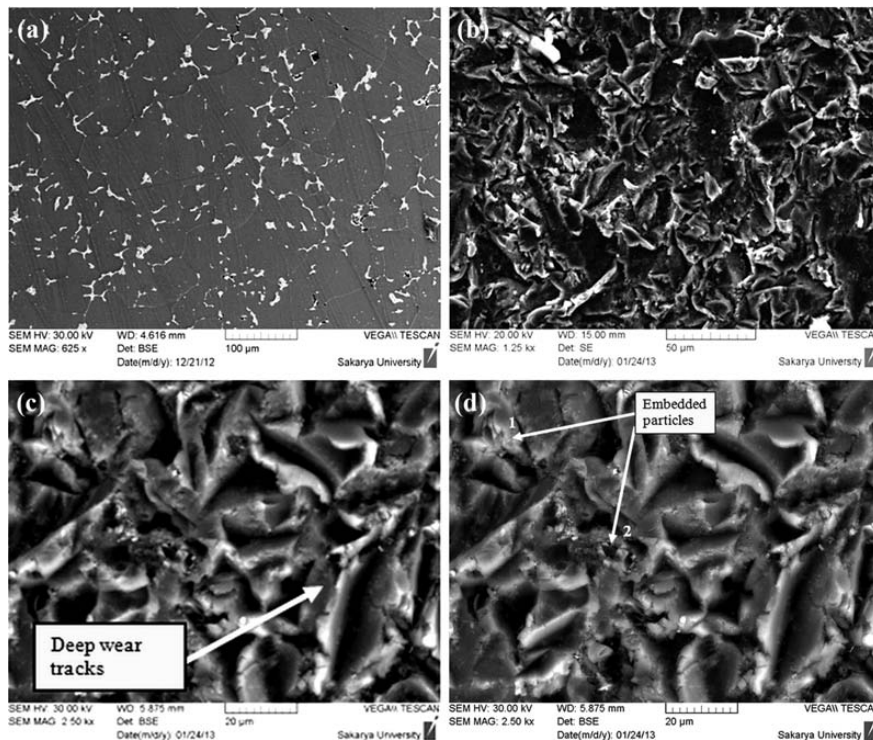

Figure 7: Erosion rates and hardness of solution heat treated, heat treated and annealed AA2014
Slika 7: Hitrosti erozije in trdote raztopno žarjenega, toplotno obdelanega in mehko žarjenega AA2014

equipment demonstrated in **Figure 1** with the parameters explained in **Table 2**. The results from the experiments are showed in **Table 2**. The code numbers indicated in the first column of **Table 2** define the surfaces of the samples exposed to different heat-treatment conditions. K1$_f$ means the front surface of the square cross-section for the sample prepared by the solution treated AA2014. Similarly, K1$_b$ means the back side of the solution-treated sample of AA2014. The code numbers of K2$_f$ and K2$_b$ mean the front side and back side of the samples prepared from the AA2014 extrusion under T6 conditions. The third sample, coded as K3$_f$, K3$_b$, means the front and back sides of the samples prepared from AA2014 under the annealed condition of the samples after the T6 precipitation hardening. Furthermore, to analyze the erosion rates and the hardness of samples on the different heat-treated AA2014 by keeping a constant erosion time, the impingement angle and air pressure, a graphical representation was indicated in **Figure 7**.

3.3 Interpretation on Surface Morphology of the Eroded Samples

In this section, the idea was to examine and understand the effects of the heat-treatment conditions on the surface morphology of the samples before and after the erosion tests. Moreover, the aim was to detect and discuss the dominant erosion mechanisms. Hence, in **Figures 8** to **10**, SEM image studies of the surfaces of

Table 2: Erosive test parameters applied to the AA2014 and the measured results
Tabela 2: Parametri preizkusa erozije na AA2014 in izmerjeni rezultati

Sample Code	Constant parameters applied to testing of each samples	Initial mass m_1/g	Final mass m_2/g	Δm/mg	Δm (mean)/ 1000 mg	Erosion rate (mg/g) ×1000
K1$_f$		35.81	35.79	16.70		
K1$_b$	Erosion time (s): 20	35.79	35.78	14.50	15.60	115.38
K2$_f$	Impingement Angle (°): 45	34.70	34.67	25.30		
K2$_b$	Pressure (bar): 3	34.67	34.64	30.40	27.85	205.99
K3$_f$	Mesh: 180	35.54	35.52	25.00		
K3$_b$	Mass volume (g/s): 6.76	35.52	35.49	25.00	25.00	184.91

Figure 8: SEM images of solution heat treated AA2014 samples: a) surface before erosion (SE mode), b) eroded surface (SE mode), c) eroded surface (BSE mode), d) indicated points of EDS analysis of the solutionised and eroded sample
Slika 8: SEM-posnetki raztopno žarjenih vzorcev AA2014: a) površina pred erozijo (način SE), b) erodirana površina (način SE), c) erodirana površina (način BSE), d) označena mesta EDS-analiz raztopno žarjenega in erodiranega vzorca

the solutionised, annealed and heat-treated samples were performed. The SEM images of the samples were taken before and after the erosion process and were taken in the SE (secondary electron) and BSE (back scattered electron) modes in the SEM. Furthermore, an EDS analysis of the eroded surfaces of the samples were taken along with the SEM investigations and were given in this section. In **Figures 8a** to **8d**, SEM images and EDS results of the solutionised alloy were given. The micro-cutting and the micro-ploughing erosion mechanisms can be seen in **Figures 8b** to **8d**.

The erosion of the surface of the samples caused by the impact of the erodent particles can be seen by comparing **Figures 8b**, **9b** and **10b**. Although the solutionised aluminium AA2014 has low erosion rates, as indicated in **Figure 7**, the surfaces of the samples after exposing to solid particle erosion were also damaged significantly. In **Figure 8d** an EDS analysis of the surfaces of the solutionised aluminium alloy were given. The existence of the O and Fe atoms in a high percentage was the evidence for the embedded erodent garnet particles to the surfaces of the samples. Based upon the EDS analysis results, it was concluded that the erodent particles were embedded in the surfaces of the aluminium alloy during the erosion process.

Moreover, it was also concluded that this could be possible because of the ductile behaviour of the aluminium alloy. In the literature[7,12] of solid particle erosion,

most metals undergo erosion by ductile erosion behaviour and the erodent particles with high velocities can be embedded to the surfaces of the samples specifically at obtuse impingement angles, such as 75° and 90°. However, in this study the samples were eroded at 45° impingement angles and it was not expected to detect the embedded erodent particles. The embedded particles on the surfaces of the solutionised aluminium alloy were clearly observed in SEM studies. Thus, it can be concluded that erodent particles can also be embedded in the surfaces of the aluminium alloys at acute impingement angles, which have not been mentioned in the literature before. In **Figures 9a** to **9d**, the SEM images and EDS results of the artificially aged T6 AA2014 alloy were given. The micro-cutting and the micro-ploughing erosion mechanisms can be seen in **Figures 9b** to **9d**.

Hence, it can be concluded that the solid particle erosion causes significant damage on the surfaces of the artificially aged (T6) aluminium alloy. The low plastic deformation and the shallow depth of the craters and lips can be observed on the specimens of T6-treated AA2014. In **Figure 9d** an EDS analysis of the surface of the T6 treated AA2014 specimen was given. Similarly, the existence of the O and Fe atoms in a high percentage was the evidence of the embedded erodent garnet particles to the surfaces of the samples. Based upon the EDS analysis results, it was concluded that the erodent particles were embedded in the surfaces of the aluminium
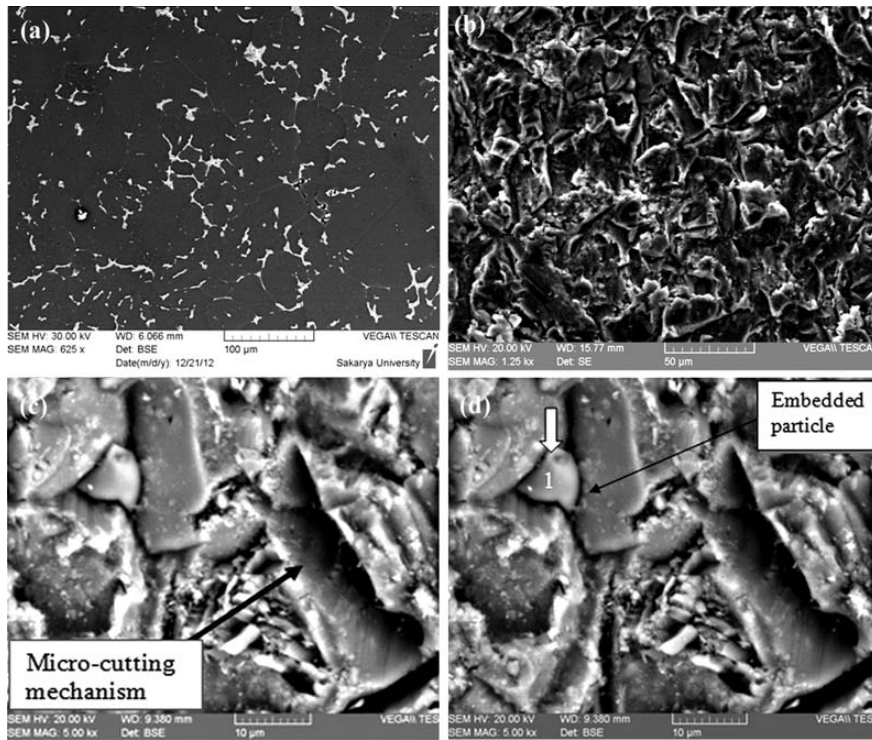
Point 1: O 33.1, Fe 25.5, Si 18.1, Al 14.7, Mg 6.8, Ca 1.3, C 0.6 (mass fractions, *w*/%)
Figure 9: SEM images of artificially aged (T6) AA2014 samples: a) surface before erosion (SE mode), b) eroded surface (SE mode), c) eroded surface (BSE mode), d) indicated point of EDS analysis of artificially aged (T6) sample
Slika 9: SEM-posnetki umetno staranih (T6) AA2014 vzorcev: a) površina pred erozijo (način SE), b) erodirana površina (način SE), c) erodirana površina (način BSE), d) označeno mesto EDS-analize umetno staranega vzorca
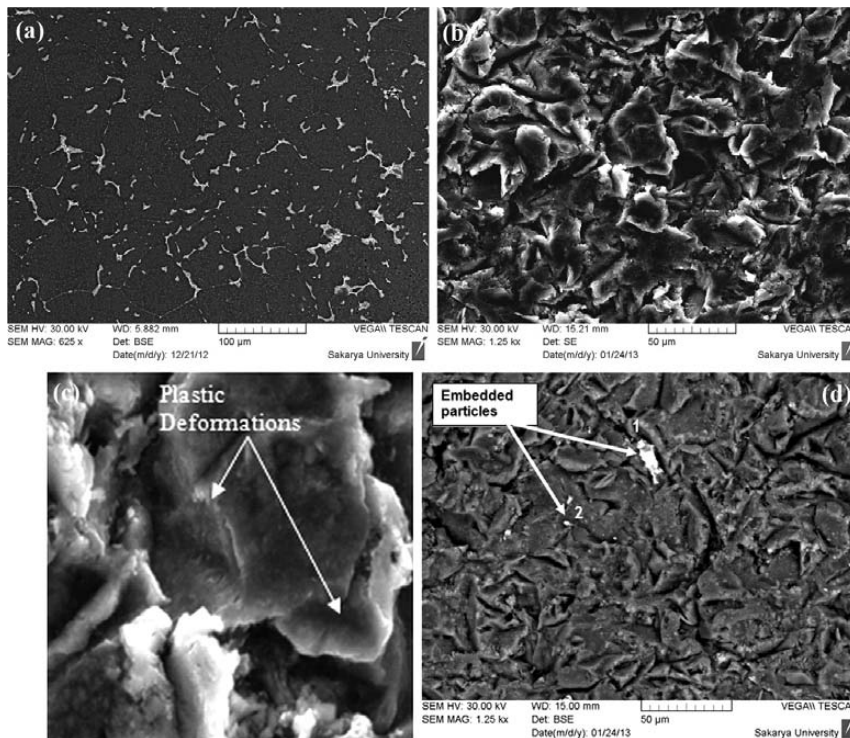
Point 1: Fe 75.0, N 19.4, Al 4.8, Si 0.4; **Point 2:** Al 47.4, O 30.7, Ca 11.5, C 4.0, Cu 2.2, Si 1.6, Fe 1.6, Mg 1.2 (mass fractions, *w*/%)
Figure 10: SEM images of annealed AA2014 samples: a) surface before erosion (SE mode), b) eroded surface (SE mode), c) eroded surface (BSE mode), d) indicated points of EDS analysis of the annealed sample
Slika 10: SEM-posnetki mehko žarjenih AA2014 vzorcev: a) površina pred erozijo (način SE), b) erodirana površina (način SE), c) erodirana površina (način BSE), d) označena mesta EDS-analiz mehko žarjenega vzorca

alloy during the erosion process. However, in this study the samples were eroded at 45° impingement angles and it was not expected to detect embedded erodent particles. The embedded particles on the surfaces of the aluminium alloy AA2014 applied artificial aging seen on the **Figure 9d** were clearly seen in the SEM studies. Hence, it can be concluded that the erodent particles can also be embedded in the surfaces of the aluminium alloys at acute impingement angles (45°), which have not been mentioned in the literature before.

In **Figures 10a** to **10d** the SEM images and EDS results of the annealed AA2014 alloy are given. The micro-cutting and the micro-ploughing erosion mechanisms can be seen in **Figures 10b** to **10d**. Hence, it can be concluded that solid particle erosion causes significant damage on the surfaces of the annealed aluminium alloy. The depth of the craters created by the blocking of the kinetic energy of the accelerated particles is lower than the solutionised structure.

The flake formation and work-hardened layer are generated when the surface suffers extensive plastic deformation. The impacts of solid particles break the flake and the outer work-hardened layer. Thus particles cause the erosive loss of the material. In **Figure 10d** an EDS analysis of the surfaces of the annealed aluminium alloy is given. The existence of the O and Fe atoms in high percentages was the evidence of the embedded erodent garnet particles to the surfaces of the samples. Based upon the EDS analysis results, it was concluded that the erodent particles were embedded in the surfaces of the aluminium alloy during the erosion process. Annealed AA2014 has a ductility higher than AA2014 T6, so that the material erosion rate is lower. This means that if the machine parts designed with light metals are exposed to particle erosion owing to functionality of the process, they should be used in ductile conditions in the construction rather than the T6 artificial aging hardening state.

4 CONCLUSION

The alloy AA2014 was exposed to erosive wear by keeping constant the variables such as attack angle, air pressure, particle mass flow and changing ductility conditions of the material. From the studied parameters, the results can be summarized as:

- Experiments indicated that the erosive wear of the aluminium AA2014 increases with increasing hardness of the material. Increasing of the material hardness caused increasing of the brittleness and decreasing ductility. Thus, the kinetic energy of the moving particles takes the chip easily from the brittle surface of the AA2014, so that the loss of the material occurs at higher rates from the metal matrix exposed to precipitated hardness.

- To obviate a higher metal-removal rate against excessive particle impingements, material AA2014 should be used under low hardness conditions. The total kinetic energy of the erodent is exhausted in the crater formation. Due to the large difference in the hardness of the erodent and the specimen surface, a crater would be easily created on the surface.

- Wear mechanisms at the different rated surfaces take place by cutting, impingement and removal of the material from the surface of the specimen. Furthermore, embedded erodent particles were observed on the surfaces of the solutionised, heat-treated and annealed specimens of aluminium AA2014. It was concluded that the erodent particles can also be embedded in the surfaces of the aluminium alloys at acute impingement angles due to the ductility of the samples.

5 REFERENCES

[1] Y. I. Oka, K. Okamura, T. Yoshida, Practical Estimation of Erosion Damage Caused by Solid Particle Impact Part 1: Effects of Impact Parameters on A Predictive Equation, Wear, 259 (**2005**), 95–101

[2] A. R. Harne, Life Improvement of Thermal Power Station Component: A War Against Wear Workshop on Wear and Erosion of Materials in Thermal Power Station, CPRI, Bangalore, 1989

[3] B. Yücel, E. A. Güven, L. Çapan, Extrusion of EN AW-2014 Alloy in Semisolid state, Materials Science and Technology, 27 (**2011**), 1851–1857

[4] B. K. Prasad, S. Das, A. K. Jha, O. P. Modi, R. Dasgupta, A. H. Yegneswaran, Factors Controlling the Abrasive Wear Response of a Zinc-Based Alloy Silicon Carbide Particle Composite, Composites A, 28 (**1997**), 301–308

[5] A. K. Jha, A. Gachake, B. K. Prasad, R. Dasgupata, A. H. Yegneswaran, High Stress Abrasive Wear Behavior of Some Hard Faced Surfaces Produced by Thermal Spray, Journal of Materials Engineering and Performance, 11 (**2002**) 1, 37–45

[6] K. Sanjay, D. P. Mondal, A. K. Jha, Effect of Microstructure And Chemical Composition of Hard Facing Alloy on Abrasive Wear Behavior, Journal of Materials Engineering and Performance, 9 (**2002**) 6, 649–655

[7] I. Finnie, K. Natesan, The mechanism of erosion wear in ductile material: Corrosion behavior of materials [J]. TMS-AIME, (1980), 118–126

[8] T. Denga, M. S. Bingleya, M. S. A. Bradleya, S. R. De Silva, A Comparison of The Gas-Blast and Centrifugal-Accelerator Erosion Testers: The Influence of Particle Dynamics; Wear, 265 (**2008**), 945–955

[9] W. Zhu, Z. Y. Mao, Wear of Material [C]// LUDEMA K C ed. Proceeding of Conference Wear of Material, ASME, 787, 1987

[10] R. G. Desale, K. Bhupendra, S. C. Gandhi, Improvement In the Design of a Pot Tester to Simulate Erosion Wear due to Solid-Liquid Mixture, Wear, 259 (**2005**), 196–202

[11] H. M. H. Throhe, Y. Xie, S. K. Yick, A New Coriolis Slurry Erosion Tester Design for Improved Slurry Dynamics, Wear, 255 (**2003**), 170–180

[12] T. Denga, M. S. Bingley, M. S. A. Bradley, Understanding Particle Dynamics in Erosion Testers – A Review of Influences of Particle Movement On Erosion Test Conditions, Wear, 267 (**2009**), 2132–2140

INFLUENCE OF NON-METALLIC INCLUSIONS ON THE FORMATION OF HOT CRACKS IN THE WELD AND HEAT-AFFECTED ZONE

VPLIV NEKOVINSKIH VKLJUČKOV NA NASTANEK VROČIH RAZPOK V ZVARU IN TOPLOTNO VPLIVANI CONI

Borut Zorc[1,2], Mustafa Imamović[3], Ladislav Kosec[2], Borut Kosec[2], Aleš Nagode[2]

[1]Welding Institute Ltd, Ptujska 19, 1000 Ljubljana, Slovenia
[2]University of Ljubljana, Faculty of Natural Sciences and Engineering, Aškerčeva 12, 1000 Ljubljana, Slovenia
[3]University of Zenica, Faculty of Mechanical Engineering, Fakultetska br. 1, 72000 Zenica, Bosnia and Herzegovina
borut.zorc@i-var.si

A thick-walled casting of unalloyed cast steel with a high content of non-metallic inclusions was built up with the submerged arc-welding (SAW) process. Hot cracks were detected in the built-up, tough inner layer of unalloyed steel (near the fusion line alongside the edge of the prepared groove). The cause for it was an inappropriate "bead-to-bead" technique of building up, with a strong remelting of the base material and a strong contamination of the weld pool with non-metallic inclusions. The chemical composition of the inclusions also indicated an insufficient attention or technical difficulties during building, since some inclusions were based on the welding slag. The smallest possible content of the base-material admixture must be ensured, the welding slag fully removed and, if needed, before welding the next bead, the narrow and deep interpass groove must be widened and rounded off by grinding.

Keywords: surfacing, non-metallic inclusions, strong remelting of the base metal, hot cracking

Pri debelostenskem ulitku iz nelegirane jeklene litine z veliko vsebnostjo nekovinskih vključkov, navarjenem po postopku varjenja pod praškom (EPP), so bile v navarjeni žilavi vmesni plasti iz nelegiranega jekla v prvem sloju oziroma blizu linije spajanja ob robu pripravljenega utora ugotovljene vroče razpoke. Vzrok je bila neprimerna tehnika navarjanja "varek do varka", kar je imelo za posledico močno pretaljevanje osnovnega materiala in zato močno onesnaženje zvarne kopeli z nekovinskimi vključki. Kemijska sestava vključkov kaže tudi na nepazljivost ali na tehnološke težave med navarjanjem, saj so nekateri vključki na osnovi varilske žlindre. Nujno je zagotoviti čim manjše primešanje osnovnega materiala, dobro odstraniti varilsko žlindro in pred varjenjem naslednjega varka po potrebi z brušenjem razširiti in zaobliti nastale ozke in globoke medvarkovne žlebove.

Ključne besede: navarjanje, nekovinski vključki, močno pretaljevanje osnovnega materiala, pokljivost v vročem

1 INTRODUCTION

Cracks and ruptures always form due to an excessive tensile-stress concentration at the places of their nucleation due to different causes. One possible cause is the global overload of the construction. When dealing with calculated acceptable loads, an important role is played by the local-construction fatigue-notch factors and local metallurgical factors of the metal (segregation, intercrystalline impurities and brittle phases, coarse non-metallic inclusions such as slag inclusions and remains of the moulding sand, etc.). Constructional faults and metallurgical defects cause an occurrence and propagation of cracks at the stresses lower than the material's tensile strength or even the yield strength (the latter is characteristic of fatigue cracks). In this case, the construction overloading does not equal the material overloading. Due to unfamiliar metallurgical negative factors, the material overloading cannot be reliably stress determined, timed or calculated.

Among the metallurgically caused cracks there are also intercrystalline hot cracks (crystallization, liquation and polygonization cracks) that form during welding at high temperatures (in steels at $T > 800$ °C [1]). Hot cracks are a consequence of a weld and heat-affected-zone shrinkage during cooling, which, in connection with a rigid, cold surrounding environment, causes tensile stresses in the weld range.[1–5] If the deformation capacity of the metal at high temperatures during weld cooling is not sufficient, hot cracks appear because of its inability to withstand the tensile stresses at critical places (usually at the grain boundaries, contaminated with low-melting phases or eutectics of the sulphide, phosphide, carbide, boride and oxide types).[1–5] Along with the impurities (sulphur, phosphorus), the steel alloy elements of carbon, boron, niobium, nickel[1–5], titanium, zirconium and copper[5] also increase the possibility of a hot-crack formation and, due to the possible diffusion-originated segregations on grain boundaries, chromium, manganese and silicon also have this effect.[1,2,5] Intercrystalline segregations of sulphur, phosphorus and oxygen (oxide films) can be a consequence of non-optimum metallurgical reactions in the weld pool, but they may also occur in welds when the base material contaminated with non-metallic inclusions is remelted.[1,2] Galaxite-oxide

films (Al_2O_3.MnO) are often found at the crystal boundaries of the welds made from unalloyed low-carbon steels using the SAW process.[1,2] The steels most susceptible to hot cracking are austenitic stainless steels.

This article presents the findings of a case investigation of hot cracking in the built-up tough, soft layers (an interlayer at hard facing) of a thick-walled cast (a diameter of 4500 mm, a thickness from 60 mm to 110 mm) from unalloyed cast steel with a high content of non-metallic inclusions.

2 EXAMINATION

The chemical analyses of the base material, interlayer welds and the first built-up layer (quantometer Thermo Electron Corporation ARL 3460) were made, as well as a chemical analysis and electron microscopy of non-metallic inclusions (scanning electron microscope JEOL JSM-5610 with an EDX spectrometer), macroscopy (grinding with sandpaper up to # 800, etching with Adler's reagent), optical microscopy (grinding with sandpaper up to # 4000, polishing with diamond paste of # 2 μm, etching with 2 % nital), hardness measurements, HV (device: GNEHM Härteprüfer Swiss Max 300) and the measurements of the impact toughness with ISO-V and DVM test specimens (impact testing machine AIT-300 EN). The tensile strength and yield strength could not be determined due to a lack of the material.

3 RESULTS AND DISCUSSION

3.1 Base-material analysis

The base material, on which the layers of soft steel are built-up, is a cast steel with the following chemical composition (the middle value of three analyses) in mass fractions, w/%: C = 0.30; Si = 0.37; Mn = 0.62; P = 0.023; S = 0.019; Cr = 0.16; Ni = 0.27; Cu = 0.18; Al = 0.0017. The chemical composition corresponds to grade 65–35 (ASTM A27) with the highest allowed carbon content,[6,7] being comparable with GS-45 according to DIN 1681 (see also [8]) or 1.0446 (EN 10027-2). The cast-steel hardness is 175 HV (the average of seven measurements), which is characteristic for a normalized condition with a polygonal ferrite-pearlite microstructure (**Figure 1a**) and the standard requirements.[6,7] The impact toughness of the cast steel is lower (DVM: 17–26 J) than the minimum required standard value (DVM: ≥ 27 J).

A considerable quantity of non-metallic inclusions is mostly present in the microstructure of ferrite (**Figure 1a**) due to their effect on the nucleation of ferrite during the cooling of austenite from the normalization temperature. The non-metallic inclusions are unevenly distributed in the matrix, having round and angular shapes and different sizes, as stringers of isolated particles, uneven lines (**Figures 1b** and **1c**) and rosette shapes. The line- and rosette-shaped inclusions are large, their quantity is

locally very high and it is clear that they solidified from the liquid phase. The pointy angular inclusions are probably the non-molten residue of the moulding sand.

The non-metallic inclusions are sulphides and oxides. The sulphides (the examples with the chemical composition in mass fractions, w/%: Fe = 52.6; Mn = 23.7; Cr = 1.5; S = 22.2 or Fe = 5.3; Mn = 44.4; Cr = 2.3; S = 48.0) are light grey (**Figure 1c**, mark No. 1). The oxides are darker (**Figure 1c**, mark Nos. 2, 3, 4) and mostly based on iron (w/%): Fe = 95.3–97.2; O = 1.4–3.9; Ca + Cr + Mn + Si ≈ 1.0). In the oxide inclusions, slightly higher contents of sulphur and phosphorus were also found (w/%): S = 0.17–0.34; P = 0.21).

Due to a combined effect of carbon and a high number of inclusions, the impact toughness of the cast steel is poor. Its susceptibility to the hot-crack formation depends on the chemical composition of steel and it is determined by calculating the index of the hot-crack susceptibility, U_{CS}. When welding the C–Mn steels with the SAW process, the following equation is used[9–11]:
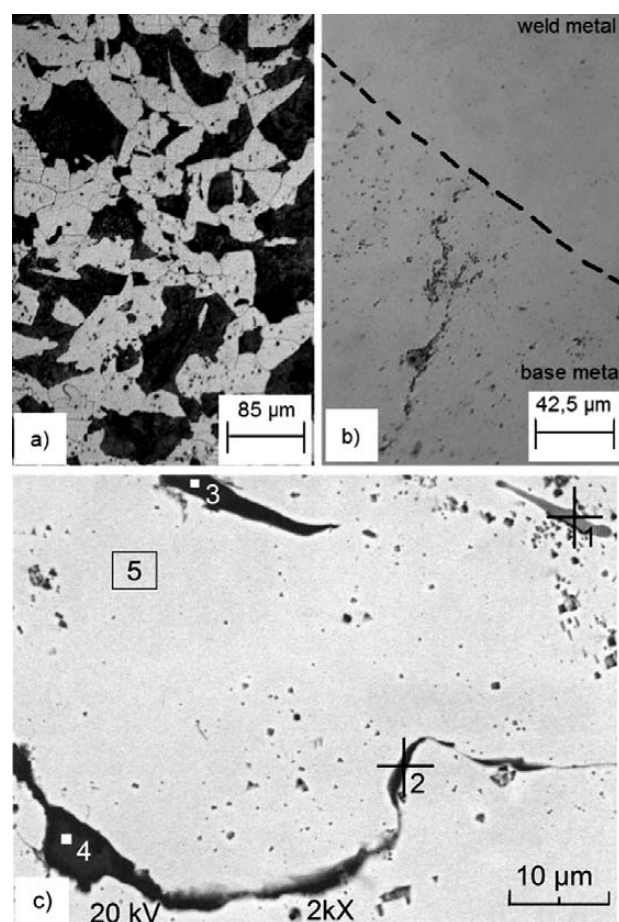
Figure 1: Microstructural characteristics of the cast-steel base material: a) normalized ferrite-pearlite microstructure with non-metallic inclusions (dark dots in the ferrite); b), c) unevenly arranged inclusions of various shapes (unetched)
Slika 1: Mikrostrukturne značilnosti navarjene jeklene litine: a) normalizirana feritno-perlitna mikrostruktura z nekovinskimi vključki (temne pike v feritu); b), c) neenakomerno razporejeni vključki različnih oblik (nejedkano)

$$U_{CS} = 230 \cdot C + 190 \cdot S + 75 \cdot P + 45 \cdot Nb - 12.3 \cdot Si -$$
$$- 5.4 \cdot Mn - 1 \qquad (1)$$

C, S, etc. – chemical elements ($w/\%$)

Note: at $w(C) < 0.08\,\%$ the value of 0.08 is used in the equation

In general, the steels with $U_{CS} < 10$ are well resistant to hot cracking, while those with $U_{CS} > 30$ are poorly resistant. The hot cracking of fillet welds can occur at $U_{CS} > 20$ and the hot cracking of butt joints at $U_{CS} > 25$ depending on the shape of the weld pool.[11] Even though equation (1) was only tested with the steel-carbon content of up to $w(C) \le 0.23\,\%$ (this does not mean that the equation cannot be applied to higher-carbon contents), it was also used with the investigated cast steel for the purpose of a comparison with the added filler material. The result of the calculation shows that, due to its chemical composition, the analysed remelted cast steel has a strong tendency to hot-crack formation ($U_{CS} \approx 65.5$). A high content of oxides additionally increases the susceptibility of cast steel to hot cracking (the typical temperature at the centre of the weld pool $T = 2000$–$2500\,°C$ [3], since the melting point of the most known oxides occurring in the metallurgy of iron and steel is $T_L < 2000\,°C$ [12]). The oxide inclusions are admixed to the weld pool and solidified at the transcrystal boundaries.

3.2 Analysis of the built-up tough interlayers

Before hard facing in the preheated state ($T_p = (240 \pm 10)\,°C$) and with a controlled interpass temperature ($T_{mw} = 230$–$300\,°C$), welding current $I = 450$–$550\,A$, voltage $U = 25$–$30\,V$ and welding speed $v = 25$–30 cm/min, the interlayers were built up on the cast steel surface that was prepared by turning. The SAW process with the wire S2 (EN 756) and the agglomerated welding powder SA FB 1 55 AC HP 5 (EN 760) was used. According to reference[13], the chemical composition (in vol. fractions, $\varphi/\%$) of the powder (the fluoride-based type) was: $(CaO + MgO) = 40$, $CaF_2 = 25$, $(Al_2O_3 + MnO) = 20$, $(SiO_2 + TiO_2) = 15$. When used with the S2 wire and appropriate welding parameters, this welding powder ensures the welds with the yield strength $R_y > 330\,N/mm^2$, the tensile strength $R_m = 450$–$550\,N/mm^2$, the impact toughness at room temperature ISO-V >
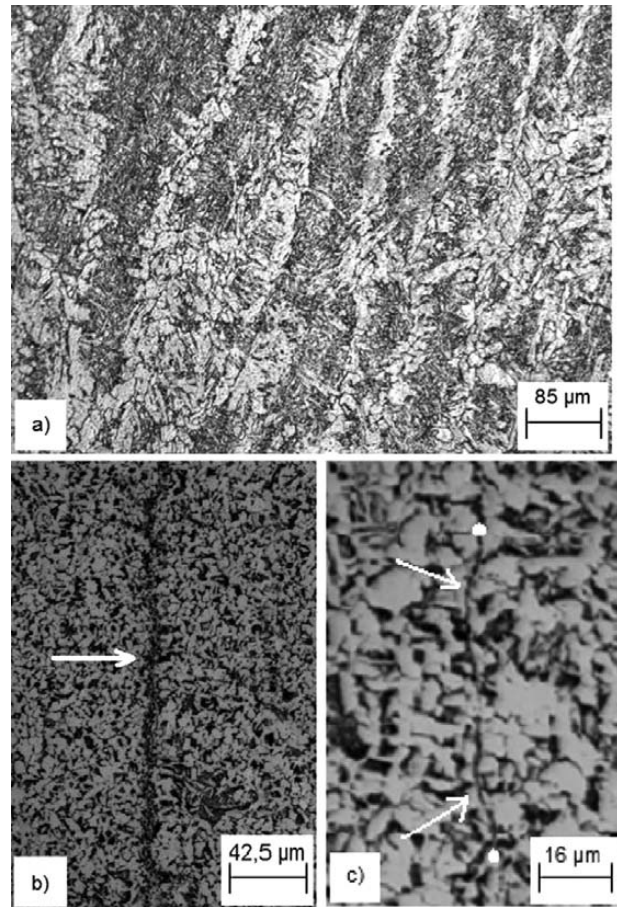
Figure 2: Microstructure of a built-up interlayer: a) the welded state, b) the normalized multi-pass region with non-metallic inclusions (arrows)

Slika 2: Mikrostruktura navarjene vmesne plasti: a) varjeno stanje, b) normalizirano medvarkovno področje z nekovinskimi vključki (puščice)

160 J, and the following deposited-metal chemical composition ($w/\%$): $C = 0.06$; $Si = 0.20$; $Mn = 0.90$.[13] The actual chemical composition of the interlayer welds away from the base material was ($w/\%$): $C = 0.05$; $Si = 0.12$; $Mn = 0.81$; $P = 0.017$; $S = 0.005$; $Cr = 0.047$; $Al = 0.011$ and the impact toughness of the interlayer at room temperature (ISO-V: 190–203 J) justified the use of the appropriate welding materials. The interlayer consists of low-carbon steel with a typical microstructure of the used materials and welding technology. Because of the
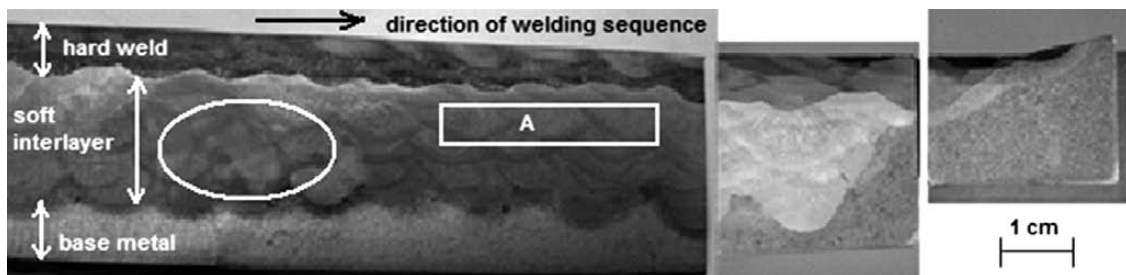
Figure 3: Cross-section through the part of a soft built-up interlayer (b. m. – base material, s. i. – soft interlayear, h. w. – hard surfacing metal)
Slika 3: Prečni prerez skozi del navarjene mehke plasti (b. m. – osnovni material, s. i. – mehka vmesna plast, h. w. – trdi navar)

multi-pass welds, the coarse columnar grains (pro-eutectoid ferrite at the grain boundaries, a fine acicular ferrite-carbide aggregate inside the grains, **Figure 2a**) and the reheated zones (a normalized ferrite-perlite microstructure, **Figures 2b** and **2c**) exist in the deposited layers.

Based on the results of the chemical analysis and the high impact toughness, it can be concluded that the used welding parameters were appropriate. All the weld metal is well resistant to hot cracking, since, according to the measured values of the chemical elements, the index of the hot-crack susceptibility $U_{CS} \approx 13.8$ is low. A problem arises when a significant quantity of the weld metal is contaminated with the base material with a high content of non-metallic inclusions and with a high content of carbon.

3.3 Analysis of the region with a built-up interlayer

The interlayer with a thickness of approximately 15 mm consisted of multilayers with a distinct wavy fusion boundary between the first layer and base material (**Figure 3**), revealing the "bead-to-bead" build-up welding technique with a minimum overlapping of the neighbouring beads. The very deep bead penetration into the base material (**Figure 4a**) caused a large admixture of the base material into the first built-up layer and the chemical composition of the first layer was (w/%): C = 0.18–0.23; Si = 0.23–0.27; Mn = 0.73–0.76; P = 0.023–0.024; S = 0.019–0.021. The first beads, thus, consist of approximately 60–75 % of the base material. In the heat-affected zone (HAZ) the lines between individual beads reveal the leaning towards the outer edge of the groove (in each layer shown in **Figure 3** they occur from left to right). During the build-up welding there were some technological difficulties. In the central part of the macroscopic pattern, an area of an uneven weld laying and unequal bead dimensions is visible (**Figure 3**, a dashed ellipse), which is a sign of grinding and redeposition in this region.

Larger cracks, visible to the naked eye, exist in the built-up layers (**Figure 4a**). Their visible length in the transverse surfacing weld is up to 3 mm (this does not mean that some cracks in the built-up interlayer are not longer). In the base material, the HAZ cracks are of a microscopic size (**Figure 4b**). Even though the U_{CS} index of the welds is small, the interlayers are more susceptible to the crack formation as a consequence of the solidification and growth of the columnar grains from the melt, due to which the impurities and low-melting phases segregate on the longitudinal boundaries of the columnar grains.

In the HAZ of the base material, the shape of the cracks depends on the shape of the non-metallic inclusions, for example, the shape of a rosette (**Figure 4b**). This is a clear indication of a melting of the non-metallic inclusions. These hot cracks are of the liquation type. Due to the non-metallic inclusions in the fusion-line region, a crack in the HAZ may propagate into a bead (**Figure 4b**). If a non-metallic inclusion is near the fusion line, this does not necessarily result in the melting of this inclusion and a crack formation in the HAZ. Liquation cracks only form when the melting point of an inclusion is sufficiently low with respect to the melting point of the base material. Such inclusions in steels are
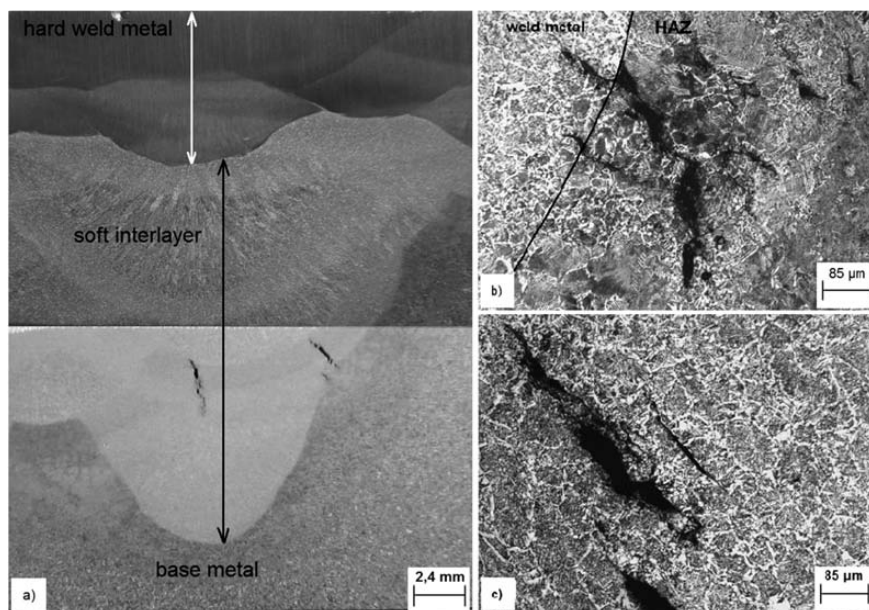
Figure 4: Hot cracks in the built-up interlayer and the base-material HAZ: a) cracks in the edge beads of the built-up interlayer, b) cluster of inclusions with the cracks in the base-material HAZ, c) cracks on the boundaries of the columnar grains in the welds

Slika 4: Vroče razpoke v navaru vmesne plasti in TVC osnovnega materiala: a) razpoke v robnih varkih navarjene vmesne plasti, b) gnezdo vključkov z razpokami v TVC osnovnega materiala, c) razpoke na mejah transkristalnih zrn v navaru

FeO (T_L = 1377 °C) and some complex oxides, for example FeO · SiO$_2$ (T_L = 1217 °C).[12] The inclusion in **Figure 1b** did not melt because of a high melting point and though its position was next to the joining line, the liquation crack did not form. However, when the same inclusion is admixed into the weld pool, it melts due to high temperatures and can cause a solidification crack in the weld.

Cold cracks in the HAZ that would be a consequence of a brittle microstructure with a high hardness were not found. The possibility of a cold-crack formation is minimal despite a higher content of the carbon and a great thickness of the base material due to a multi-pass build-up in the preheated state and a sufficiently high interpass temperature (the low critical cooling time needed for the formation of 100 % martensite in cast steel GS-45 is t_{cr} < 5 s)[8]; its absence in the microstructure is proven with a relatively low hardness of the HAZ (220–270 HV).

Microscopic examinations have shown that, despite a large admixture of the base material, the first beads are already very pure in comparison with the base material (**Figure 1b**). Due to the functioning of the basic-type welding powder and the intensive melt movement during welding, a large portion of non-metallic inclusions is displaced in the slag. Inconveniently arranged intercrystalline non-metallic inclusions do not necessarily lead to a formation of solidification cracks. If the stress state is favourable, the cracks do not occur.

The cracks are only found in the welds on the edge of the prepared groove (**Figure 4a**). As the internal stresses depend on the weld shape, the formation of hot cracks in the beads on the boundary of the groove is logical due to the mutual position of the previous beads and the edge of the welding groove which causes the situation, typical for but welds. A great stiffness due to a great thickness of the welded material causes huge transverse tensile stresses in these edge welds during cooling. In the synergy with the admixed base molten material with a large number of non-metallic inclusions and a high susceptibility to hot-crack formation, this creates the perfect conditions for the formation of hot cracks. With a 60 %
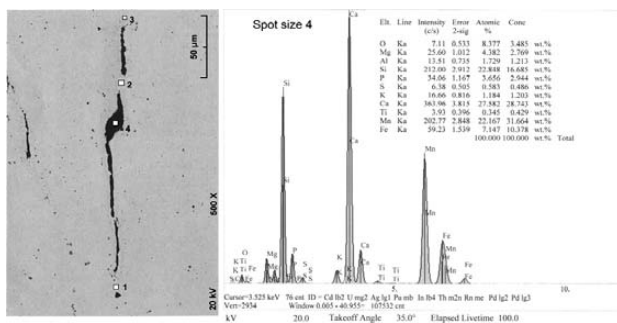
admixture of the base material, the resistance of the first beads to hot cracking is still very low (U_{CS} = 39, calculated from the measured chemical composition; if the index is calculated with the indexes of the base material and added material according to the rule of mixtures, it is a bit higher, U_{CS} = 44.8).

The crack orientation is the same as the direction of the transcrystalline growth; the cracks are situated at the grain boundaries (**Figure 4c**) and they are wide and open. The formation of the cracks is closely related to the presence of non-metallic inclusions at the grain boundaries prolonging the crack line in several places. Longitudinal inclusions are also present in the normalized HAZ between individual beads (**Figures 2b** and **2c**). Due to the normalization of this region, it seems that the non-metallic inclusions were not related to the columnar microstructure of the built-in material. However, a comparison shows that their direction is identical to the longitudinal direction of the columnar grains.

The non-metallic inclusions on the columnar grain boundaries are of very different types: iron oxides (w/%): Fe = 93.4–95.5; Mn = 0.9–1.4; O = 2.3–4.1; Ca + Si < 1) with slightly increased contents of sulphur and phosphorus (w/%): S = 0.34–0.37; P = 0.24–0.39), iron oxi-phosphides (w/%): Fe = 92.6–96.0; O = 0.5–1.1; P = 1.0–1.25; Si = 0.4–3.1; Mn, Cr, Ca: < 1,0) and more complex inclusions of oxi-sulphide (w/%): Mn = 37.0; Fe = 30.8; Si = 6.4; Al = 5.3; Ti = 1.3; S = 16.3; O = 1.9; Cr + Mg ≈ 1.0) and oxi-phosphide (w/%): Mn = 31.7; Fe = 10.4; Ca = 28.7; Si = 16.7; Mg = 2.8; Al = 1.2; K = 1.2; P = 2.9; O = 3.5; Ti + S < 1.0). An inclusion of the oxi-phosphide type with numerous small surrounding inclusions and an EDX spectrogram are shown in **Figure 5** (point of measurement No. 4). Their chemical composition proves that the complex inclusions originate from the welding powder, indicating that the welding-slag-based inclusions exist in the welds, too. These can be a consequence of an inadequate welding technology and the related uncontrolled motion of the weld pool or of the remelting of the slag residue from the previously welded beads. The susceptibility of the weld pool to the formation of hot cracks is, thus, additionally increased by the liquid-slag residues. The metal matrix near the inclusion (points of analysis Nos. 1, 2, 3, **Figure 5**) has an increased content of sulphur (w/%): S = 0.13–0.28), which is probably related to the grain-boundary segregation of sulphur during solidification.

Figure 5: Complex longitudinal non-metallic inclusion in the soft interlayer weld (polished)
Slika 5: Kompleksni trakasti nekovinski vključek v navaru mehke plasti (polirano)

4 CONCLUSIONS

Low-carbon steel was built up on unalloyed cast steel 1.0446 (EN 10027-2) with the highest allowed content of carbon and a high content of non-metallic, sulphide and oxide inclusions. The cast-steel melt was, thus, very susceptible to hot cracking. Individual microscopic liquation cracks are present in the HAZ. They are related

to the sulphide and oxide inclusions. The liquation cracks in the cast-steel HAZ present a smaller problem. The cracks of a few millimetres in the individual beads of the built-up interlayer are more critical.

The use of the "bead-to-bead" build-up technique resulted in a large admixture (60–75 %) of impure cast steel and, thus, the first built-up layer was greatly contaminated with the non-metallic inclusions. In the synergy with the generated high tensile stresses, this resulted in a formation of typical crystallization cracks in the built-up layers along the base material.

The cracks are directly connected to the non-metallic inclusions of the oxide, sulpho-oxide and oxi-phosphide types on the longitudinal grain boundaries of the columnar grains. The non-metallic inclusions are mostly due to the remelting of cast steel, while some (mainly those with a complex chemical composition) are due to the welding slag. Their chemical composition is similar to the welding-powder composition (Ca, K, Mg, Al and higher amounts of Si and Mn; some of these elements are not present in the base material or pure welds, while others appear in small amounts). This reveals either local difficulties during the build-up and uncontrolled, strong and turbulent motion of the weld pool or a poor removal of the welding slag from the narrower and deeper grooves between the beads. In practice, there is a strong, but wrong conviction that because of a powerful electric arc the welding slag is easily removed from a narrow weld groove. This could be one of the reasons for the presence of complex slag inclusions in individual welds.

Hot cracks do not form if the melting volume of the cast steel with non-metallic inclusions is small. This indicates a build up with a sufficient overlapping of the neighbouring beads, ensuring the minimum thickness of the base-material remelt (when using the SAW procedure with a wire electrode, the remelting thickness of the base material can be thinner than 2 mm). The joining line achieved in this way is practically straight and parallel with the base-material surface. The sufficient overlapping of the neighbouring beads also prevents a formation of narrow and deep grooves between the beads, in which the welding slag may be caught and not removed from the weld pool completely by the deposition of the following bead. However, if these narrow and deep grooves do occur in some places, they must be ground into sufficiently wide and rounded grooves prior to welding other beads so that the liquid slag rises to the surface of the weld pool.

5 REFERENCES

[1] I. Hrivňák, Zvariteľnoť oceli (Serbian translation-Ljubomir Nedeljković), Zavarljivost čelika, IRO Građevinska knjiga, Beograd 1982, 31–38

[2] I. Hrivňák, Theory of weldability of metals and alloys, Elsevier, Amsterdam 1992, 61–63, 108–116

[3] ASM Handbook®, Vol 6: Welding, Brazing and Soldering, ASM International®, Materials Park, 2000, 45–54, 88–96

[4] D. Radaj, Welding residual stresses and distortion, Rev. ed., DVS Verlag GmbH, Düsseldorf 2003, 281–282

[5] R. Castro, J. J. de Cadenet, Welding metalurgy of stainless and heat-resisting steels, Cambridge University Press, London 1974, 95–106

[6] M. Blair, T. L. Stevens, Steel Castings Handbook, 6th ed., ASM International®, Materials Park, 1995, 19–7

[7] Standard ASTM A27/A27M-13

[8] P. Seyffarth, B. Meyer, A. Scharff, Großer Atlas Schweiß-ZTU-Schaubilder, DVS Verlag GmbH, Düsseldorf 1992, 140–141

[9] J. Lancaster, Handbook of structural welding, Abington Publishing, Cambridge 1997, 72–78

[10] Standard EN 1011-2:2001, Annex E

[11] FAQ: How can I minimize the risk of solidification cracking in SAW Welds? TWI 2012, http://www.twi.co.uk/ tehnical-knowledge/faqs/

[12] Metalurški priročnik (Handbook of metalurgy), Tehniška založba Slovenije, Ljubljana 1972, 510–511

[13] Elektrode Jesenice, d. o. o., Welding consumables, Jesenice 2006, R5

ŠOLSKI CENTER ŠKOFJA LOKA KONČAL INVESTICIJI V SKUPNI VREDNOSTI 5,5 MILIJONA EVROV

Šolski center (ŠC) Škofja Loka je 3. decembra 2013 slovesno predal namenu Medpodjetniški izobraževalni center (MIC) in uradno obeležil končanje projekta energetske sanacije šolskih objektov. Skupna vrednost obeh projektov je bila približno 5,5 milijona evrov. Odprtja se je udeležil tudi državni sekretar na Ministrstvu za izobraževanje, znanost in šport Aljuš Pertinač, ki je poudaril, da tovrstni projekti "*predstavljajo koalicijo, ki prinaša razvoj in dodano vrednost*". Dnevno dogajanje s prireditvijo ob odprtju sta popestrila bogat kulturni program in interaktivna predstavitev obeh projektov.

ŠC Škofja Loka nadgrajuje svoje izobraževalno-razvojno poslanstvo in odmevne projekte. Potem, ko je v letošnjem letu v sodelovanju z Inštitutom Metron že predelal in v uporabo predal električni avto, je v septembru 2013 končal investiciji gradnje MIC-a in energetske sanacije šolskih objektov. Vzpostavitev MIC-a je bila sofinancirana iz Evropskega sklada za regionalni razvoj, projekt energetske sanacije pa iz Kohezijskega sklada.

Energetska sanacija je bila izvedena na lokacijah Podlubnik 1 b in Kidričeva 59, kar zajema skoraj 13000 m² ogrevanih površin. Poleg zamenjave energetsko neustreznih oken, izvedbe ustrezne toplotne izolacije na zunanjem ovoju in stropih proti neogrevanemu podstrešju ter vgrajene razsvetljave z digitalno DALI-regulacijo je posebnost te energetske sanacije v tem, da ima osrednji objekt prezračevanje z več kot 80-odstotnim vračanjem toplote iz odpadnega zraka (rekuperacija).

Na lokaciji Podlubnik 1 b je sedaj osnovni energent zemeljski plin v kombinaciji s toplotno črpalko za pripravo tople sanitarne vode zunaj kurilne sezone. Kotel na kurilno olje je bil na lokaciji Kidričeva 59 zamenjan s kotlom na lesno biomaso, kar je pomemben korak k energetski samopreskrbi. Nova kurilnica bo namreč omogočila uporabo lesnih ostankov, ki nastanejo v okviru izobraževalnega procesa, za lastno oskrbo s toplotno energijo.

Sistem prezračevanja in hlajenja prostorov je bil povezan v centralni nadzorni sistem, kjer je mogoče upravljati objekt s spletno aplikacijo. Na saniranih objektih je bil vzpostavljen sistem digitalnega obratovalnega monitoringa energetskega upravljanja (DOM:EU), s katerim je mogoče v vsakem trenutku na daljavo spremljati porabo toplotne in električne energije ter vode in stanje klimatskih razmer objekta.

"*Poraba toplotne energije se bo lahko na podlagi izvedenih ukrepov po strokovni oceni zmanjšala za 65 %, poraba električne energije pa za okoli 15 %,*" je na uradnem odprtju pojasnil direktor ŠC Škofja Loka Martin Pivk. Skupna vrednost investicije je 2 395 854 evrov, delež sofinanciranja pa je 91,7 % vrednosti investicije.

Martin Pivk je v svojem govoru predstavil tudi projekt gradnje MIC-a. Povedal je, da "*je bil na okoli 2200 m² uporabnih površin zgrajen objekt, ki omogoča*

izvajanje kakovostnega poklicnega in strokovnega izobraževanja, usposabljanja ter povezovanja z gospodarstvom," in poudaril, da "*je MIC vez med šolstvom in gospodarstvom*". Gospodarstvo tako v MIC-u pridobiva partnerja, ki lahko v kratkem času zagotovi fleksibilno in potrebam naročnika prilagojeno izobraževanje. Na didaktičnih strojih, ki so enakovredni profesionalni opremi v gospodarstvu, je mogoče tudi razvijati in preizkušati izdelke.

V okviru gradnje MIC-a Škofja Loka je bilo dobavljene tudi nekaj nove opreme. MIC tako danes razpolaga z najsodobnejšim tehnološkim laboratorijem za poučevanje CNC-tehnologij, s CAD- učilnicami s 3D-skenerjem in 3D-tiskalnikom, z laboratorijem za avtomatizacijo in robotiko, laboratorijem za merilno tehniko ter z orodjarsko, inštalatersko in avtoservisno delavnico za področje strojništva. Celovitost ponudbe na tem področju

dopolnjujeta sodobno opremljena varilnica in večnamensko pripravljalno mesto za avtokaroserijsko dejavnost. Za izobraževanje in usposabljanje v lesarstvu je na voljo mizarska ročna in strojna delavnica s CNC in lasersko tehnologijo ter več računalniških učilnic z računalniškimi programi za obdelavo lesa in lesno gradnjo.

Gradnja MIC-a je posredno prispevala k pomembni investiciji na Škofjeloškem, in sicer k ureditvi porečja Selške Sore s protipoplavno zaščito območja Podna. Njen pomen je na osrednji prireditvi poudaril tudi župan Občine Škofja Loka mag. Miha Ješe, ki je povedal, da "*smo s protipoplavno zaščito in MIC-em dobili najlepši del Škofje Loke*".

Skupna vrednost projekta MIC Škofja Loka je 3 080 916 evrov in je v vrednosti 2 391 818 evrov sofinancirana iz Evropskega sklada za regionalni razvoj.

Vir: Šolski center Škofja Loka